

7. SITE 866¹

Shipboard Scientific Party²

HOLE 866A

Date occupied: 6 April 1992
Date departed: 23 April 1992
Time on hole: 16 days, 22 hr
Position: 21°19.953'N, 174°18.844'E
Bottom felt (rig floor, m; drill-pipe measurement): 1372.6
Distance between rig floor and sea level (m): 10.80
Water depth (drill-pipe measurement from sea level, m): 1361.8
Total depth (rig floor, m): 3116.2
Penetration (m): 1743.6
Number of cores (including cores with no recovery): 189
Total length of cored section (m): 1743.6
Total core recovered (m): 268.98
Core recovery (%): 15.4
Oldest sediment cored:
Depth (mbsf): 1620.0
Nature: Oolitic grainstone, limestone, breccia
Age: Barremian
Measured velocity (km/s): 3.0–5.5
Hard rock:
Depth (mbsf): 1743.6
Nature: Basalt
Measured velocity (km/s): 2.5–3.5

HOLE 866B

Date occupied: 23 April 1992
Date departed: 24 April 1992
Time on hole: 17 hr, 30 min
Position: 21°19.952'N, 174°18.870'E
Bottom felt (rig floor, m; drill-pipe measurement): 1357.1
Distance between rig floor and sea level (m): 11.02
Water depth (drill-pipe measurement from sea level, m): 1346.1
Total depth (rig floor, m): 1474.5
Penetration (m): 117.4
Number of cores (including cores with no recovery): 13
Total length of cored section (m): 117.4
Total core recovered (m): 23.06
Core recovery (%): 19.6

Oldest sediment cored:

Depth (mbsf): 117.4
Nature: Wackestone
Age: late Albian
Measured velocity (km/s): 4.0–5.0

Principal results: Site 866 (proposed Site Hue-A) is located on the north rim of the summit of Resolution Guyot in the western Mid-Pacific Mountains. The site was drilled for the following goals:

1. Correlating shallow-water sediments atop the guyot, with pelagic sediments and turbidites sampled in the adjacent basin at DSDP Site 463;
2. Determining the history of carbonate platform formation, from inception to final drowning;
3. Determining the subsidence history of the guyot;
4. Developing a model of reefal and lagoonal facies anatomy for the former atoll;
5. Examining the timing and magnitudes of relative sea-level fluctuations, including emergence, karstification, and final drowning events;
6. Developing a model of seismic stratification for comparison with other guyots;
7. Studying the diagenetic history of Pacific platform carbonates;
8. Establishing an Early Cretaceous paleolatitude for the guyot;
9. Determining a reliable radiometric age for the volcanic pedestal; and
10. Comparing the geochemical and isotopic signatures of the guyot's volcanic pedestal with basalts from other western Pacific Ocean seamounts.

Drilling in Hole 866A reached nearly twice the planned depth and set a record for the greatest single-site penetration during a single ODP or DSDP leg. This occurred in part because the limestones (1) proved to be more easily drilled than anticipated and (2) produced a stable hole. Consequently, no time was lost setting up a reentry cone with casing. Extra time was spent in attaining penetration because seismic velocities in the limestone cap were underestimated and the deep, prominent reflector, identified in site surveys as probably basalt, was not the top of the volcanic pedestal. Drilling continued until basalt was cored, at 1620 mbsf, and an attempt was made to drill 200 m of basalts, as proposed in the cruise prospectus. Unstable hole conditions led to the termination of the hole after drilling 124 m of basalt. We chose to forgo extra basalt penetration in an effort to avoid losing the drill string, the hole, and the opportunity to log a remarkable limestone succession.

Because recovery with the RCB bit was poor in the upper few hundred meters of Hole 866A, an additional hole (866B) was drilled. The purpose of this second hole was to sample the zone of mineralized limestones thought to be at the top of Resolution Guyot, by analogy to Allison Guyot (Site 865). Rather than drill using the RCB bit, a diamond bit was chosen for this hole, because diamond bits had been used in carbonate platforms elsewhere with some success. This type of bit also posed a limitation: it drills a hole too small for the normal drill pipe used on the *JOIDES Resolution*. Consequently, penetration was limited to the length of undersized drill collars on board (approximately 120 m). Nevertheless, Hole 866B penetrated 117.4 mbsf, with an average recovery of 4.3% in limestones. This was a significant improvement over the same interval of Hole 866A and allowed the scientific goals to be addressed in that part of the sequence.

As at Site 865, core recovery was low in some intervals, especially in the upper third of Hole 866A. Once again, the poorly recovered limestones

¹ Sager, W.W., Winterer, E.L., Firth, J.V., et al., 1993. *Proc. ODP, Init. Repts.*, 143: College Station, TX (Ocean Drilling Program).

² Shipboard Scientific Party is as given in list of participants preceding the contents.

were porous wackestones. In the upper 300 m of shallow-water limestone in Hole 866A, the average recovery was only 1.4%. With increased cementation, sediments in the lower reaches of Hole 866A cored better: in the oolite grainstone section (Unit V), the average was 28.1% and in the bottom 220 m of dolomite, it increased to 34.2%. These rates compare favorably with typical values from Mesozoic pelagic sediments drilled by DSDP and ODP at other sites over the years.

Using combined microfossil and macrofossil biostratigraphy, visual core descriptions augmented with smear-slide and thin-section data, physical properties data, and downhole logs, eight principal stratigraphic units were recognized above volcanic basement (see "Lithostratigraphy" section, this chapter). Because core recovery was low in some intervals, downhole logs were particularly valuable when constructing a stratigraphic framework and for correlating sedimentary layers with seismic horizons (see "Seismic Stratigraphy" section, this chapter). In normal stratigraphic order (from bottom to top), the lithologic divisions are described as follows:

1. Unit VIII (1620.0–1399.7 mbsf). Barremian dolomitized and undolomitized oolitic/oncolidal grainstone. The unit is divided into two subunits on the basis of dolomitization: the lowest 19 m, overlying basalt, is almost undolomitized, whereas the upper 202 m is pervasively dolomitized and tan in color, with lighter-colored, unreplaced oncoids in places. Common biogenic components are gastropods, bivalve fragments, echinoid spines, and green algae. Coral fragments and bryozoans occur rarely. Dolomitization decreases upward and becomes patchy near the top of the unit.

2. Unit VII (1399.7–1203.4 mbsf). Barremian dolomitized oolitic/peloidal grainstone, oncolidal wackestone, and algal laminites, with clay/organic-rich layers. The main characteristic of this unit is the pervasive sucrosic dolomitization and the abundance of oncoids. It is split into four subunits by an interval of bright white, dolomitized, peloidal grainstone overlain by a layer of coral peloidal grainstone in the middle part of the unit. Components include oncoids, benthic foraminifers, peloids, fragments of rudist and other bivalve shells, serpulid worm tubes, echinoids, corals, nerineid gastropods, stromatoporoids, and dasycladacean algae. Intergranular and moldic porosity is common near the bottom of the unit.

3. Unit VI (1203.4–791.8 mbsf). Aptian cyclic packstone/wackestone with algal laminites, clay/organic-rich layers, and patchy dolomitization. The primary characteristic of Unit VI is the cyclic repetition of lithologies in meter-scale, shallowing-upward sequences that imply fluctuations in relative sea level. Cycles typically begin with peloidal wackestone or packstone and grade upward into wackestone or mudstone. The tops of these sequences are commonly truncated and show small-scale desiccation cracks, implying emergence and erosion. Unit VI is subdivided into three parts, based on the occurrence of a caprinid rudist biostrome in the middle.

4. Unit V (791.8–676.6 mbsf). Aptian oolitic grainstone. Unit V consists of 115 m of massive, well-sorted, oolite sandstone that is cross-laminated in some spots. Though grainstone is predominant, there are short intervals with rudstone, where large fossils occur, and with wackestone, where micrite is abundant. Other components are peloids, grapestones, intraclasts, rare oncoids, bivalve debris, corals, and gastropods. Locally, ooids and peloids are blackened by manganese oxides. The oolitic grainstones exhibit a high-degree of overpacking and grain interpenetration.

5. Unit IV (676.6–434.5 mbsf). Aptian cyclic packstone/wackestone with scattered clay/organic-rich layers. Bioturbated peloidal packstone, wackestone, and grainstone with gastropods and foraminifers characterize Unit IV. Meter-scale submergence-emergence cycles, similar to those in Unit VI, occur with laminated wackestone and packstone, decreasing in frequency upward in the unit. Other components in these limestones are bivalve fragments, dasycladacean algae, and scattered lignite fragments. Smectite clay layers occur in the lower part of the unit and decrease in frequency upsection.

6. Unit III (434.5–19.6 mbsf, Hole 866A; 117.4–32.8 mbsf, Hole 866B). Aptian to Albian wackestone and mudstone. This unit is predominantly wackestone with lesser amounts of mudstone, packstone, and grainstone.

Common components are gastropods, bivalves, benthic foraminifers, echinoids, ostracodes, sponges, and dasycladacean algae. Rare components are corals, serpulid worm tubes, and bryozoans. Aragonitic fossils have been largely dissolved to create a moldic porosity. Calcrete layers decrease in frequency upward. Three subunits were distinguished based on porosity and the occurrence of calcrete horizons.

7. Unit II (19.6–0.9 mbsf, Hole 866A; 32.8–23.5 mbsf, Hole 866B). Cretaceous manganiferous limestone. This poorly recovered unit is known from only a few small pebbles of manganese-encrusted limestone and from comparison with the mineralized limestone unit of Allison Guyot (Site 865). It represents the mineralized surface layer of the shallow-water limestones.

8. Unit I (0.9–0.0 mbsf, Hole 866A; 23.5–0.0 mbsf, Hole 866B). Maastrichtian to upper Pliocene foraminiferal nannofossil ooze. Unit I is the thin pelagic layer representing part of the post-drowning history of Resolution Guyot. It has been winnowed and reworked and contains iron-manganese micronodules.

Most of the preliminary shipboard biostratigraphy is based on benthic foraminifers because planktonic foraminifers and calcareous nannofossils are absent from, and palynomorphs are rare in, the shallow-water limestones. The deepest sediments from Hole 866A (1200–1620 mbsf) contain a Barremian foraminiferal assemblage. A gradual shift to an Aptian-age assemblage occurs at about 1200 mbsf. Higher up, at approximately 271 mbsf, there is a shift to Albian assemblages. The thin layer of pelagic sediment atop the guyot has nannofossils and foraminifers of Maastrichtian to late Pliocene age, some of which are in reworked layers.

Bulk density and sonic velocity measurements in the thick, shallow-water limestone sequence show remarkable trends (see "Physical Properties" section, this chapter). The shallowest 420 m of recovered limestone has relatively high seismic velocities and densities, with values of 4.4–6.5 km/s and 2.4–2.7 g/cm³, respectively. In the lower part of the limestone section, from 1200 to 1620 mbsf, high velocities and densities also are found, but there is a much larger range, approximately 2.1–6.8 km/s and 2.15–2.75 g/cm³, respectively. The large scatter is evidently caused by alternating hard dolomite and softer limestone layers. In the middle of the section, from about 420 to 1200 mbsf, is a low-velocity/density zone having consistent velocities of 1.8 to 4.5 km/s and densities of 2.1–2.4 g/cm³. These trends are a significant departure from the common monotonic increase in seismic velocity and bulk density observed in most deep-sea sediments. Their cause is undoubtedly related to a complex diagenetic history.

As at Site 865, the downhole logs from Hole 866A provided a valuable framework for understanding the core material (see "Downhole Measurements" section, this chapter). Unfortunately, collapse of the basement section of the hole prevented significant penetration of the logging tools into the basalt section. In the limestones, sonic velocity and density logs showed trends similar to those in the physical properties data, but the values were generally somewhat lower, indicating that the core material is a preferential sample of the more indurated material. Resistivity logs displayed excellent correlation with lithology. High-resistivity layers between 271 and 434 mbsf correspond to the dense, high-seismic-velocity mudstones and wackestones of lithologic Unit III. Likewise, high-resistivity layers in lithologic Units VII and VIII appear to correlate with pervasively dolomitized sediments. Geochemical and formation microscanner (FMS) logs were also recorded in Hole 866A. The geochemical logs require additional processing and interpretation, but appear to show small variations probably related to clay content. The FMS shows variations in borehole wall resistivity that suggest correlations to porosity and structure. Some of the variations appear cyclic.

Drilling in Hole 866A penetrated 123.6 m of basalt with 37% overall recovery. The basalt/limestone contact is at 1620.0 mbsf. The basalt itself is subaerial and lightly to heavily altered. Red clay zones were cored in several intervals, indicating subaerial weathering and the development of lateritic soils. Poorly recovered rubbly zones imply that the basalt flows were of the clinkery aa type. Above the basalt/limestone contact, volcani-

clastic grains are generally small, not very abundant, and restricted to the 40 m above the basalt. This probably indicates that any exposed volcanic remnant was small and not near the site.

Magnetic measurements of the basalt section at the bottom of Hole 866A show that the basalts have reversed polarity. This shows that they are older than Chron M0 (118 Ma, Kent and Gradstein, 1985), because the basalt is overlain by Barremian-age sediments.

Studies of inorganic compounds from interstitial waters in the pelagic cap and from limestones indicate that these waters are mostly indistinguishable from normal seawater. On the other hand, sulfate and ammonium concentrations indicate a slight amount of reaction with buried organic matter. Carbonate content is generally high in the limestones, typically 97% to 99%, but decreases locally in clay layers, where values as low as 22% were measured. Low (less than 0.3%) total organic carbon (TOC) values are typical of most of these limestones. In clay-rich layers and algal laminates, values were typically, but not uniformly, higher.

Hole 866A records virtually the entire history of carbonate platform formation, drowning, and diagenesis on Resolution Guyot. The story begins with the waning eruptive stages on the volcanic pedestal. Its age is as yet unknown, but reversed magnetic polarity and overlying Barremian sediments imply that it formed prior to Chron M0. The height of the pedestal was much smaller than expected. A comparison of extrapolated depth to basement at Site 463 with the depth of basement in Hole 866A implies that the volcanic edifice had a relief of only about 500 m above the basaltic plateau that underlies most of the western Mid-Pacific Mountains. An implication of this result is that a very large region of the western Mid-Pacific Mountains was at depths less than about 1 km from sea level in Barremian time. The volcanic underpinnings were quickly submerged and added little sediment to the limestones above.

The carbonate cap on Resolution Guyot is surprisingly thick, with approximately 1620 m of shallow-water limestone. This carbonate sequence ranges in age from Barremian to Albian. There are potentially several hiatuses within the limestone section. One possible lacuna, at about 1400 mbsf in the Barremian, was recognized solely on the basis of an abrupt change in the paleodepth, implied by foraminiferal assemblages. However, this and other potential breaks are of uncertain duration and significance because of limited fossil control. Nonetheless, the carbonate platform may have formed in two or more stages.

During the active stage of carbonate platform growth, the platform stayed at or near sea level. Generally, sediment facies show that most sediments were deposited in shallow, often restricted, lagoonal environments that gradually deepened and became more open marine with time. By contrast, meter-scale facies cycles in much of the limestone section imply small-amplitude, short-term fluctuations in relative sea level.

Final drowning of the platform occurred between late Albian and Maastrichtian time, when the first preserved pelagic sediments were deposited atop the shallow-water limestones. Sometime during this period, the platform was emergent and subjected to karstification, as suggested by sinkhole and other karstic features seen in 3.5-kHz and seismic profiles over the guyot (see "Site Geophysics" section, this chapter). This is also shown by fresh-water dissolution and cave deposits in the uppermost part of the shallow-water limestones at Site 866. Subaerial exposure and the increased porosity it caused also led to phosphatization of these limestones.

Diagenesis was important for modifying the shallow-water carbonates. In general, three effects were noted: differential lithification, dolomitization, and karstification. Differential lithification created alternating layers of harder and softer limestone, so that density and porosity do not increase monotonically downward. A notable interval is the denser wackestone layers at the top of the Aptian section, from about 271 to 431 mbsf. Dolomitization was locally pervasive, but patchy. Although deeper limestone layers exhibit the most dolomitization, some interbedded layers and the overlying layers were unaffected or were only lightly dolomitized. The timing of the dolomitization is uncertain, but indications are that it occurred soon after burial. Post-Albian subaerial exposure and the creation of a lens of freshwater within the uppermost limestone layers caused widespread dissolution and the formation of cavities and cavity deposits in the vadose

zone. Many cavities were later filled by fine-grained sediments and permeated with phosphate and iron-manganese oxyhydroxides.

Drilling at Site 866 changed the way we view Cretaceous, carbonate-capped guyots. For years, geophysical ships crossed these features and brought back profiles that were fitted to the classic picture of modern Pacific Ocean atolls. A prominent, deep seismic reflector was commonly seen and assumed to be the volcanic basement upon which a perimeter reef grew. This volcanic pedestal was generally thought to make up the preponderance of the guyot, typically with several kilometers of volcano capped with less than 1 km of limestone. Furthermore, prominent mounds around the guyot perimeter and scattered seismic energy at the guyot edges were presumed to show a drowned perimeter reef. Layered seismic horizons in the interior were interpreted as lagoonal limestones having relatively low seismic velocities and densities, both of which should nominally increase with depth.

Hole 866A showed that, in the Mid-Pacific Mountains at least, the volcanic pedestal makes up less than half the total height of the guyot above the surrounding basaltic basement. Owing to the diagenesis of the limestone cap, estimates of the thickness of the carbonate cap were off by a factor of two because (1) the "basement" reflector was not associated with the top of the volcanic pedestal and (2) acoustic wave velocities of the limestones were underestimated. In addition to these misinterpretations, the modern atoll model may also be inadequate. Despite drilling nearly 2 km of carbonate material at Site 866, a location less than 2 km from the edge of the guyot, little reef-derived material was recovered.

BACKGROUND AND SCIENTIFIC OBJECTIVES

Site 866 (proposed Site Hue-A) was drilled atop an unnamed guyot in the western Mid-Pacific Mountains. Its unofficial name, "Huevo," used in the prospectus, was coined during the Roundabout Expedition Leg 10 site survey when the egg-shaped plan view of the guyot was noticed on a day when *huevos rancheros* (Mexican-style eggs) were on the ship's menu. At our request, the U.S. Board of Geographic Names has bestowed the official name "Resolution Guyot" on this feature, not only because it was drilled by the *JOIDES Resolution*, but also because resolution was required to achieve the scientific and technical objectives at Site 866.

Sites 866 and 867/868 (Hue-B) were conceived as part of a transect across a Mid-Pacific Mountains guyot. Together with Site 463, drilled during DSDP Leg 62 (Thiede, Vallier, et al., 1981) and located about 24 nmi (44.4 km) away in the basin to the east (Fig. 1), they form a transect from lagoon to perimeter mound to basin. Site 866 is located at 21°19.95'N, 174°18.84'E and was placed so as to penetrate lagoonal facies limestones just behind the perimeter mound, which was thought to be an organic reef or part of a chain of perimeter islands surmounting a reef. The site was also to be a multiple-reentry site whose goal was penetration of the entire limestone cap and a significant section of the volcanic pedestal. Sites 867/868, located at 21°20.96'N, 174°18.57'E and 21°21.17'N, 174°18.56'E, respectively, are on the perimeter near Site 866. Site 867 was envisaged as a shallow hole to penetrate only the karstified, upper part of the perimeter mound, whereas Site 868 was to sample the terrace seaward of the mound.

From geophysical data collected during the Roundabout Expedition, the Leg 10 site-survey cruise, we expected that Resolution and Allison guyots (Site 865) would be more alike than different in their formational ages and sedimentation histories. With the exception that Resolution lacks a thick pelagic cap, seismic sections over the two guyots seemed similar. Resolution displays 0.03-s two-way traveltime (twtt) of pelagic sediments atop a karstified surface thought to be eroded into shallow-water limestone. Beneath that are numerous upper-level seismic reflectors and what appears to be a "basement" horizon at about 0.8-s twtt below the top of the limestones (see "Site Geophysics" and "Seismic Stratigraphy" sections, this chapter). As we were to discover, our preconceived ideas about Resolution and similar guyots were incorrect in many respects.

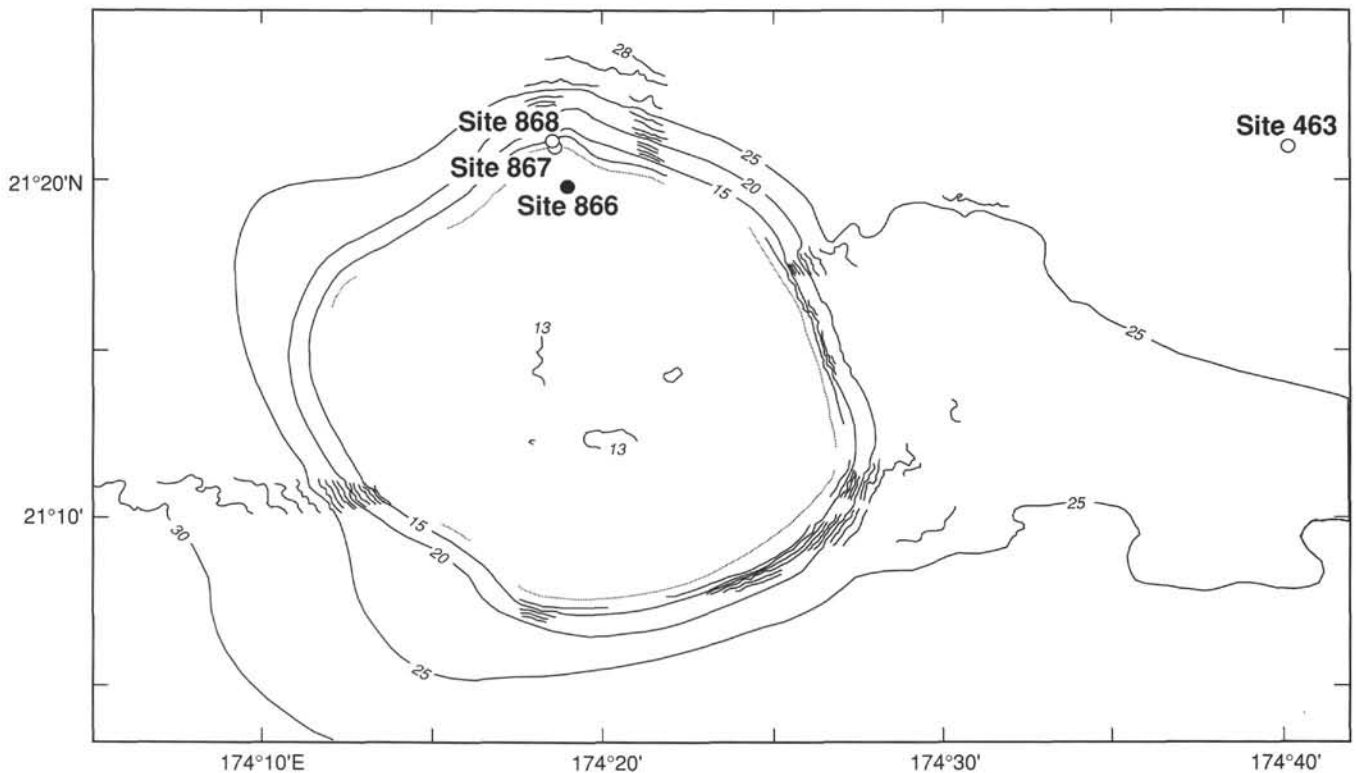


Figure 1. Bathymetry of Resolution Guyot and location of Site 866. Bathymetric contours at 100-m intervals with SeaBeam multibeam echo-sounder coverage. Solid line contours are at 500-m intervals and include data acquired during pre- and post-drilling surveys aboard the *JOIDES Resolution*. Contour labels in hundreds of meters. Gray line shows the location of the summit perimeter mound. Site 866 is shown by a filled circle; Sites 867, 868, and 463 (DSDP Leg 62; Thiede, Vallier, et al., 1981) are denoted by open circles. Site survey data were acquired in 1988 during Leg 10 of the Roundabout Expedition of the *Thomas Washington* of Scripps Institution of Oceanography.

The location of Site 866, on the north rim of Resolution Guyot, was selected to achieve the following goals:

1. Sampling the likely source material, in situ, of sediments drilled at nearby Site 463, where the oldest sediments are redeposited reef debris interstratified with pelagic sediments of late Barremian age;
2. Penetrating the oldest pelagic sediments post-dating the shallow-water limestone, and constraining the time of shallow-water drowning and the age of the underlying basaltic basement;
3. Correlating lagoonal sediment facies, ages, and horizons with those drilled at Site 865 on Allison Guyot;
4. Coring the oldest and deepest lagoonal sediments to provide constraints for the age of reef formation; and,
5. Sampling a sufficient amount of basement to determine a reliable radiometric age for the volcano and to calculate its paleolatitude.

Resolution Guyot proved to be a surprise. Volcanic material was not encountered until a depth of 1620 mbsf, rather than at the predicted depth of 995 mbsf. Moreover, its sedimentary history appears very different from that of the portion of Allison Guyot that we sampled at Site 865. With hindsight, we can see that the seismic reflectors were sequenced differently, and that the one selected as "basement" was merely the deepest coherent seismic horizon that could be imaged with a small water-gun seismic source. We also knew from the Site 865 results that our pre-cruise estimates of the seismic velocities were incorrect. Nevertheless, our drilling at Resolution was able to address all of the pre-cruise science objectives. In addition, it serendipitously provided scientific data that will cause us to rethink our ideas about the formation of guyots in general and the Mid-Pacific Mountains in particular.

Site Selection

Hole 866A was not drilled at the precise location of proposed Site Hue-A. The latter was selected along one of the Thomas Washington Roundabout Leg 10 site-survey lines where the thin pelagic sediments atop Resolution guyot were thickest (see "Site Geophysics" section, this chapter). This would allow us the best chance of successfully spudding-in the hole. Drilling at Site 865 on Allison Guyot indicated that reef debris was sparse in the lagoonal sediments, so we decided to move Site 866 toward the perimeter mound, if such a spot could be found with 20 to 30 m of pelagic sediments to support the BHA. This was done by assuming that the perimeter mound was the Cretaceous reef complex, in analogy with modern atolls. We also presumed that the perimeter mound was essentially two-dimensional and parallel to the summit edge, so that any location on the mound would yield the same results. A short survey with the 3.5-kHz echo-sounder aboard the *JOIDES Resolution* located such a spot, 1.2 nmi (2.3 km) northeast of the proposed site and approximately 1 km from the perimeter mound (see "Site Geophysics" section, this chapter).

Site 866 was also selected with respect to deeper seismic reflection horizons. Although lagoonal seismic reflectors are generally absent at the edges of guyots, probably owing to diffraction of the seismic waves by the roughness of near-reef sediments, Site 866 was positioned where deep seismic horizons were discernible. In particular, a spot was chosen where it was possible to trace the prominent reflector at approximately 0.85 s (two-way traveltime). This reflector was originally thought to be volcanic basement (see "Seismic Stratigraphy" section, this chapter). In addition, Site 866 is located where seismic layers dip from the perimeter into the center of the lagoon,

with our thinking being that reef debris would have been washed over onto this slight slope.

Drilling Objectives

Drilling at Site 866 had the following goals:

1. To develop a history of Cretaceous mid-ocean carbonate platform growth and evolution by determining the lithologic, biostratigraphic, isotopic, and seismic stratigraphic successions within the limestone cap, for use in
 - A. Direct correlation with other guyots drilled during Legs 143 and 144;
 - B. Correlations through reflection seismology among guyots in the northwestern Pacific;
 - C. Comparisons of the timing and magnitude of relative sea-level changes recorded in the guyot limestones with sea-level curves developed elsewhere in the world;
2. To examine the timing and extent of the karstification event(s) evident in the morphology and in seismic reflection profiles of Resolution and other western Pacific Ocean guyots;
3. To provide constraints on the timing and cause(s) of platform drowning;
4. To study the diagenetic history of platform carbonates;
5. To compare the shallow-water biotic assemblages to others of similar age elsewhere as a clue to migration patterns;
6. To gather pore-water samples from the lagoonal sediments, as a means to infer residence times and chemical evolution of interstitial waters;
7. To obtain a suite of downhole logs that would illuminate the structure, stratigraphy, and composition of the carbonate cap and upper volcanic layers of a guyot;
8. To collect data about seismic wave velocities in Cretaceous platform carbonates to use in the interpretation and correlation of seismic-reflection and refraction data from Pacific Ocean guyots;
9. To determine a reliable Early Cretaceous paleolatitude for constraining the tectonic history of the guyot, and the Pacific Plate as a whole;
10. To obtain a reliable radiometric date for the basalt of the volcanic pedestal for evidence of the timing of volcanism in the Mid-Pacific Mountains; and
11. To compare geochemical and isotopic signatures of the basaltic foundation of the guyot to basalts from other seamounts, for evidence of the magma source.

Objectives Addressed and Accomplished

As detailed in various sections of this site chapter, preliminary shipboard study of the samples and downhole logs collected at the site suggests that the main objectives can be met through further post-cruise study of both data and samples. Core recovery was low in the upper several hundred meters below seafloor of Hole 866A, but study of the downhole logs suggests that the recovered materials are representative of the rocks penetrated. The logs themselves are of excellent quality. In the lower part of Hole 866A, core recovery improved considerably.

The first stratigraphic set of objectives was addressed by detailed shipboard examination of the textures, structures, compositions, and fossil content of cored limestones. Shipboard age data from macrofossil and microfossil studies are preliminary, but place strong constraints on the age of the limestones. Additional age constraints should become available through post-cruise strontium-isotope measurements of samples collected. Downhole logs were an invaluable aid for reconstructing the limestone stratigraphy because they provided a continuous record of physical and chemical properties for use as a framework into which the recovered samples could be fitted.

Objectives 2 and 3, understanding karstification and drowning, were pursued by studying the sediments and fossils that bracketed the contact between pelagic cap and shallow-water limestone. Detailed lithologic and chemical analyses of the highest shallow-water limestones were used to infer the extent of karstification and the processes that led to the demise of the carbonate platform. Once again, downhole geochemical logs were an important tool because they provided a record of mineralization in the upper platform limestones. Paleontological studies and strontium-isotope measurements will yield age constraints.

The diagenesis of guyot carbonates (Objective 4) will be addressed by detailed petrographic examination of thin sections, combined with petrologic and isotopic analyses of rock compositions. Different layers of the same type of rock, or even different components of the same rock, show diagenetic differences that delineate the processes and history of diagenesis. Downhole logs will be used for further information about composition and the stratigraphic framework. In addition, other properties, such as paleomagnetism, may also give constraints on diagenetic timing.

Objective 5, biostratigraphy, has been and will be addressed by studying the fossils recovered in the cores and by comparing them with the known global distribution of Cretaceous platform biota.

Objective 6, pore-water geochemistry, was accomplished by analyzing interstitial waters squeezed from whole-round samples taken from the pelagic cap sections of Holes 866A and 867A.

Downhole logs, acquired to meet Objective 7, proved to be extremely valuable for interpreting the drilling results at Site 865; thus, obtaining a similar set of data for Sites 866 and 867 became an especially high priority. Geophysical and geochemical tool strings were run to obtain bulk physical (sonic velocity, gamma-ray, bulk density, resistivity) and geochemical properties. These logs showed cyclical variations that imply alternating hard and soft layers, subtle compositional differences probably caused by sea-level fluctuations and emergent layers. The FMS was run to yield high-resolution resistivity maps of the borehole wall, which can be interpreted in terms of structure and rock texture.

Objective 8, the derivation of velocity/depth data for seismic interpretation, was attacked from several directions. One tack was to obtain downhole logs of in-situ sonic wave velocity and density. Another was to perform complementary measurements in the recovered cores. In addition, a seismic refraction line was shot across the guyot summit with an expendable sonobuoy (see "Operations" section, this chapter).

Objectives 9 to 11, paleolatitudes, radiometric dating, and basalt geochemistry, were addressed by continuing to drill Hole 866A deep into the volcanic pedestal of the guyot. A paleolatitude was determined by averaging magnetic field inclinations recorded by different flow units at the time the basalts were erupted. Dating will be accomplished by shore-based ^{40}Ar - ^{39}Ar whole-rock and isochron analyses. In addition, fusion analyses will be attempted on individual crystal separates. Finally, the cored basalts will be studied using a variety of analytical techniques to obtain compositional information.

OPERATIONS

Transit from Site 865 to Site 866

The transit to Site 866 began at 0115 UTC, 5 April 1992, and ended at 2029 UTC, 6 April 1992, when an acoustic beacon was dropped at the site. We began the transit by steaming a short distance south of Site 865, to stream seismic gear, and then turning on a course that brought us over Site 865 and then northward across the western part of Allison Guyot (see Fig. 2 and "Site 865" chapter, this volume). Steaming at 6 kt, a normal-incidence, seismic-reflection record was obtained over the guyot using a 200-in.³ water gun. An expendable sonobuoy was deployed near Site 865 as we steamed northward, and an attempt was made to obtain a wide-angle sonobuoy recording. The

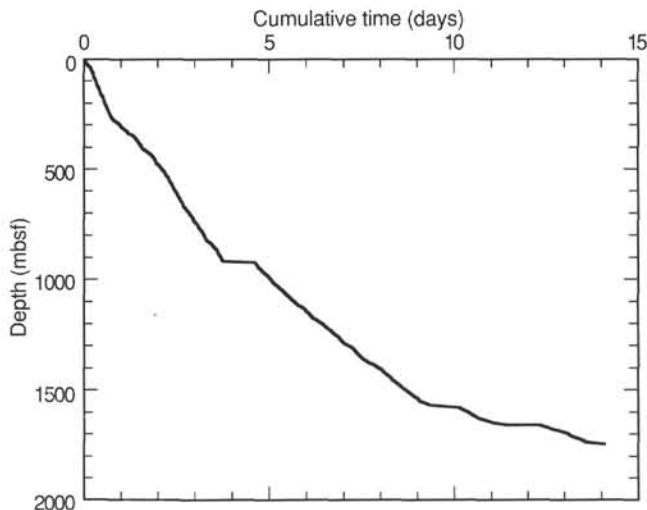


Figure 2. Plot of depth in Hole 866A vs. elapsed time on site. The "shelves" at 917, 1569, and 1658 m identify pauses for changing bits.

reception on the radio receiver was poor and so was the analog record. In addition, digital data were not properly recorded, partly owing to incorrect settings of the delay times on the digital recorder.

At the north edge of the guyot, the ship turned on a west-northwest course directly toward Resolution Guyot, and speed was increased to about 10.5 kt. We continued to obtain seismic-reflection records using the 200-in.³ water gun as our sound source during the transit. Our course took the vessel directly over the top of Hamilton Guyot, and a classical drowned-atoll profile was obtained over this feature.

At a point a few miles directly east of Resolution Guyot, we slowed to 6 kt to begin a survey, using the 200-in.³ water gun and the 3.5-kHz system. The ship's track, followed during the survey, as well as reproductions of the seismic and 3.5-kHz records appear in the "Site Geophysics" section (this chapter).

The survey revealed a location, about 1.2 nmi east-northeast of the proposed drill site (Hue-A) that appeared preferable because it showed a thicker (0.03 vs. 0.02 s) lens of post-reef pelagic sediments in which we could spud closer to the perimeter than at proposed Site Hue-A. Therefore, this more advantageous site was chosen as the place to drop the acoustic beacon.

Coring Operations at Hole 866A

About 6.5 hr after dropping the beacon, the drill string, with a standard rotary coring bit, was at the seafloor and the first core was taken (Table 1); we recovered 0.91 m of upper Pliocene nannofossil foraminiferal ooze and established the water depth as 1372.6 mbrf, or 1361.8 mbsf. In spite of the evidence from the 3.5-kHz record of about 20 to 25 m of pelagic sediment overlying limestone, we recovered no sediment at all in the interval from 0.9 to 38.4 mbsf, nor was there any large change in coring characteristics. The driller noted alternating "soft and hard" intervals that began at about 18 mbsf, but coring rates did not slow down at all until Core 143-866A-6R (38.4–47.8 mbsf), which took 30 min to core, vs. about 10 min for preceding cores. Recovery was about 10 cm of fossiliferous wackestone and grainstone, which established that we were seated in the Cretaceous limestone.

Coring proceeded normally and without significant interruption to a depth of 917 mbsf (Core 143-866A-97R), at 2115 UTC, 10 April 1992. Our rate of progress was about 250 m/day (Fig. 2), while core recovery increased irregularly from less than 10% near the surface to values from 10% to 40% deeper in the column (Fig. 3). The actual rotation time to cut each successive core (Fig. 4) increased from about 10–20 min in the upper part of the hole to 20–40 min in the lower part, with a notable departure in this general trend in the interval

occupied by the hard, tan mudstone and wackestone, from about 280 to 430 mbsf.

At 917 mbsf, it was deemed prudent to make a round trip to change the bit. While pulling out of the hole, the pipe became stuck when the bit was at a level of about 233 mbsf. After working the pipe up and down and circulating mud for about 1 hr, the pipe was freed.

A free-falling minicone was assembled next over the moon pool and released to slide down the drill pipe to the seafloor. A television camera showed that the cone was buried about 2 m into the ooze, with only two of the three small glass float balls visible. The drill string was pulled out of the hole, and the old bit was replaced with a new one. The used bit was judged to be still in fairly good condition, after about 43 hr of rotation.

Reentry was successful, but was complicated by the cone's being buried and possibly out of vertical alignment. On our fourth try, the pipe entered the hole, and after conditioning the hole, we were ready to begin coring again at about 1730 UTC, 11 April. No difficulty was experienced in the interval where the pipe stuck during pullout, nor were there more than a few meters of fill at the bottom of the hole.

Penetration rates gradually slowed below 917 mbsf (Fig. 2), and recovery rates gradually increased from about 10% to about 35% at 1569.3 mbsf (Core 143-866A-165R) (Fig. 3). Core cutting times gradually increased from about 20 to about 60 min/core over the same depth interval (Fig. 4).

Being uncertain of the depth to basaltic basement, but resolved to reach it, and having expended about 53 hr of turning time on the bit, we elected to make another round trip to change bits. Before lifting the bottom-hole assembly (BHA) out of the seafloor, the television camera was lowered to inspect the condition of the hole we would have to reenter. We saw a conical hole about 2 to 3 m wide at the top that tapered downward for about 1 to 2 m, with the pipe centered in the hole. One of the glass float balls attached to the rim of the minicone was visible. We pulled the pipe out of the seafloor, changed bits, and started running in pipe for the second reentry.

Inspection of the bit showed that three of the four core guides (vertical metal straps between the roller cones and the mouth of the bit that guide the core into the core barrel) had snapped off and that these cones were beginning to rotate inward because of deterioration of the sealed bearings. It appeared that the bit would likely have failed, perhaps catastrophically, had we continued to core with it much longer.

The second reentry was smooth and uneventful, and coring resumed. Penetration rates continued to decrease, partly owing to the progressive increase in depth of retrieval of the core barrel (Fig. 2). The time to cut a core increased from about 60 to 100 min, but average recovery rates also increased to about 40%, down to about 1620 mbsf, in Core 143-866A-171R, where basalt was encountered. The interval from 1620 to 1628.8 mbsf yielded about 4 m of very altered basalt that was laced with veins and dotted by vesicle fillings of calcite, and cut by fractures partly filled by dark reddish brown clay.

The next 9.5-m core (Core 143-866A-172R) returned an empty barrel, and drilling, although slow (about 3 m/hr), appeared normal. Thinking that a piece of basalt might have jammed the bit throat, an unplugging tool was sent down, and then another core was tried. Core 143-866A-173R yielded only two small angular pieces of hard basalt in the core catcher. Core 143-866A-174R penetrated only 4.7 m, from 1648.0 to 1652.7 mbsf, but returned with only one angular piece of hard basalt, about 6 cm long. The unplugging tool was sent down four consecutive times, and then a core barrel with a center bit was run in to try to drill up any rubble in the hole that might be blocking entrance through the bit. A last 5-m core, from 1652.7 to 1657.7 mbsf (Core 143-866A-175R), recovered nothing, forcing us to conclude that the bit must be blocked up to a level that prevented the core barrel from latching in. We decided to make yet another round trip to change bits. The bit was on deck at 2215 UTC, 18 April; it contained two cylindrical chunks of basalt that had been cut by the bit from the rock, and a number of small angular pieces, in all a total of about 22 cm in length, as placed in a core liner (Core 143-866A-177B, for "bit core").

The third reentry went quickly, and coring resumed at 1659.4 mbsf after clearing out cuttings accumulated while reaming the hole (Core 143-866A-178W, for "wash core"). Coring rates in the basalt averaged about 2.5 m/hr, while recovery was generally from 40% to 60%.

While retrieving Core 143-866A-188R from 1735.9 mbsf, the drill string became stuck: the pipe would not rotate nor move freely up and down. Efforts to free the pipe were successful, but we decided to pull the bit back above the basalt and to circulate mud to try to remove whatever cuttings might have been binding the pipe. After 12 hr of circulating and pumping mud, the bit was back on bottom, and Core 143-866A-189R was begun. Mindful that coring should be terminated within another 6 hr, to allow time for logging, and after extensive consultation and weighing of the possible risks of continuing to core ahead in a hole that had shown some signs of instability, vs. the benefits to be won by obtaining more basalt for paleomagnetic studies, the co-chief scientists asked the ODP operations superintendent to cease coring and to begin hole conditioning in preparation for logging. The total depth of Hole 866A was 1743.6 mbsf.

Logging Operations at Hole 866A

The deep penetration in Hole 866A (1743.6 mbsf), taken together with the apparently good condition of the hole and the reasonably good recovery rates, at least from the lower half of the hole, afforded an unparalleled opportunity for obtaining a full suite of downhole logs. Moreover, platform carbonates have seldom been both cored and logged, either at DSDP and ODP or in industry. We appreciated the great potential of the sonic, resistivity, density, gamma-ray, and FMS logs for aiding in the documentation and interpretation of the cored section. We were less certain about the usefulness of the chemical logs in the particular types of rocks in this hole, dominated by nearly pure limestone and dolomite, and into which we had pumped about 2000 barrels of smectite-based drilling mud. The documentation available to us about the borehole televiewer was scant. Nonetheless, we elected to bend every effort to exploit all the logging tools available to us.

Logging operations began at 0515 UTC on 21 April, with the conditioning of the hole, and the pulling of the bottom of the BHA to a depth of about 100 mbsf. The heave compensator was turned on at 187 mbsf for all logging runs. The logs obtained from Hole 866A are summarized in Table 2. Logging Run 1 was with a long string of Schlumberger tools that comprised the gamma-ray, caliper, sonic-velocity, neutron-porosity, lithodensity, resistivity, and temperature tools. Logs of gamma-ray and resistivity were taken on the downward run, but the tools stopped at a depth of about 1646 mbsf at some blockage or constriction in the hole. Efforts to push through partly succeeded and, eventually, with several more levels of blockage, a depth of 1679 mbsf was reached, where logging upward began with all tools operating. Although some sections of the hole, particularly in the upper 270 m, were enlarged beyond the reach of the calipers (about 16 in., or 40 cm), long sections of the hole appeared to have been logged successfully. The tools for logging Run 1 were back on deck at 0655 UTC, 22 April 1992.

Logging Run 2 was with the LDGO-Schlumberger FMS tool string, which was run along with the gamma-ray tool for intercorrelation of the separate logging runs. The deepest level reached with the FMS was 1639 mbsf. The upper few hundred meters of the hole are so enlarged that the FMS logs may not be useful in that section of the hole. Logging Run 2 took about 6 hr.

Logging Run 3 was with the Japanese three-component magnetometer, which has a sensitivity suitable for basalt, but not for a platform-carbonate sedimentary sequence. The tool reached to 1636 mbsf, which is only about 16 m deeper than the top of the basalt, at 1620 m. The magnetometer run took 4 hr.

Logging Run 4 was with the Lamont borehole televiewer. Monitoring during logging runs indicated that normal data were being collected, but after completion of the 9-hr run, and in spite of an elab-

orate search by the ODP computer systems manager, the data could not be found in any computer file, and owing to some defect in the program installed aboard by the Lamont-Doherty Borehole Research Group, the data were apparently never passed through the buffer to disk storage.

Logging Run 5 was with the Schlumberger geochemical tool and began at a depth of 1625 mbsf, just barely within the basalt. Because this tool must be run at only about 200 m/hr, the run lasted about 15.5 hr, which included running in and out of the hole and rigging time. At 1700 UTC, 23 April, we began pulling out of the hole, and the bit was back on deck at 2030 UTC.

Coring Operations at Hole 866B

Having decided to try to core the uppermost, possibly karstified and mineralized Albian limestones at Site 866, we made up a BHA that was composed of a small-diameter (6.75 in.) diamond core barrel (DCB) and a Longyear carbonado surface-set diamond bit, 7.25 in. in diameter. This bit was thought to have a better chance for recovering the limestones that the rotary coring bit had mainly missed. We offset the ship about 30 m east of Hole 866A and began coring Hole 866B; we recovered the first core at 0100 UTC, 23 April (Table 1), from the interval at 1357.1 to 1363.1 mbrf. Recovery from the core was a complete 6 m of ooze; thus, we established the depth of the seafloor at Hole 866B as 1357.1 mbrf, which is about 15.5 m shallower than the nominal "bookkeeping" seafloor at Hole 866A, just meters away on a virtually flat sea bed. Clearly, coring at Hole 866A did not begin at the seafloor, but near the top of the firm ooze cored at depth in Hole 866B. Thus, the "true" depth of Hole 866A below the seafloor is about 1759.1 m, rather than the 1743.6 mbsf value used for depth accounting.

At Hole 866B, the soft Cenozoic pelagic ooze was about 27 m thick, but, surprisingly, when we hit the top of the Albian limestone, coring (penetration) rates were fairly fast—typically 20 to 30 min for a 9.6-m core. Recovery was only about 4% to 5% (Table 1), but this was much better, by a factor of four, than rates in the same strata using the rotary coring system. Thus, the rock samples were much more useful for facies analysis.

Hole 866B was terminated at a depth of 117.4 mbsf because we had reached the depth that corresponded to the length of the special slender drill collars used with the diamond core barrel, and thus could go no deeper.

Because Site 867 was nearby, over a nearly flat sea bed, we needed only to pull the bit off the bottom about 100 m. This done, all operations were completed at Site 866 at 1200 UTC, 24 April, about 17.6 days after the beacon was dropped at the site.

SITE GEOPHYSICS

Although for years Resolution Guyot has appeared on bathymetric charts (Chase et al., 1971; Mammerickx and Smith, 1985), the geophysical data archives at the National Geophysical Data Center contain no ships' tracks (i.e., ships having precision depth recorders) that cross this feature. Thus, we knew little about this guyot before the site survey, except that turbidites and debris flows containing reef debris, apparently formed on the guyot summit, were cored at Site 463 (see description in "Introductions and Scientific Objectives" chapter, this volume), 24 nmi (44.4 km) to the east. Virtually all of the pre-Leg 143 data available for Resolution Guyot come from the site survey conducted during Leg 10 of the Roundabout Expedition of the *Thomas Washington*.

Site Survey of Roundabout Leg 10

From 0900 UTC, 1 December 1988, to 0400 UTC 2, December 1988, Resolution Guyot was dredged and partially surveyed during Leg 10 of the Roundabout Expedition aboard the Scripps Institution of Oceanography research vessel *Thomas Washington*. Geophys-

Table 1. Coring summary for Holes 866A and 866B.

Core no.	Date (April 1992)	Time (UTC)	Depth (mbsf)	Length cored (m)	Length recovered (m)	Recovery (%)
Hole 866A						
1R	07	0115	0.0-0.9	0.9	0.91	100.0
2R	07	0145	0.9-10.2	9.3	0.00	0.0
3R	07	0230	10.2-19.6	9.4	0.05	0.5
4R	07	0315	19.6-28.9	9.3	0.00	0.0
5R	07	0450	28.9-38.4	9.5	0.00	0.0
6R	07	0520	38.4-47.8	9.4	0.10	1.1
7R	07	0620	47.8-57.3	9.5	0.31	3.3
8R	07	0655	57.3-67.2	9.9	0.14	1.4
9R	07	0720	67.2-76.9	9.7	0.04	0.4
10R	07	0800	76.9-86.5	9.6	0.07	0.7
11R	07	0825	86.5-96.1	9.6	0.09	0.9
12R	07	0855	96.1-105.8	9.7	0.07	0.7
13R	07	0915	105.8-115.4	9.6	0.05	0.5
14R	07	1000	115.4-125.0	9.6	0.13	1.4
15R	07	1030	125.0-134.7	9.7	0.15	1.5
16R	07	1105	134.7-144.4	9.7	0.03	0.3
17R	07	1150	144.4-155.1	10.7	0.03	0.3
18R	07	1230	155.1-164.8	9.7	0.02	0.2
19R	07	1255	164.8-174.5	9.7	0.08	0.8
20R	07	1325	174.5-184.2	9.7	0.06	0.6
21R	07	1410	184.2-193.8	9.6	0.03	0.3
22R	07	1450	193.8-203.4	9.6	0.13	1.4
23R	07	1520	203.4-213.1	9.7	0.03	0.3
24R	07	1550	213.1-222.7	9.6	0.04	0.4
25R	07	1645	222.7-232.4	9.7	0.46	4.7
26R	07	1715	232.4-242.0	9.6	0.05	0.5
27R	07	1745	242.0-251.6	9.6	0.05	0.5
28R	07	1830	251.6-261.3	9.7	0.07	0.7
29R	07	1930	261.3-271.0	9.7	0.16	1.7
30R	07	2030	271.0-280.6	9.6	0.07	0.7
31R	07	2245	280.6-289.9	9.3	1.30	14.0
32R	08	0015	289.9-299.5	9.6	0.26	2.7
33R	08	0130	299.5-309.2	9.7	0.07	0.7
34R	08	0310	309.2-318.9	9.7	0.12	1.2
35R	08	0430	318.9-328.5	9.6	0.70	7.3
36R	08	0555	328.5-338.0	9.5	0.40	4.2
37R	08	0740	338.0-342.7	4.7	1.16	24.7
38R	08	0840	342.7-347.7	5.0	0.54	10.8
39R	08	1005	347.7-357.3	9.6	1.12	11.6
40R	08	1055	357.3-367.0	9.7	0.21	2.2
41R	08	1200	367.0-376.6	9.6	0.41	4.3
42R	08	1250	376.6-386.3	9.7	0.14	1.4
43R	08	1355	386.3-395.9	9.6	0.22	2.3
44R	08	1455	395.9-405.6	9.7	0.25	2.6
45R	08	1700	405.6-415.3	9.7	0.34	3.5
46R	08	1830	415.3-424.7	9.4	2.17	23.1
47R	08	2045	424.7-434.4	9.7	0.70	7.2
48R	08	2145	434.4-444.0	9.6	0.56	5.8
49R	08	2245	444.0-453.7	9.7	0.10	1.0
50R	08	2330	453.7-463.4	9.7	0.38	3.9
51R	09	0015	463.4-473.0	9.6	0.37	3.9
52R	09	0045	473.0-482.7	9.7	0.12	1.2
53R	09	0145	482.7-492.3	9.6	0.67	7.0
54R	09	0245	492.3-501.9	9.6	0.65	6.8
55R	09	0345	501.9-511.6	9.7	0.24	2.5
56R	09	0445	511.6-521.3	9.7	0.56	5.8
57R	09	0545	521.3-531.0	9.7	0.76	7.8
58R	09	0640	531.0-540.7	9.7	0.79	8.1
59R	09	0715	540.7-550.3	9.6	0.47	4.9
60R	09	0750	550.3-559.9	9.6	0.60	6.3
61R	09	0855	559.9-569.6	9.7	1.01	10.4
62R	09	0945	569.6-579.3	9.7	1.74	17.9
63R	09	1020	579.3-589.0	9.7	2.24	23.1
64R	09	1100	589.0-598.6	9.6	2.17	22.6
65R	09	1150	598.6-608.3	9.7	1.59	16.4
66R	09	1245	608.3-618.0	9.7	1.00	10.3
67R	09	1330	618.0-627.7	9.7	0.61	6.3
68R	09	1410	627.7-637.2	9.5	0.10	1.1
69R	09	1455	637.2-646.9	9.7	0.24	2.5
70R	09	1550	646.9-656.5	9.6	1.54	16.0
71R	09	1730	656.5-666.2	9.7	1.93	19.9
72R	09	1830	666.2-675.8	9.6	0.89	9.3
73R	09	1930	675.8-685.5	9.7	1.16	11.9
74R	09	2030	685.5-695.1	9.6	2.81	29.3
75R	09	2130	695.1-704.7	9.6	3.76	41.8
76R	09	2230	704.7-714.5	9.8	3.45	35.2
77R	09	2330	714.5-724.1	9.6	3.62	37.7
78R	10	0045	724.1-733.8	9.7	4.76	49.1
79R	10	0200	733.8-743.5	9.7	5.18	53.4
80R	10	0300	743.5-753.1	9.6	0.78	8.1
81R	10	0400	753.1-762.8	9.7	2.83	29.2

Table 1 (continued).

Core no.	Date (April 1992)	Time (UTC)	Depth (mbsf)	Length cored (m)	Length recovered (m)	Recovery (%)
Hole 866A						
82R	10	0500	762.8-772.5	9.7	2.68	27.6
83R	10	0600	772.5-782.2	9.7	0.81	8.4
84R	10	0640	782.2-791.8	9.6	0.55	5.7
85R	10	0740	791.8-801.5	9.7	3.14	32.4
86R	10	0915	801.5-811.2	9.7	2.06	21.2
87R	10	1025	811.2-820.9	9.7	1.09	11.2
88R	10	1200	820.9-830.6	9.7	1.24	12.8
89R	10	1350	830.6-839.9	9.3	1.75	18.8
90R	10	1455	839.9-849.5	9.6	0.13	1.4
91R	10	1600	849.5-859.2	9.7	1.34	13.8
92R	10	1715	859.2-868.7	9.5	0.25	2.6
93R	10	1800	868.7-878.4	9.7	0.31	3.2
94R	10	1840	878.4-888.0	9.6	1.00	10.4
95R	10	1930	888.0-897.7	9.7	0.58	6.0
96R	10	2030	897.7-907.4	9.7	0.32	3.3
97R	10	2115	907.4-917.0	9.6	0.52	5.4
98R	11	1730	917.0-923.9	6.9	1.95	28.2
99R	11	1900	923.9-933.4	9.5	1.00	10.5
100R	11	2015	933.4-943.1	9.7	0.47	4.8
101R	11	2145	943.1-952.7	9.6	0.35	3.6
102R	11	2315	952.7-962.4	9.7	1.76	18.1
103R	12	0035	962.4-971.7	9.3	0.55	5.9
104R	12	0200	971.7-981.3	9.6	0.73	7.6
105R	12	0315	981.3-990.9	9.6	0.87	9.1
106R	12	0430	990.9-1000.5	9.6	0.62	6.5
107R	12	0535	1000.5-1010.2	9.7	0.24	2.5
108R	12	0645	1010.2-1019.9	9.7	0.51	5.3
109R	12	0810	1019.9-1029.6	9.7	1.86	19.2
110R	12	0935	1029.6-1039.3	9.7	2.43	25.0
111R	12	1100	1039.3-1048.9	9.6	1.42	14.8
112R	12	1235	1048.9-1058.5	9.6	0.82	8.5
113R	12	1400	1058.5-1068.2	9.7	0.37	3.8
114R	12	1540	1068.2-1077.9	9.7	1.22	12.6
115R	12	1715	1077.9-1087.5	9.6	0.90	9.4
116R	12	1830	1087.5-1097.1	9.6	1.50	15.6
117R	12	2000	1097.1-1106.8	9.7	1.66	17.1
118R	12	2145	1106.8-1116.5	9.7	2.50	25.8
119R	13	0015	1116.5-1126.1	9.6	0.78	8.1
120R	13	0200	1126.1-1135.7	9.6	0.56	5.8
121R	13	0315	1135.7-1145.4	9.7	0.83	8.6
122R	13	0430	1145.4-1155.1	9.7	0.69	7.1
123R	13	0530	1155.1-1164.8	9.7	0.43	4.4
124R	13	0710	1164.8-1174.4	9.6	1.03	10.7
125R	13	0945	1174.4-1184.0	9.6	3.76	39.1
126R	13	1135	1184.0-1193.5	9.5	1.83	19.2
127R	13	1315	1193.5-1203.2	9.7	0.47	4.8
128R	13	1500	1203.2-1212.9	9.7	1.32	13.6
129R	13	1630	1212.9-1222.6	9.7	1.36	14.0
130R	13	1845	1222.6-1232.2	9.6	1.80	18.7
131R	13	2015	1232.2-1241.9	9.7	1.40	14.4
132R	13	2200	1241.9-1251.6	9.7	0.79	8.1
133R	13	2330	1251.6-1261.2	9.6	3.00	31.2
134R	14	0100	1261.2-1270.9	9.7	2.48	25.5
135R	14	0215	1270.9-1280.2	9.3	1.40	15.0
136R	14	0330	1280.2-1289.8	9.6	0.38	4.0
137R	14	0640	1289.8-1299.5	9.7	3.12	32.1
138R	14	0835	1299.5-1309.2	9.7	1.10	11.3
139R	14	0950	1309.2-1318.9	9.7	0.63	6.5
140R	14	1100	1318.9-1328.6	9.7	0.20	2.1
141R	14	1230	1328.6-1338.2	9.6	0.20	2.1
142R	14	1350	1338.2-1347.9	9.7	2.03	20.9
143R	14	1510	1347.9-1357.5	9.6	0.73	7.6
144R	14	1715	1357.5-1366.8	9.3	3.10	33.3
145R	14	1915	1366.8-1376.4	9.6	2.20	22.9
146R	14	2200	1376.4-1386.1	9.7	1.87	19.3
147R	15	0045	1386.1-1395.7	9.6	2.78	28.9
148R	15	0330	1395.7-1405.4	9.7	4.62	47.6
149R	15	0440	1405.4-1415.1	9.7	1.99	20.5
150R	15	0610	1415.1-1424.8	9.7	5.02	51.7
151R	15	0740	1424.8-1434.5	9.7	0.12	1.2
152R	15	0930	1434.5-1444.1	9.6	3.21	33.4
153R	15	1055	1444.1-1453.8	9.7	1.78	18.3
154R	15	1235	1453.8-1463.5	9.7	4.16	42.9
155R	15	1415	1463.5-1473.2	9.7	3.02	31.1
156R	15	1550	1473.2-1482.8	9.6	3.61	37.6
157R	15	1730	1482.8-1492.5	9.7	3.65	37.6
158R	15	1945	1492.5-1500.9	8.4	2.07	24.6
159R	15	2145	1500.9-1511.7	10.8	3.92	36.3
160R	15	2330	1511.7-1521.3	9.6	0.76	7.9
161R	16	0105	1521.3-1531.0	9.7	1.17	12.0

Table 1 (continued).

Core no.	Date (April 1992)	Time (UTC)	Depth (mbsf)	Length cored (m)	Length recovered (m)	Recovery (%)
Hole 866A						
162R	16	0300	1531.0–1540.3	9.3	3.41	36.6
163R	16	0440	1540.3–1549.9	9.6	0.86	9.0
164R	16	0755	1549.9–1559.6	9.7	3.76	38.7
165R	16	1035	1559.6–1569.3	9.7	2.44	25.1
166R	17	0605	1569.3–1580.4	11.1	5.28	47.6
167R	17	0900	1580.4–1590.1	9.7	5.61	57.8
168R	17	1130	1590.1–1599.8	9.7	6.20	63.9
169R	17	1330	1599.8–1609.4	9.6	3.00	31.2
170R	17	1600	1609.4–1619.1	9.7	5.54	57.1
171R	17	2045	1619.1–1628.8	9.7	4.98	51.3
172R	18	0100	1628.8–1638.3	9.5	0.00	0.0
173R	18	0615	1638.3–1648.0	9.7	0.04	0.4
174R	18	0905	1648.0–1657.7	4.7	0.06	1.3
175R	18	1520	1652.7–1657.7	5.0	0.00	0.0
176R	18	1630	1657.7–1659.4	1.7	0.00	0.0
177B	18	2215	1659.4–1659.4	0.0	0.22	55.0
178W	19	1015	1659.4–1659.4	0.0	0.56	(wash core)
179R	19	1400	1659.4–1667.4	8.0	5.51	68.9
180R	19	1800	1667.8–1675.8	8.0	6.90	86.2
181R	19	2130	1675.8–1682.8	7.0	3.91	55.8
182R	20	0045	1682.8–1687.3	4.5	4.68	104.0
183R	20	0300	1687.3–1692.3	5.0	1.16	23.2
184R	20	0440	1692.3–1697.3	5.0	2.75	55.0
185R	20	0710	1697.3–1707.0	9.7	4.52	46.6
186R	20	1020	1707.0–1716.7	9.7	2.56	26.4
187R	20	1400	1716.7–1726.3	9.6	0.93	9.7
188R	20	1715	1726.3–1734.9	8.6	3.96	46.0
189R	20	0515	1734.9–1743.6	8.7	4.06	46.6
Coring totals				1743.6	268.42	15.4
Washing totals				0.0	0.56	
Combined totals				1743.6	268.98	
Hole 866B						
1M	24	0100	0.0–6.0	6.0	5.95	99.1
2M	24	0145	6.0–14.1	8.1	4.49	55.4
3M	24	0230	14.1–23.5	9.4	8.55	90.9
4M	24	0330	23.5–32.8	9.3	0.19	2.0
5M	24	0430	32.8–42.2	9.4	0.20	2.1
6M	24	0540	42.2–51.7	9.5	0.65	6.8
7M	24	0620	51.7–61.1	9.4	0.40	4.3
8M	24	0720	61.1–70.5	9.4	1.52	16.2
9M	24	0805	70.5–79.9	9.4	0.28	3.0
10M	24	0845	79.9–89.2	9.3	0.12	1.3
11M	24	0930	89.2–98.5	9.3	0.13	1.4
12M	24	1020	98.5–107.8	9.3	0.50	5.4
13M	24	1050	107.8–117.4	9.6	0.08	0.8
Coring Totals				117.4	23.06	19.6

ical data collected were SeaBeam multibeam echo-sounder bathymetry, gravity, total magnetic field measurements, 3.5-kHz echo-sounder profiles, and seismic reflection profiles from an 80-in.³ water-gun source.

The vessel first crossed the guyot from west to east and continued seismic profiling east to Site 463 (Fig. 5), tracing seismic layers from the guyot to the drill site. Returning to its summit, the ship ran a SeaBeam profile along the part of the perimeter reef facing Site 463 and also ran two north-south seismic profiles across the summit. Two dredges were taken along the summit of the perimeter reef on the south side of the guyot (Fig. 5).

One dredge (Roundabout dredge D64) recovered only a bag full of manganese nodules, but the other (Roundabout dredge D65) gathered rudists (*Praeacprina?* sp.), hermatypic coral fragments of several types, and phosphatized pelagic ooze (van Waasbergen, 1992).

SeaBeam data show that Resolution Guyot rises to a minimum depth of approximately 1290 m (unless specified otherwise, depths given in this section are in uncorrected meters) and stands about 1250 m above the seafloor to the east, where Site 463 is located in water

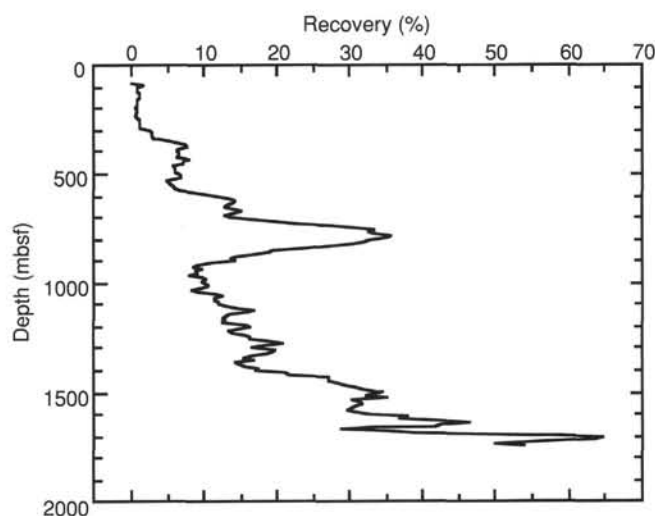


Figure 3. Core recovery rate for Hole 866A, as a function of depth of the hole. The data have been smoothed with a 10-core running average.

2532 m deep (drill-pipe measurement). The summit of Resolution Guyot is subcircular in plan view and has dimensions of about 12 × 13 nmi (22 × 37 km). The summit region has a total relief of about 100 m. The edge of the summit occurs consistently at a depth of approximately 1355 m and has a break in slope between the summit and flanks. Typical flank slopes are 15° to 20°.

Around the edge of the summit is a small mound, generally 5 to 10 m high and 200 to 300 m wide. This was thought to be a Cretaceous perimeter reef. In 3.5-kHz profiles over the summit edge (Fig. 6), a trough can be seen behind the perimeter mound. The bottom of this trough is generally 1.0 to 1.5 km inward from the reef summit and about 30 m below it (Fig. 6). Beneath the thin pelagic cover, summit topography is commonly stepped or punctuated by holes (Figs. 6 and 7). The back-reef trough, steps, and holes are all thought to have been caused by emergence and karstification of the guyot summit (van Waasbergen and Winterer, in press). An additional feature near the perimeter that may be related to fluctuations in relative sea level is a small bench that can be observed just seaward of the perimeter mound during many crossings of the summit edge (Fig. 6). This bench is about 30 m lower than the mound summit and perhaps 200 m wide. It may be a wave-cut terrace, reef bench, or combination of both that formed during a lowstand in relative sea level.

Unlike many western Pacific Ocean guyots, Resolution does not stand high above the surrounding seafloor. Instead, it is located on a raised platform having depths of between about 2500 to 3000 m. This platform measures approximately 72 × 132 nmi (133 × 244 km) in area above the 3000-m contour and contains two other guyot summits that rise to the same depths as Resolution (Mammerickx and Smith, 1985).

To the south, in the interior of the Mid-Pacific Mountains province, the seafloor descends to depths of between 4000 and 4500 m. To the northwest, depths are mainly greater than 5500 m, which is typical of Jurassic-age abyssal oceanic crust. This depth difference is partly because of thick sediment layers ponded among the seamounts, but there also appears to be a low basaltic plateau beneath most of the seamounts, approximately 1.0 to 1.5 km in height above the surrounding deep ocean floor (Nemoto and Kroenke, 1985).

Jurassic M-series magnetic lineations are located northwest of Resolution Guyot, which is on a line with lineation M23 (Nakanishi et al., 1989). This might imply that the age of the lithosphere beneath Resolution can be extrapolated to be 154 Ma (using the time scale of Kent and Gradstein, 1985). On the other hand, lineations M0–M4 have been tentatively identified just west of Allison Guyot (Nakanishi et al., 1992), implying that a large age discontinuity exists, perhaps a

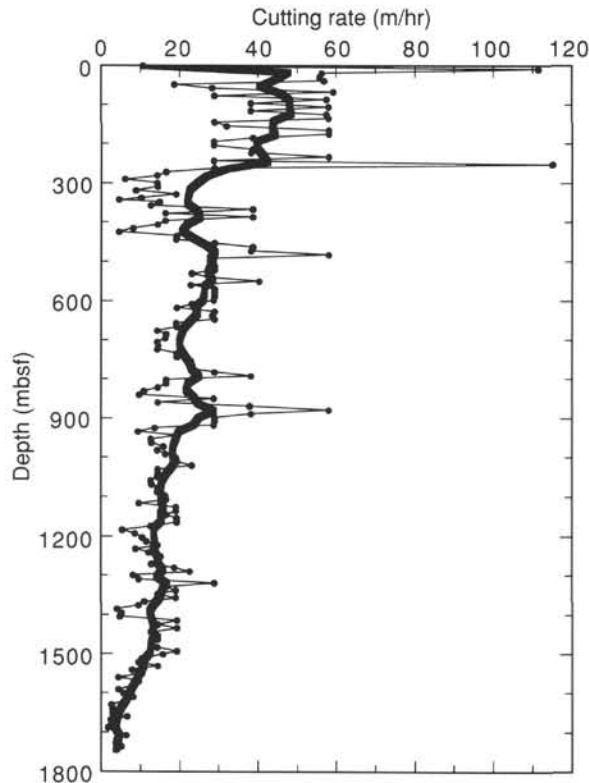


Figure 4. Cutting rate for cores from Hole 866A as a function of depth in the hole. Dots connected by thin line represent each individual core; heavy line is a smoothed curve through the points.

fracture zone offset, beneath, or at the northwest margin of, the Mid-Pacific Mountains; thus, an extrapolated lithospheric age for Resolution must be interpreted with caution.

An 80-in.³ water-gun seismic profile across Resolution Guyot shows a thin, acoustically transparent pelagic layer on top of a strong reflective horizon at the top of the shallow-water limestone (Fig. 7). Beneath this is a nearly transparent zone that overlies a series of moderately strong seismic horizons down to 2.2-s twtt (approximately 0.3-s twtt below the top of the limestone). Deeper reflections are weak, though several coherent horizons can be discerned (see "Seismic Stratigraphy" section, this chapter). The deepest one that is obvious in the Roundabout survey lines is at approximately 2.7-s twtt (0.8-s twtt below the top of the limestone). Before drilling, it was thought that this reflector probably represented volcanic basement, and a depth of about 1000 mbsf was predicted using an acoustic wave velocity of 2.5 km/s.

Site Survey for Leg 143

The *JOIDES Resolution* approached Resolution Guyot from the east, heading toward its center. A magnetometer, seismic streamer, 200-in.³ water gun, and 3.5-kHz echo-sounder were used to collect geophysical data. At a distance of 4 nmi (7.4 km) from the edge of the guyot, the ship slowed to 6 kt to obtain better quality seismic reflection records.

Before arriving at Resolution Guyot, we decided that a location closer to the perimeter mound would be more valuable scientifically than the proposed Site Hue-A. Consequently, a short site survey was conducted by zig-zagging the *JOIDES Resolution* over the northeastern perimeter of the guyot summit (Fig. 5). We were looking for a location having 20 to 30 m of pelagic sediment (for spudding-in) in the back-reef trough, where it would be possible to get within about 1 km of the perimeter reef mound. We found such a place about 1 nmi east of the proposed Site Hue-A.

Table 2. Well-log data for Hole 866A.

Log type	Depth (mbsf) ^a
Resistivity	76.0–1668.2
Bulk density	75.5–1659.4
Neutron porosity	75.5–1649.0
Sonic velocity	79.8–1647.7
^b Gamma ray/U-Th-K	20.0–1607.2
^b Aluminum	46.0–1615.4
^b Geochemistry	46.0–1622.2
Caliper	75.5–1659.4
Formation microscanner	238.5–1631.3
Lamont temperature	0–1671.5

^a Assumes seafloor at 1372.6 m and with all logs correlated and depth shifted to the gamma-ray log from the geophysical tool string.

^b These logs were recorded in drill pipe from 76.0 to 46.0 mbsf.

Seismic reflection profiles acquired using the 200-in.³ water-gun showed deeper layers more clearly than the 80-in.³ Roundabout Leg 10 seismic profile (Figs. 8 and 9). The reflective layers between 2.0 and 2.2 s twtt can be seen prominently in the record. In addition, a prominent reflective horizon can be seen at approximately 2.6-s twtt (about 0.80-s twtt below the top of the guyot) that we thought might be volcanic basement. In between are numerous "patchy" reflectors that are continuous for a short distance, and a few that span the entire profile. These imply sedimentary and/or diagenetic facies that are not continuous across the entire lagoon. Most reflectors have low amplitudes, but some are strong. Drilling suggests that the strong reflector thought to be volcanic basement instead is probably the top of a heavily dolomitized layer (See "Seismic Stratigraphy" and "Lithostratigraphy" sections, this chapter). A discontinuous reflector approximately 0.20 to 0.25 s twtt farther below may actually be the reflection from the volcanic section.

Site 867 (proposed Site Hue-B) was chosen to be at the morphologic reef summit near Site 866. It is about 0.5 nmi east of the original proposed location, but should be little different because the perimeter mound is two-dimensional and strikes approximately parallel to the guyot summit edge and perpendicular to the geophysical line. To get to Site 867, we moved the ship on thrusters while watching the 3.5-kHz echo-sounder record for the bump at the mound summit. After crossing it, we retraced our track and dropped a beacon. Because of a strong current from the east, it was difficult to keep the ship precisely on the *JOIDES Resolution* sounding line (Fig. 6); thus, Site 867 is located between this line and the *Thomas Washington* seismic line.

Site 868 is located approximately 200 m north of Site 867 (Fig. 8), on the terrace 30 m below the perimeter mound summit (Fig. 6). Crabbing northward using the ship's thrusters, we chose the site by watching the 3.5-kHz echo-sounder profile for increasing depths that indicated the transition to the flank of the guyot.

Upon leaving Resolution Guyot, we gathered additional geophysical data from the unsurveyed western side of the feature. The ship steamed westward, across the summit edge, and then zig-zagged to the north side of the guyot (Fig. 5). This produced seismic reflection profiles that showed the adjacent sediment wedges. A seismic profile using two 200-in.³ water guns was shot across the guyot, from north to south, that included Sites 866 and 867 (See "Underway Geophysics" chapter, Line 3, 1830 UTC, April 28–0700 UTC, April 29, this volume). An expendable sonobuoy was dropped at the northern edge of the guyot to obtain seismic refraction data. After this transect, the ship continued southwest to Site 869, in the basin southwest of Wodejebato Guyot in the Marshall Islands.

LITHOSTRATIGRAPHY

Lithologic units have been defined by characteristics such as color, carbonate and clay contents, fossil and particle constituents, lithification, structure, and diagnostic log signatures. Several of the lithologic

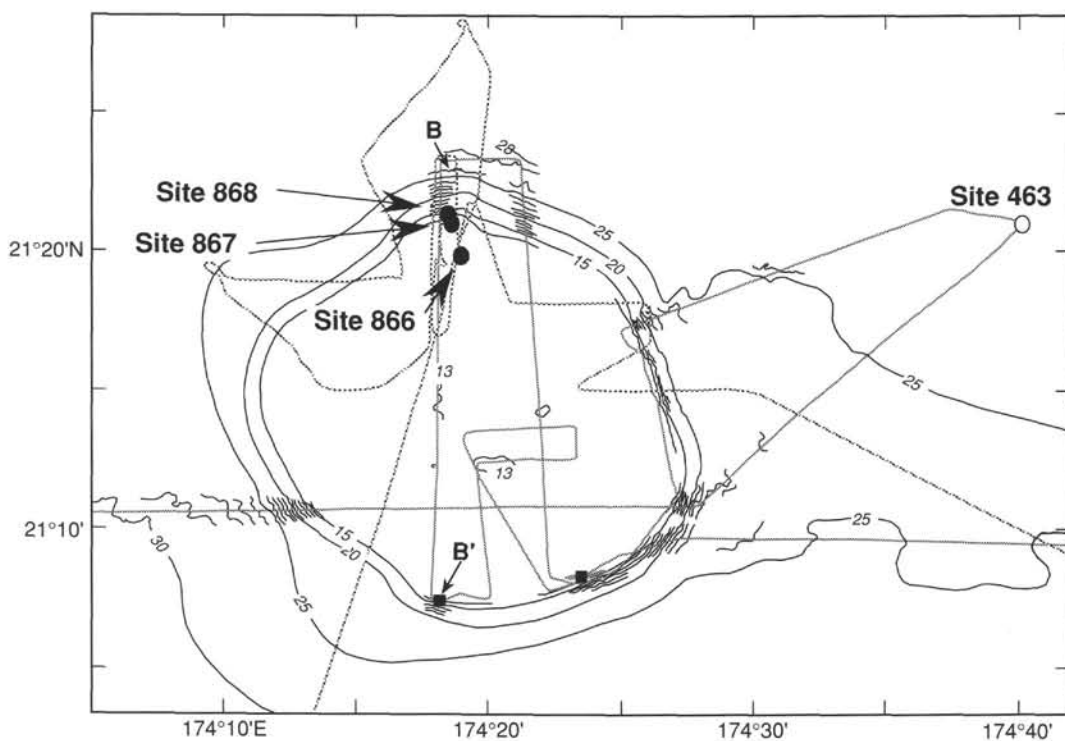


Figure 5. Bathymetry of Resolution Guyot and geophysical ships' tracks. Thin contours shown at 100-m intervals where SeaBeam multibeam data are available; heavy contours show 500-m intervals. Contours labeled in hundreds of meters. Thin gray lines show ships' tracks: site-survey cruise, Roundabout Leg 10 of the Scripps Institution of Oceanography research vessel *Thomas Washington* and path of *JOIDES Resolution*. Roundabout cruise dredges shown by filled squares. B-B' denote ends of seismic reflection lines shown in Figure 7.

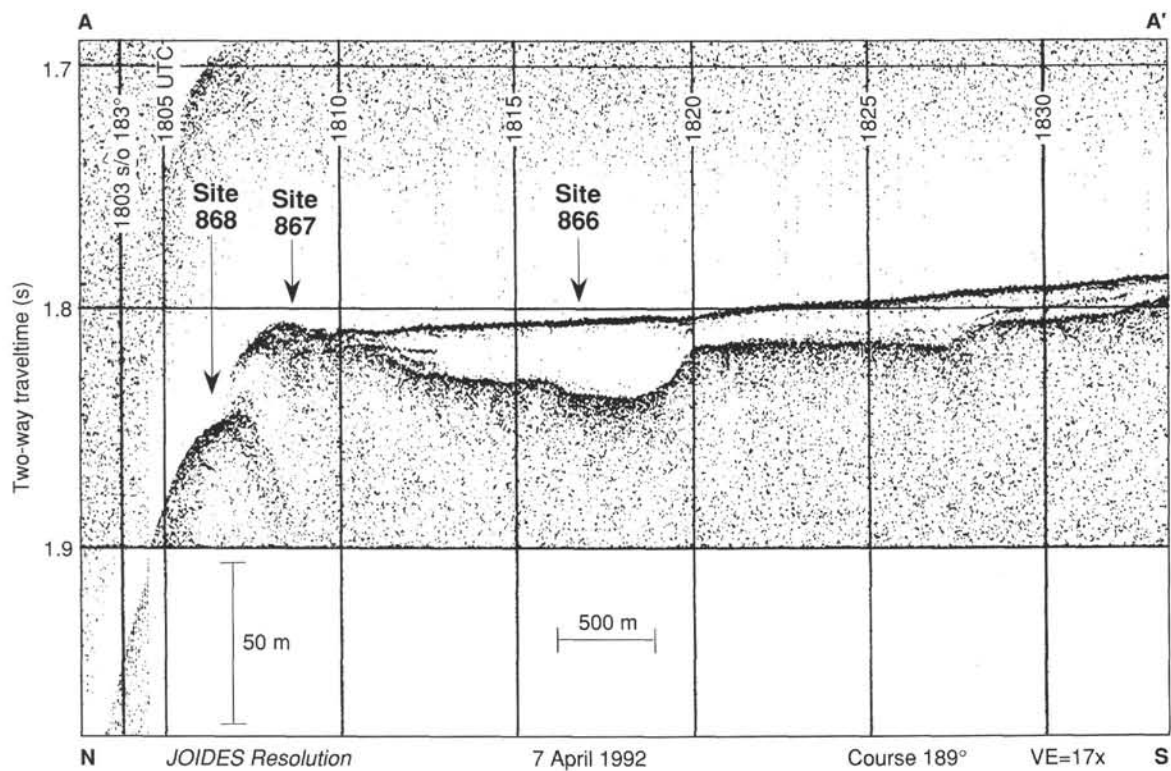


Figure 6. 3.5-kHz echo-sounder profile over Sites 866, 867, and 868 taken on board the *JOIDES Resolution* during pre-drilling survey. Time plotted along horizontal axis; two-way traveltime plotted vertically. Location shown by A-A' in Figure 8.

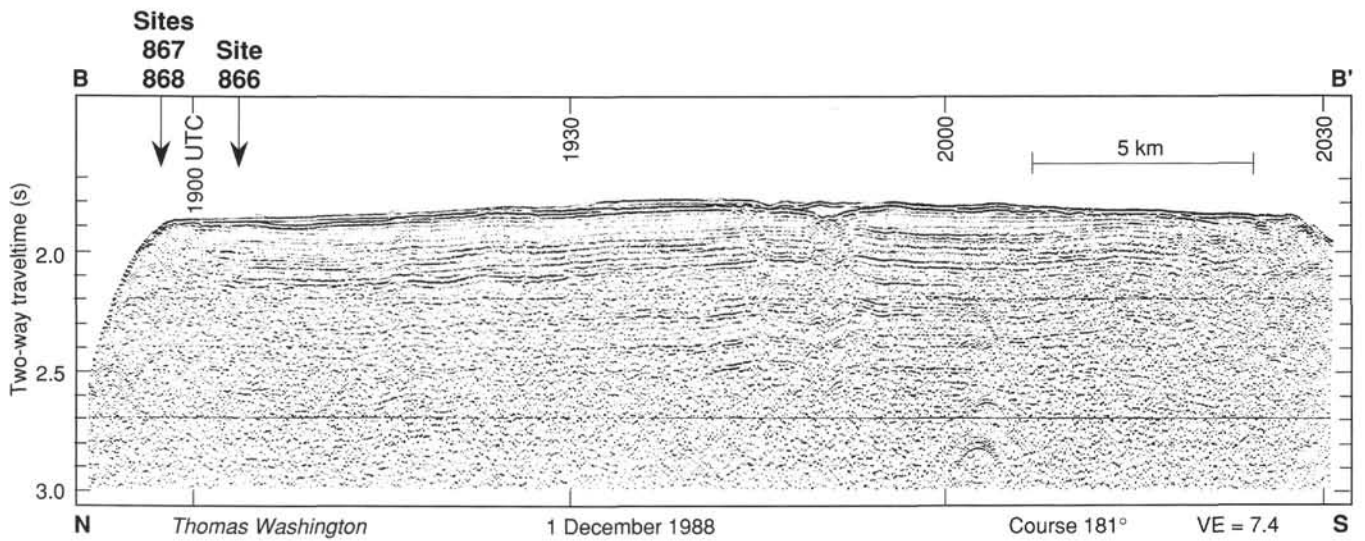


Figure 7. Seismic reflection profile across Resolution Guyot, taken by the *Thomas Washington* during the Roundabout Leg 10 site-survey cruise. Time plotted along horizontal axis; two-way traveltme plotted vertically. Location shown by B–B' in Figure 5. Seismic source was an 80-in.³ water gun; ship's speed was 9.2 kt. Locations of Sites 866, 867, and 868 were projected to this line from their actual locations approximately 0.5 to 1.2 nmi (0.9 to 1.9 km) to the east.

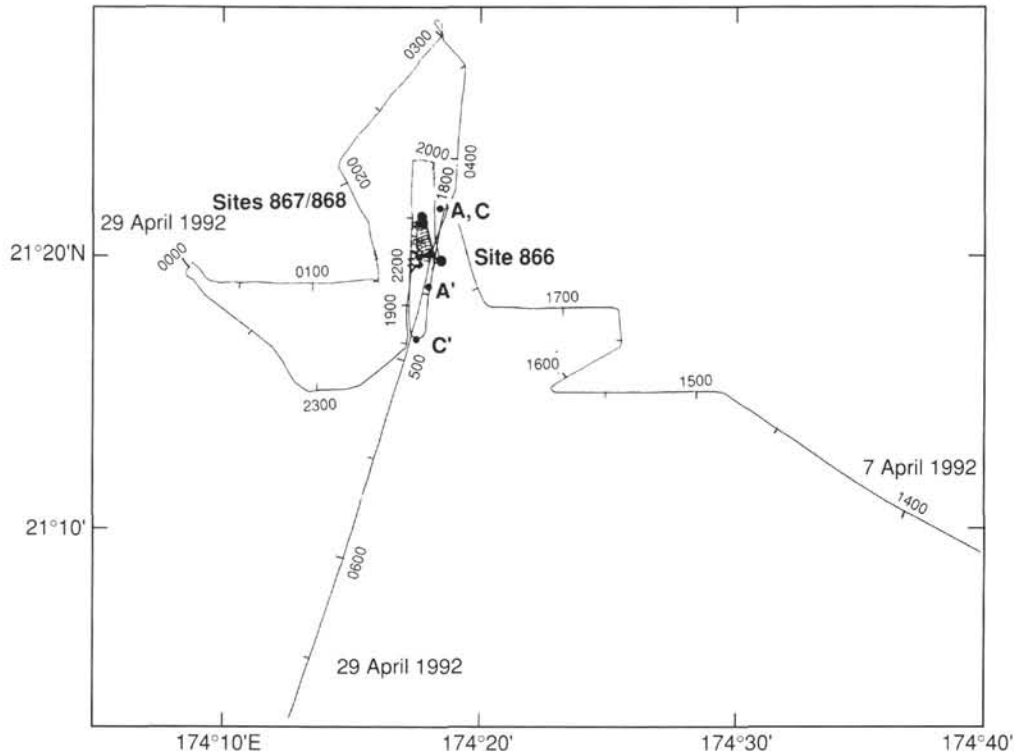


Figure 8. Annotated track of *JOIDES Resolution* approaching and leaving Sites 866 and 867. Ticks are at 1/2-hr intervals. A–A' indicates the location of the profile of Figure 6 and C–C' = the profile of Figure 9.

boundaries coincide well with seismic discontinuities and signals in the downhole logs, as do some lithologic features of the sediments. The sequence was divided into eight major lithologic units: (1) buff-colored foraminifer nannofossil ooze; (2) phosphatized and manganese oxyhydroxide-encrusted pelagic limestone; (3) white shallow-water limestones (mostly wackestones) that contain a fauna of abundant gastropods, sponge spicules, and dasycladacean algae as well as re-

peated calcrite horizons; (4) buff-colored to white shallow-water limestones, developed in cycles of packstone-wackestone with thin intervals of organic-rich mudstones; (5) buff-colored to beige oolitic grainstone, locally cross-laminated; (6) generally buff to white shallow-water limestones dominated by a cyclic peloidal packstone-wackestone succession with algal laminites, clay/organic-rich intervals and patchy dolomitization; (7) a heterogeneous unit containing some

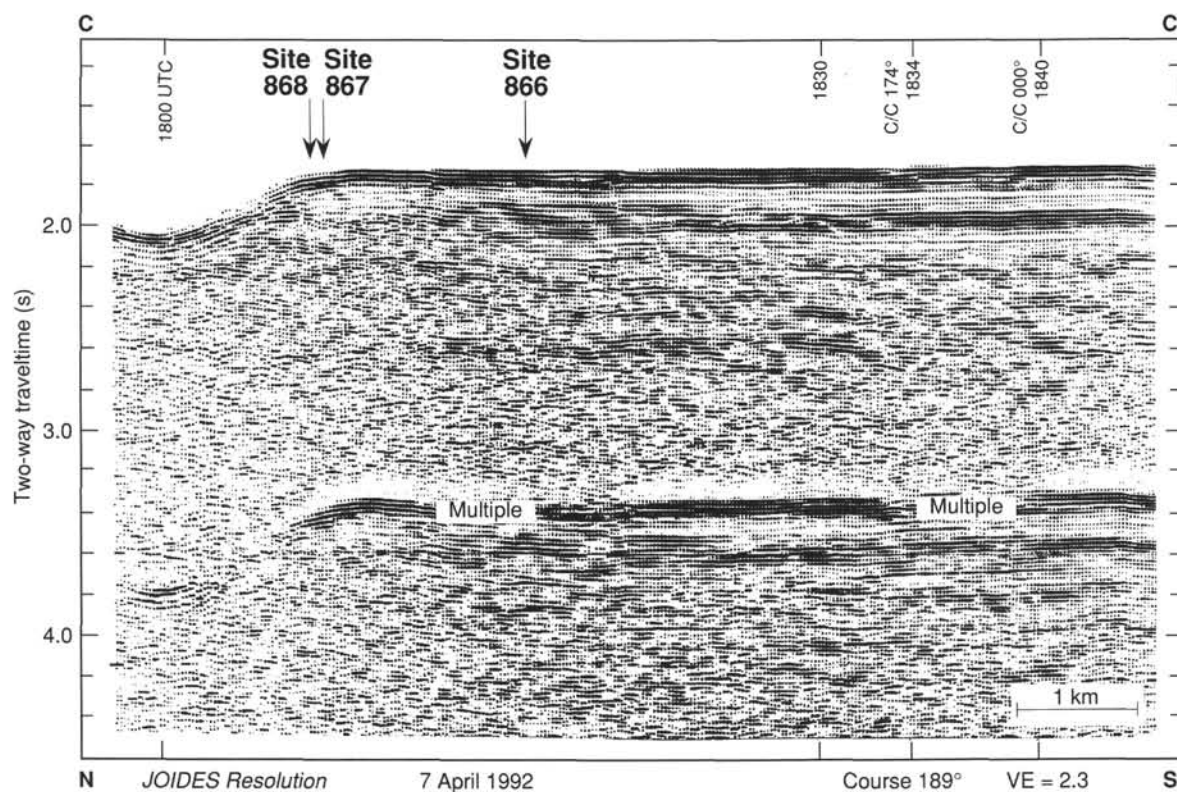


Figure 9. Seismic reflection profile over Resolution Guyot, taken by *JOIDES Resolution* during pre-drilling survey. Time plotted along horizontal axis; two-way travelttime plotted vertically. Location shown by C-C' in Figure 8. Seismic source was a 200-in.³ water gun; ship's speed was 6.0 kt.

lithologies similar to those in Unit VI but also containing brown and white dolomitized peloidal and oolitic-peloidal-oncolitic grainstones, together with an interval of coral-bearing grainstones; (8) brownish shallow-water oolitic-oncolitic grainstones, pervasively dolomitized and gray oolitic grainstones; and (9) basalt (Fig. 10).

Lithologic Units

Unit I

Sections 143-866A-1R-1 to -1R-CC
Depth: 0–0.9 mbsf
Age: late Pliocene

Cores 143-866B-1M to -3M
Depth: 0–23.5 mbsf
Age: Maastrichtian–late Pliocene

Lithologic Unit I consists of buff-colored foraminiferal nannofossil ooze and nannofossil-foraminiferal ooze, somewhat sandy in texture in the upper portions, containing scattered centimeter-scale white to yellow mottles, interpreted as burrows. Black-brown specks disseminated within this sand probably represent iron-manganese oxyhydroxide micronodules. The base of this unit is defined by contact with the hypothetical underlying unit.

Unit II

Cores 143-866A-2R to -3R
Depth: 0.9–19.6 mbsf
Age: Cretaceous

Core 143-866B-4M

Depth: 23.5–32.8 mbsf
Age: Cretaceous

Unit II comprises poorly defined manganese-encrusted limestone, whose existence is based on the recovery of one manganese-encrusted pebble at Hole 866A and a similar black-stained fragment at Hole 866B, plus a comparison with the stratigraphy of Allison Guyot (Holes 865A and 865B). Phosphatization of this part of the section cannot be proved from the recovered material, nor from the downhole logs because of the absence of critical data. However, observations from Hole 867B suggest that penetrative phosphatization has indeed taken place. The base of this unit is defined by the contact, albeit unrecovered, with the underlying unit. The exact thickness of this unit is unknown, and its assignment to particular cores is essentially a device of convenience.

Unit III

Core 143-866A-4R to Section 143-866A-48R-1, 8 cm
Depth: 19.6–434.5 mbsf

Cores 143-866B-5M to -13M
Depth: 32.8–117.4 mbsf
Age: Aptian to Albian

The upper limit of Unit III has been tentatively set at the base of Core 143-866A-3R, although the two subsequent cores gave no recovery. This unit extends downward into the top of Section 143-866A-48R-1, where a rapid facies change from whitish wackestone to yellowish grainstone-packstone places its lower limit at 8 cm from the top of the curated section, which corresponds approximately to 434.5 mbsf. This depth coincides with an abrupt discontinuity in dry

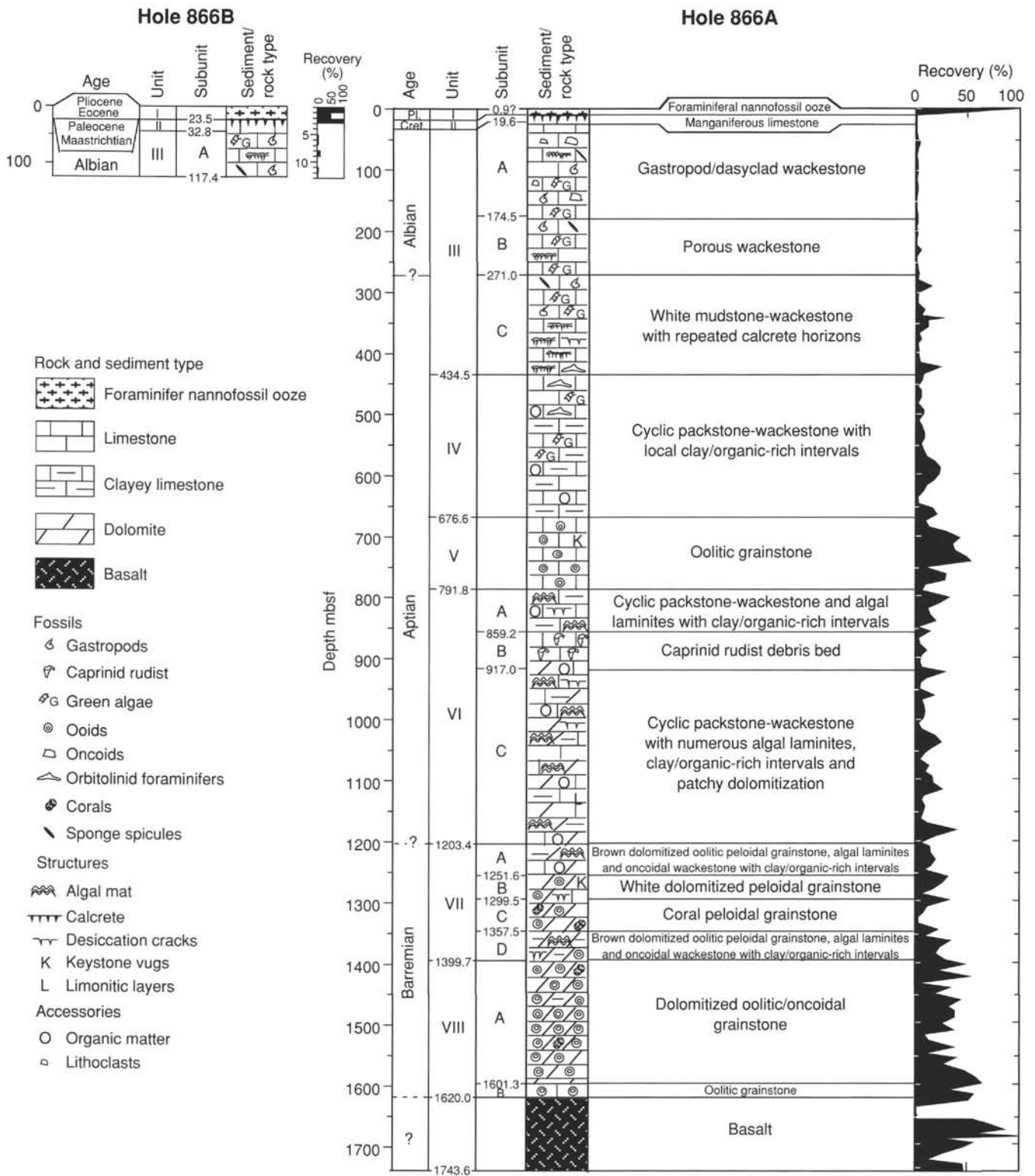


Figure 10. Interpretative stratigraphic column of Holes 866A and 866B. Age and lithologic units shown in left columns; recovery shown in right columns. Age boundaries are uncertain owing to low recovery and sparse diagnostic fossils. (Note added in proof: Recent biostratigraphic work suggests that Albian age should extend to the bottom of Unit III [A. Vanneau, pers. comm., 1992]).

density and velocity of the measured samples (see “Physical Properties” section, this chapter).

The facies of the recovered material in Unit III are dominated by wackestones, although mudstones, packstones, and grainstones are scattered. Fauna and flora include gastropods, bivalves, benthic foraminifers, echinoids, ostracodes, sponges and sponge spicules, and dasycladacean algae. Corals, serpulids, and bryozoans are rare. Originally, aragonitic fossils have been dissolved to leave a moldic porosity, which in many places is solution-enhanced, thus rendering identification of fossils difficult. This is particularly the case with the dasycladacean algae. Intraclasts of mudstone are common, and oncoids occur in some places. Peloids are distributed in the micritic matrix, but in many places are concentrated as geopetal fills in burrows. Isolated coated grains are scattered.

The limestones are light-colored, but in many cases display yellow or reddish staining. Small black pebbles occur in Sections 143-866A-6R-CC and -39R-2. Brown, laminated calcrete crusts or evidence for incipient calcretization occur in Sections 143-866A-8R-CC, -25R-1, -39R-2, -43R-CC, -44R-CC, and -46R-2, becoming more common in the lower part of the unit. Calcretization is independent of the substrate and has occurred above mudstone of subtidal origin (Fig. 11), as well as on grainstone that exhibits intertidal keystone vugs (Fig. 12). Desiccation cracks and fenestrae have been identified in Sections 143-866A-7R-CC, -16R-CC and -37R-2.

Although the general lithologies appear to be similar in Unit III, three subunits have been distinguished, based on the degree of porosity and the abundance of calcrete horizons.

Subunit IIIA

Cores 143-866A-4R to -19R
Depth: 19.6–174.5 mbsf

Cores 143-866B-5M to -13M
Depth: 32.8–117.4 mbsf
Age: Albian

This subunit displays the above-mentioned faunal and floral assemblages, but contains some intervals with gravel-sized intraclasts. Incipient calcretization and white glaebules were observed only in Core 143-866A-8R. At approximately the same depth below the top of the shallow-water carbonates, Section 143-866B-8M-2 displays small desiccation fissures and circumgranular cracking. In Section 143-866B-8M-1, a 30-cm-thick, graded bed of brownish, shell-rich packstone to floatstone can be interpreted as tempestite. The same facies fills *Thalassinoides*-like burrows in Section 143-866B-8M-2.

Subunit IIIB

Cores 143-866A-20R to -29R
Depth: 174.5–271.0 mbsf
Age: Albian

This subunit is characterized by high moldic porosity and a chalky texture. A prominent level of grainstone to rudstone, including planar beach lamination, keystone vugs, and thin calcrete crusts, occurs in Section 143-866A-25R-1 (Fig. 12).

Subunit IIIC

Core 143-866A-30R to Section 143-866A-48R-1, 8 cm
Depth: 271.0–434.5 mbsf
Age: Albian–Albian

The third subunit is dominated by relatively dense mudstones to wackestones and contains four calcrete horizons. Green illitic clays with traces of kaolinite, both confirmed by XRD analyses, are commonly associated with the calcrete or other emersion features and occur exclusively in this subunit. Orbitolinids occur near the bottom of this subunit in Section 143-866A-47R-1 (see “Biostratigraphy” section, this chapter). XRD analyses have identified apatite as being present in Section 143-866A-36R-1.

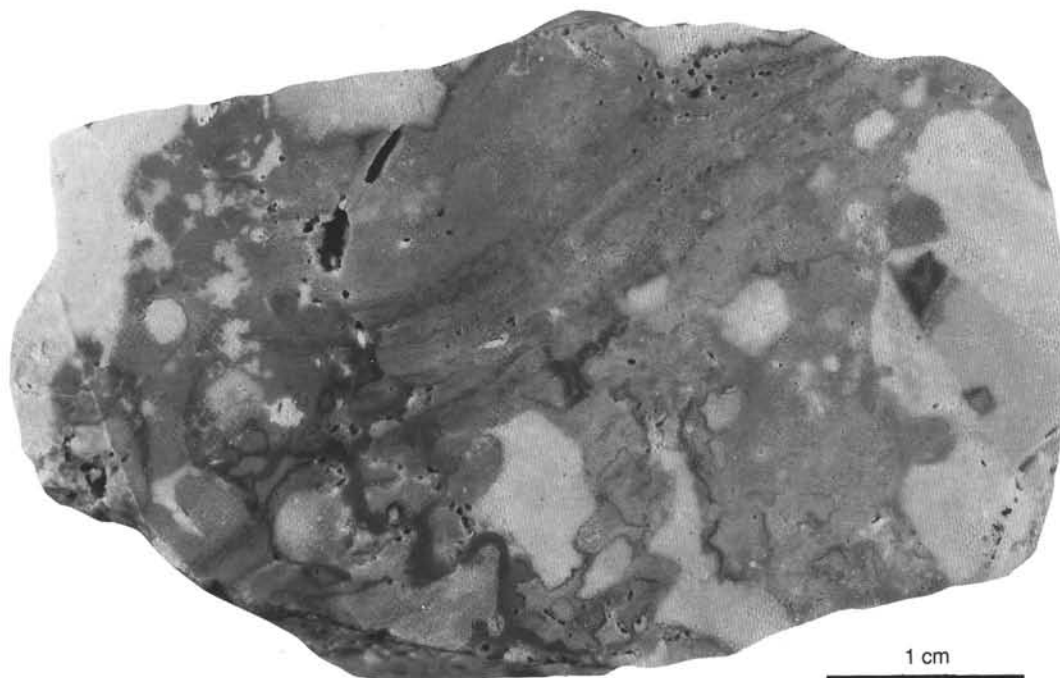


Figure 11. Laminated calcrete crust and mottling due to calcification of mudstone and wackestone. Darker linings and patches in photograph are brown in color (Sample 143-866A-39R-1, 22–23 cm; age, Aptian).

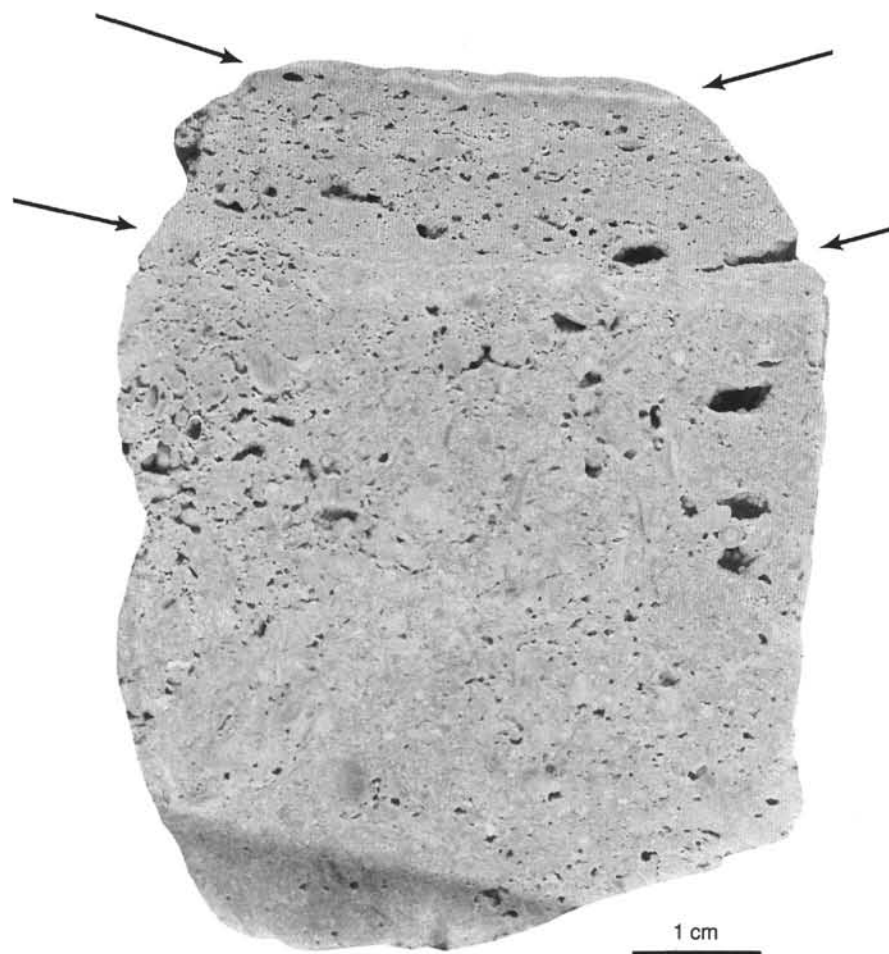


Figure 12. Grainstone to rudstone with planar lamination and abundant keystone vugs, indicating deposition in the swash zone of a beach. Thin crusts in the upper part of sample (arrows) represent incipient calcretization (Interval 143-866A-25R-1, 15–23 cm; age, Albian).

Unit IV

Sections 143-866A-48R-1, 8 cm, to -73R-1, 75 cm
 Depth: 434.5–676.6 mbsf
 Age: Aptian–Albian

This unit consists of white to pale-brown and gray bioturbated peloidal packstone, wackestone, and grainstone with gastropods and foraminifers. Other components include small shell fragments of bivalves and gastropods, together with dasycladacean algae. Orbitolinid foraminifers occur in Cores 143-866A-48R through 143-866A-56R, generally in the bioturbated packstone and grainstone intervals. Blackened peloids and intraclasts are common. Dark, organic-rich laminated wackestone, packstone, and scattered mudstone intervals occur at some levels and become increasingly abundant and distinctive downhole. Lignitic fragments occur first in Core 143-866A-50R and intermittently in the cores below. Core 143-866A-50R also exhibits desiccation cracks.

The major lithologies are organized into recurring meter-scale packets, which typically begin as laminated organic-rich mudstones, grade upward into bioturbated, less organic-rich packstones and grainstones, and finally, into white wackestones with benthic foraminifers and gastropod molds (Fig. 13). The coarser-grained intervals are moderately porous, with much intergranular and moldic porosity. The organic-rich intervals contain abundant stylolites, which in some places are stacked so close together as to give the material a laminated appearance (Fig. 13). Primary sedimentary lamination in wackestone

and mudstone occurs from Core 143-866A-61R downward. Organic-rich layered mudstones and packstones are commonly associated with an abundance of platy mudstone intraclasts. This association becomes more evident in the bottom part of the unit, especially in Cores 143-866A-64R through -71R. The laminated lime mudstones do not contain a significant proportion of clay, but its presence becomes noticeable in Core 143-866A-55R and becomes increasingly apparent in deeper cores: smectite is the dominant clay mineral in this part of the sequence. A 10-cm-thick bed of dark green claystone occurs in Section 143-866A-71R-2. XRD analysis identified this material as illite. In the Interval 143-866A-62R-1, 1–26 cm, a large, vertically oriented, coalified plant fragment was recovered, that may be fossilized bark (Figs. 14 and 15). The base of this unit occurs in Section 143-866A-73R-1, 75 cm, where a sharp transition to the underlying oolitic grainstone is seen.

Unit V

Section 143-866A-73R-1, 75 cm, to Core 143-866A-84R
 Depth: 676.6–791.8 mbsf
 Age: Aptian

This unit consists of 115 m of massive oolitic grainstone. It is generally buff to beige in color, locally cross-laminated, and generally well-sorted, although grain-size populations may be hydraulically separated in a number of intervals and some levels may show bimodal distribution. Keystone vugs are present in several discrete horizons.

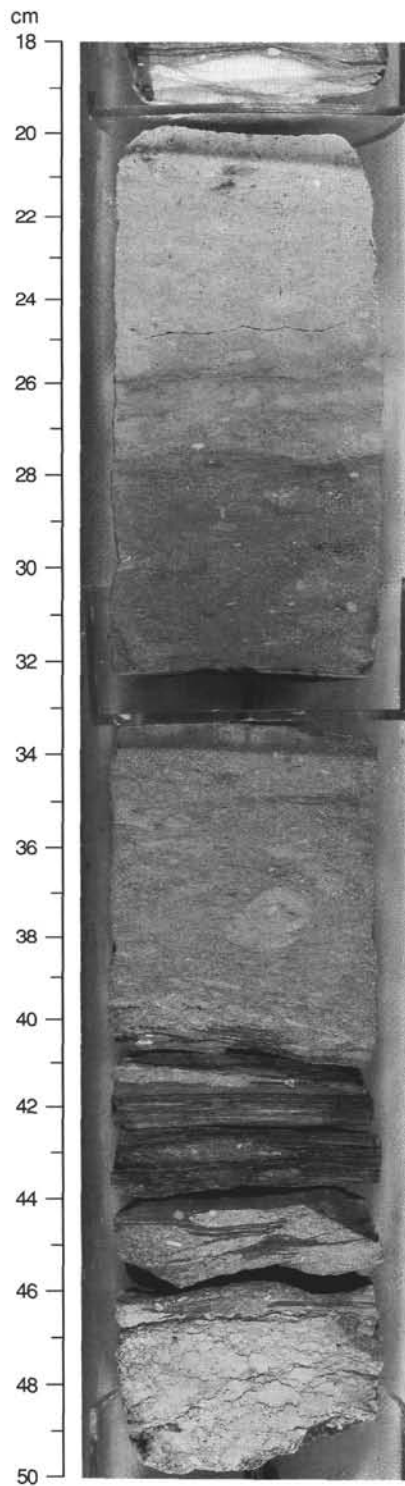


Figure 13. Lithologies common in Unit IV, bioturbated wackestone (gray) and algal laminites (dark gray); lower lithology is heavily stylolitized (Interval 143-866A-56R-1, 18–50 cm; age, Aptian).

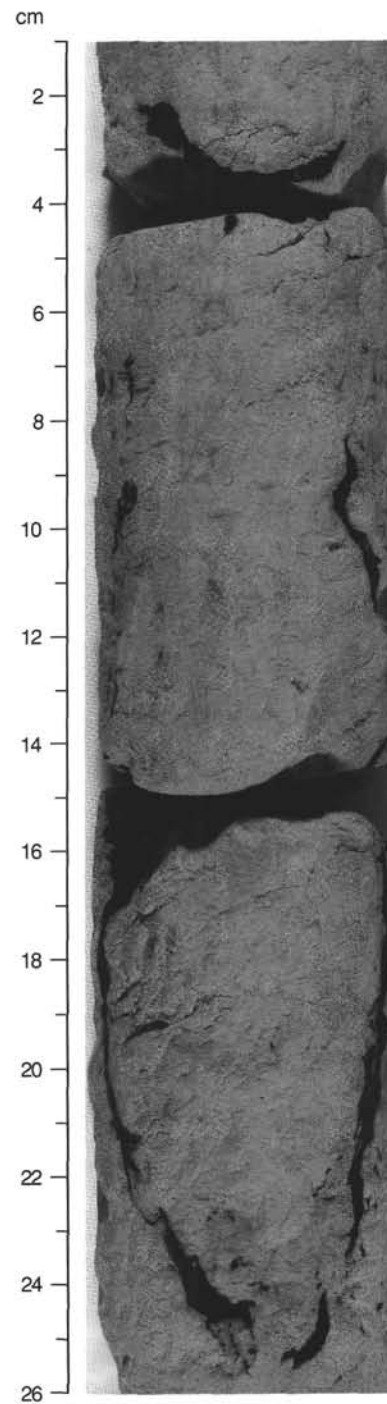


Figure 14. Vertically orientated, coalified plant fragment which may be fossilized bark (Interval 143-866A-62R-1, 1–26 cm; age, Aptian).

Accompanying the ooids are peloids, grapestones, intraclasts up to centimeter scale, rare oncoids, and a range of bioclastic material, particularly bivalve debris, echinoderm plates, foraminifers, and dasy-cladacean algae, together with corals and gastropods. Locally, the ooids and peloids are blackened. Although grainstones constitute the bulk of the section, there are small intervals of rudstone, where large fossils are present, as well as packstone, where micrite is abundant; locally, peloids replace ooids as the dominant grain type. Limited bioturbation was observed with a few recognizable burrows containing material of different grain size than that in the matrix.

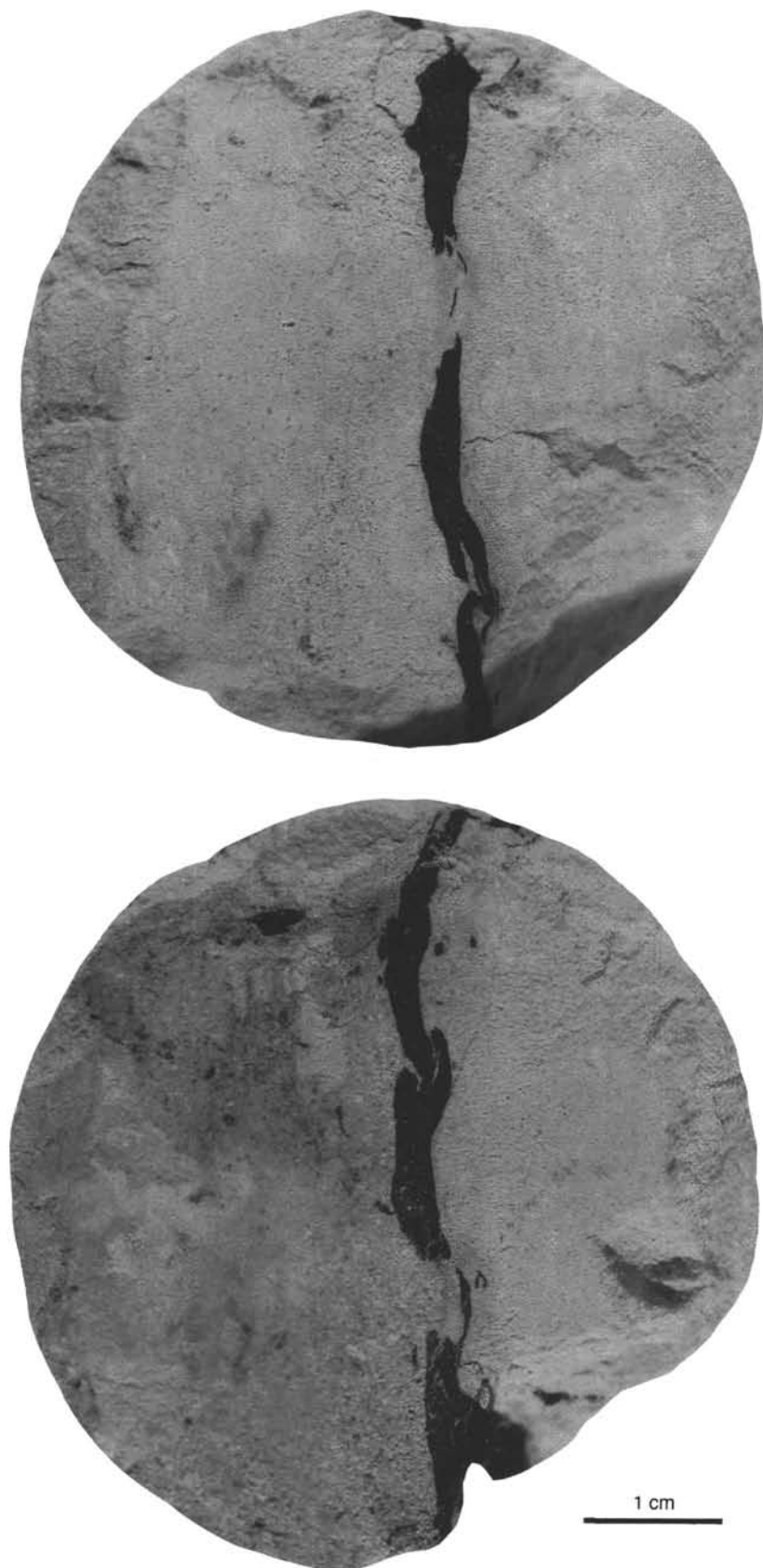


Figure 15. Transverse sections of coalified plant fragment shown in previous figure displaying interlocking elements of possible bark (Interval 143-866A-62R-1, 15 cm).

Thin-section study reveals all gradations between peloids and ooids with the latter heavily micritized or primarily micritic, although their dominant structure is clearly radial. Echinoderm fragments exhibit particularly well-developed syntaxial overgrowths; cementation elsewhere is patchy and can either fill much of the pore space or be represented merely by a thin fringe cement or more blocky equant crystals. The most notable feature about the ooids is their high degree of overpacking, manifested by significant interpenetration of grains.

Unit VI

Core 143-866A-85R to Section 143-866A-128R-1, 20 cm
Depth: 791.8–1203.4 mbsf
Age: Aptian

Unit VI comprises 412 m of buff-colored packstone-wackestone, dark-gray algal laminites, and interstratified centimeter-thick intervals of dark gray clay/organic-rich mudstone. The characteristic feature of the unit is the cyclic arrangement of lithologies and the occurrence of laminoid-fenestral fabrics, keystone vugs, tepee structures, and desiccation cracks. The base of the unit is defined as the upper surface of the brown dolomitized limestone in Section 143-866A-128R-2. The occurrence of distinctive caprinid rudist debris and a stratigraphically associated rudist biostrome (Section 143-866A-92R-1 through -97R-1; 859.2–908.0 mbsf) and the occurrence of secondary dolomite below the biostrome allowed us to subdivide the unit into three subunits.

Subunit VIA

Cores 143-866A-85R to -91R
Depth: 791.8–859.2 mbsf
Age: Aptian

This subunit is composed of buff-colored peloidal packstone-wackestone that alternates with dark gray algal laminites, up to 20 cm thick, and centimeter-thick dark gray to greenish-gray millimeter-laminated clay/organic-rich mudstone. Interval 143-866A-89R-1, 92–101 cm, contains an example of the latter facies, which is dark green at the top and grades down into a black very organic-carbon-rich level (14.19% TOC; see “Organic Geochemistry” section, this chapter); similar but less well-developed claystones occur in Sections 143-866A-88R-1 and -91R-1. As for the interval in Core 143-866A-89R, correlation with the deep-marine, organic-rich and bentonitic limestones of nearby DSDP Site 463 in the Mid-Pacific Mountains (Dean et al., 1981) is compatible with the available stratigraphy and in both sites the organic matter has a low hydrogen index and resembles Type III kerogen. XRD analyses indicate that the clay fraction in the carbon-rich layer of Hole 866A is dominantly illite with minor smectite. Smear slides and XRD data from the black claystones in Intervals 143-866A-91R-1, 10–12 cm, and 26–28 cm, reveal the presence of minerals of igneous derivation, such as feldspars and zeolites.

The fauna within the bioturbated packstone-wackestone includes gastropods, bivalves, small-sized benthic foraminifers, and dasycladacean algae. The algal laminites and clay/organic-rich mudstones locally contain abundant ostracodes and blackened peloids. The meter-scale sequences that constitute much of this unit ideally commence with centimeter-thick, dark gray layers of clay/organic-rich mudstone that grades up into peloidal packstone-wackestone and, thence, into algal laminites. Fenestrae, tepee structures (Fig. 16), and desiccation features occur within the algal laminites.

Subunit VIB

Cores 143-866A-92R to -97R
Depth: 859.2–917.0 mbsf
Age: Aptian

This subunit is characterized by the presence of abundant rudists and their debris. The caprinids are preserved in two different facies: peloidal packstones to wackestones, containing some benthic foraminifers and oyster fragments in the lower part of the unit, and in well-washed grainstones to rudstones in the upper part. Cores 143-866A-96R and -97R have some complete specimens as well as large fragments. In these, the primary aragonite has been completely dissolved, leaving a void supported only by the muddy sediment that has collapsed to varying degrees. Hence, details of canals have almost invariably been lost, as has the original shape of the valves. In some places, a well-cemented peloidal grainstone is preserved inside the body cavity; in others, where shell fragments have protected a space in the sediment, the base of the cavity is filled with blue-gray clay that has been capped by sparry cement.

By contrast, in the shell hash of Cores 143-866A-92R to -95R, the originally aragonitic inner shell wall of the rudists developed micrite envelopes, which were preserved after dissolution of the skeletal aragonite, producing supported voids (Fig. 17). In addition, some later growth of sparitic calcite has lined the cavities. Other facies include a well-washed peloidal grainstone with some gastropod molds and well-preserved calcitic oyster fragments.

Subunit VIC

Core 143-866A-98R to Section 143-866A-127R-1, 20 cm
Depth: 917.0–1203.4 mbsf
Age: Aptian

This subunit displays considerable lithologic similarity to Subunit VIA. Cream-colored bioturbated peloid wackestone-packstones contain ooids, coated grains, ostracodes, dasycladacean algae, miliolid foraminifers, minor caprinid rudist debris, bivalves, and blackened intraclasts. Moldic porosity is widespread. Intervals of algal laminites are common and in many places display bird's-eyes and desiccation cracks. Stylolites are generally concentrated at bedding contacts in the algal laminites. A 15-cm-thick stromatolite occurs in Section 143-866A-109R-1 (Fig. 18). One lithology unique to this subunit is dark gray organic-rich clay/lime mudstone laminite (Fig. 19). Overall, the facies are grouped into meter-scale cycles as in Subunit VIA. Patchily distributed dolomite occurs throughout the subunit but becomes more common downhole. A prominent brown to dark yellow-stained laminated limonitic mudstone occurs between 49 and 51 cm in Section 143-866A-121R-1. Similar, but less well-developed, limonitic levels are found in Sections 143-866A-123R-1 and -124R-1.

The lower part of this subunit clearly shows small-scale shallow-upward sequences. The major lithologies are organized into meter-scale packets, which typically begin as peloidal wackestone-packstone with miliolids, fragments of shells (including rudists), and grade upward to mudstone-wackestone levels, including one or several of the following elements: bird's-eye vugs, oncoids and algal mats, with the latter two being commonly dolomitized. In some places, minor organic-rich clayey limestones occur at the bottom of each sedimentary packet, whereas the top is commonly truncated and shows small-scale desiccation cracks.

Below the dark yellow-stained laminated limonitic mudstone (Section 143-866A-121R-1), peloidal wackestone-packstones with fragments of rudists are dominant.

Unit VII

Sections 143-866A-127R-1, 20 cm, to -148R-4
Depth: 1203.4–1399.7 mbsf
Age: Barremian

Unit VII consists of pale brown to brown and white dolomitized oolitic/peloidal grainstone, oncoidal wackestone, and algal laminites with clay/organic-rich intervals. The characteristic feature of this unit

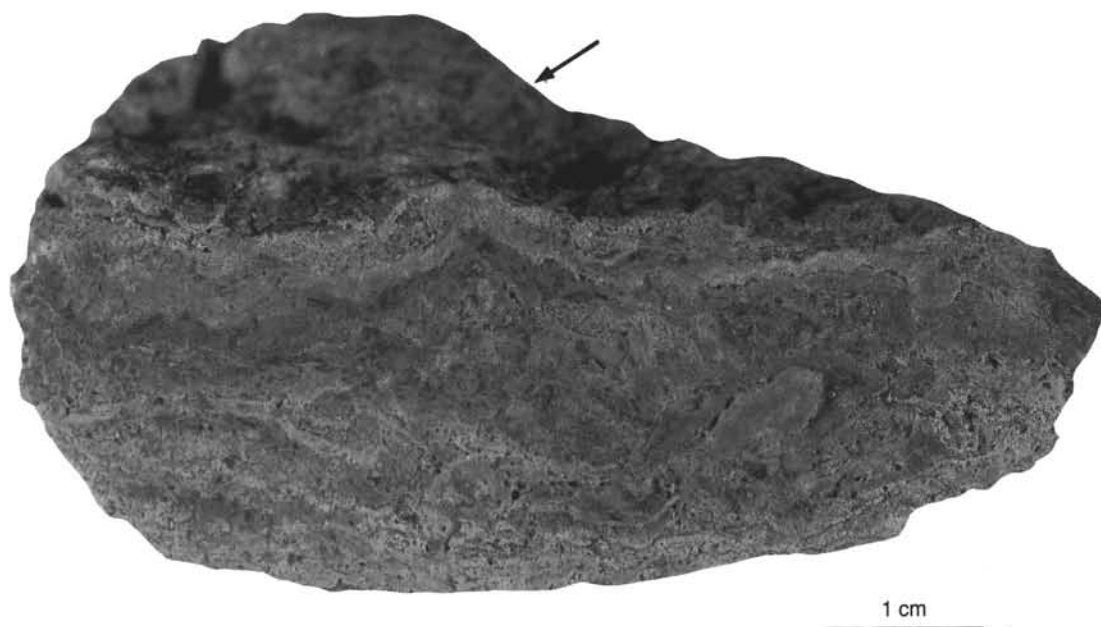


Figure 16. Calcified algal laminites displaying tepee structures (arrows) and disruption caused by desiccation (Interval 143-866A-86R-2, 76 cm; age, Aptian).



Figure 17. Caprinid rudist debris, Subunit VIB (Interval 143-866A-92R-1, 12–18 cm; age, Aptian).

is its pervasive sucrosic dolomitization and the increased contribution of oncoids. Bird's-eye and keystone vugs occur at several intervals throughout this unit. The components include oncoids, peloids, bivalve shells, serpulid worm tubes, echinoids, rudists, corals with *Lithophaga*-like borings, and nerineid gastropods. The presence of a distinctive white dolomitized peloidal grainstone (Sections 143-866A-

133R-1 to -138R-1) initially divides the unit into three, and the basal portion can be further subdivided on the basis of the facies characteristics. The bottom of the unit is recognized at the abrupt lithologic change to the more thickly bedded oolitic-oncoidal grainstone of Unit VIII.

Subunit VIIA

Section 143-866A-127R-1, 20 cm, to Core 143-866A-132R
Depth: 1203.4–1251.6 mbsf
Age: Barremian

This subunit consists of pale brown to brown dolomitized wackestone to grainstone. Dolomitization is pervasive in many parts of this unit, and although crystal size commonly exceeds 1 mm, the fabric of the rock still preserves bird's-eye and keystone vugs. The outlines of peloids, ooids, blackened intraclasts, bivalves, algal-encrusted gastropods, oncoids, small benthic foraminifers, and serpulid worm tubes remain visible. The wackestones display widespread bioturbation. The upper part of this subunit is characterized by the same small-scale sequences as the lower part of Subunit VIC. Toward the bottom, peloidal oolitic packstone-grainstone disappears, and the sequence is mainly represented by facies having desiccation phenomena that are generally dolomitized. The basal boundary of this subunit is marked by an abrupt change to the brilliant white dolomite of the underlying subunit.

Subunit VIIB

Cores 143-866A-133R to -137R
Depth: 1251.6–1299.5 mbsf
Age: Barremian

This subunit consists of white sucrosic dolomite, in part stained light red, that has replaced the original peloidal grainstone to a varying degree. Rudists occur in Core 143-866A-136R and echinoid fragments in Sections 143-866A-137R-1 and -2. Depositional features (such as keystone vugs) are preserved in Sections 143-866A-133R-1 and -2. The organization and inter-relationship of facies in this subunit are unknown because of its extensive dolomitization.

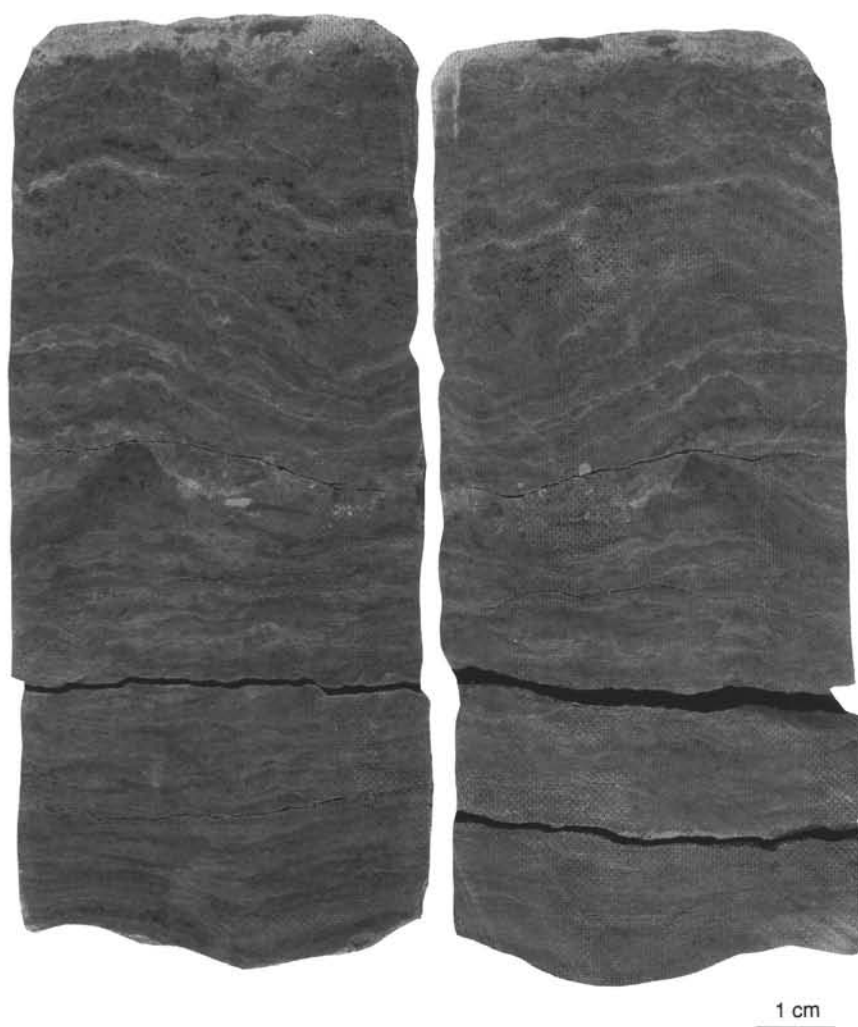


Figure 18. Algal stromatolite, Subunit VIC (Interval 143-866A-109R-1, 31–43 cm; age, Aptian).

Subunit VIIC

Cores 143-866A-138R to -143R
 Depth: 1299.5–1357.5 mbsf
 Age: Barremian

This subunit consists of buff-colored peloidal grainstone, locally oolitic, which is rich in bivalve and gastropod shell debris. Other constituents include small spherical colonies of corals (Fig. 20), rudist shell fragments, echinoids, stromatoporoids, algae, and possible sclerosponge fragments. Corals and rudists are more abundant in the lower part of the subunit. Bird's-eye vugs occur in Section 143-866A-138R-1. Intercrystalline and moldic porosity is developed throughout. Several large stylolitic structures occur. The top of this subunit is marked by a change, through finer-grained wackestones that contain a solution breccia and possible bird's-eyes, to the underlying brown dolomitized peloidal grainstone in Section 143-866A-138R-1, 114 cm. Dolomitization is variable. The base of the subunit is marked by the appearance of algal laminites.

Subunit VIID

Core 143-866A-144R to Section 143-866A-148R-4, 44 cm
 Depth: 1357.5–1399.7 mbsf
 Age: Barremian

This subunit consists of buff to white to brown oolitic peloidal grainstone, oncoidal wackestone, and local mudstone with interstratified algal laminites. Patchy dolomitization is developed throughout. Ooids, peloids, intraclasts, and oncoids constitute the principal grain types and the fauna includes gastropods, bivalves, corals, dasycladacean algae, oysters, echinoids, and benthic foraminifers. Well-preserved ostracodes, together with miliolid foraminifers, occur between 111 and 113 cm in Section 143-866A-146R-1. Algal laminites occur throughout the subunit, and several of these exhibit fenestral structures. In a few places, the algal laminites have been concentrated to a significant degree to produce clay/organic-rich, centimeter-thick layers. Desiccation cracks occur in some of the algal laminites. A typical sequence would show well-developed peloidal wackestone-packstone with miliolid foraminifers at the bottom, passing up into more-or-less dolomitized mudstone-wackestone having bird's-eye vugs, oncoids, and algal mats at the top. Intergranular and moldic porosity is characteristic of the entire subunit. Stylolites are abundant. A notable feature of the base of this subunit is the occurrence of pebbles and a boulder of the oolitic-oncoidal grainstone of the underlying Unit VIII within the enclosing clay/organic-rich mudstones (Fig. 21).

Unit VIII

Sections 143-866A-148R4, 44 cm, to -171R-2, 23 cm
 Depth: 1399.7-1620.0 mbsf
 Age: Barremian

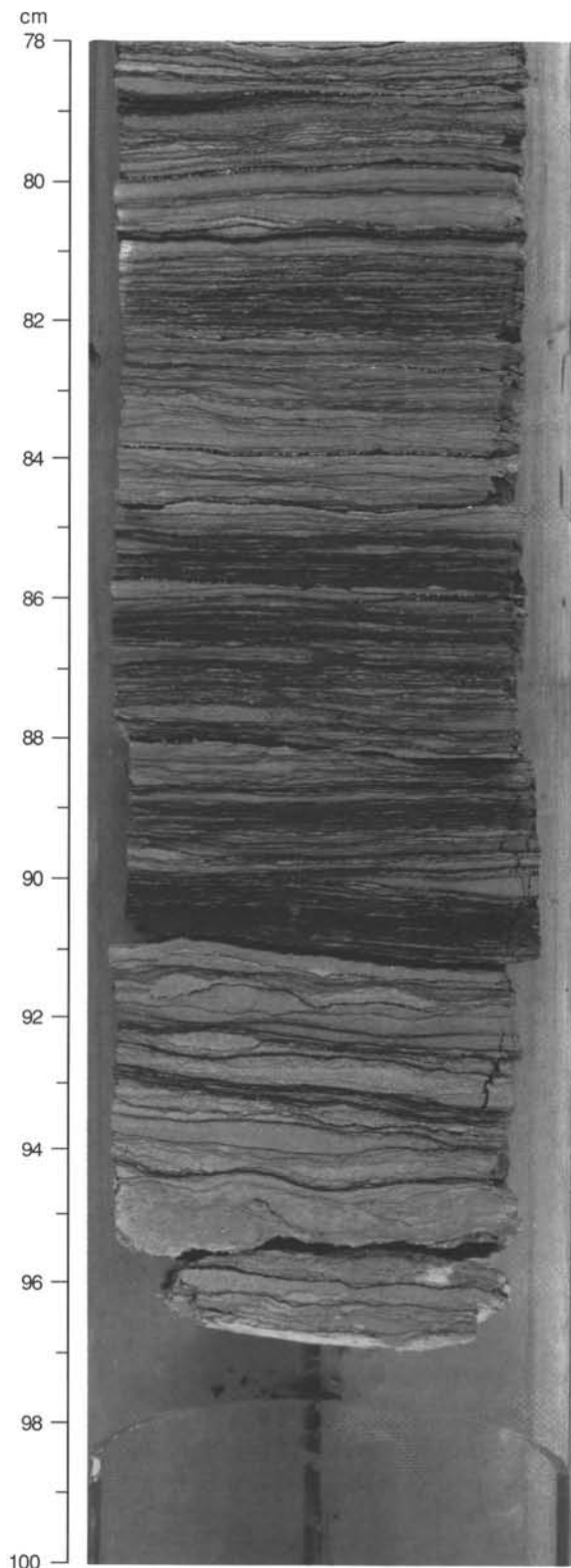


Figure 19. Algal laminites in Subunit VIC; alternating clay-rich organic-rich and carbonate mudstones. Rhythmic layering may be due to tidal cycles (Interval 143-866A-110R-2, 78–100 cm; age, Aptian).

This unit is constituted by tan-colored, pervasively dolomitized oolitic grainstones that contain lighter-colored unreplaced oncoids of up to centimeter-scale (Fig. 22). In general, dolomitization increases downhole, except for the basal 23.6 m of largely undolomitized oolite, which rest on basalt. This difference permits a ready subdivision of the section into two subunits.

Subunit VIIIA

Sections 143-866A-148R-4, 44 cm, to -169R-2, 0 cm

Depth: 1399.7–1601.3 mbsf

Age: Barremian

This subunit is composed of buff-colored oolitic and peloidal grainstones that locally contain intraclasts and grapestones. Some cross-lamination is seen, and sorting is generally good. Typical faunal and floral elements include gastropods, green algae, bivalve fragments, scattered corals and echinoid spines and rare bryozoans. Packstones, wackestones, and local mudstone levels also occur. Oncoids are characteristic of this subunit; they exhibit typical concentric structure and commonly reach or exceed diameters of 3 cm. Locally, they are hydrodynamically sorted and some of them have been bored. Grading is apparent in Section 143-866A-164R-2. Where oncoids are particularly abundant the sediment can be classified as rudstone (Fig. 23). Algal laminites are recorded from Section 143-866A-153R-1. Scattered black anastomosing clay seams of millimeter to centimeter-scale, stylolites, and traces of bioturbation are also observed.

Dolomitization is patchy and irregular in the upper part of the section, although there are some thin (few tens of centimeters), entirely dolomitized levels, but it becomes more significant downhole, at first sparing the oncoids, which remain as calcitic relics, but in places ultimately replacing even these and rendering them into vague spheroidal outlines or molds. The dolomite is typically colored various shades of tan through brown, more rarely black, and is sucrosic and vuggy. Pieces of lignite occur within the dolomite in the mid- to lower part of the section, where traces of bioturbation are also recognizable. Pyrite and a green authigenic mineral also occur in these lower levels.

Thin-section study reveals a range of ooid types, most of which are dominantly micritic. Radial structure is discernible in some of the ooid cortices; others are entirely featureless, and a number exhibit a tightly wound, concentric structure and, in fact, may be micro-oncoids. They conform exactly to the description of redeposited Aptian-Albian ooids from the East Mariana Basin, described by Haggerty and Premoli-Silva (1986). Dolomitization is represented by different styles, from solitary rhombs that replace parts of ooids or peloids, to interstitial. Interstitial dolomite is present either as thin cement fringes or as a coarser-grained fill. Considerable void space (10%–20%) still remains in some facies. Overpacking and interpenetration of grains is particularly apparent in these poorly lithified levels, but markedly less so in those cemented by coarse-grained interstitial dolomite. In Cores 143-866A-166R and -167R, tiny basaltic clasts locally act as ooid nuclei.

Subunit VIIIB

Sections 143-866A-169R-2, 0 cm, to -171R-2, 23 cm

Depth: 1601.3–1620.0 mbsf

Age: Barremian

This subunit, a mere 15 m thick, comprises gray pyritic oolitic grainstones; the pyrite typically resides in the cores of ooids as well as in the matrix, and peloids and distinctive green clasts also occur. Given that small altered grains of basalt constitute the nuclei of some ooids, these clasts probably represent altered basaltic material. Cementation is generally good. Oncoids, typically several millimeters in diameter, locally accompany the ooids. Skeletal remains include gastropods, which may possess oncoidal coatings, together with corals and foraminifers, plus bivalve, bryozoan, and echinoderm frag-

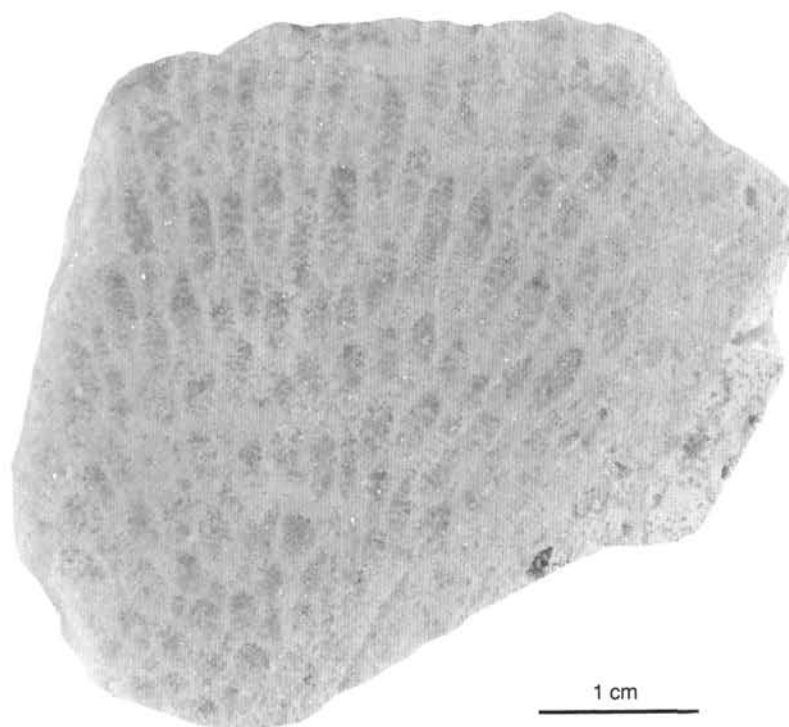


Figure 20. Fragments of colonial coral (Interval 143-866A-142R-1, 11–13 cm; age, Barremian).

ments. Thin-section study reveals a range of ooid types, including micritic, concentric and radial, and composite particles that include more than one fabric; intraclasts of oolitic sediment also occur. Grains show a modest degree of overpacking; remaining void space is about 10%. The amount of dolomite is modest and occurs only as a scattered interstitial rhomb or as a very thin fringing cement around ooids.

The contact with the basalt is irregular and, in a small pocket or vein trending downward into the igneous rock, the oolite contains a few subrounded clasts of basalt of up to centimeter-scale and, hence, appears conglomeratic (Fig. 24).

Interpretation of Sedimentary Environments

In this section, the effect of diagenetic dolomitization on the sequence has been ignored and the depositional history reconstructed on the basis of primary lithology or interpreted primary lithology. The nature and significance of carbonate diagenesis and dolomitization are discussed below.

The nature of the contact between the basalt and the overlying oolitic grainstone, with clasts of the former in the latter, is consistent with an interpretation of the contact as essentially sedimentary (see "Igneous Petrology" section, this chapter). Submillimeter-scale basaltic fragments were available to act as ooid nuclei for some considerable time after deposition of the oolitic grainstone of Subunit VIII B began, but no substantial volcanoclastic deposits were developed. A fundamental question raised with respect to the Unit VIII grainstones concerns their rate of sedimentation and whether any of them were redeposited. In the absence of any refined stratigraphic data to determine anomalous depositional rates, recourse must be made to sedimentary structures. Evidence for graded bedding exists in one section only and, in general, the whole of the unit appears to have been generated and laid down in shallow turbulent water on an open platform or ramp. The normal marine fauna of corals, bryozoans, and echinoids is consistent with this view, as is the local development of cross-lamination and hydraulic sorting.

The radial types of ooids suggest a primary calcitic or high-magnesian calcitic mineralogy, the precipitate thought to have been fa-

vored during the Cretaceous (Sandberg, 1983). However, the genetic difference between the oncoids of centimeter-scale size and the laminated micritic ooid-scale particles that exhibit fine concentric lamination may be very small and both may owe their origin to a cyanobacterial film.

A major facies change occurred with the beginning of deposition of Unit VII. The dominant finer-grained grainstones to packstones to mudstones with algal laminites, oncoids, desiccation voids, miliolid foraminifers, and scattered centimeter-thick organic/clay-rich layers indicate a significant environmental change to more variable, restricted, shallow-lagoonal to intertidal conditions. The rapidity of this change within the cores may betray the presence of a significant sedimentary gap. Water depth has been interpreted as generally being extremely shallow, with episodes of local emergence. The dark organic/clay-rich laminated facies locally pass up into more typical calcified algal laminites, and this is attributed to small negative oscillations of sea level to produce intertidal facies (Fig. 25). However, the overlying grainstone to boundstone interval, with its richer fauna of gastropods, bivalves, green algae and particularly echinoids, corals, and possible sclerosponges or stromatoporoids (characteristic of Subunit VIIC) that were deposited somewhat later, clearly indicate fully marine subtidal conditions. Whether the corals and associated hydrozoans indicate elements of a patch reef or a more substantial structure cannot be discerned from the recovered material. The peloidal grainstones of Subunit VIIB also possess a fully marine fauna (echinoids, rudists, gastropods, dasycladacean algae), similarly indicating normal salinities. During the later depositional history of Unit VII (Subunit VIIA) conditions became less turbulent with the deposition of mudstones to wackestones plus scattered grainstones with oncoids, together with algal laminites, organic/clay-rich intervals, blackened intraclasts, and bird's-eye and keystone vugs. The fauna, apart from scattered rudists, is notably more limited than that which flourished in the preceding interval. In general, these facies strongly resemble those of Subunit VIID and mark a return to restricted shallow-lagoonal to intertidal conditions.

Unit VI differs from the underlying unit in a reduction of the component of coated grains (ooids and oncoids) in the sediment and

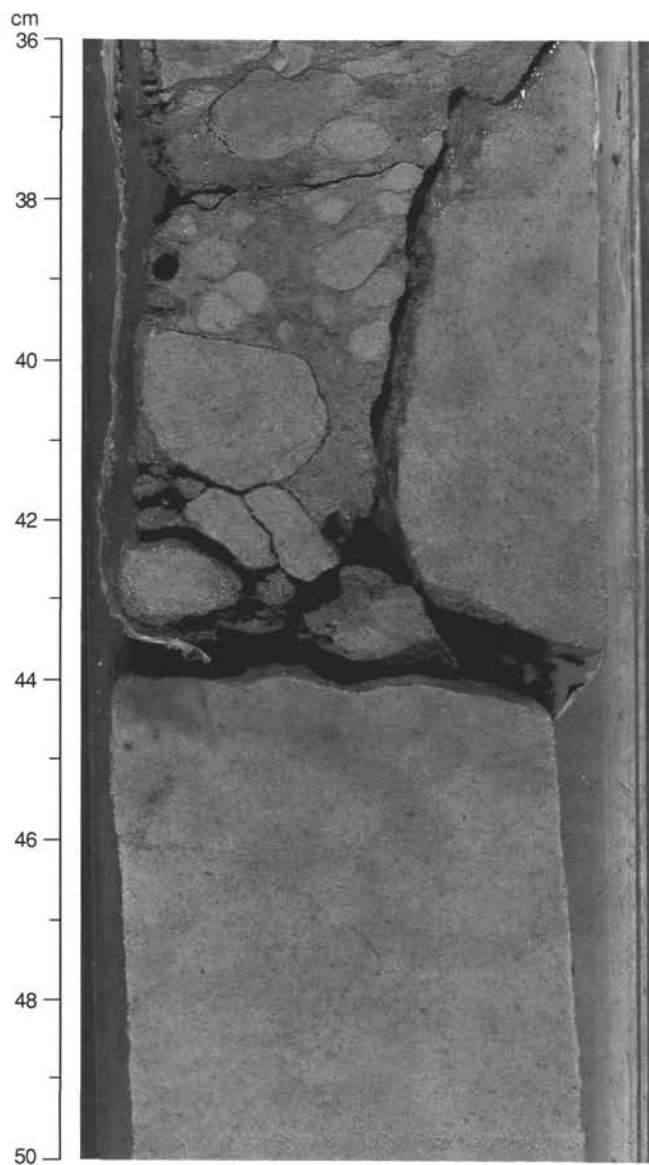


Figure 21. The base of Unit VII is represented by poorly sorted conglomerate including a boulder and pebbles of the underlying oolitic grainstone (Interval 143-866A-148R-4, 36–50 cm; age, Barremian).

an increase in the amount of algal-laminite and clay-rich facies. The blackened intraclasts formed by reworking of limestone impregnated by organic matter and pyrite, which implies the presence of locally anoxic shallow-subtidal to intertidal conditions (Strasser, 1984).

Unit VI is characterized by meter-scale sequences whose facies evolution implies cyclic changes of the depositional environment from subtidal to intertidal-supratidal and back to subtidal (Fig. 25). Emergence of the substrate during low relative sea level is indicated by desiccation cracks or by calcified algal mats, including bird's-eyes and tepee structures. A relative rise of sea level resulted in flooding of the emergence surface and in reworking of mud chips and flakes of dried algal mat, forming flat-pebble conglomerates (Fig. 26). Clays and organic matter of terrestrial or mixed terrestrial-marine origin (see "Organic Geochemistry" section, this chapter) were deposited during this early phase of transgression. Water depth then increased and led to a more-or-less restricted, shallow-lagoonal depositional setting. Carbonate production soon outpaced the rise in relative sea level, thus creating a shallowing-upward facies sequence that terminated in

intertidal and supratidal deposits. In some places, the sequences are incomplete: either a decrease in relative sea level directly exposed subtidal facies, preventing further deposition (Fig. 27), or the organic/clay-rich early transgressive deposits were never deposited (Fig. 28), or the sediment was never subaerially exposed (Fig. 28). Similar small-scale peritidal sequences described from many ancient and recent carbonate environments (e.g., James, 1977; Shinn, 1983) can in some cases be ascribed to sea-level fluctuations caused by climatic cycles in the Milankovitch-frequency band (e.g., Strasser, 1991).

Deposition of Subunit VIB marked a temporary change to a more turbulent environment in an otherwise quiet-water sequence. At the base is the caprinid rudist biostrome. The mostly intact shells have been entombed in a normal-marine peloidal packstone with benthic foraminifers and dasycladacean algae, reflecting an environment similar to that in which this type of rudist typically lived; during life, one valve would have been implanted in the sediment. Overlying this unit are debris beds where the shells are broken and concentrated and from which the mud has been winnowed. This succession suggests the progradation of outer banks and shoals over the lagoonal sediments in a short-lived transgression. A transition to the overlying muddy sediments is not recorded in the recovered sequence so there is no information bearing on the relative speed of the subsequent regression.

Subunit VIA marks a return to cyclical algal laminite facies, but with more coated grains and common dasycladacean algae, suggesting greater proximity to shoal-type environments than during deposition of Unit VIC.

With the onset of deposition of the Unit V oolitic grainstones, conditions changed abruptly. The presence of cross-lamination, particularly in the higher part of the unit where bioturbation is not so pervasive, together with evidence of hydraulic sorting and comminuted fossils, suggests deposition in shallow turbulent water in an exposed environment. The fauna, particularly the echinoderms and corals, similarly suggest normal-marine conditions. Particularly diagnostic are the keystone vugs, which typically form, immediately above the wave swash zone, by the escape of air bubbles from intergranular pores as they are flooded with marine waters during the flood tidal cycle across a beach (Inden and Moore, 1983). The presence of keystone vugs is consistent with present-day observations of ooid generation, which demonstrates their formation in waters of a few meters depth (e.g., Bathurst, 1975).

Another major facies boundary was crossed with the beginning of deposition of Unit IV. The dominant organic-rich laminated wackestone-packstone intervals and bioturbated peloidal packstone-wackestones indicate a significant environmental change from subtidal open-marine turbulent (Unit V) to more variable restricted shallow-lagoonal to intertidal conditions. The disappearance of echinoids and increase in abundance of ostracodes (see "Biostratigraphy" section, this chapter) is consistent with this interpretation. The abruptness of the facies change points to the presence of a possible sedimentary gap at this level. Despite this change from open-marine turbulent water to restricted subtidal-intertidal conditions, the basal deposits of Unit IV might mark the first stage of the transgression and flooding of a previously exposed surface. From the bottom to the top, cyclic variations in facies occur. The organic-rich, laminated wackestone-packstones probably formed in intertidal swamps or marshes, whereas the bioturbated, less organic-rich packstones-grainstones and white wackestones with benthic foraminifers and gastropods imply deposition in intertidal to subtidal channels and more marine lagoonal environments. Lignitic fragments and abundance of bioturbation are consistent with this model and show that terrestrial plant material was occasionally transported seaward. Although some intervals display desiccation cracks, the environments of deposition gradually deepened and became more open marine. These features may indicate a significant transgressive phase on the subsiding platform which is marked by the appearance of large benthic foraminifers, especially orbitolinids.

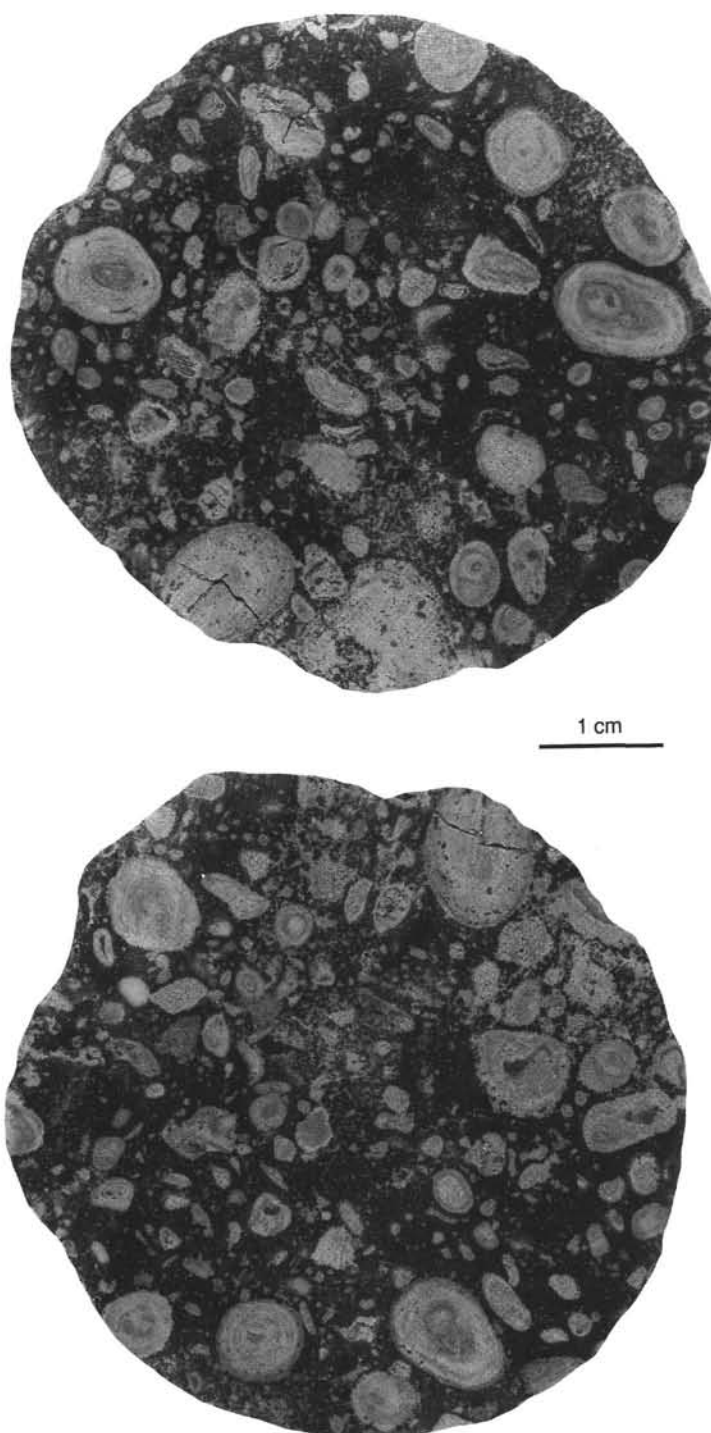


Figure 22. View of bedding surfaces showing abundant light-colored oncoids of varying size in dark brown dolomitized matrix, Unit VIII (Interval 143-866A-154R-3, 56–60 cm; age, Barremian).

The depositional environment of the recovered limestones in Unit III was basically that of a protected shallow lagoon. The overall poor diversity of fauna and flora as well as the local abundance of dasycladacean algae and small gastropods suggest restricted conditions, whereas the local appearance of echinoids points to episodic intrusions of normal-marine waters. In thin-section, the echinoid material appears abraded and micritized and may have been intro-

duced by storms and subsequently mixed into the sediment by bioturbation. Sponges and sponge spicules become more abundant in the upper part of the unit and imply a general opening of the lagoon through time. Water turbulence was low, allowing for the deposition of facies rich in carbonate mud (mudstones and wackestones). However, the abundance of bioturbation and the absence of dark-colored limestones implying dysaerobic conditions indicate that the lagoon

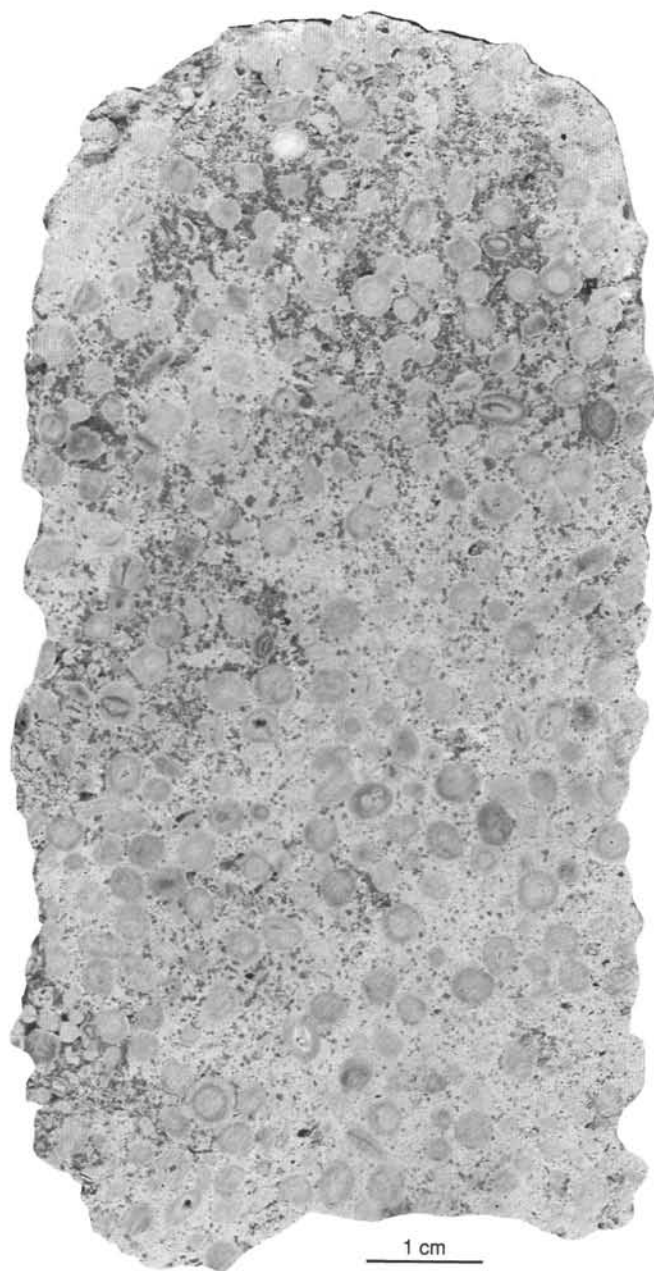


Figure 23. Well-sorted ooloids in oolitic-peloidal grainstone, the characteristic lithology of Unit VIII (Interval 143-866A-156R-2, 38–49 cm; age, Barremian).

was well oxygenated. Storms occurred at times, ripping up clasts from the cohesive muddy substrate or forming graded beds, such as those in Section 143-866B-8M-1. In some cases, the storm deposits were preserved only in burrows, while the material on the seafloor was reworked or eroded (Tedesco and Wanless, 1991). Coarse-grained intervals in the upper part of the unit (floatstones and rudstones in Cores 143-866A-6R, -7R, and -8R) are suggestive of washover deposits.

Several features indicate that the lagoon was repeatedly subjected to emergence. Planar lamination and keystone vugs in Section 143-866A-25R-1 formed in the swash zone of a high-energy beach, whereas vertical and horizontal cracks and fenestrae in mudstones or wackestones were created during short periods of desiccation. Calcretization of the substrate and formation of laminar calcretes suggest longer episodes of subaerial exposure. The green illitic clays associated with

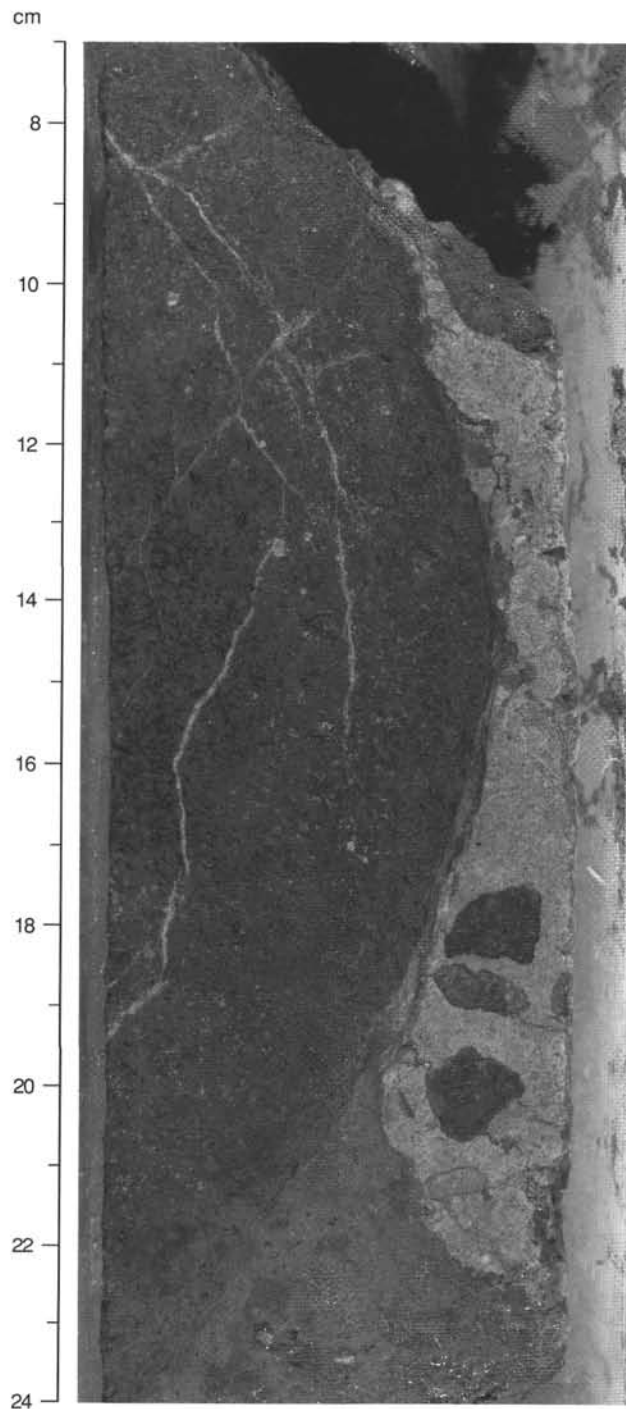


Figure 24. Contact of light gray oolitic grainstone (Subunit VIII B) and dark gray altered basalt (Unit IX). The oolitic grainstone is extensively pyritized and the precise nature of the contact is equivocal (Interval 143-866A-171-2, 7–24 cm; age, Barremian).

the emergence horizons are most probably authigenic and may have formed by transformation of windblown detrital clay through repeated wetting and drying in a peritidal setting (Deconinck and Strasser, 1987). Scattered black pebbles incorporated in subtidal facies probably derived from nearby intertidal to supratidal facies belts. Note that in many places desiccation features or calcrete directly

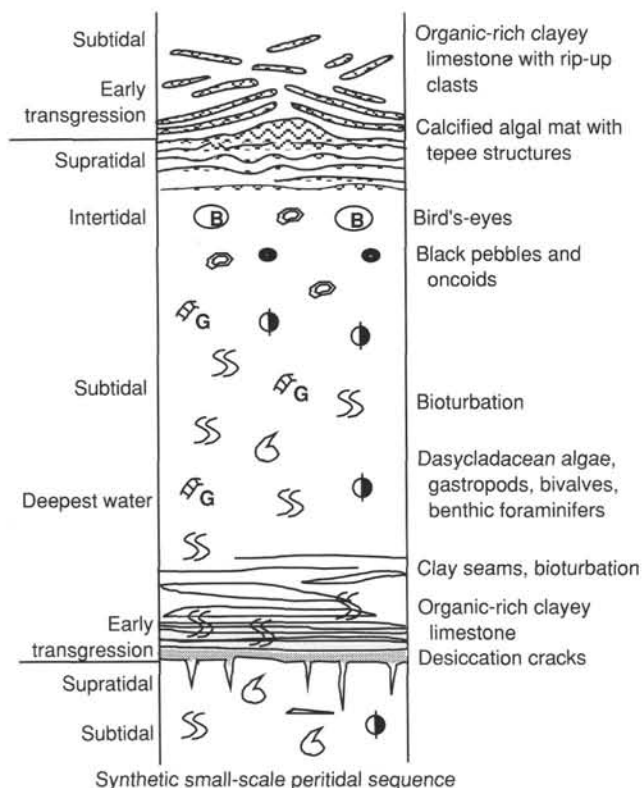


Figure 25. Sketch of idealized, small-scale peritidal sequence commonly developed in Units VI and VII, and to a lesser extent in Unit IV. No exact scale envisaged, but the thickness of section illustrated would be in the range of 50 to 500 cm.

overlie subtidal facies. This implies a relative fall in sea level, which exposed subtidally deposited sediment to subaerial conditions without passing through an intertidal depositional phase.

The rapid change from yellow grainstones-packstones to light-colored wackestones at the lower boundary of Unit III and the change from the clay-rich Unit IV to the basically clay-free Unit III suggest that the volcanic islands no longer furnished terrigenous material or had disappeared altogether. The carbonate platform remained very shallow, and short-term fluctuations of relative sea level periodically exposed the sediment to subaerial conditions. The subaerial events became less frequent through time, suggesting a general opening of the lagoon. However, abundant carbonate production maintained the water depths at a very shallow level. It is possible that the amplitude of sea-level fluctuations decreased during deposition of the upper part of the unit, thus creating less significant emergence events.

The subsequent history of Resolution Guyot is shrouded in mystery because of poor recovery of critical intervals. However, by drawing on regional studies and data from Allison Guyot (Site 865), some tentative interpretations may be made. Given that the surface of Resolution is karstified, it seems likely that it too, like Allison, was uplifted in Albian time, or at least influenced by relative sea-level fall, and deeply dissected before ultimate submergence. The manganese-encrusted and stained pebbles used to characterize Unit II suggest the formation of a mineralized submarine hardground across this irregular surface. Such hardground material was dredged on the outer rim of the guyot during the site survey. It is probable that this crust is associated with Cretaceous pelagic sediments that record the early drowning history of Resolution Guyot, but the only trace of this is given by Maastrichtian nannofossils found at the base of the ooze section at Hole 866B (see "Biostratigraphy" section, this chapter). Furthermore, it is likely that a substantial period of nondeposition and

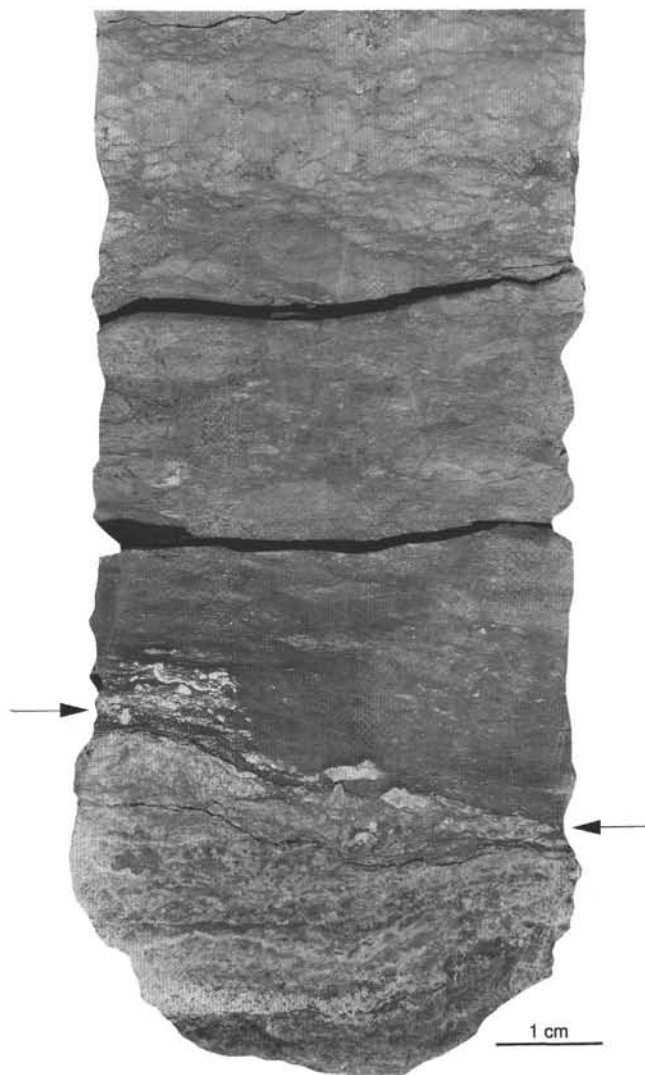


Figure 26. Boundary of small-scale sequence in Subunit VIA displaying calcified algal mats below, rip-up clasts in a matrix of clay/organic-rich mudstone (arrows), and gradual upward decrease of clay. Mottling in clay-rich sediment is from bioturbation (Interval 143-866A-89R-1, 20–33 cm; age, Aptian).

erosion took place before the foraminiferal-nannofossil oozes of Unit I could be deposited. The somewhat sandy texture of these oozes, given that they are of Pliocene age, suggests that they are being actively winnowed at the present time.

Interpretation of Diagenetic History

A dominant diagenetic theme discernible throughout the sequence has been the dissolution of aragonite: all aragonitic fossils are present only as molds and, in some places, voids have collapsed, giving rise to breccias with a matrix of sparry calcite. Nowhere is this more apparent than in Unit III, which shows particularly high moldic porosity, where pores are solution-enhanced and cementation is absent. This suggests an active fresh-water diagenetic environment with high percolation rates that constantly evacuated the dissolved materials. Periodic emergence of the platform top allowed for regular recharge of the aquifers. Early diagenesis may have led to the formation of well-cemented levels (e.g., diagenetic caps on small-scale depositional sequences), which contrast with less indurated sediment. This may explain the poor recovery in Unit III, where possibly only

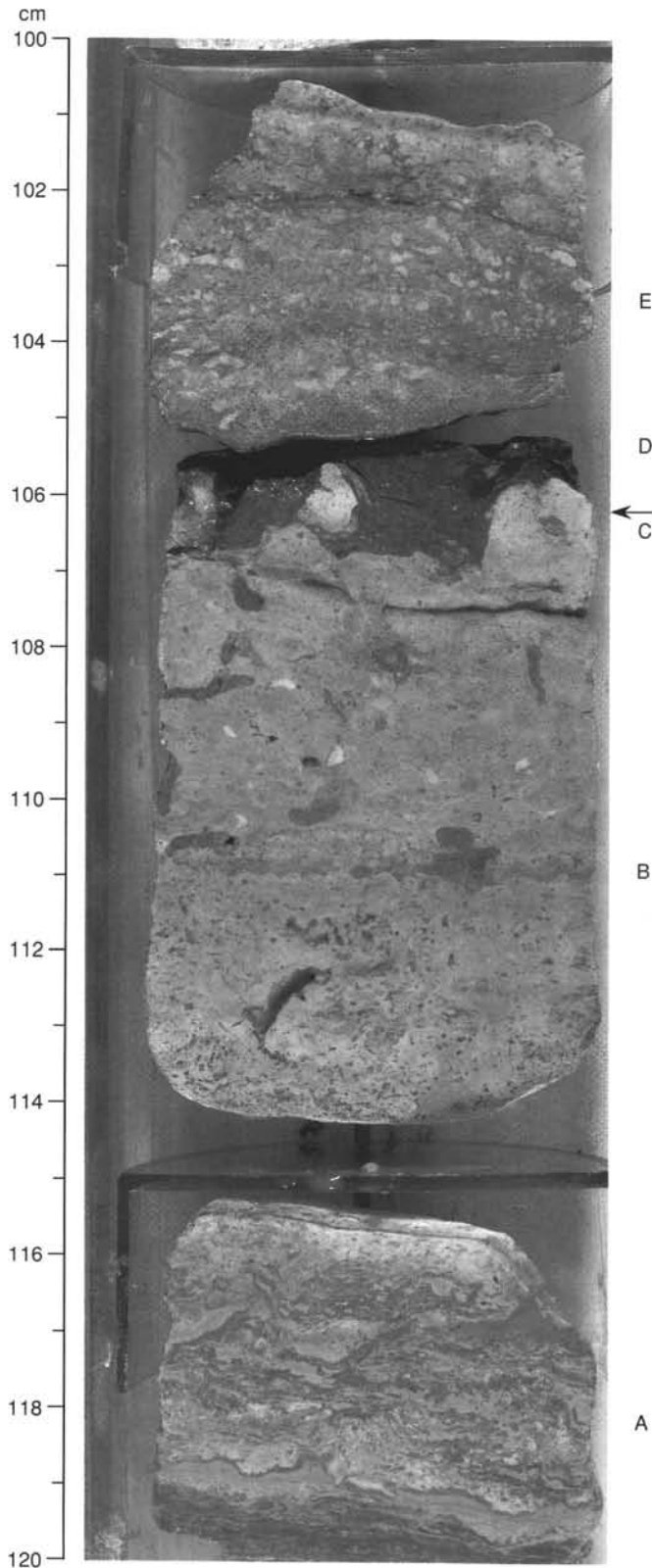


Figure 27. Small-scale peritidal sequence in Subunit VIIA, where calcified algal mats with tepee structures (A) pass gradually into bioturbated subtidal facies (B). Karstification and erosion (C) occur directly on the subtidal sediment, implying a rapid decrease in relative sea level. Some clasts were reworked in a layer of organic/clay-rich mudstone during early transgression (D). The top of the photograph again shows subtidal bioturbated sediment (E) (Interval 143-866A-130R-1, 100–120 cm; age, Barremian).

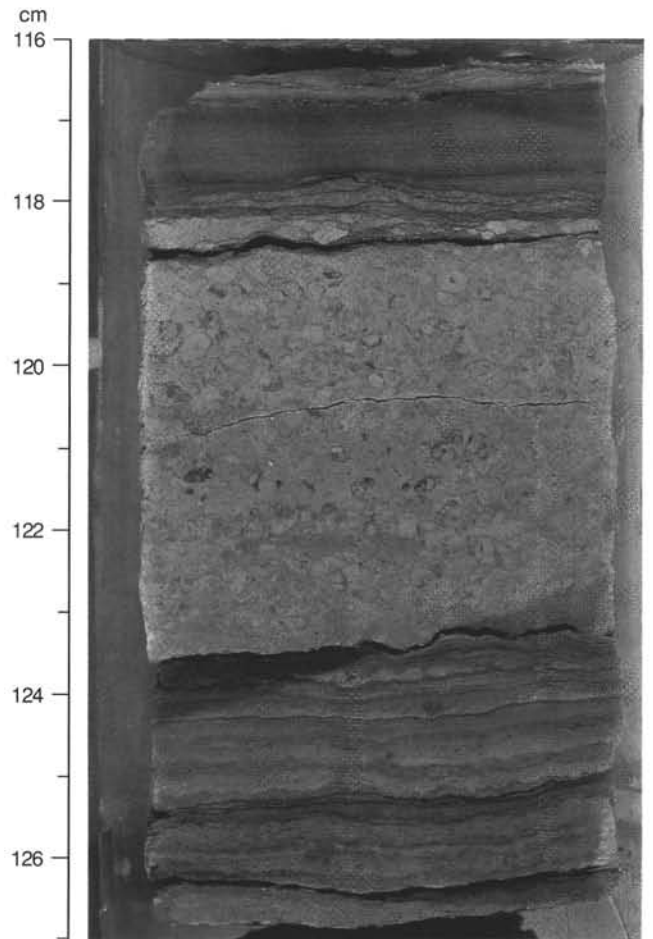


Figure 28. Small sequence in Subunit VIC. Gastropod-rich subtidal wackestone overlies calcified supratidal algal mats and passes rapidly into organic/clay rich layers above, without showing intertidal or supratidal exposure (Interval 143-866A-111R-1, 116–127 cm; age, Aptian).

the top parts of depositional and/or diagenetic sequences were lithified enough to survive the coring process. Cementation is variable throughout the rest of the sequence and most visible in the grainstones, which, however, generally retain substantial pore space. Fringe cements are visible in many of the oolitic deposits, and the overpacking and interpenetration of ooids suggest that much of this cement may have derived from pressure solution and reprecipitation.

The most obvious diagenetic feature observed in the cores is the presence of dolomite. This mineral first appears as discrete replacement crystals in Unit VI and continues to increase downhole. Lower down, especially in Unit VII, several stratigraphic intervals exhibit pervasive dolomitization. Thin-section examination indicates that the process of dolomitization commenced after initial compaction of the sedimentary pile because suturing of grains occurred prior to their being replaced by dolomite. However, dolomitization began soon after this because many of the fabric features (such as keystone vugs and fenestrae) have been preserved in the coarsely crystalline rock. The degree of overpacking of ooids is also greater in those samples that lack substantial interstitial dolomite.

Dolomitization proceeded in a manner whereby the ooids and oncoids in some places escaped dolomitization or exhibit only incipient dolomite crystallization in the center of the particles (Fig. 22). In other places, the calcite grains remaining in the dolomitized groundmass have undergone further dissolution, with some of their moldic porosity being filled during a secondary phase of dolomite precipita-

tion (Fig. 29). The susceptibility of grainstone to be selectively replaced in preference to the wackestone is suggestive of a permeability control on dolomitization. Furthermore, the process of incipient dolomitization in Subunit VIC may have been confined to discrete intervals by impermeable clay layers at the base of small-scale depositional cycles.

Pervasive dolomitization does not extend as far as the contact with the basalt. The possibility exists that the basalt has played no role in the dolomitization process other than to act as an impermeable barrier to the circulating fluids.

BIOSTRATIGRAPHY

The sedimentary sequence cored in Hole 866A consists of a thin (0.9 m) veneer of Pliocene foraminiferal nannofossil ooze overlying 1619.1 m of middle Cretaceous shallow-water platform and lagoonal sediments that rest on altered basalt. Unrecovered at the Cretaceous/Paleocene contact is a younger Cretaceous pelagic limestone cap analogous to that found at Allison Guyot (Holes 865A and 865B). The shallow-water carbonate sequence ranges from Barremian to Albian in age. Dating of the sequence is based on smaller benthic foraminifers. Orbitolinids are limited to a narrow stratigraphic interval, as are identifiable large rudist fragments; however, rudist debris can be found throughout the Cretaceous sequence. Calcareous nannofossils and planktonic foraminifers are absent, and palynomorphs are rare.

Calcareous Nannofossils

Hole 866A

An upper Pliocene nannofossil assemblage was observed in the interval from Samples 143-866A-1R-1, 20 cm, to -1R-CC. This includes *Discoaster asymmetricus*, *Discoaster brouweri*, *Discoaster pentaradiatus*, *Discoaster surculus*, *Discoaster tamalis*, and *Pseudemiliana lacunosa*. *Discoaster triradiatus* was found in the top of the core. *Reticulofenestra pseudoumbilica* was not observed in this interval, indicating a correlation to Zone NN16 of Martini (1971). More than 200 smear slides of shallow-water carbonates from Hole 866A were prepared, but none contain nannofossils.

Hole 866B

Calcareous nannofossil biostratigraphy of the pelagic cap sequence in Hole 866B indicates that the Cenozoic section recovered is from the Quaternary, upper Pliocene, middle Eocene, and lower Paleocene. These intervals are likely separated by unconformities. One sample was observed in each section. The interval from Sample 143-866B-1M-1, 0 cm, to -1M-1, 117 cm, belongs to Quaternary Zone NN21 of Martini (1971), based on the common occurrence of *Emiliana huxleyi*. Reworking of upper Pliocene nannofossils is pervasive in these samples. Sample 143-866B-1M-2, 80 cm, belongs to Pleistocene Zone NN19, based on the domination of *Pseudemiliana lacunosa*, the rarity of *Gephyrocapsa* sp. and *E. huxleyi*, and the absence of discoasters. The interval from Sample 143-866B-1M-3, 80 cm, to -2M-1, 15 cm, is correlated to upper Pliocene Zone NN16 by the occurrence of *D. surculus*, *D. pentaradiatus*, *D. tamalis*, *Discoaster variabilis*, *D. brouweri*, and *P. lacunosa* and the absence of *Reticulofenestra pseudoumbilica*. While preservation is moderate to good in this uppermost part of the section, it deteriorates drastically in the interval from Sample 143-866B-2M-2, 20 cm, to -3M-5, 120 cm. This interval is characterized by a very sparse nannofossil assemblage of late Paleocene (Sample 143-866B-2M-2, 20 cm) and early-middle Eocene (Sample 143-866B-2M-3, 20 cm, through -3M-5, 120 cm) age. The late Paleocene-age assemblage consists of *Fasciculolithus tympaniformis*, *Discoaster mohleri*, *Discoaster multiradiatus*, *Toweius pertusus*, and *Toweius eminens*. This assemblage is indicative of Zone NP9 of Martini (1971). The early-middle Eocene-age assemblage, which varies from sample to sample, consists of a mixture

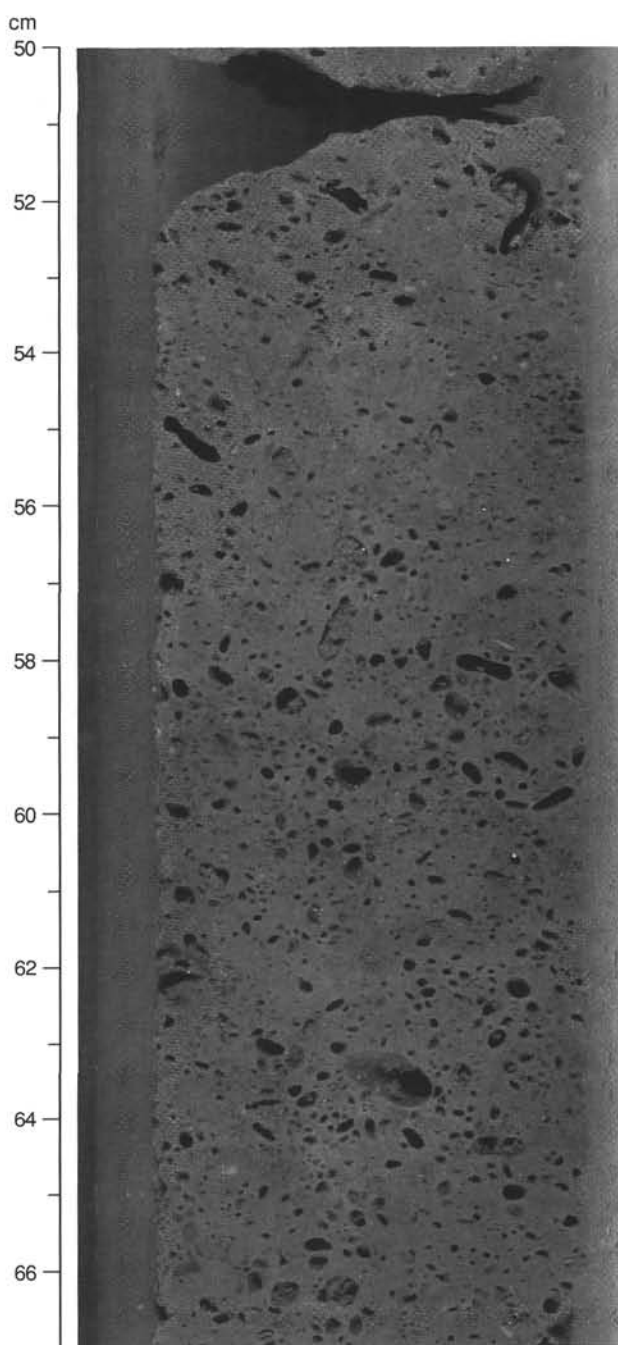


Figure 29. Brown, completely dolomitized oolitic-ooloidal grainstone in Subunit VIIIA. Complete dissolution of the calcitic ooids has taken place with subsequent precipitation of dolomite in some of the molds (Interval 143-866A-162R-1, 50–67 cm; age, Barremian).

of the following species: *Ericsonia formosa*, *Reticulofenestra dictyoda*, *Sphenolithus conspicuus*, *Sphenolithus editus*, *Sphenolithus radians*, *Sphenolithus moriformis*, *Toweius callosus*, *Toweius occultatus*, *Campylosphaera dela*, *Chiasmolithus grandis*, *Chiasmolithus consuetus*, *Cruciplacolithus cribellum*, *Discoaster barbadiensis*, *Discoaster lodoensis*, and *Lophodolites acutum*. This assemblage lacks zonal markers, but is generally indicative of Zones NP11 to NP14. The sparsity of this flora, the inversion of zones, and the fact that the rich planktonic foraminifers in this interval yield younger middle Eocene ages indicate that the nannofossil assemblages have

been reworked, with the original assemblage having been removed by apparently strong current activity that size-sorted these sediments during an earlier depositional episode. Samples 143-866B-3M-6, 60 cm, and -3M-CC yield a largely in-situ middle Eocene assemblage that is characterized by *R. umbilica*, *Reticulofenestra dictyoda*, *Sphenolithus furcatolithoides*, *C. grandis*, *Dictyococites scrippsae*, and rare *Discoaster bisectus*. This assemblage indicates a correlation with Zone NP16. Reworked specimens of *Chiasmolithus gigas*, *D. multi-radiatus*, and various species of *Toweius* have been observed in both samples.

Calcareous nannofossil biostratigraphy has been used to date the oldest pelagic sediment recovered above the shallow-water carbonate section and a karstic cavity within the shallow-water limestone. Sample 143-866B-4M-1, 17–19 cm, which consists of calcareous ooze, yielded a lower Paleocene nannofossil assemblage consisting of *Toweius pertusus*, *Cruciplacolithus tenuis*, *Cruciplacolithus primus*, *Ericsonia cava*, *Ericsonia subpertusa*, *Ellipsolithus* sp., and *Sphenolithus primus*. This assemblage, combined with the absence of *Fasciculithus tympaniformis* and *Heliolithus kleinpellii*, indicates a correlation with lower Paleocene Zone NP4. Resting in this disturbed ooze, a piece of chalk at Interval 143-866B-4M-1, 14–16 cm, yielded a mixed Cretaceous–lower Paleocene assemblage. The diverse Cretaceous assemblage includes *Parhabdololithus regularis*, *Cretarhabdus surirellus*, *Broinsonia enormis*, *Microrhabdulus decoratus*, *Micula decussata*, and *Eiffelithus turrisseiffelii*. The presence of *P. regularis*, and the obvious absence of *Eiffelithus eximius*, points to a Maastrichtian age for this assemblage, with a likely correlation to Zones CC24 to CC26 of Sissingh (1977) or NC21 to NC23 of Roth (1978). This sample also contains lower Paleocene species, including *T. pertusus*, *Cruciplacolithus tenuis*, *E. cava*, and *Ericsonia subpertusa*, which probably also belong to Zone NP4. A similar age is suggested for the infilling in a karstic cavity in Sample 143-866B-4M-1, 33–36 cm, which includes the above taxa, *Placozygus sigmoides*, and *Prinsius bisulcus*. The age of this filling and the oldest pelagic drape recovered indicate that the final burial episode of the shallow-water limestone in this location began in the early Paleocene.

Planktonic Foraminifers

Hole 866A

Cenozoic planktonic foraminifers from Hole 866A are limited to Sample 143-866A-1R-CC. The assemblage includes *Globorotalia miocenica*, *Globorotalia multicamerata*, *Dentoglobigerina altispira*, *Dentoglobigerina globosa*, *Globigerinoides extremus*, and *Sphaeroidinellopsis seminulina* and has been assigned a late Pliocene age (Zones N19–N20).

Hole 866B

Cores 143-866B-1M through -4M contain Cenozoic planktonic foraminifers that range in age from Pliocene to Paleocene. The foraminifers are common to abundant but moderately well to poorly preserved. Sample 143-866B-1M-CC contains a late Pliocene-age assemblage, apparently identical to that of Sample 143-866A-1R-CC, and has been assigned to Zones N19–N20. Species present include *Globorotalia miocenica*, *Globorotalia multicamerata*, *Globigerinoides fistulosus*, *Globigerinoides extremus*, and *Sphaeroidinellopsis seminulina*, among others. Rare, reworked Eocene species are present. Sample 143-866B-2M-CC is middle Eocene (Zone P12) in age based on the presence of *Morozovella lehneri*, *Morozovella spinulosa*, *Acarinina topilensis*, *Turborotalia pomeroli*, and *Subbotina* sp. cf. *S. frontosa*. Reworked late Paleocene and early Eocene-age species are common in the assemblage.

Sample 143-866B-3M-CC is slightly older and was placed in the middle Eocene (Zone P11). Species present include *M. lehneri*, *Morozovella aragonensis*, *Acarinina topilensis*, *Subbotina higginsii*,

Globigerinatheka mexicana, *Globigerinatheka subconglobata*, and *Pseudohastigerina micra*. Reworked late Paleocene-age species are still present. The lower Paleocene (Zone P2) was noted in Sample 143-866B-4M-1, 14–16 cm, by the presence of *Morozovella praecursoria*, *Morozovella trinidadensis*, *Morozovella uncinata*, *Parasubbotina pseudobulloides*, and *Planorotalites compressus*. No reworked material was present in the sample.

Benthic Foraminifers

Hole 866A

Age

Cretaceous ages are based on thin-section examination of benthic foraminifers from indurated shallow-water carbonates. Samples routinely contain rare-to-common, mostly poorly preserved, smaller benthic foraminifers. Miliolids and textulariids are pervasive through the sequence with lesser amounts of cuneolinids and other benthic groups. Samples 143-866A-3R-CC, 0–1 cm, through -29R-CC, 15–16 cm, contain elements of an assemblage that includes *Cuneolina* sp. cf. *C. pavonia*, *Nezzazata* sp. cf. *N. simplex*, and *Saubaudia* sp. cf. *S. minuta*, together with several valvulinids and arenobuliminids. This assemblage was assigned an Albian age and apparently is analogous to the shallow-water Cretaceous assemblage at Site 865 on Allison Guyot.

A different assemblage appears in Sample 143-866A-30R-CC, 0–1 cm, that includes thick-walled cuneolinids that tentatively have been assigned to *Vercorsella laurentii* and *Vercorsella scarsellai*, together with other constituents, such as rare specimens of *Praechrysalidina infracretacea*, *Bolivinopsis* sp. cf. *B. ammovitrea*, *Belorusiella* sp. cf. *B. textilaroides*, and *Debarina hahounerensis*. Larger foraminifers also occur in this assemblage (Samples 143-866A-35R-1, 129–130 cm, -47R-1, 94–96 cm, and -57R-1, 80–82 cm), but are limited to poor sections of rare specimens that do not display the embryonic apparatus and, thus, remain undated. Missing are specimens of *Nezzazata* and *Saubaudia*. This assemblage is indicative of the Aptian.

The lower boundary of the Aptian assemblage is difficult to recognize owing to (1) the poor recovery and poor preservation of foraminifers in a dolomitized interval (Cores 143-866A-127R to -138R), (2) the rarity of specimens other than the ubiquitous miliolids and textulariids, and (3) the gradual appearance of new forms. Consequently, the Aptian/Barremian boundary has been placed tentatively at 1200 mbsf, based on the appearance of forms resembling *Belorusiella textilaroides*, *Bolivinopsis* sp. cf. *B. capitata*, and *Bolivinopsis* sp. cf. *B. labeosa* between Samples 143-866A-124R-1, 99–101 cm, and -132R-1, 28–30 cm. Accompanying this change is an increase in trochospiral forms related to both *Valvulinaria* and *Conorboides*, and at deeper levels, the assemblage includes forms similar to *Nautiloculina bronnimanni* in Samples 143-866A-148R-4, 119–120 cm, and -150R-2, 103–106 cm. The Barremian assemblage continues down-hole to the contact with the underlying altered basalt at 1620.0 mbsf. (Note added in proof: Recent work identifying orbitolinid foraminifers suggests sediments as deep as Core 143-866A-47R may be Albian in age. [A. Vanneau, pers. comm., 1992]).

Paleoenvironment

Variations in the Cretaceous shallow-water depositional environment between open-marine and restricted-lagoonal conditions are shown by the relative abundance of the dominant benthic foraminiferal groups and other biogenic constituents (Fig. 30). The background fauna of miliolids and textulariids, found in nearly every sample taken for foraminiferal analysis from the various marine lithofacies, documents the shallow nature of the environment throughout the Barremian-to-Albian sequence. The overall uniformity in the miliolid and

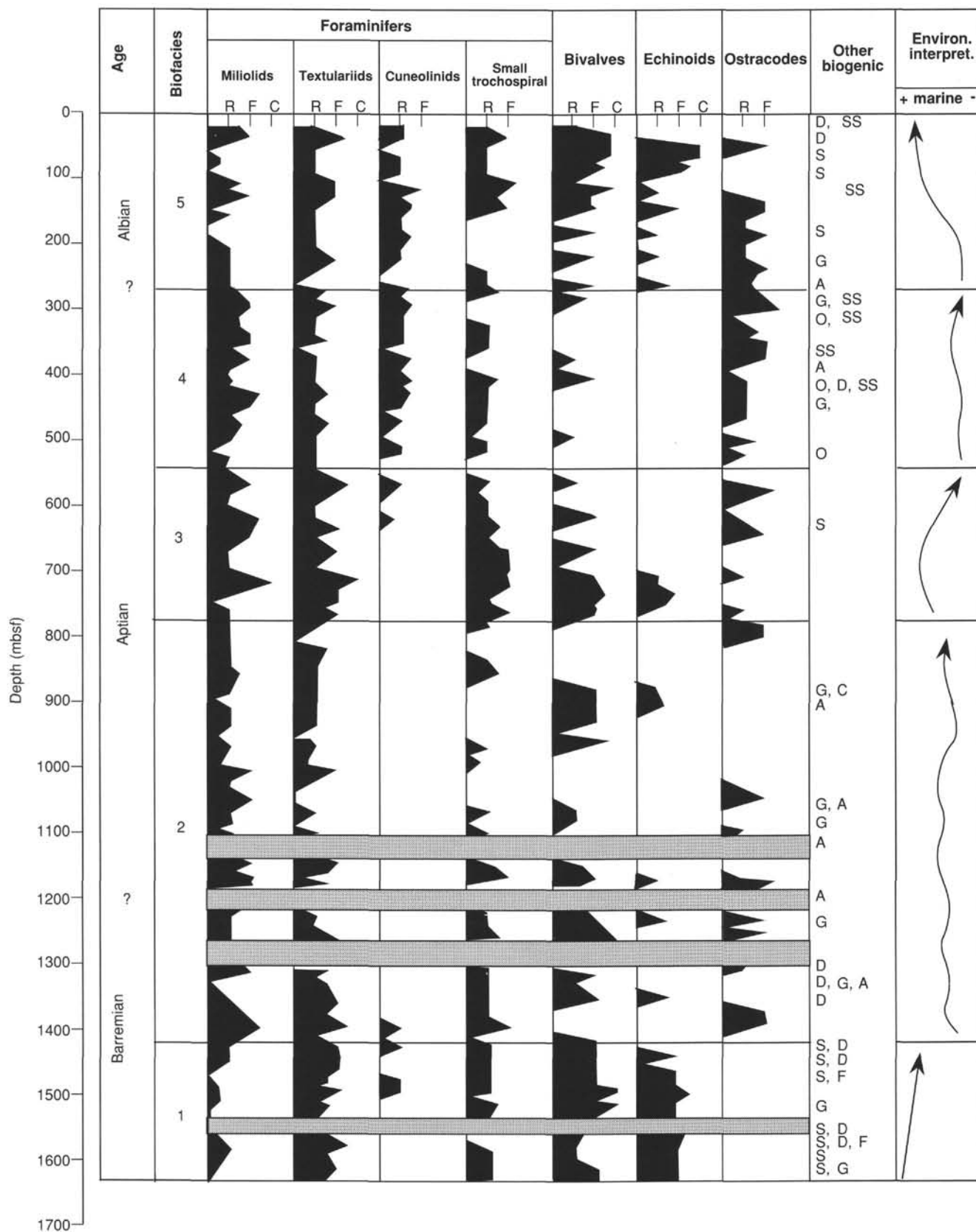


Figure 30. Relative abundances of dominant benthic foraminiferal groups and other biogenic constituents in Hole 866A. Major biofacies changes are shown by horizontal lines. Shaded intervals indicate poor preservation caused by dolomitization. Other biogenic: A = green or blue-green algae, D = dasycladacean algae, S = solenoporacean algae, G = gastropods, O = orbitolinids, F = other calcareous benthic foraminifers, SS = sponge spicules. Arrows show trends toward open marine (+) or restricted marine (-).

textulariid curves no doubt reflects in part a sampling bias toward finer-grained sediments, as well as hydraulic mixing in the intertidal to shallow platform facies. Nevertheless, differences in amplitude of the miliolid and textulariid abundance curves are evident and, when combined with the greater amplitude variations in the curves of the other biogenic constituents, provide the basis for identifying both major and minor changes in the environment.

Major changes in biofacies are shown in Figure 30 by the four horizontal lines. The first boundary occurs between Cores 143-866A-148R (bottom at 1405.4 mbsf) and -150R (top at 1415.1 mbsf). Below this level, Biofacies 1 contains numerous textulariids and small trochospiral forms with rare cuneolinids and miliolids. Bivalve and echinoid fragments are common, and fragments of solenoporacean algae occur throughout, together with rare fragments of dasycladacean algae, gastropods, bryozoans, and calcareous benthic foraminifers. Biofacies 1 corresponds to the largely oolitic and peloidal grainstones of lithologic Unit VIII, which rests on basalt.

Biofacies 2 consists of an interval of low, but variable, biogenic recovery that extends upward to 772.5 mbsf between Cores 143-866A-82R and -83R. Samples containing more abundant miliolids, textulariids, ostracod fragments, and skeletal blue-green algae tend to alternate with samples that have more abundant trochospiral forms and fragments of bivalves and echinoids. Gastropod fragments occur in this interval, as do dasycladacean algae, especially between 1300 and 1400 mbsf, and very rare solenoporacean algae. Biofacies 2 corresponds to lithologic Units VI and VII and is characterized by interstratified packstone-wackestone and mudstone/algal laminites that are dolomitized in Unit VII. The pulse of bivalve and echinoid fragments near 900 mbsf, which includes rudists, gastropods, and sponge spicules, corresponds to lithologic Subunit VIB.

Biofacies 3 begins with a noticeable increase in bivalve and echinoid fragments and small trochospiral foraminifers that decline in abundance upward. Miliolids, textulariids, and ostracod fragments show major pulses in abundance in this biofacies, and the decline in these pulses near 540.7 mbsf plus the increased abundance of cuneolinids was used to define the upper boundary. Skeletal blue-green algae occur in the lower half of the biofacies, rudist fragments are found near the base, and solenoporacean algae are very rare. Biofacies 3 corresponds to most of lithologic Unit V that consists of massive oolitic grainstone and the lower half of Unit IV that includes laminated wackestone, packstone, and mudstone.

Biofacies 4 contains relatively abundant miliolids, rare but consistently present textulariids and cuneolinids, a noticeable increase in ostracod fragments, a reduction in bivalve fragments, and a lack of echinoid fragments. Rare orbitolinids are restricted to this biofacies and were found together with sponge spicules in two of the three occurrences. Gastropod fragments are rare, as are dasycladacean and skeletal blue-green algae. Biofacies 4 corresponds to the less clay-rich upper half of lithologic Unit IV and the mudstone-wackestone dominant lithologic Subunit IIIC.

Biofacies 5 begins at the decrease in miliolids and ostracod fragments, and the increase in bivalve fragments and reappearance of ostracod fragments between Cores 143-866A-29R and -30R at 271.0 mbsf and extends to the top of the recovered Cretaceous sequence. The biofacies contains greater fluctuations in miliolid abundance than in the underlying biofacies, and bivalve and echinoid fragments become more abundant upward, accompanied by a decrease in ostracod fragments. Sponge spicules become more abundant, in many places forming dense patches; gastropod fragments are rare, and solenoporacean algae reappear. This biofacies corresponds to lithologic Subunits IIIA and IIIB that consist primarily of wackestone.

The following depositional history for the Cretaceous sequence has been interpreted from the recovered biogenic material. This record was biased toward the most indurated sediment by the coring process, and less indurated facies likely were not recovered. Biofacies 1 represents a relatively uniform shallow-marine environment shore-

ward of a reef shoal or bank edge with hard substrates that was open to normal marine waters. The environment changed abruptly in Biofacies 2 with the advent of alternating marine subtidal and restricted lagoonal conditions that were interrupted rarely by more marine inundations. The presence of desiccation cracks in the lower and upper parts of the biofacies indicates periods of emergence, and algal laminites throughout the unit attest to the restricted nature of the environment. The rudist-bearing beds near the top of the biofacies represent the most prominent open marine cycle within the biofacies. The abrupt change between Biofacies 1 and 2 may indicate the presence of a hiatus at this horizon within the Barremian section.

Biofacies 3 records the rapid onset of more open-marine conditions, followed by the gradual restriction of the environment and the appearance of organic-rich mudstone. Restricted marine conditions continued in Biofacies 4 and intensified at the top, corresponding to the occurrence of desiccation cracks and calcretes in the lithologic sequence. The limited occurrence of orbitolinids and sponge spicules within this biofacies, however, identifies the onset of short, normal marine pulses. Normal marine pulses continued and intensified in Biofacies 5, but the environment never reached the open marine conditions evident in Biofacies 1. The presence of incipient calcretization and desiccation cracks in the lithologic sequence provides continued, though diminishing, evidence of subaerial emergence.

Finally, when comparing the miliolid-rich lagoonal sediments of Site 866 with those of Site 865, note that the subsurface anoxic conditions at Site 865 (recognized by the pyritic infillings and coatings of the foraminifers) were not observed at Site 866. Apparently, the sediments at Site 866 remained oxygenated despite the presence of algal laminites and organic-rich intervals, perhaps related to the reduced amount of clay and, thus, better subbottom circulation, or from the absence of iron-rich surface exposures.

Hole 866B

Cores 143-866B-4M to -13M are Albian in age, based on the thin-section examination of the recovered limestone. The samples from this interval contain a common assemblage of mostly rare *Cuneolina* sp. cf. *C. pavonia*, *Nezzazata* sp. cf. *N. simplex*, and *Sabaudia* sp. cf. *S. minuta*, together with more common miliolids, textulariids, and small trochospiral forms. The assemblage appears identical to that from the Albian-aged limestone at both Hole 866A and Site 865. The foraminiferal assemblage and associated bivalve and echinoid fragments, dasycladacean algae, ostracodes, gastropods, and sponge spicules identify a shallow-water, restricted marine environment of deposition.

Palynology

The following samples from Hole 866A were processed for palynology: 143-866A-50R-CC, 78–79 cm; -57R-1, 38–40 cm; -58R-1, 90–91 cm; -71R-1, 102–104 cm; -71R-2, 46–50 cm; -72R-1, 61–62 cm; -89R-1, 95–96 cm; -110R-2, 92–93 cm; -111R-1, 85–86 cm; -114R-1, 30–32 cm; -116R-1, 33–35 cm; -128R-1, 58–60 cm; -147R-1, 45–46 cm; and -148R-4, 0–3 cm. Sample 143-866A-50R-CC, 78–79 cm, was taken from an interval containing a piece of coaly black organic material, perhaps woody tissue. The processed sample likewise contains only unrecognizable black fragments of organic material. Most other samples were taken from either algal laminated horizons or from dark clayey horizons. Samples 143-866A-57R-1, 38–40 cm, through -71R-2, 46–50 cm, contain predominantly amorphous organic matter, with sparse fragments of organic linings of foraminifers (microforaminifers), and rare, nondescript spores. The abundant amorphous material contains sparse circular structures, which may be some type of remnant cell outline from the algae that formed the laminated mats. Also, the amorphous matter commonly has a flat, tissue-like appearance. Samples 143-866A-72R-1, 61–62 cm, and -110R-2, 92–

93 cm, through -148R-4, 0–3 cm, also contain predominantly amorphous organic matter, but have increasing amounts of clay and fine-grained opaque minerals (pyrite?) toward the bottom of the hole. The amorphous organic matter has a more clotted appearance than described above. The interpretation of all this material as predominantly of restricted marine, algal mat origin agrees well with its geochemical characterization of Type II or mixed Type II–III organic matter (see “Organic Geochemistry” section, this chapter).

In contrast to Hole 865A at Allison Guyot, most samples analyzed from Hole 866A contain almost no recognizable terrestrial plant fragments. The one exception to this was found in Sample 143-866A-89R-1, 95–96 cm, which is a dark claystone that contains common plant debris, spores, and perhaps some rare pollen. The overall facies is indicative of predominantly terrestrial organic matter. This agrees with the geochemical analysis of a sample that was taken adjacent to this one, which contained 14% organic matter and which was characterized as Type III organic matter (see “Organic Geochemistry” section, this chapter).

Rudists

Rudists were encountered in Cores 143-866A-92R to -97R, -103R, and -142R at 859.2–917.0, 962.4–971.7, and 1338.2–1347.9 mbsf, respectively. Only the rudist specimens from Cores 143-866A-92R to -97R were preserved sufficiently well to allow identification. Rudists in Cores 143-866A-96R and -97R may be caprinids, in which case they are likely to be the same form as in Cores 143-866A-92R to -95R (as they have the same external dimensions), but the possibility cannot be excluded that they are a different caprinid, or even a caprotonid.

Most specimens of the form have a valve diameter of 1 to 2 cm, but fragments of larger forms up to 7 cm in diameter were also seen. Both right and left valves are about 2 to 3 cm in length. A very thin, originally calcitic layer can be seen in places covering what was the aragonitic layer. A small ligamentary invagination exists and probably one accessory cavity (although it is uncertain on which side, as it has not been possible to distinguish between the valves). A single row of rectangular pallial canals envelops the valves.

The single row of rectangular pallial canals (i.e., without bifurcation of the intervening walls) indicates a relatively primitive form. *Praeacprina* has no bifurcations at all, and *Planocaprina* supposedly has rare incipient bifurcations on the ventral side (but these could well be a preservational artifact—see “Biostratigraphy” section, “Sites 867/868” chapter, this volume). More importantly, in *Planocaprina* the canals are teardrop-shaped, whereas in *Praeacprina* they are more rectangular. The most significant characteristic for distinguishing these two genera is that *Praeacprina* has canals only in the FV, and they are not present on the ventral side. In *Planocaprina*, canals are found around the entire margin of both valves.

In preliminary investigations, it was not possible to distinguish between the valves, although because canals were present in every fragment examined, it seems most likely that they are present in both valves. This and the presence of canals around the entire margin suggest affinities with *Planocaprina*. However, the shape of those canals is more reminiscent of *Praeacprina*. A more complete identification awaits further study.

Praeacprina was first described from and is best known in the French Urgonian (Paquier, 1903) in beds assigned to the lower Aptian (Maillard, 1965). From the Tethyan Province it is now known from France, Spain, Sicily, and Oman in the lower Aptian and possibly uppermost Barremian (J.P. Masse, pers. comm., 1992.). One record of the species is from the Caribbean Province, in the Upper Sligo Formation of Texas in the upper lower Aptian (Skelton 1982). *Planocaprina* was described by Palmer (1928, figs. 7-8, p. 66–67) from Jalisco, Mexico, and co-occurred with the more advanced caprinids *Coalcomana* plus *Caprinuloidea* in beds now thought to be from the upper Albian.

PALEOMAGNETISM

Sediments

Rotary-cored sections of pelagic ooze from Site 866 (Hole 866A and 866B) were too disturbed for meaningful shipboard magnetic measurement. We restricted our study to the well-lithified limestones and dolomites recovered from Hole 866A. A total of 58 samples from Cores 143-866A-122R through -165R were measured; six of these were 12-cm³ discrete samples from working halves of these cores. The remaining samples were large (50–70 cm³) pieces from the archive halves of these cores that were measured as discrete samples in an effort to increase the accuracy of the measurements by increasing sample volumes. Intensities are very weak, on the order of a few milliamperes per meter or less, close to the noise level of the shipboard cryogenic magnetometer.

Magnetic characteristics may depend on lithology, and specific statements regarding this relationship must await more detailed measurements. In general, the dolomitized rocks seem to carry the more stable magnetization (Fig. 31). Shipboard demagnetization of such samples, however, defined directions that did not trend toward the origin of the orthogonal vector plots and, therefore, did not characterize fully the vector component content of the samples. The oolitic grainstones, which are not dolomitized, are very weakly magnetized and exhibit a large, low-coercivity overprint (Fig. 32). After removal of this low-coercivity overprint, the remaining vector did not trend toward the origin with further AF demagnetization. Clearly, detailed shore-based measurements will be needed to evaluate the potential of these sediments as recorders of primary (or early diagenetic) magnetizations.

Basalts

Pass-through measurements were performed on suitably complete sections of the basalt archive halves of Cores 143-866A-171R through 143-866A-189R. Measurements of the natural remanent magnetization (NRM) and magnetization after demagnetization at 15 mT were performed with a 5-cm spacing. Most NRM values have positive inclinations. As at Site 865, discrete samples were drilled from core pieces to determine whether the basalt NRM values have

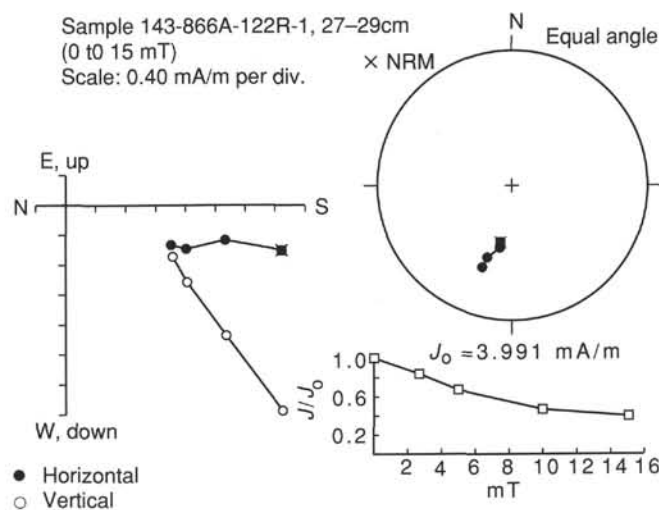


Figure 31. Sample 143-866A-122R-1, 27–29 cm, shows magnetic behavior of partially dolomitized rocks. Equal angle/stereonet plot (upper right) of magnetization vector end points at 0 (NRM), 5, 10, and 15 mT AF demagnetization steps. Plot (lower right) showing normalized intensity remaining at various AF demagnetization steps. Orthogonal vector plot (left) of magnetization during AF demagnetization.

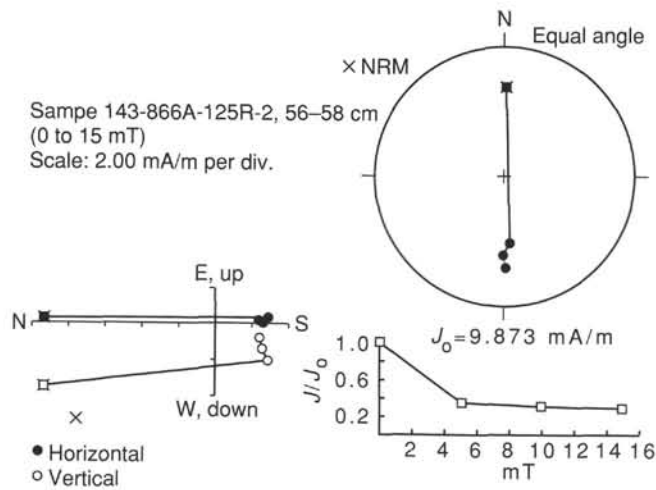


Figure 32. Sample 143-866A-125R-2, 56–58 cm, shows typical magnetic behavior of nondolomitized oolitic grainstones. These samples are very weakly magnetized and exhibit a large, low-coercivity overprint. Plot conventions as in Figure 31.

been dominated by a primary magnetization; however, only a few discrete samples were measured on board the ship for reasons outlined below. Stepwise AF demagnetization of these discrete samples revealed both differences among samples and differences from the magnetic behavior exhibited by the Site 865 basalts. Two samples (Samples 143-866A-171R-3, 107–109 cm; 143-866A-171R-3, 134–136 cm) revealed a stable, positive inclination magnetization after removal of a small component of possible viscous origin (Fig. 33). Complete demagnetization of this component, however, was not achieved in AF fields as high as 80 mT. Possible sources of this high-coercivity component, which was not observed in the Site 865 basalts, include hematite and extremely fine-grained magnetite. Hematite might have been a product of weathering, while fine-grained magnetite may have grown from associated hydrothermal fluids; evidence for both processes is present in the rocks (see “Igneous Petrology” section, this chapter). A conclusive identification of the mineral or minerals responsible for this high-coercivity magnetization must await further shore-based study. In contrast to this demagnetization behavior, another sample showed the removal of a substantial component of magnetization with the application of low (2.5–5 mT) AF fields (Sample 143-866A-171R-3, 34–36 cm) (Fig. 34). After the application of higher AF demagnetization levels (50–80 mT), declinations moved in a systematic manner, possibly defining a great circle path. The final direction has been incompletely defined, even after demagnetization at 80 mT. Based on the incomplete demagnetization achieved by AF field demagnetization, the differential response of samples to this demagnetization and the limited recovery of vertically oriented material, the measurement of further discrete samples was deferred for shore-based studies. Nevertheless, the available data from the discrete samples indicate that the characteristic magnetization has a positive inclination. The simplest interpretation of this inclination is that it records a reversed-polarity geomagnetic field, while Resolution Guyot was in the Southern Hemisphere.

To obtain a preliminary estimate of inclination from Hole 866A basalts, shipboard data from the pass-through measurements were checked visually for segments that contained consistent values of inclination, declination, and intensity. These regions were compared to the shipboard visual core descriptions to ensure that they matched portions of the cores where long, continuous core pieces were observed (Table 3). While making this comparison, it was noted that some continuous core segments had irregular magnetizations. Such intervals also showed substantial changes between the NRM values

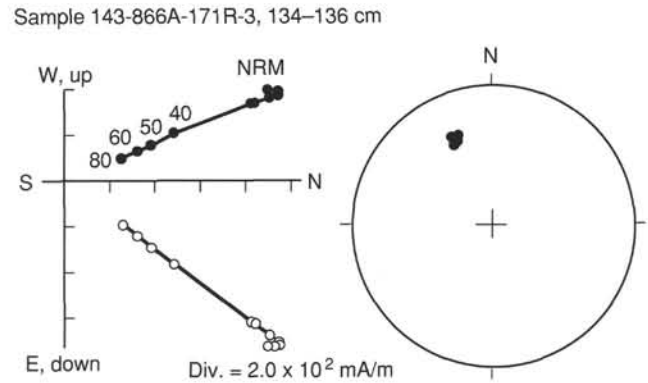


Figure 33. Orthogonal vector plot (left) of progressive AF demagnetization of basalt Sample 143-866A-171R-3, 134–136 cm. Open circles = inclination; closed small circles = declination (unoriented); vector end points after demagnetization are labeled in mT. Demagnetization steps shown (mT): 0, 5, 10, 40, 50, 60, 80. Stereonet plot (right) of vector end points after progressive AF demagnetization.

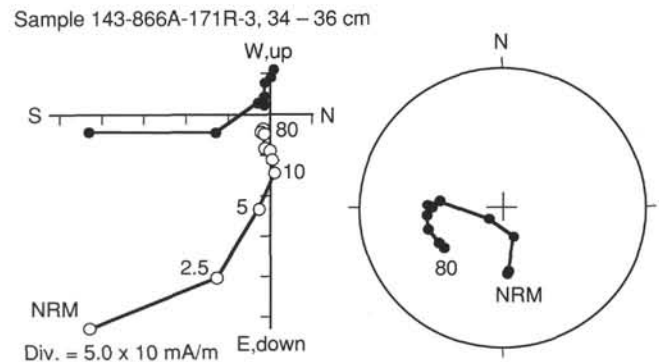


Figure 34. Orthogonal vector plot (left) of progressive AF demagnetization of basalt Sample 143-866A-171R-3, 34–36 cm. Plot conventions as in Figure 33.

and values after demagnetization at 15 mT. These latter segments may reflect the presence of a substantial, but differential, overprint that was also detected in the discrete sample data. Inclinations from the intervals having consistent magnetizations after 15 mT were averaged to obtain a series of inclination estimates for the basalt sequence. Additional inclination information also was available from limited discrete measurements: as at Site 865, we used the vector end point after demagnetization at 15 mT only for the two discrete samples that displayed a simple demagnetization behavior (Sample 143-866A-171R-3, 107–109 cm: $I = 32.9^\circ$; Sample 143-866A-171R-3, 134–136 cm: $I = 34.4^\circ$); the sample showing a more complex behavior was not used for estimating inclination.

Combining data from the archive halves with those discrete samples, only three inclination groups can be distinguished (Table 4). Only six of the 12 petrologic units are represented in these data. While shore-based study may reveal the presence of additional inclination groups, the depth range and well-grouped inclination values represented in inclination Group 3 suggest that the base of the basalt sequence represents a short time interval. The upper portion of the sequence may be more promising as a recorder of additional magnetic units.

Overall, the data define a nominal paleolatitude range of 12° to 29° S. Previously, Tarduno (1990) reported two inclination groups from siliceous limestones of DSDP Site 463, which is on the carbonate apron derived from Resolution Guyot. The sediment inclinations from Site 463 are unusual in the sense that they are not significantly shallower than inclinations predicted from apparent polar wander

Table 3. Inclination averages for core pieces displaying relatively constant inclination, declination, and intensity after AF demagnetization at 15 mT.

Core no.	Piece number	Petrologic unit	I°	σ
143-179R-2	1a-1c	5	28.5	2.5
143-180R-1	3a-3b	6	48.5	2.4
	1	6	45.3	1.5
	-3	6	48.4	1.6
143-183R-1	18a-18b	9	23.9	2.9
143-184R-1	5c-5d	10	23.9	2.6
143-185R-1	2a-2b	10	22.5	1.0
143-188R-3	3-4d	12	17.9	1.5
143-189R-1	5b-5c	12	22.5	0.9

Note: I° = arithmetic mean inclination; σ = standard deviation; for petrologic unit, see "Igneous Petrology" section (this chapter).

paths, based on igneous data sets (see also Gordon, 1990). Tarduno (1990) postulated that early silicification may have prevented compaction-induced inclination shallowing in the Site 463 sediments. The inclinations from Site 463 suggest paleolatitudes of approximately 17° and 13°S for Resolution Guyot in Albian-Aptian and Aptian time, respectively (Tarduno, 1990). The paleolatitude range suggested by the shipboard measurements, given the caveats of potential incomplete demagnetization and inadequate averaging of secular variation is broadly consistent with the Site 463 values. The basalt recovered at Hole 866A must represent an older time interval, however, as discussed in detail next.

Polarity Chron Assignment: Comparison with DSDP Site 463

Magnetostratigraphic study of Site 463 delineated a record of reversed polarity Chron M0 of early Aptian age (Tarduno et al., 1989). Below CM0 at Site 463, redeposited shallow-water debris was recovered. Because Site 463 lies downslope from Resolution Guyot (see "Site Geophysics" section, this chapter), it is reasonable to postulate that erosion of the guyot supplied this shallow-water debris. Therefore, the reversed-polarity chron represented by the basalt of Hole 866A must represent a stratigraphic record of one of the M-sequence marine magnetic anomalies older than M0 (i.e., Barremian or older). If a major temporal gap does not exist between the first sediments and the last basalts at Site 866, this suggests that the reversed-polarity chron recorded by the basalts is M1 or M3, because the overlying sediments are thought to be Barremian in age (see "Biostratigraphy" section, this chapter, and assignment of polarity chrons to geologic stage given by Kent and Gradstein, 1985). The validity of such a conclusion, which now rests entirely on the nature of the sediment/basalt contact, can be tested by shore-based radiometric age-dating of the basalt.

INORGANIC GEOCHEMISTRY

Interstitial Waters

Forty-eight samples were taken for analysis of interstitial waters from Holes 866A and 866B. Only four samples from the pelagic cap (Sections 143-866A-1R-2 and 143-866B-1M-3 to -3M-5) could be squeezed directly. The recovered limestones and dolomites were too lithified for pore-water extraction using normal squeezing techniques.

Some indication of the composition of the platform-interior waters was provided by nonstandard techniques. Waters were recovered from 18 limestone or dolomite samples after they were broken-up by pounding with a mallet before squeezing. The exterior surfaces of these rocks had been exposed to seawater, yet they were too lithified to clean by scraping. Some samples were just wiped with a paper

Table 4. Inclination groups derived from measurement of discrete samples in archive-half sections (see text).

Group	Cores	I°	α ₉₅	κ	n
1	143-866A-171R-3 to -179R-2	32.0	11.0	349	3
2	143-866A-180R-1 to -180R-3	47.4	6.5	992	3
3	143-866A-183R-1 to -189R-1	22.2	3.9	538	5

Note: I° = maximum-likelihood estimate of inclination; α₉₅ = 95% confidence limits on I°; κ = Fisher's precision parameter; all calculated using McFadden and Reid's method (1982). n = number of averaged inclinations.

towel ("Crush/S" in Table 5), while others were dipped in nanno-pure water for 1 min before being wiped with a paper towel to reduce the potential of contamination with seawater strontium for Sr isotope studies ("D-Crush/S" in Table 5). Water yields ranged from 0.5 to 9 mL. All resulting water samples were analyzed according to the methods outlined in the "Explanatory Notes" chapter (this volume.)

Salinity and Chlorinity

Pore-water salinities range from 34 to 37, and chlorinities are all within the range of normal seawater composition (540–568 mM Cl⁻; Fig. 35).

pH, Alkalinity, Calcium, and Magnesium

Only the four samples from the pelagic cap yielded enough water for pH, alkalinity, calcium, and magnesium analyses. The pH (\bar{x} = 7.70 ± 0.03), alkalinity (\bar{x} = 2.76 mM ± 0.15), calcium (\bar{x} = 10.4 mM ± 0.1), and magnesium (\bar{x} = 53.0 mM ± 0.2) values are similar to those of the surrounding seawater.

Sodium, Potassium, and Strontium

Sodium (\bar{x} = 476 ± 41 mM), potassium (10.4 ± 0.9 mM), and strontium (76.7 ± 9.5 μM) concentrations remain nearly constant with depth, and all are similar to seawater (Fig. 35).

Ammonium and Sulfate

The ammonium contents of the limestones and dolomites varied between 35 and 426 μM, with a mean value of 130 μM (Fig. 35). The presence of trace amounts of ammonium indicate that reactions associated with organic-matter decomposition have altered these fluids slightly. The sulfate concentrations within the limestones and dolomites range between 23.0 and 27.7 μM (\bar{x} = 25.6 ± 1.7), which are values significantly less than that of seawater and suggests that some sulfate reduction has occurred.

Comparison Between Sampling Techniques

The compositions of major elements of the dipped and undipped crushed samples of platform limestones have standard deviations about the mean, with overlapping ranges. Thus, the major-element compositions did not seem to be sensitive to surface exposure by either seawater (during drilling) or the distilled water (from the nannopure dip).

Summary

The ionic concentrations that were obtained for the interstitial water samples indicate that in-situ pore-water compositions in the interior of Resolution Guyot have a major-element composition similar to seawater, but some sulfate reduction and slight ammonium enrichment has taken place. No significant variations in the composition occur with depth, and no indication of the occurrence of either evaporite deposits or residual fresh water can be seen within this carbonate platform.

Table 5. Interstitial-water data from Holes 866A and 866B.

Core, section, interval (cm)	Depth (mbsf)	Sample handling	Water (mL)	Salinity (‰)	K ⁺ (mM)	Na ⁺ (mM)	Sr ⁺² (μM)	Cl ⁻ (mM)	NH ₄ (μM)	SO ₄ (mM)	Si ⁺⁴ (μM)
143-866A-											
1R-2, 47-48	0.72	S	77.0	34.5	9.95	483.	93.8	539.	0	28.2	61.
53R-1, 41-44	483.11	Crush/S	3.0	36.0	10.19	478.	83.4	551.	150	24.9	63.
70R-2, 76-80	648.47	D-Crush/S	3.0	35.5	9.23	477.	79.8	541.	228	26.5	73.
71R-1, 12-14	656.62	D-Crush/S	4.0	34.0	10.89	513.	74.8	523.	96	25.9	71
73R-1, 13-16	675.93	D-Crush/S	4.0	35.0	10.15	473.	77.6	533.	105	26.4	
76R-1, 53-56	705.23	D-Crush/S	3.0	35.0	9.35	472.	82.9	542.	56	26.3	24.
78R-2, 105-111	726.54	D-Crush/S	9.0	34.0	9.35	469.	75.8	545.	95	24.6	99.
84R-1, 42-45	782.62	D-Crush/S	5.0		9.89	444.	76.2	519.	426	24.9	
86R-1, 86-89	802.36	D-Crush/S	2.0	35.0	9.90	462.	70.3	538.	164	24.3	92.
91R-1, 104-107	850.54	D-Crush/S	1.5	36.0	10.41	467.	76.9	544.	160	23.8	71.
97R-1, 33-36	907.73	Crush/S	3.0	36.5	10.89	483.	86.1	561.	53	27.0	22.
97R-1, 33-36	907.73	D-Crush/S	2.5	34.5	10.32	463.	83.6	537.	45	25.7	63.
98R-1, 11-16	917.57	Crush/S	3.0	34.5	10.19	466.	78.8	552.	79	26.5	12
102R-1, 16-20	952.86	D-Crush/S	1.0	35.5	9.93	467.	74.1	543.		24.5	
102R-1, 16-20	952.86	Crush/S	2.0	35.5	9.94	641.	78.8	589.	60	24.3	
116R-1, 22-27	1087.72	D-Crush/S	1.0		9.79	458.	72.9	577.	325		
116R-1, 22-27	1087.72	Crush/S	1.5		10.05	472.	78.3	571.		23.5	
120R-1, 34-38	1126.44	Crush/S			65.95	614.	80.0			1.1	
143R-1, 90-93	1348.80	Crush/S	1.0	37.0	12.23	473.	81.5	585.	204	24.3	
154R-1, 1-4	1453.81	Crush/S	4.0	36.0	11.86	451.	69.4	572.	35	24.8	
156R-3, 70-74	1476.68	Crush/S	2.0		12.32	455.	67.4	561.	50	23.4	
162R-1, 15-19	1531.15	Crush/S	1.5		11.52	445.	46.7	561.	62	26.7	
SSW	0.10				10.30	464.	89.5	597.	0		
143-866B-											
1M-3, 145-150	4.45	S	40.0	35.0	10.19	431.	79.3	552	2	27.4	178
2M-2, 145-150	8.95	S	40.0	35.5	9.65	440.	80.0	549	23	27.9	160
3M-5, 145-150	20.87	S	42.0	35.0	9.56	441.	79.7	550	9	28.1	155

Note: Core-designations include the core drill type (R, rotary core barrel; M, diamond core barrel) and section number; S = normal ODP squeezing technique was used; Crush/S = samples were broken up with a mallet before squeezing; D Crush/S = sample was dipped in nannofossil-pure water for 1 min before crushing and squeezing; water = water yield in the analyzed samples; SSW = surface seawater.

ORGANIC GEOCHEMISTRY

Two hundred and sixteen samples from Hole 866A and 19 from Hole 866B were analyzed for carbonate content using the Coulometrics carbon dioxide coulometer. Total nitrogen, sulfur, carbon, and organic carbon contents were measured by means of an NA 1500 Carlo Erba NCS analyzer. Twenty-three samples were analyzed using a Geofina hydrocarbon meter (GHM) to assess the origin and maturation stage of the organic matter preserved in the Cretaceous sediments of Resolution Guyot. The procedures used for these analyses are outlined in the "Explanatory Notes" chapter (this volume).

Inorganic Carbon

According to the calcium-carbonate record (Table 6 and Fig. 36), the sedimentary sequence at Hole 866A can be divided into five parts. These correspond fairly well to the lithologic units defined in the "Lithostratigraphy" section (this chapter). The upper 436.0 mbsf is characterized by high carbonate content that ranges from 97.5% to 99.6%, except for the first sample from Core 143-866A-1R (89.7%). In the second part, which corresponds to lithologic Unit IV, the carbonate content varies from 81.5% to 99.5%. The green clay bed at 658.47 mbsf is completely devoid of carbonate. The third part, characterized by consistent values around 99%, coincides with the oolitic grainstone of lithologic Unit V. The fourth part is characterized by high-amplitude variations that range from 22% in clay-rich intervals to 99% in white, laminated packstones. The lowermost part is mostly characterized by very high calcium carbonate content related to dolomitic limestones of lithologic Units VII and VIII, but some clayey intervals show lower values between 43% and 67% CaCO₃. The standard method for reporting inorganic carbon as a percentage of calcium carbonate is inadequate for sediments that contained significant concentration of dolomite. Because dolomite contains

approximately 13 wt% carbon (compared to 12 wt% for calcite) samples containing abundant dolomite yield concentrations of calcium carbonate that exceed 100%. We have not attempted to correct the carbonate content data, considering the presence/absence of dolomite, because we do not have mineralogy data for all samples.

At Hole 866B, the carbonate content ranges from 94.7% to 100% (Table 7; Fig. 37). Most of the sediments are characterized by consistent values around 99%. Nevertheless, a slight decrease is recorded in the white ooze from the upper 15 mbsf, where the percentages of calcium carbonate decline progressively from 99.8% in Section 143-866B-2M-2 to 94.7% in Section 143-866B-1M-1.

Organic Carbon Content

The total organic carbon (TOC) content recorded in Hole 866A is presented in Table 6. We observed very low to low TOC values in lithologic Units III, V, Subunit VIB, VII, and VIII (Fig. 38). Most TOC amounts are below 0.3%. The highest observed organic content values are in dark gray claystone-rich intervals and algal laminated packstones from lithologic Unit IV and Subunits VIA and VIC. The values of these range from 0.6% to 14.2%. Nevertheless, the highest TOC values are not everywhere recorded in dark claystone intervals. Although the richest sample is clay-rich, some of these layers contain little organic matter (Fig. 39). Both carbonate-rich brown to gray laminated packstones and algal mats show moderate-to-high TOC amounts that range from 0.9% to 2.86% (Fig. 39).

It is commonly accepted that TOC/N ratios are higher for terrestrial than for marine organic matter. Generally, marine organic matter shows TOC/N ratios below 10, while terrestrial organic matter has ratios higher than 30. TOC/S ratios provide clues for the oxygenation of environment during settling of the organic matter. In Hole 866A, the total nitrogen and sulfur concentrations were commonly below the detection threshold of the NCS analyzer (Table 6). TOC/N and

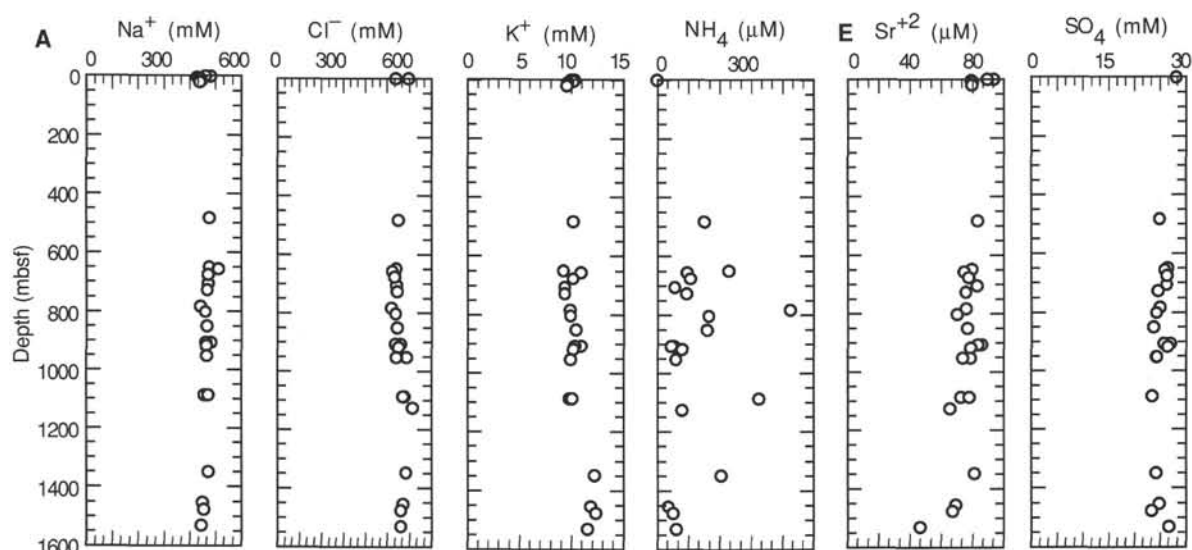


Figure 35. Concentration of determined pore-water parameters as a function of depth in Holes 866A and 866B. Concentration values remain constant at near-seawater values.

TOC/S ratios tend to be highly variable; the highest ratios are generally recorded in samples that are very low in both nitrogen and sulfur. Owing to this fact, only the GHM data have been used to determine the origin of organic matter. Twenty-three samples were analyzed for thermal maturity, hydrocarbon potential, and source character using the GHM. The resulting values are presented in Table 8.

The reproducibility of the T_{\max} parameter was relatively good. T_{\max} values produced by GHM analyses are 60°C higher than those of the Rock-Eval pyrolysis. Both T_{\max} values are reported in Table 8. Most of the samples show immature to early mature organic matter (Fig. 40). The equivalent Rock-Eval T_{\max} values range from 419° to 435°C. Three samples (866A-75R-1, 71–72 cm; 866A-102R-2, 14–15 cm, and 866A-144R-2, 149–150 cm) present abnormally low T_{\max} values. The low carbon content in Samples 143-866A-75R-1, 71–72 cm, and -144R-2, 149–150 cm, may explain these low T_{\max} values. Their S_2 peaks were so flat that T_{\max} is difficult to situate on the chromatogram. But for Sample 143-866A-102R-2, 14–15 cm, which contains 1.91% TOC, alteration must be postulated to interpret the 396°C T_{\max} value.

The S_1 values represent the amount of free-hydrocarbons contained in the rock. The analyzed samples show very low S_1 contents (0.01–0.38 mg HC/g of rock), which corroborate the low maturation stage of the organic matter. The S_2 values represent the amount of hydrocarbons that can be released from the kerogen during pyrolysis or thermal maturation of whole sediment. For the 23 samples analyzed, S_2 varies from 0.1 to 23.06 mg HC/g of rock. Highest values were recorded in organic-rich samples with an average of 9 mg HC/g. The hydrogen index ($HI = S_2/TOC \times 100$) approximates the H/C ratio of the kerogen and provides an estimate of the origin of organic matter. At Hole 866A, HI values range from 5 to 570, according to different lithologies (Table 8). Based on the sample distribution in the HI-TOC diagram (Fig. 41), four groups can be distinguished:

1. The algal mats, some dark laminated packstones, and one dark claystone sample show HI values of around 500, probably indicating Type II (marine) organic matter;

2. The sample containing 14.2% TOC shows a relatively low HI, which may indicate either Type III (terrestrial) organic matter or strongly altered marine organic matter;

3. Other dark claystones and various lithologies, such as pyritic wackestone or clayey limestone have medium values, which may be related to a mixture of Types II and III; and

4. Oolitic grainstones having low organic contents are reported as Type IV (altered) organic matter.

The pyrolysis gas chromatograms of organic-rich samples show mainly C_9 – C_{30} alkene/alkane doublets, with a large proportion of aromatic compounds (Fig. 42). This may indicate a mainly marine origin of the organic matter in most samples. A pyrolysis-gas chromatogram for Sample 143-866A-89R-1, 97–98 cm, which contains 14.2% TOC, show abundant light hydrocarbons having a sharp decrease beyond C_{17} and higher alkanes (Fig. 43). This may indicate a more terrestrial organic matter, as suggested by the low HI and high TOC/N ratio.

IGNEOUS PETROLOGY

The volcanic basement beneath the carbonate succession of the guyot (lithologic Unit IX; see “Lithostratigraphy” section, this chapter) was first encountered at 1620.0 mbsf and was subsequently drilled to a total depth of 1743.6 mbsf. The 123.6 m of penetration through the volcanic rocks yielded an average recovery of 37%. The succession is interpreted as a sequence of subaerial lava flows separated by rubbly to clayey interbasaltic intervals.

The nature of the contact between the volcanic rocks and the overlying sedimentary sequence is ambiguous owing to patchy recovery. Going downhole, the first indications of approaching basement occur in Core 143-866A-166R (1570 mbsf), where sparse volcanogenic components, such as altered ferromagnesian minerals and small feldspar-bearing clasts, start to appear in the carbonate sediments. These occur both as discrete detrital grains and as the nuclei of ooids. At 1619.8 mbsf, a ~20-cm lobate piece of lava (gray, 5Y 6/1) has a near-vertical contact with a matrix-supported breccia, comprising oolitic grainstone that contains basalt pebbles (Interval 143-866A-171R-2, 17–19 cm). The lava is very highly altered, virtually devoid of ferromagnesian minerals, and riddled with secondary calcite and pyrite. It appears to have a narrow chilled zone, about 3 mm wide, at its contact with the adjacent sediment. Because the rock matrix has been totally replaced by clay minerals, carbonate, and pyrite, the chill is distinguishable only because of a reduction in the size of plagioclase laths from about 0.2 to 0.5 mm. Separating the volcanic rock from the oolitic grainstone is a fracture, ~2 mm wide, filled with sparry calcite. Some of the individual ooids are truncated by this fracture. Other

Table 6. Concentrations of total, inorganic, and organic carbon and of total nitrogen and sulfur in sediments from Hole 866A.

Core, section, interval (cm)	Depth (mbsf)	Sample type ^a	TC (%)	IC (%)	TOC (%)	CaCO ₃ (%)	N (%)	S (%)	TOC/N	TOC/S
1R-2, 47-48	0.72	IWSC	11.46	10.77	0.69	89.7	0.00	0.00		
10R-CC, 9-10	76.99	CARB	11.98	11.81	0.17	98.4	0.02	0.02	8.5	8.5
12R-CC, 1-2	96.11	CARB	11.86	11.86	0.00	98.8	0.00	0.00		
14R-CC, 2-3	115.42	CARB	12.03	11.81	0.22	98.4	0.00	0.00		
16R-CC, 2-3	134.72	CARB	11.87	11.87	0.00	98.9	0.00	0.01		0.0
20R-CC, 7-8	174.57	CARB	11.95	11.87	0.08	98.9	0.01	0.01	8.0	8.0
22R-CC, 7-8	193.87	CARB	11.97	11.79	0.18	98.2	0.00	0.00		
25R-1, 30-31	223.00	CARB	12.00	11.91	0.09	99.2	0.01	0.00	9.0	
26R-CC, 2-3	232.42	CARB	11.89	11.89	0.00	99.0	0.00	0.00		
28R-CC, 2-3	251.62	CARB	11.87	11.86	0.01	98.8	0.00	0.04		0.2
31R-1, 16-20	280.76	IWSC	12.15	11.93	0.22	99.4	0.00	0.00		
31R-1, 120-122	281.80	CARB	11.92	11.92	0.00	99.3	0.01	0.00	0.0	
35R-1, 67-70	319.57	IWSC	12.24	11.90	0.34	99.1	0.00	0.00		
35R-1, 80-81	319.70	CARB	11.93	11.93	0.00	99.4	0.00	0.00		
36R-1, 37-38	328.87	CARB	12.23	11.85	0.38	98.7	0.01	0.01	38.0	38.0
37R-1, 24-25	338.24	CARB	11.88	11.88	0.00	99.0	0.01	0.00	0.0	
38R-1, 24-25	342.94	CARB	11.89	11.81	0.08	98.4	0.01	0.28	8.0	0.3
38R-1, 61-62	343.31	CARB	11.97	11.70	0.27	97.5	0.00	0.03		9.0
39R-1, 66-67	348.36	CARB	11.94	11.91	0.03	99.2	0.00	0.01		3.0
39R-2, 35-36	348.94	CARB	12.02	11.92	0.10	99.3	0.01	0.00	10.0	
40R-CC, 30-31	357.60	CARB	11.98	11.70	0.28	97.5	0.00	0.02		14.0
41R-1, 5-7	367.05	IWSC	12.23	11.96	0.27	99.6	0.00	0.00		
41R-1, 26-27	367.26	CARB	11.99	11.90	0.09	99.1	0.01	0.00	9.0	
42R-CC, 16-17	376.76	CARB	11.93	11.77	0.16	98.0	0.00	0.00		
44R-CC, 9-10	395.99	CARB	11.95	11.78	0.17	98.1	0.02	0.00	8.5	
45R-CC, 29-31	405.89	CARB	11.95	11.87	0.08	98.9	0.01	0.01	8.0	8.0
46R-1, 6-7	415.36	CARB	11.64	11.64	0.00	97.0	0.01	0.00	0.0	
46R-1, 72-75	416.02	IWSC	12.03	11.90	0.13	99.1	0.00	0.00		
46R-2, 19-20	416.99	CARB	11.95	11.94	0.01	99.5	0.00	0.00		
46R-2, 71-73	417.51	CARB	11.96	11.92	0.04	99.3	0.01	0.00	4.0	
47R-1, 56-58	425.26	CARB	11.80	11.80	0.00	98.3	0.01	0.00	0.0	
50R-CC, 10-12	453.80	CARB	12.04	11.86	0.18	98.8	0.01	0.00	18.0	
53R-1, 41-44	483.11	IWSC	11.82	11.79	0.03	98.2	0.00	0.00		
53R-1, 71-76	483.41	XRD	11.81	11.78	0.03	98.1	0.02	0.00	1.0	
55R-CC, 2-3	501.92	CARB	11.15	10.80	0.35	90.0	0.01	0.19	35.0	1.8
55R-CC, 40-41	502.30	XRD	11.82	11.81	0.01	98.4	0.02	0.00	0.5	
56R-1, 3-4	511.63	CARB	11.80	11.80	0.00	98.3	0.01	0.06	0.0	0.0
56R-1, 49-52	512.09	IWSC	11.94	11.87	0.07	98.9	0.00	0.00		
57R-1, 36-38	521.66	CARB	12.25	11.64	0.61	97.0	0.00	0.00		
58R-1, 29-32	531.29	CARB	12.32	11.72	0.60	97.6	0.00	0.01		60.0
58R-1, 51-54	531.51	CARB	12.65	11.73	0.92	97.7	0.03	0.00	30.0	
58R-1, 109-111	532.09	XRD	13.79	10.93	2.86	91.0	0.00	0.00		
59R-1, 8-11	540.78	IWSC	12.35	11.95	0.40	99.5	0.00	0.00		
60R-1, 64-65	550.94	XRD	10.65	10.27	0.38	85.5	0.04	0.39	9.5	1.0
62R-1, 84-87	570.44	IWSC	12.67	11.84	0.83	98.6	0.01	0.00	83.0	
62R-2, 38-39	571.48	CARB	10.47	9.78	0.69	81.5	0.03	0.25	23.0	2.7
63R-1, 29-33	579.59	CARB	12.29	11.79	0.50	98.2	0.00	0.00		
64R-1, 75-76	589.75	CARB	12.24	11.83	0.41	98.5	0.00	0.00		
65R-1, 21-24	598.81	IWSC	12.22	11.85	0.37	98.7	0.03	0.17	12.0	2.2
65R-1, 128-129	599.88	CARB	12.47	11.76	0.71	98.0	0.00	0.10		7.1
69R-CC, 20-23	637.40	CARB	12.49	11.67	0.82	97.2	0.01	0.09	82.0	9.1
70R-2, 76-80	648.47	IWSC	12.12	11.84	0.28	98.6	0.00	0.00		
71R-1, 12-14	656.62	IWSC	12.31	11.83	0.48	98.5	0.00	0.00		
71R-2, 69-70	658.47	CARB	0.20	0.17	0.03	1.4	0.00	2.72		0.0
72R-1, 59-60	666.79	XRD	9.28	8.78	0.50	73.1	0.03	2.90	16.0	0.2
73R-1, 13-16	675.93	IWSC	12.01	11.56	0.45	96.3	0.00	0.01		45.0
73R-1, 28-29	676.08	CARB	11.48	10.57	0.91	88.0	0.02	1.49	45.0	0.6
73R-1, 108-109	676.88	CARB	12.37	11.80	0.57	98.3	0.01	0.12	57.0	4.7
74R-1, 74-75	686.24	CARB	12.28	11.90	0.38	99.1	0.01	0.04	38.0	9.5
74R-2, 71-72	687.49	CARB	11.39	10.97	0.41	91.4	0.01	0.00	41.0	
75R-1, 70-71	695.80	XRD	11.52	11.46	0.06	95.5	0.02	0.30	3.0	0.2
75R-1, 71-72	695.81	CARB	12.17	11.72	0.45	97.6	0.00	0.22		2.0
75R-3, 60-61	698.14	CARB	12.25	11.90	0.35	99.1	0.01	0.00	35.0	
76R-1, 53-56	705.23	IWSC	12.02	11.90	0.12	99.1	0.00	0.00		
76R-2, 98-99	707.18	CARB	11.92	11.90	0.02	99.1	0.02	0.00	1.0	
76R-3, 35-36	707.98	CARB	12.18	11.87	0.31	98.9	0.02	0.00	15.0	
77R-1, 77-78	715.27	CARB	11.91	11.90	0.01	99.1	0.01	0.00	1.0	
77R-3, 54-55	718.04	CARB	11.89	11.88	0.01	99.0	0.03	0.00	0.3	
78R-1, 56-57	724.66	CARB	11.99	11.88	0.11	99.0	0.02	0.00	5.5	
78R-2, 105-111	726.54	IWSC	12.37	11.92	0.45	99.3	0.01	0.01	45.0	45.0
78R-3, 49-50	727.48	CARB	11.94	11.87	0.07	98.9	0.02	0.00	3.0	
79R-1, 122-124	735.02	CARB	11.88	11.88	0.00	99.0	0.02	0.00	0.0	
79R-4, 6-7	738.15	CARB	11.79	11.76	0.03	98.0	0.02	0.00	1.0	
80R-1, 59-63	744.09	IWSC	12.33	11.92	0.41	99.3	0.00	0.00		
80R-1, 85-87	744.35	CARB	11.86	11.85	0.01	98.7	0.01	0.00	1.0	
81R-2, 78-81	754.40	PP	11.92	11.89	0.03	99.0	0.02	0.09	1.0	0.3

Table 6 (continued).

Core, section, interval (cm)	Depth (mbsf)	Sample type ^a	TC (%)	IC (%)	TOC (%)	CaCO ₃ (%)	N (%)	S (%)	TOC/N	TOC/S
82R-1, 4-9	762.84	IWSC	12.44	11.93	0.51	99.4	0.00	0.00		
82R-2, 68-69	764.86	CARB	11.92	11.91	0.01	99.2	0.02	0.00	0.5	
83R-1, 54-55	773.04	CARB	12.05	11.94	0.11	99.5	0.03	0.00	3.6	
84R-1, 42-45	782.62	IWSC	12.52	11.91	0.61	99.2	0.01	0.00	61.0	
85R-2, 49-51	793.74	CARB	11.92	11.91	0.01	99.2	0.00	0.00		
86R-1, 86-89	802.36	IWSC	12.31	12.00	0.31	100.0	0.03	0.00	10.0	
86R-1, 149-150	802.99	CARB	11.93	11.79	0.14	98.2	0.02	0.00	7.0	
86R-2, 19-20	803.19	CARB	13.63	11.31	2.32	94.2	0.08	0.30	29.0	7.7
87R-1, 102-103	812.22	CARB	12.08	11.38	0.70	94.8	0.03	0.00	23.0	
88R-1, 122-123	822.12	CARB	11.99	11.81	0.18	98.4	0.02	0.00	9.0	
88R-1, 129-131	822.19	IWSC	12.03	11.69	0.34	97.4	0.00	0.17		2.0
89R-1, 97-98	831.57	CARB	16.85	2.66	14.19	22.2	0.30	3.50	47.3	4.1
89R-2, 37-38	832.47	CARB	11.69	11.55	0.14	96.2	0.01	0.07	14.0	2.0
91R-1, 10-11	849.60	CARB	4.49	4.42	0.07	36.8	0.03	1.80	2.0	0.0
91R-1, 104-107	850.54	IWSC	11.95	11.89	0.06	99.0	0.02	0.00	3.0	
91R-2, 14-15	850.90	CARB	11.72	11.58	0.14	96.5	0.01	0.05	14.0	2.8
92R-1, 2-3	859.22	CARB	11.94	11.82	0.12	98.5	0.04	0.00	3.0	
93R-1, 21-22	868.91	CARB	11.93	11.91	0.02	99.2	0.02	0.00	1.0	
95R-1, 45-46	888.45	CARB	11.86	11.85	0.01	98.7	0.01	0.00	1.0	
96R-1, 10-16	897.80	IWSC	12.09	11.84	0.25	98.6	0.01	0.00	25.0	
96R-1, 35-36	898.05	CARB	11.94	11.94	0.00	99.5	0.00	0.00		
97R-1, 25-26	907.65	CARB	11.97	11.89	0.08	99.0	0.02	0.00	4.0	
97R-1, 33-36	907.73	IWSC	11.94	11.86	0.08	98.8	0.00	0.00		
98R-1, 57-58	917.57	CARB	11.70	11.65	0.05	97.0	0.02	0.01	2.0	5.0
98R-2, 25-27	918.75	CARB	11.94	11.67	0.27	97.2	0.02	0.01	13.0	27.0
99R-1, 76-77	924.66	CARB	12.35	11.48	0.87	95.6	0.04	0.16	22.0	5.4
100R-1, 28-29	933.68	CARB	11.71	11.65	0.06	97.0	0.01	0.00	6.0	
101R-1, 32-34	943.42	CARB	11.69	11.52	0.17	96.0	0.01	0.00	17.0	
102R-1, 16-20	952.86	IWSC	12.01	11.89	0.12	99.0	0.14	0.00	0.9	
102R-1, 86-87	953.56	CARB	11.98	11.12	0.86	92.6	0.02	0.01	43.0	86.0
102R-1, 91-92	953.61	CARB	12.26	11.83	0.43	98.5	0.03	0.10	14.0	4.3
102R-2, 14-15	954.34	CARB	13.12	11.21	1.91	93.4	0.07	0.46	27.3	4.2
102R-2, 35-36	954.55	CARB	12.60	11.70	0.90	97.5	0.03	0.10	30.0	9.0
103R-1, 48-49	962.88	CARB	12.76	11.66	1.10	97.1	0.03	0.23	36.6	4.8
104R-1, 20-21	971.90	CARB	12.08	11.55	0.53	96.2	0.02	0.10	26.0	5.3
104R-1, 57-61	972.27	IWSC	12.10	11.85	0.25	98.7	0.00	0.00		
105R-1, 49-51	981.79	CARB	12.54	11.89	0.65	99.0	0.01	0.00	65.0	
106R-1, 23-24	991.13	CARB	12.34	11.85	0.49	98.7	0.00	0.03		16.0
108R-1, 11-12	1010.31	CARB	12.17	11.86	0.31	98.8	0.00	0.00		
108R-1, 15-18	1010.35	IWSC	12.06	11.82	0.24	98.5	0.00	0.00		
109R-1, 44-45	1020.34	CARB	12.33	11.81	0.52	98.4	0.03	0.09	17.0	5.8
109R-1, 79-80	1020.69	CARB	11.60	11.47	0.13	95.5	0.02	0.26	6.5	0.5
109R-2, 7-8	1021.11	CARB	12.16	11.82	0.34	98.5	0.00	0.00		
109R-2, 41-42	1021.45	CARB	12.16	11.83	0.33	98.5	0.00	0.07		4.7
110R-1, 51-52	1030.11	CARB	12.10	11.70	0.40	97.5	0.01	0.12	40.0	3.3
110R-1, 120-124	1030.80	IWSC	12.23	11.90	0.33	99.1	0.00	0.00		
110R-2, 44-45	1031.48	CARB	11.63	11.37	0.26	94.7	0.00	0.13		2.0
111R-1, 77-78	1040.07	CARB	7.14	6.51	0.63	54.2	0.03	2.96	21.0	0.2
112R-1, 94-96	1049.84	CARB	12.62	10.95	1.67	91.2	0.02	0.56	83.5	3.0
112R-1, 102-104	1049.92	CARB	12.48	11.75	0.73	97.9	0.02	0.18	36.0	4.0
113R-CC, 36-37	1058.86	CARB	12.47	10.83	1.64	90.2	0.08	0.71	20.5	2.3
114R-1, 99-100	1069.19	CARB	12.58	11.51	1.07	95.9	0.00	0.05		21.4
115R-1, 34-35	1078.24	CARB	11.58	11.93		99.4	0.00	0.00		
115R-1, 77-78	1078.67	CARB	11.63	11.45	0.18	95.4	0.00	0.00		
116R-1, 22-27	1087.72	IWSC	12.36	12.66		105.5	0.00	0.06		
116R-1, 45-46	1087.95	CARB	12.22	11.81	0.41	98.4	0.00	0.07		5.8
117R-2, 50-51	1099.10	CARB	1.81	1.18	0.63	9.8	0.01	14.78	63.0	0.0
118R-1, 73-74	1107.53	CARB	11.97	11.80	0.17	98.3	0.04	0.00	4.2	
118R-2, 124-128	1109.54	IWSC	12.79	11.75	1.04	97.9	0.00	0.11		9.5
118R-2, 140-142	1109.70	CARB	12.27	11.98	0.29	99.8	0.04	0.09	7.2	3.2
119R-1, 44-45	1116.94	CARB	11.92	11.90	0.02	99.1	0.00	0.00		
120R-1, 30-31	1126.40	CARB	12.00	11.91	0.09	99.2	0.00	0.00		
120R-1, 34-38	1126.44	IWSC	11.98	11.92	0.06	99.3	0.00	0.00		
121R-1, 10-11	1135.80	CARB	12.44	12.10	0.34	100.8	0.01	0.00	34.0	
121R-1, 30-34	1136.00	CARB	12.06	12.25		102.0	0.00	0.00		
122R-1, 29-30	1145.69	CARB	12.06	11.80	0.26	98.3	0.01	0.00	26.0	
123R-1, 16-18	1155.26	CARB	12.56	12.40	0.16	103.3	0.02	0.00	8.0	
124R-1, 14-16	1164.94	CARB	12.02	11.92	0.10	99.3	0.00	0.00		
124R-1, 34-35	1165.14	CARB	11.94	11.94	0.00	99.5	0.05	0.00	0.0	
125R-2, 58-59	1176.48	CARB	12.27	11.94	0.33	99.5	0.02	0.03	16.0	11.0
125R-3, 86-90	1178.19	IWSC	12.15	11.94	0.21	99.5	0.07	0.01	3.0	21.0
126R-1, 1-2	1184.01	CARB	12.11	11.74	0.37	97.8	0.03	0.32	12.0	1.1
126R-1, 52-53	1184.52	CARB	11.97	11.96	0.01	99.6	0.02	0.03	0.5	0.3
127R-1, 6-8	1193.56	CARB	12.37	12.36	0.01	103.0	0.00	0.13		0.1
128R-1, 103-104	1204.23	CARB	12.80	12.62	0.18	105.1	0.00	0.00		
128R-2, 27-28	1204.61	CARB	12.61	12.64		105.3	0.00	0.00		

Table 6 (continued).

Core, section, interval (cm)	Depth (mbsf)	Sample type ^a	TC (%)	IC (%)	TOC (%)	CaCO ₃ (%)	N (%)	S (%)	TOC/N	TOC/S
129R-1, 50–51	1213.40	CARB	8.46	8.12	0.34	67.6	0.00	0.88		0.4
129R-2, 7–12	1214.47	IWSC	11.81	11.61	0.20	96.7	0.01	0.00	20.0	0.00
130R-1, 4–6	1222.64	CARB	12.32	11.92	0.40	99.3	0.01	0.01	40.0	40.0
131R-1, 34–36	1232.54	CARB	11.27	10.82	0.45	90.1	0.00	0.80		0.6
131R-1, 122–124	1233.42	CARB	12.94	12.68	0.26	105.6	0.01	0.35	26.0	0.7
132R-1, 85–86	1242.75	CARB	12.38	12.71		105.9	0.01	0.01		
133R-1, 0–5	1251.60	IWSC	12.68	12.64	0.04	105.3	0.01	0.00	4.0	
133R-2, 50–52	1253.60	CARB	13.02	12.78	0.24	106.5	0.00	0.00		
133R-3, 41–47	1254.96	CARB	12.89	12.78	0.11	106.5	0.02	0.00	5.5	
134R-2, 65–66	1263.35	CARB	12.88	12.72	0.16	106.0	0.02	0.00	8.0	
135R-1, 111–112	1272.01	CARB	12.75	12.67	0.08	105.5	0.00	0.11		0.7
136R-1, 3–4	1280.23	CARB	11.92	11.99		99.9	0.02	0.00		
137R-1, 26–28	1290.06	CARB	12.87	12.78	0.09	106.5	0.00	0.00		
137R-3, 79–80	1293.18	CARB	12.87	12.58	0.29	104.8	0.04	0.00	7.2	
138R-1, 97–98	1300.47	CARB	12.18	11.36	0.82	94.6	0.01	0.05	82.0	16.0
139R-1, 29–30	1309.49	CARB	11.91	11.96		99.6	0.03	0.01		
140R-1, 14–15	1319.04	CARB	11.73	12.29		102.4	0.03	0.03		
142R-2, 17–18	1339.73	CARB	13.04	12.48	0.56	104.0	0.01	0.00	56.0	
143R-1, 11–12	1348.01	CARB	12.05	12.01	0.04	100.0	0.01	0.08	4.0	0.5
143R-1, 90–93	1348.80	IWSC	12.36	12.03	0.33	100.2	0.00	0.21		1.6
144R-1, 81–82	1358.31	CARB	12.23	11.83	0.40	98.5	0.02	0.00	20.0	
144R-2, 149–150	1360.49	CARB	5.66	5.25	0.41	43.7	0.05	1.48	8.2	0.3
145R-2, 79–80	1369.09	CARB	12.07	11.25	0.82	93.7	0.02	0.14	41.0	5.8
146R-1, 81–82	1377.21	CARB	11.85	11.72	0.13	97.6	0.02	0.00	6.5	
146R-1, 122–124	1377.62	CARB	11.87	11.87	0.00	98.9	0.01	0.00	0.0	
147R-1, 9–10	1386.19	CARB	12.25	12.11	0.14	100.9	0.00	0.12		1.1
147R-1, 125–129	1387.35	IWSC	12.27	11.87	0.40	98.9	0.00	0.00		
147R-2, 92–93	1388.52	CARB	11.76	11.70	0.06	97.5	0.00	0.23		0.3
148R-1, 53–55	1396.23	CARB	12.52	12.39	0.13	103.2	0.00	0.09		1.4
148R-1, 116–119	1396.86	IWSC	12.06	11.97	0.09	99.7	0.00	0.00		
148R-2, 51–52	1397.63	CARB	11.86	11.86	0.00	98.8	0.02	0.05	0.0	0.0
148R-4, 94–95	1400.24	CARB	11.96	11.94	0.02	99.5	0.00	0.00		
152R-1, 27–28	1434.77	CARB	12.21	11.94	0.27	99.5	0.00	0.00		
153R-2, 15–16	1445.67	CARB	12.02	11.88	0.14	99.0	0.00	0.00		
154R-1, 1–4	1453.81	IWSC	12.82	12.71	0.11	105.9	0.00	0.00		
154R-1, 49–50	1454.29	CARB	12.04	11.92	0.12	99.3	0.00	0.01		12.0
154R-2, 38–41	1455.55	CARB	11.98	11.88	0.10	99.0	0.00	0.06		1.6
154R-3, 93–96	1457.60	CARB	12.77	12.61	0.16	105.0	0.00	0.00		
155R-1, 91–92	1464.41	CARB	12.25	11.95	0.30	99.5	0.00	0.00		
156R-2, 57–58	1475.16	CARB	12.44	12.02	0.42	100.1	0.00	0.06		7.0
156R-3, 70–74	1476.68	IWSC	12.28	11.91	0.37	99.2	0.00	0.00		
157R-3, 43–44	1486.19	CARB	12.41	11.94	0.47	99.5	0.00	0.00		
158R-1, 136–137	1493.86	CARB	12.12	11.99	0.13	99.9	0.00	0.00		
159R-1, 102–104	1501.92	CARB	12.28	12.21	0.07	101.7	0.00	0.00		
159R-2, 97–99	1503.37	CARB	12.02	11.97	0.05	99.7	0.00	0.03		1.0
159R-3, 8–9	1503.98	CARB	13.07	12.99	0.08	108.2	0.00	0.00		
159R-3, 95–99	1504.85	IWSC	12.74	12.68	0.06	105.6	0.00	0.00		
160R-1, 43–45	1512.13	CARB	12.54	12.39	0.15	103.2	0.27	0.00	0.6	
160R-1, 70–71	1512.40	CARB	12.53	12.18	0.35	101.5	0.00	0.00		
161R-1, 23–24	1521.53	CARB	12.13	11.90	0.23	99.1	0.00	0.05		4.6
162R-1, 15–19	1531.15	IWSC	12.95	12.70	0.25	105.8	0.00	0.00		
162R-1, 104–106	1532.04	CARB	12.74	12.73	0.01	106.0	0.00	0.00		
162R-2, 5–6	1532.50	CARB	12.71	12.64	0.07	105.3	0.00	0.00		
163R-1, 41–43	1540.71	CARB	12.63	12.16	0.47	101.3	0.00	0.00		
164R-3, 2–3	1552.76	CARB	12.63	12.49	0.14	104.0	0.00	0.00		
165R-2, 75–76	1561.74	CARB	13.16	12.65	0.51	105.4	0.00	0.19		2.7
166R-1, 82–83	1570.12	CARB	12.03	11.86	0.17	98.8	0.00	0.00		
167R-1, 89–90	1581.29	CARB	11.90	11.89	0.01	99.0	0.00	0.00		
167R-3, 78–79	1584.14	CARB	12.70	12.45	0.25	103.7	0.00	0.15		1.6
168R-2, 89–89	1592.43	CARB	13.05	12.65	0.40	105.4	0.00	0.01		40.0
168R-5, 21–26	1596.16	IWSC	12.87	12.68	0.19	105.6	0.00	0.00		
169R-2, 89–90	1602.19	CARB	12.44	12.21	0.23	101.7	0.00	0.01		23.0
169R-3, 22–23	1602.84	CARB	12.11	11.68	0.43	97.3	0.00	0.08		5.4
170R-1, 116–117	1610.56	CARB	12.16	11.92	0.24	99.3	0.00	0.05		4.8

^aSamples: CARB = carbonate; IWSC = interstitial-water squeeze cake; PP = physical property; XRD = X-ray diffractometry.

clasts in the immediate vicinity are of the order of 2 cm across and are composed of highly altered basalt, wackestone, and ooids. This contact is underlain by a rubbly zone (Interval 143-866A-171R-2, 23–55 cm) consisting of fragments of completely altered basalt mixed with reddish (2.5YR 4/6) clay. Secondary pyrite cubes (<2 mm) are especially abundant at this level, and smaller pyrite crystals are

dispersed throughout the dolomitic grainstone from Core 143-866A-166R (1569.3 mbsf) downward.

Two main interpretations may be postulated for the semirounded piece of basalt seen at the contact. First, it may be a clastic component in the basal conglomerate deposited on the eroded surface of the real volcanic basement prior to the deposition of the oolitic grainstone. If

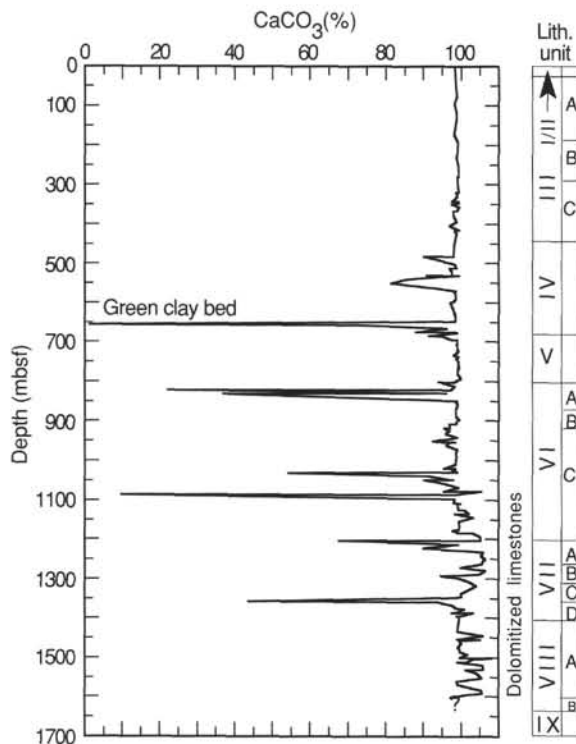


Figure 36. Depth distribution of calcium carbonate in Hole 866A.

this is the case, then the piece of basalt is not chilled against the limestone. Its chilled margin is coincidental and was acquired during an earlier intrusive or extrusive event, (e.g., it may be a redeposited part of a pillow or pahoehoe lobe). The sparry calcite separating the basalt from the oolitic grainstone breccia therefore does not represent thermally induced recrystallization, but simply the later infilling of a fracture that opened between the boulder and the sedimentary matrix. An alternative explanation is that the lobe of basalt represents part of a small intrusive emplaced between the volcanic basement and the overlying sediments. In this alternative, it must be regarded as having chilled against the basal conglomerate of the oolitic grainstone, with the sparry calcite forming a zone of recrystallization.

Once it had become apparent that the underlying volcanic succession was composed of subaerial lava flows, the interpretation of the contact zone diminished in importance. If there is a small (~20 cm) sill at the contact, then it is a minor feature unrepresentative of the lava flows beneath.

Volcanic "Basement"

The volcanic sequence consists of 125 m of lava flows and intervening rubbly (interbasaltic) intervals (Fig. 44). Estimates of average thickness are suspect because of poor recovery, especially in the depth range of 1625 to 1660 mbsf, and it is likely that more friable intervals are under-represented in the recovered core. With such reservations, the average thickness of the flows appears to be about 10 m (range is from 4 to 26 m).

The lava flows are moderately to very highly altered rocks. They are sparsely to moderately phyrific basalts, with variations based largely on the relative proportions of the phenocryst phases olivine, pyroxene, and plagioclase. Because the ferromagnesian constituents are mainly completely pseudomorphed by alteration products, discrimination between olivine and pyroxene may not be reliable everywhere. Nonetheless, olivine appears to be ubiquitous and therefore the principal ferromagnesian phenocryst. While olivine-pyroxene phyrific lavas are the most common, plagioclase becomes an additional phenocryst phase in the middle of the drilled section (1662–1687 mbsf), where it makes up 1% to 3% of the total rock volume. Nomenclature is somewhat complicated by the appearance of plagioclase megacrysts, interpreted as xenocrysts, or cumulo-phyrific clusters of plagioclase, in association with pyroxene and olivine, in some of these lavas (Units 6, 8, and 12; Fig. 45).

Most of the lavas are gray (7.5 YR 5/0) or dark gray (7.5 YR 4/0), although dark brown (7.5 YR 3/2) to reddish-gray (10R 6/1) basalt forms Unit 11 and greenish-gray (5B 5/1) is the prevalent color of Unit 12. On the whole, the lavas are vesicular, although the actual vesicle content varies from sparse (<1%) to as much as 25% (Unit 10). Although there seems to be no systematic variation in vesicle content, zones (e.g., Interval 143-866A-184R-2, 80–89 cm) are seen in which vesicles are conspicuously concentrated (Fig. 46): they vary in size from 0.2 mm to 5.0 cm and in shape from rounded to subrounded, elongate, and highly irregular. The stretching or elongation is generally subhorizontal and presumably reflects flow direction. Fracturing of the lava is also highly variable, ranging from 1% volume to as much as 15% (again in Unit 12). Vesicles and fractures are filled mainly

Table 7. Concentrations of total, inorganic, and organic carbon and of total nitrogen and sulfur in sediments from Hole 866B.

Core, section, interval (cm)	Depth (mbsf)	Sample type ^a	TC (%)	IC (%)	TOC (%)	CaCO ₃ (%)	N (%)	S (%)	TOC/N
1M-1, 76–77	0.76	CARB	12.03	11.37	0.66	94.7	0.01	0.00	66.0
1M-3, 145–150	4.45	IWSC	11.76	11.47	0.29	95.5	0.14	0.00	2.1
2M-1, 39–40	6.39	CARB	11.81	11.55	0.26	96.2	0.00	0.00	
2M-2, 145–150	8.95	IWSC	12.17	11.98	0.19	99.8	0.01	0.00	19.0
2M-3, 77–78	9.77	CARB	12.01	11.97	0.04	99.7	0.04	0.00	1.0
3M-1, 90–91	15.00	CARB	11.91	11.79	0.12	98.2	0.01	0.00	12.0
3M-3, 73–74	17.83	CARB	11.90	11.85	0.05	98.7	0.00	0.00	
3M-5, 77–78	20.87	CARB	11.90	11.89	0.01	99.0	0.00	0.00	
3M-5, 145–150	21.55	IWSC	12.04	11.88	0.16	99.0	0.00	0.00	
3M-CC, 3–4	22.56	CARB	12.17	11.99	0.18	99.9	0.02	0.00	9.0
4M-1, 35–37	23.85	CARB	11.84	11.83	0.01	98.5	0.00	0.00	
5M-1, 26–30	33.06	IWSC	12.19	11.96	0.23	99.6	0.00	0.00	
5M-1, 37–38	33.17	CARB	12.02	11.93	0.09	99.4	0.00	0.02	
6M-1, 88–89	43.08	CARB	12.11	11.94	0.17	99.5	0.00	0.00	
7M-1, 1–2	51.71	CARB	11.91	11.84	0.07	98.6	0.00	0.00	
8M-1, 76–77	61.86	CARB	12.00	11.96	0.04	99.6	0.00	0.00	
10M-1, 13–14	80.03	CARB	12.05	12.00	0.05	100.0	0.00	0.00	
11M-CC, 8–9	89.28	CARB	11.98	11.97	0.01	99.7	0.00	0.00	
12M-1, 7–10	98.57	IWSC	11.95	11.87	0.08	98.9	0.00	0.00	

^aSample type: CARB = carbonate; IWSC = interstitial-water squeeze cake.

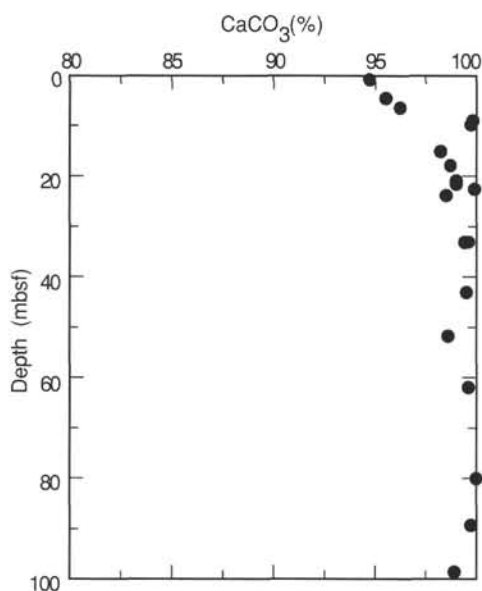


Figure 37. Depth distribution of calcium carbonate in Hole 866B.

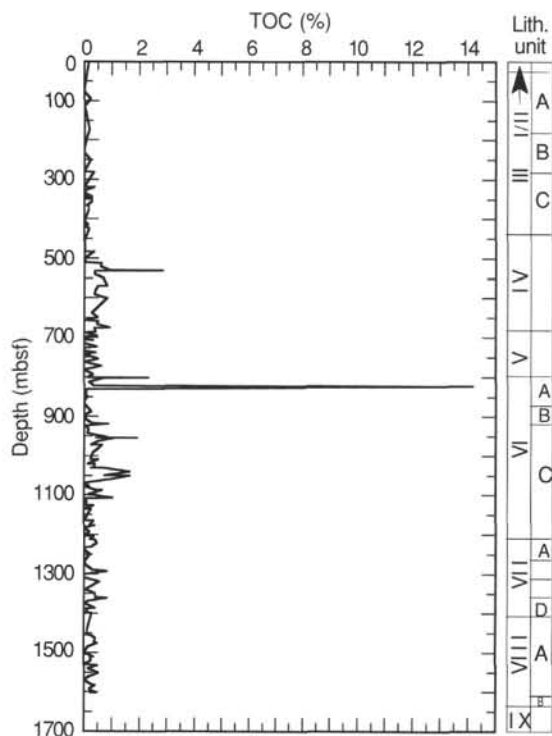


Figure 38. Depth distribution of total organic carbon concentrations in Hole 866A.

with a grayish-green (10G 8/1) clay mineral (smectite?) that protruded from vesicles and warped as it dried out, but also with calcite and, to a lesser extent, zeolites.

Interbasaltic Horizons and Their Origin

Recovery from these rubbly or clayey intervals was probably somewhat limited as much of the material may have washed out during drilling. In some places, the interval was represented in the core mainly by basalt fragments, the only material to have survived

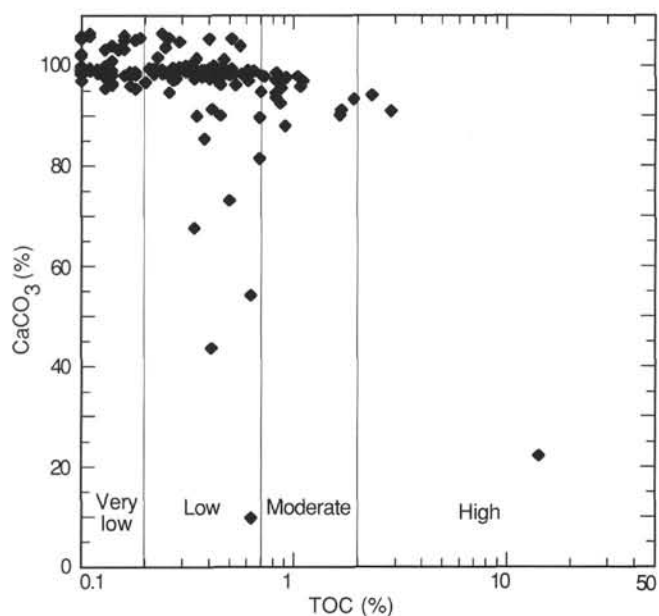


Figure 39. Concentrations of total organic carbon vs. calcium carbonate content of sediments from Hole 866A.

(e.g., Unit 7 and top portion of Unit 11). But in most places, recovery extends to a mixture of lumps of clay enclosing very highly to completely altered basalt clasts and fragments of highly altered basalt (e.g., intervals between Units 8, 10, 11, and 12; Fig. 44). All but one of these intervals are less than 1 m (range 29 to 82 cm) thick, and their average thickness is 52 cm, which should be regarded as a minimum. Unit 7, which comprises 9 m of volcanic breccia and clay, in many respects resembles the other interbasaltic intervals, but because of its exceptional thickness, it has been designated a lithologic unit. As a group the interbasaltic horizons share the following characteristics:

1. They range from clast to matrix-supported breccias in which the clasts are generally subangular to subrounded fragments of vesicular and amygdaloidal basalt that are highly to completely altered and appear to be similar to the associated flows.
2. The matrix of the breccia consists of red (2.5YR 4/6), weak red (10R 5/4) to dark reddish brown (5YR 3/3) sandy clay or soil.
3. In some places, red clay forms distinct horizons within the breccia (e.g., at Interval 143-866A-180R-5, 54–57 cm) and at others (e.g., Interval 143-866A-184R-2, 16–26 cm) it fills interstices between the lava fragments (Fig. 47).
4. Fractures in the volcanic breccia are commonly filled with clay minerals, calcite, and zeolites, but in some places are open.

The interbasaltic intervals are likely to be the product of a range of processes operating on the volcanic land surface. Each represents an interval, perhaps an appreciable period of time (decades to centuries?) between one set of lava flows and the next. This does not, of course, imply a period of dormancy of that duration, but only that a longish interval elapsed before one particular set of flows was covered by another. In contrast, each individual lava flow represents a comparatively short period of time (days or weeks?). The interbasaltic horizons represent a period of exposure and weathering. Soils may have developed on the flows, have formed what are now the red clays (smectite and hematite), and any organic material may have been lost: such surfaces are sometimes referred to as boles. On the other hand, organic material may never have been present and the weathering may simply have produced a lateritic surface. The presence of kaolinite in the horizon is consistent with this suggestion (see "Lithostratigraphy" section, this chapter). In either case the matrix-supported breccia most

Table 8. Results of Geofina hydrocarbon meter analyses and concentrations of carbonate, total organic carbon, and nitrogen for selected samples from Hole 866A.

Core, section, interval (cm)	Depth (mbsf)	Sample type ^a	Lithology	CaCO ₃ (%)	TOC (%)	T _{max} ^b GHM ^b (°C)	RE ^c (°C)	S ₁ (mgHC/g)	S ₂ (mgHC/g)	HI	N (%)	TOC/N
55R-CC, 2-3	501.92	CARB	Gray packstone	90.0	0.35	385	325	0.03	0.09	25	0.01	35.0
58R-1, 109-111	532.09	XRD	Brown to gray laminated packstone	91.0	2.86	479	419	0.84	15.14	529	0.00	
60R-1, 64-65	550.94	XRD	Dark laminated packstone	85.5	0.38	482	422	0.00	0.15	40	0.04	9.5
62R-2, 38-39	571.48	CARB	Dark gray-green clayey limestone	81.5	0.69	494	434	0.01	0.93	134	0.03	23.0
72R-1, 59-60	666.79	XRD	Glauconitic mudstone	73.1	0.50	460	400	0.00	0.10	20	0.03	16.0
73R-1, 28-29	676.79	CARB	Gray-green pyritic wackestone	88.0	0.91	495	435	0.08	2.25	247	0.02	45.0
74R-2, 71-72	687.49	CARB	Blackened oolitic grainstone	91.4	0.42			0.00	0.02	5	0.01	42.0
75R-1, 71-72	695.81	CARB	Oolitic grainst. with organic matter	97.6	0.45			0.00	0.01	22	0.00	
86R-2, 19-20	803.19	CARB	Dark gray claystones	94.2	2.32	491	431	0.38	13.23	570	0.02	29.0
89R-1, 97-98	831.57	CARB	Dark gray claystones	22.2	14.19	479	419	0.05	23.06	162	0.30	47.3
91R-1, 10-11	849.60	CARB	Green-black claystones	36.8	0.07						0.03	2.0
102R-2, 14-15	954.34	CARB	Dark algal mats	93.4	1.91	456	396	0.14	4.39	229	0.07	27.3
103R-1, 48-49	962.88	CARB	Light brown packstone	97.1	1.10	494	434	0.03	3.34	304	0.03	36.6
111R-1, 77-78	1040.07	CARB	Dark laminated claystones	54.2	0.63	490	430	0.08	0.98	154	0.03	21.0
112R-1, 94-96	1049.84	CARB	Red-greenish algal mats	91.2	1.67	495	435	0.08	8.39	502	0.02	83.0
112R-1, 102-104	1049.92	CARB	Algal mats with black laminae	97.9	0.73	500	440	0.08	3.54	484	0.02	36.0
113R-CC, 36-37	1058.86	CARB	Black laminated packstone	90.2	1.64	488	428	0.26	8.37	510	0.08	20.5
115R-1, 77-78	1078.67	CARB	Mudstone with gray-brown laminae	95.4	0.19						0.00	
117R-2, 50-51	1099.10	CARB	Gray to black claystones	9.8	0.63	480	420	0.29	0.63	100	0.01	63.0
121R-1, 31-34	1136.00	CARB	Gray dolomitic mudstone	102.0	0.00						0.00	
126R-1, 1-2	1184.01	CARB	Wackestone with blackened peloids	97.8	0.37	497	437	0.00	0.33	87	0.03	12.0
129R-1, 50-51	1213.40	CARB	Claystones	67.6	0.34	488	428	0.02	0.32	95	0.00	
144R-2, 149-150	1360.49	CARB	Gray-greenish clayey limestone	43.7	0.41	452	392	0.04	0.36	87	0.05	8.2

^aSample type: CARB = carbonate; XRD = X-ray diffractometry.

^bGHM = Geofina hydrocarbon meter provides T_{max} values 60°C higher than Rock-Eval values.

^cRE = Rock-Eval.

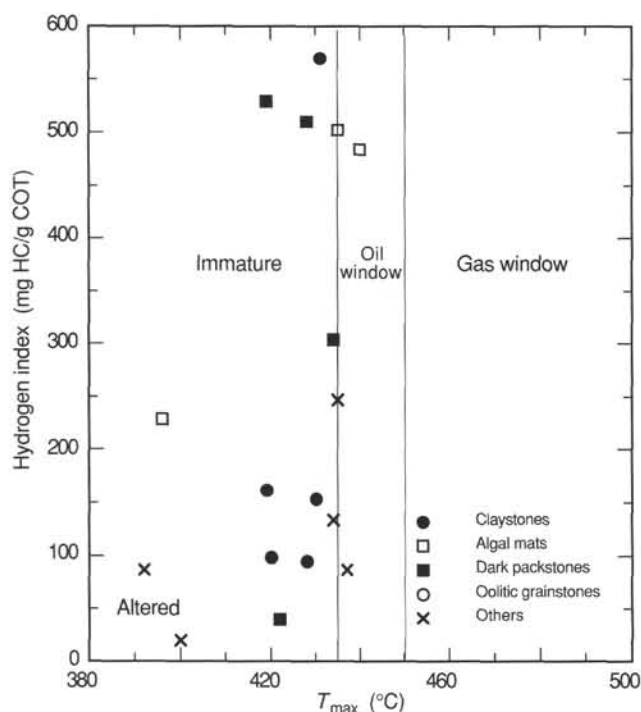


Figure 40. Hydrogen index vs. T_{max} diagram for selected samples from Hole 866A, distinguished by their sedimentological classification.

probably represents surficial and oxidized weathering products containing basalt clasts. In other intervals, the weathered products seem to have washed down beneath the lava surface to form a matrix. Because the lava surface itself seems to have been rubbly at the time of matrix emplacement, the clast-supported breccias probably developed in situ.

The 9-m breccia constituting Unit 7 is too thick to have formed in either of the ways described above. It is significant that the breccias

in this unit are matrix-supported, indicating that they have undergone redeposition and are not residual or in-situ deposits. They may have accumulated in a depression fed intermittently by screes, mud flows, or debris slides, but show no evidence of reworking by water. The texture rules out an origin as either the rubbly surface of an aa flow or as a coarse-grained pyroclast-fall deposit.

The highly porous and heavily fractured nature of the Unit 7 breccia has provided ready access for hydrothermal fluids. Veins are commonly filled with calcite, clay minerals, and zeolites, but particularly notable are the more open fractures and cavities in Section 143-866A-181R-2. These contain large (<6 mm), clear, colorless crystals (n = 1.488, weak birefringence, hardness 5.5), which proved from XRD analysis (Sample 143-866A-181R-2, 64-66 cm) to be analcime (Fig. 48).

Petrography

As the lavas are moderately to very highly altered, inferences about their primary mineralogy may not be entirely reliable. Of the ferromagnesian phenocrysts, olivine is completely pseudomorphed by clay minerals and iron oxides, and pyroxene is rarely preserved. Plagioclase is generally clearly identifiable, although generally partially altered to clays and albitized. The main petrographic distinctions are based on the relative proportions of phenocryst phases and, in particular, the appearance of plagioclase phenocrysts or megacrysts in the central part of the succession (Units 6-10). These units are defined as flow units, separated on the basis of the intervening lateritic or rubbly intervals that were recovered and do not necessarily correspond to significant petrographic changes. Descriptions of samples representative of the main petrographic types are given below.

1. *Unit 1.* Highly pyritized and calcified basalt at contact with oolitic grainstone (Sample 143-866A-171R-2, Piece 1, 17-19 cm). This is a fine-grained to microcrystalline feldspathic basalt having a lobate but near-vertical contact with the oolitic limestone. There is a slight suggestion of possible olivine and pyroxene phenocrysts, but if these are present, they have been completely altered to calcite and pyrite. The lava is composed largely of plagioclase and opaque oxide

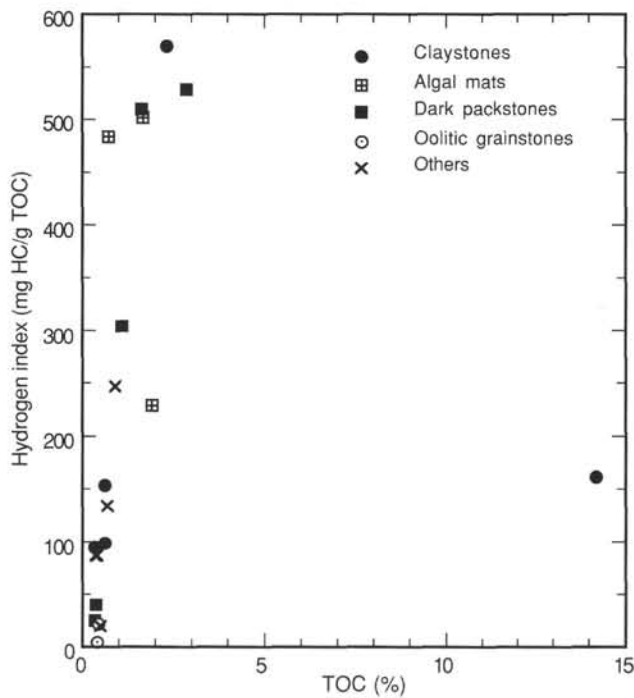


Figure 41. Organic-richness (% TOC) vs. hydrogen index of selected samples from Hole 866A, distinguished by their sedimentological classification.

minerals together with abundant secondary minerals. Plagioclase (55%; <0.5 mm) forms cloudy subhedral laths, and its composition is now about An_{20} . The opaque oxide minerals (2%; <0.2 mm) are in the form of subhedral to anhedral grains. Dominant among the secondary minerals is pyrite (20%), which replaces possible ferromagnesian minerals, forms a large cluster of grains (<1 cm in diameter) and is also finely disseminated throughout the rock. It is closely followed in abundance by calcite (16%), which is dispersed in irregular patches and may also be replacing ferromagnesian minerals. Green and brownish clay minerals, probably smectite, (10%) and chlorite (<2%) make up the rest of the rock. Grain size decreases toward the contact with the limestone, which is indicative of chilling. However, the interpretation is equivocal, as explained earlier.

2. *Unit 4.* Phyrlic olivine-plagioclase-clinopyroxene basalt (Sample 143-866A-177B-1, 22–23 cm). This small sample, which had jammed in the bit, proved to be the freshest specimen recovered from Hole 866A. It is a moderately phyrlic olivine-plagioclase-clinopyroxene basalt in which the olivine (originally 5%; 0.3–2.3 mm) forms subhedral crystals, completely pseudomorphed by clay minerals. Plagioclase (4%; 0.25–7.0 mm) occurs as subhedral laths zoned within the range of An_{60} to An_{44} . The larger plagioclase crystals, probably best regarded as megacrysts, have embayed or resorbed boundaries and are peppered with inclusions (clay minerals, originally glass?). Clinopyroxene (1%; 0.25–2.0 mm) forms subhedral to anhedral phenocrysts that are only slightly altered, and scattered microphenocrysts of opaque oxide minerals also are seen (trace amount; 0.1–0.5 mm). The groundmass has an intergranular texture and consists of plagioclase laths, together with small (<0.2 mm) grains of pyroxene, opaque oxide minerals, pseudomorphed olivines, and very small (<0.1 mm) dark brown spinels as inclusions in olivine. A tendency also exists for subparallel alignment of plagioclase laths, giving the groundmass a directive texture.

3. *Unit 6.* Phyrlic plagioclase-olivine-pyroxene basalt (Sample 143-866A-179R-3, Piece 1c, 46–48 cm). This highly phyrlic plagioclase-olivine-clinopyroxene basalt is also highly altered and amygdaloidal. The phenocryst assemblage is dominated by plagioclase

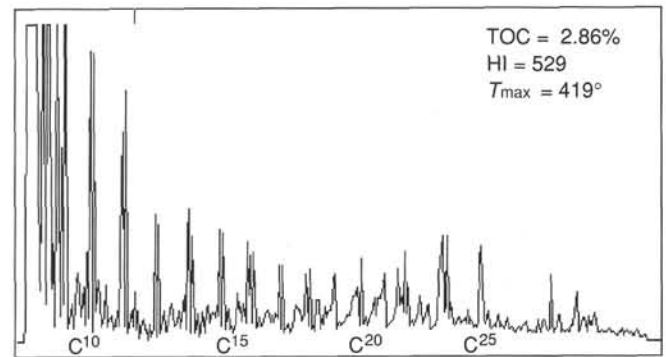


Figure 42. Pyrolysis-gas chromatogram of Sample 143-866A-58R-1, 109–111 cm, from Hole 866A.

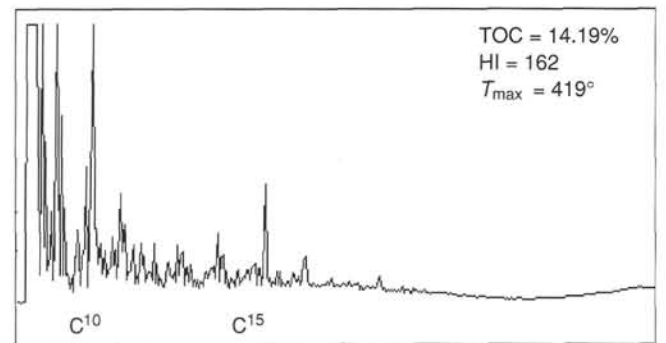


Figure 43. Pyrolysis-gas chromatogram of Sample 143-866A-89R-1, 97–98 cm, from Hole 866A.

(20%; 0.5–10 mm) having a rather sodic composition that could not be determined more precisely because of alteration. There may be two generations of plagioclase phenocrysts. The first type consists of megacrysts or xenocrysts (>5 mm) that have resorbed margins and inclusions (now clay, originally glass?). These megacrysts are distinct from the second type of plagioclase phenocrysts (0.5–5.0 mm), which are inclusion-free and appear to be more or less in textural equilibrium with the groundmass. The subhedral olivine phenocrysts (3%; 0.3–1.6 mm) have been completely pseudomorphed by clay minerals, as also have the pyroxenes (1%; 0.3–0.8 mm). The only other phenocryst phase is a euhedral to anhedral opaque oxide mineral (<1%; 0.1–0.8 mm). The intergranular groundmass, which also has a directive texture, is composed of plagioclase laths (An_{28} – An_{18}), associated with grains of pyroxene and opaque oxide minerals. Alteration products are largely (40% of whole-rock) brown and green clays (smectite?) with traces of zeolites, chlorite, and Fe-oxyhydroxide minerals.

4. *Unit 11.* Microphyric olivine basalt (Sample 143-866A-187R-1, 86–88 cm). This is a sparsely microphyric olivine basalt in which the small subhedral olivine microphenocrysts (3%; 0.25–0.8 mm) have been completely pseudomorphed by reddish brown clay (smectite?). Also occurring as scattered microphenocrysts are subhedral clinopyroxenes (<1%; 0.25–0.6 mm) and opaque oxide minerals (<1%; 0.1–0.25 mm). The intergranular groundmass consists of subhedral plagioclase laths, together with anhedral grains of pyroxene, opaque oxide minerals, and olivine, which also encloses very small (<0.1 mm) spinels. Secondary minerals are mainly brownish clay (smectite?) with traces of zeolites, chlorite, and Fe-oxyhydroxides. Vesicles (1%; 0.2–2.0 mm) are randomly distributed, irregular in shape, and filled with clay minerals and zeolites.

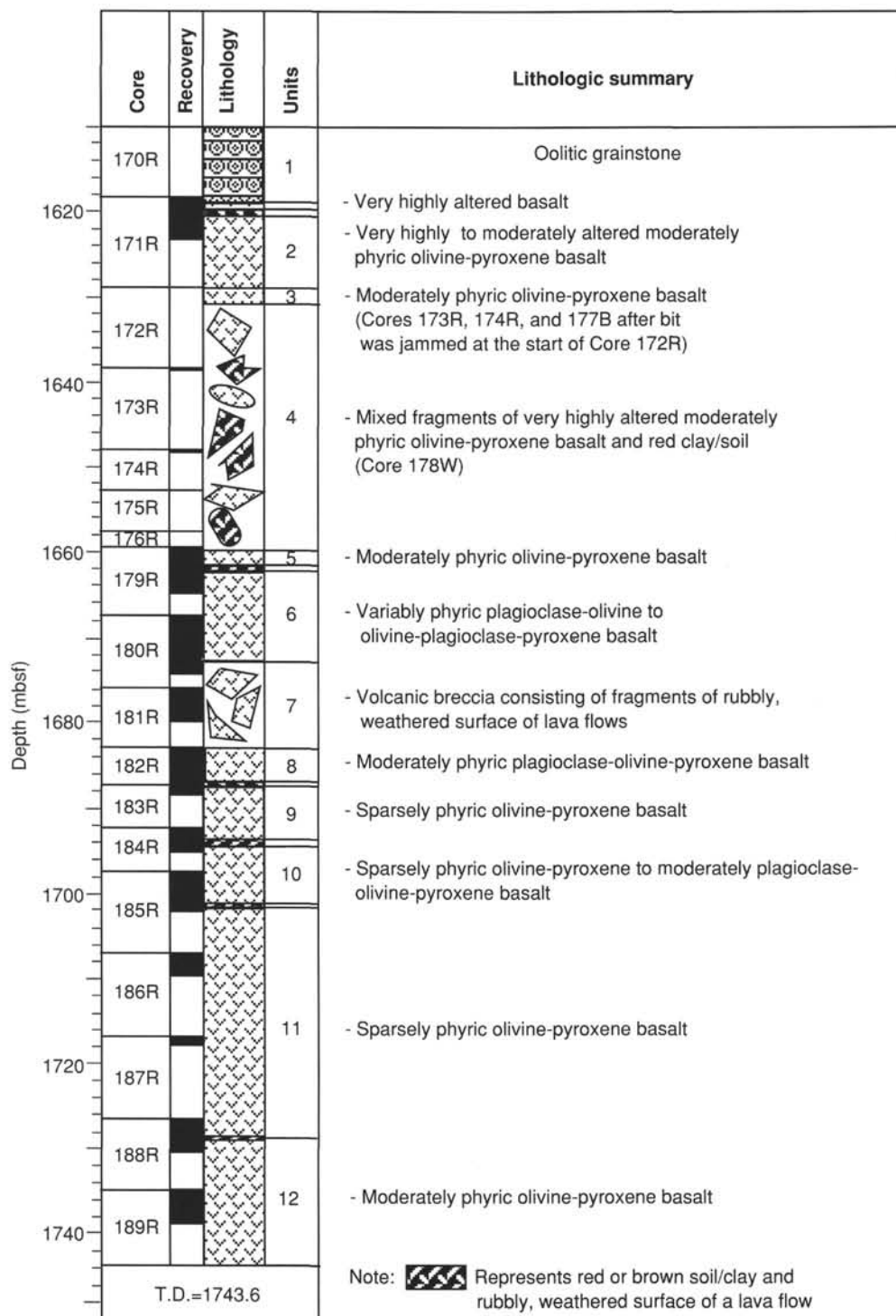


Figure 44. Lithologic summary of igneous rocks from Hole 866A.

Geochemistry

Seven samples of volcanic rocks from Site 866 were analyzed by X-ray fluorescence for abundances of major and trace elements. Analytical procedures are given in the "Explanatory Notes" section (this volume). The results are presented in Table 9.

As with the igneous rocks from Site 865, those from Site 866 also have been moderately to very highly altered. Some of the geochemical

consequences of alteration discussed above (see "Igneous Petrology" section, "Site 865" chapter, this volume) are equally applicable here.

SiO₂ shows a tendency to increase with depth from 47.3 to 49.1 wt% and the same applies to MgO, which varies from 6.5 to 12.6 wt%. K₂O increases sympathetically with SiO₂ from 0.4 to 3.7 wt%. There is significant systematic co-variation between pairs of less mobile trace elements, such as Nb and Zr and Y and Zr. In contrast, there is a general absence of correlation between the more

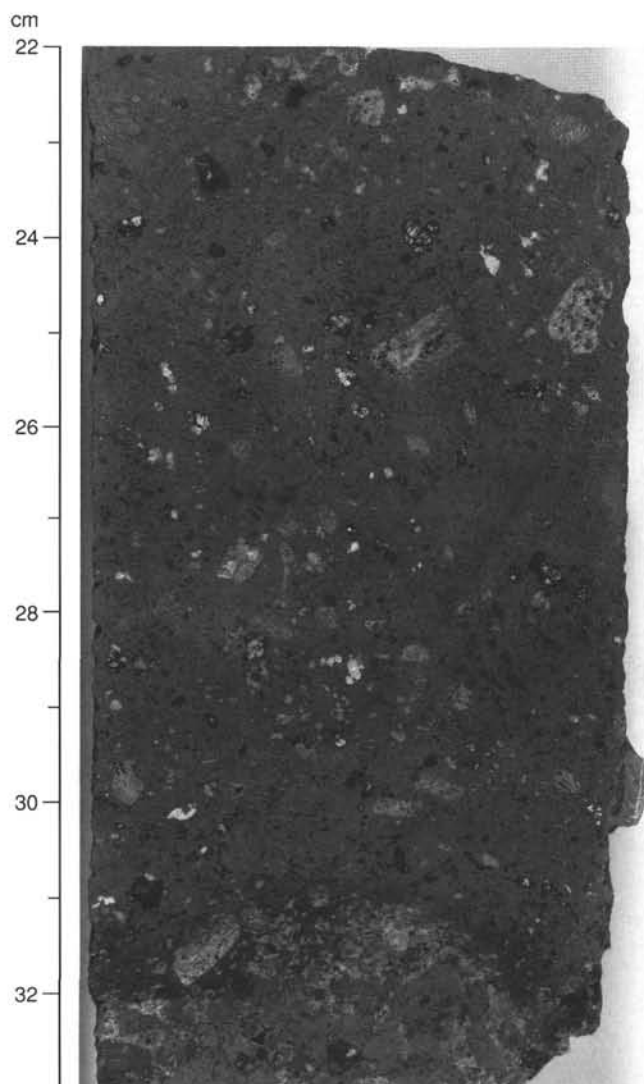


Figure 45. Typical phyrlic plagioclase-olivine-pyroxene basalt (Interval 143-866A-181R-2, 22–33 cm, Piece 2c).

mobile elements, such as K, Rb, and Ba, apart from the fact that all three attain their maximum abundances in Sample 143-866A-189R-3, 115–117 cm. This poor correlation is most probably the result of the geochemical consequences of alteration discussed above. Thus, as with the altered igneous rocks from Site 865, little significance can be attached to concentrations of mobile elements in Site 866 basalts. There is a large variation in CaO (2.5 to 10.5 wt%), much of which is probably also attributable to alteration. Al_2O_3 ranges from 12.6 to 17.5 wt% and total iron (as Fe_2O_3) is generally high (11.1–14.5 wt%). TiO_2 , one of the least mobile of the elements, remains remarkably constant (2.6–2.7 wt%). Although the abundances of Na_2O and K_2O must be suspect, values have been plotted on a total alkalis vs. silica diagram (Fig. 49), which suggests that they are similar to the Site 865 rocks and may be classified as transitional to mildly alkalic.

Two distinct groups appear to exist within this small selection of basalts from Site 866. These are depth-related, with the separation being between 1671.4 and 1678.6 mbsf. This coincides with the 9-m volcanic breccia constituting Unit 7 (Fig. 44), and it is likely that this deposit reflects a significant break in activity. Compared with samples from below this level, the upper lavas are characterized by higher

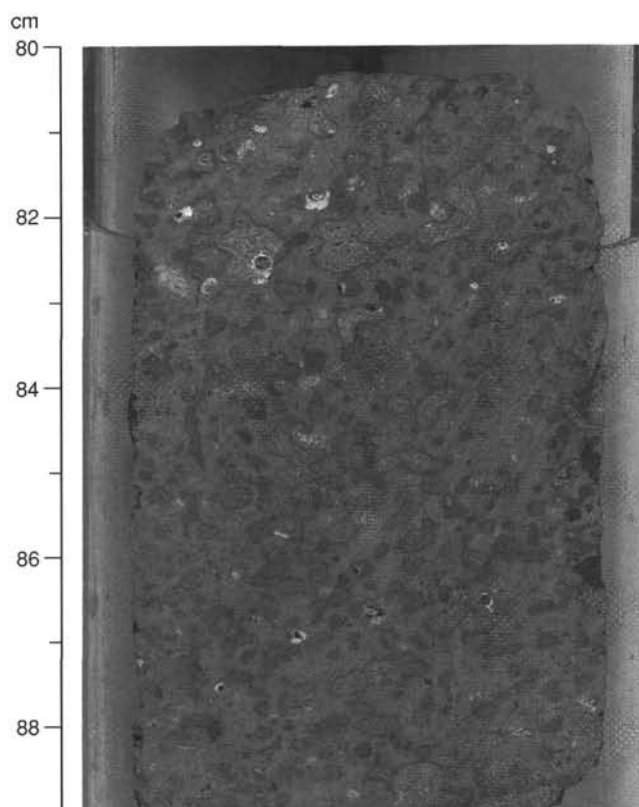


Figure 46. Highly amygdaloidal basalt (Interval 143-866A-184R-2, 80–89 cm, Piece 11).

contents of CaO, Sr, and V and lower abundances of MgO, K_2O , P_2O_5 , Nb, Zr, Rb, and Ce: these also exhibit decidedly lower losses on ignition. The differences between the two groups of lavas are apparent in Figure 50, a MORB-normalized trace-element plot. In this diagram, the scatter of the large ion lithophile elements (LILE) is almost certainly due to alteration, but the regularity of the trends for the less-mobile, high-field-strength elements (HFSE), from Nb to Y, is more meaningful. This suggests that the upper lavas are generally less enriched and less alkalic in character than the lower lavas. The contrast with the lavas from Site 865 is even more marked. The latter show greater enrichment in incompatible elements and a generally stronger alkalic or intraplate signature (e.g., Pearce, 1983). On the other hand, basalts from Site 866, especially those belonging to the upper group, show similarities with tholeiites from Hawaii and Easter Island (Fig. 51). The lavas forming the basement of Resolution Guyot likely were generated by relatively high degrees of partial melting from a source that was perhaps already somewhat depleted in incompatible trace elements.

Conclusions

1. The occurrence of dispersed volcanogenic grains in the carbonate sediments from Cores 143-866A-166R to -170R (1569–1619 mbsf) suggests that a vestigial volcanic source persisted above sea level at this time. On the other hand, the trace amounts (<1%) of these components argues against any significant subaerial exposure. The substantial volcanic edifice undoubtedly generated a large volume of volcanoclastic sediments not represented in the subsequent back-reef, lagoon, or carbonate platform environments. These sediments presumably are to be found in basinal deposits beyond the outer slopes of the reef or platform.



Figure 47. Volcanic breccia from Unit 7 showing basaltic lava fragments in a red matrix of smectite and hematite (Interval 143-866A-184R-2, 16–26 cm, Piece 3).

2. The contact between the carbonate sediments and the underlying volcanic succession does not provide unambiguous evidence of the nature of this boundary. The material recovered might be interpreted as pointing to either a basal conglomerate or to an intrusive relationship, with a small sill being emplaced along the junction between the sediment and extrusive rocks.

3. The drilled part of the volcanic basement consists of a succession of subaerial lava flows, averaging about 10 m in thickness and separated by interbasaltic intervals that generally are about 0.5 m thick. No pyroclastic deposits were encountered. The thickness of the lavas and their rubbly surfaces suggest that they were of aa type.

4. The lavas are mainly phyrlic olivine-pyroxene basalts that have been moderately to very highly altered. A group of phyrlic plagioclase-olivine-pyroxene basalts occurs in the middle part of the drilled section: it includes partially resorbed megacrysts or xenocrysts of plagioclase. Nonetheless, the preponderance of phyrlic olivine-pyroxene types suggests an alkalic affinity.

5. The reddened interbasaltic intervals are thought to represent periods of exposure to tropical or subtropical weathering. The layers may represent soil, laterite, in-situ weathering of the rubbly tops of lava flows or, in one instance, redeposited rubble.

6. The basalts from Hole 866A may be separated into two groups at the level of the thick interbasaltic interval constituting Unit 7: the upper group is less enriched in incompatible elements. The Resolution Guyot lavas appear to have intraplate tholeiitic or mildly alkalic characteristics and to lack the strongly defined alkalic signature of the Allison Guyot sills.



Figure 48. Analcime crystals in open fracture cutting volcanic breccia in Unit 7 (Interval 143-866A-181R-2, 47–92 cm, Pieces 6, 8, 12, and 13).

PHYSICAL PROPERTIES

Introduction

The objectives of the physical-property (PP) measurement program at Site 866 were essentially identical to those at Site 865, but were limited to lithified carbonate sediment and basalt: (1) to measure index properties and to measure *P*-wave velocities in lithified sediments (carbonate platform succession) and basalts and (2) to identify PP units for correlation among holes and downhole logs at Leg 143 sites. This last objective includes the detailed comparison of the downhole logs (sonic velocity, gamma ray, and density) with measurements of *P*-wave velocity and bulk density of discrete samples to estimate to what extent the recovered sediments represent the sedimentary strata present in the boreholes.

Two holes, tens of meters apart, were drilled at Site 866 (Holes 866A and 866B). Hole 866A was drilled to a depth of 1743.6 mbsf; Hole 866B reached a depth of 117.4 mbsf. Sediments recovered at Site 866 consist of pelagic ooze (0–0.9 mbsf in Hole 866A and

0–23.5 mbsf in Hole 866B), a thick section of shallow-water carbonate platform sediment (0.9–1620.0 mbsf) and basalt (1620.0–1743.6 mbsf). The platform limestones include wackestone, mudstone, packstone, and grainstone to rudstone. The fabric of the rock varies from tight and dense to porous and open. Predominant grain-types are fragments of green algae, gastropods, oolites, and oncolites. Some intervals are characterized by clay-rich layers and/or strong dolomitization. The upper part of the core has numerous calcretes (0.9–434.4 mbsf). Below 434.4 mbsf, the limestone contains more clay than higher strata, and on a gross scale, shows interbedding among laminated packstone and wackestone, coarse sucrosic dolomite, and oolitic to oncolitic grainstone and rudstone.

Only index properties were measured in the recovered pelagic ooze. In the lithified platform sediments, cored with the rotary core barrel (RCB), *P*-wave velocity was measured in both longitudinal and transverse directions in cubes (1-in. diameter and vertical axis), as well as in minicores cut from adjacent samples (1-in. diameter). Anisotropy was calculated for each pair of horizontal and vertical velocity measurements. In addition, index properties, bulk density, water content (% dry weight), porosity, and grain density were measured in each cube. No corrections were made for salt, as the shipboard measurement of weight and volume is several orders of magnitude less accurate than the actual salt-correction. As for the determination of grain density, a comparison was made between that calculated from the dry weight (after oven-drying for 24 hr at 110°C) and volume measured by the pycnometer, and that calculated from a crushed subsample. Figure 52 demonstrates the inaccuracy in the second approach. Therefore, we decided to use the first method as a standard approach for measuring index properties of lithified carbonate sediment. A total of 128 cubes

and 83 minicores were analyzed for both *P*-wave velocity and index properties. No measurements for thermal conductivity were performed.

Correlation among laboratory measurements of *P*-wave velocity and index properties in general is excellent, in part because of relatively good recovery (on average, 15.2%).

Physical Property Units

Five major PP units were defined for Site 866, based on significant downhole trends in index properties and *P*-wave values (Tables 10 to 12; Figs. 53 to 58). The upper boundaries of most of these units are associated with lithologic features. These features did not serve as definition criteria for the PP units. Depending on recovery, most boundaries for PP units have been arbitrarily placed midway between discrete samples (see Fig. 57, recovery log). In the following section, unless otherwise mentioned, data presented for sonic velocity are those measured in the vertical direction in cubes. Similarly, information about index properties concerns those data measured from cubes. *P*-wave velocity and index properties measured in discrete samples may only partially reflect in-situ properties; in general, these are higher end members, because partial recovery limits the degree to which the data set is representative.

Physical Property Unit 1 (Hole 866A: 0–0.9 mbsf; Hole 866B: 0–23.5 mbsf)

The pelagic sediment overlying the platform top, though only two samples were measured for index properties in Hole 866A, is PP Unit 1. Bulk density, from both holes, ranges from 1.57 to 1.77 g/cm³,

Table 9. Analyses of major and trace elements in Hole 866A basalts.

Site-hole: 143-866A								
Core-section:	177B-1	179R-5	180R-3	181R-2	184R-2	188R-1	189R-3	BHVO
Interval (cm):	26–28	60–62	144–146	29–23	105–106	40–42	115–117	
Depth (mbsf):	1629.30	1664.50	1671.40	1677.60	1694.80	1726.70	1739.0	
Major elements (wt%)								
SiO ₂	46.89	47.32	46.91	48.61	48.84	47.89	49.06	49.94
TiO ₂	2.73	2.63	2.60	2.58	2.71	2.62	2.57	2.75
Al ₂ O ₃	14.91	17.42	16.80	16.29	14.96	17.46	12.61	13.62
Fe ₂ O ₃	12.87	11.09	12.15	11.97	12.59	11.70	14.51	12.21
MnO	0.21	0.23	0.17	0.25	0.17	0.18	0.09	0.17
MgO	8.66	6.51	7.62	10.90	11.10	9.35	12.59	7.09
CaO	10.51	10.29	10.25	3.49	4.27	6.60	2.55	11.41
Na ₂ O	2.45	2.79	2.74	2.26	3.23	2.89	2.25	2.95
K ₂ O	0.46	0.40	0.40	3.06	1.33	1.25	3.71	0.59
P ₂ O ₅	0.26	0.22	0.22	0.36	0.35	0.30	0.31	0.28
Total	99.93	98.88	99.84	99.74	99.53	100.21	100.21	101.0
LOI	2.230	2.190	2.018	6.720	4.240	4.186	4.958	
Trace elements (ppm):								
Ba	96	87	95	89	80	96	127	126
Ce	26	24	25	54	49	48	55	33
Cr	454	208	210	353	184	426	203	291
Cu	82.8	61.0	77.6	82.6	35.2	79.2	84.2	135.5
Nb	20.3	16.4	16.0	34.4	31.2	32.1	39.1	18.2
Ni	239	141	137	218	146	173	169	122
Rb	6.5	4.0	5.0	19.8	11.0	4.8	14.4	9.1
Sr	480	490	466	214	305	406	212	397
V	272	269	265	252	232	233	204	312
Y	25.7	23.3	23.0	25.7	26.0	27.1	18.9	25.6
Zn	89.6	73.0	73.3	147.1	92.4	95.6	81.5	108.2
Zr	160	141	138	187	196	230	203	173

Note: The major-element data for each sample represent an average of two analyses; that for BHVO is an average of four. The trace-element data for BHVO are an average of three analyses. LOI (loss on ignition) was determined gravimetrically. Total Fe is expressed as Fe₂O₃, where Fe₂O₃/FeO is set at 0.15.

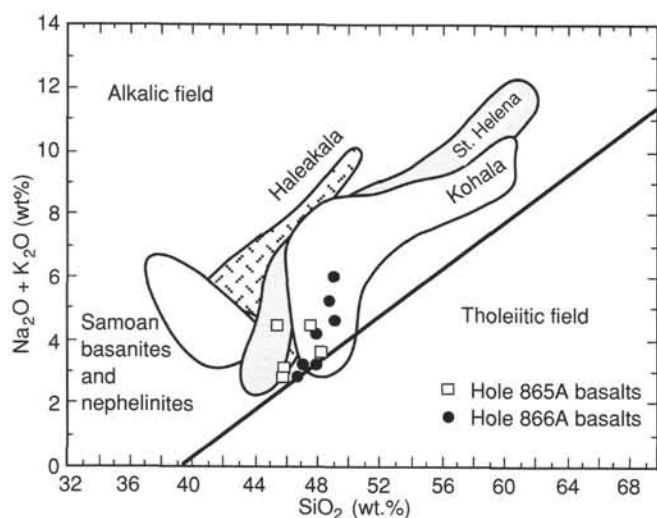


Figure 49. Plot of total alkalis ($\text{Na}_2\text{O} + \text{K}_2\text{O}$) vs. silica for basalts from Hole 866A, compared with those from Hole 865A. Alkalic rocks from Hawaii (Kohala and Haleakala), St. Helena, and Samoa are shown for comparison.

and porosity (both holes) from 56.7% to 76.6%. The lower boundary has been arbitrarily placed at 0.9 mbsf, as Hole 866A is the deepest hole containing all the PP units.

Physical Property Unit 2 (Hole 866A: 0.9–430 mbsf; Hole 866B: 23.5–117.4 mbsf)

The top of this unit is the sharp contact between lithified platform sediment and overlying pelagic sediment. Unfortunately, this contact was not recovered and, overall, recovery in this PP unit was low (less than 2%). The lower boundary is abrupt and correlates with the boundary between dense white-beige mudstone and wackestone from lithologic Subunit IIIC and the underlying clayey packstone and wackestone from lithologic Unit IV. Values for physical properties in this unit are from both Holes 866A and 866B. *P*-wave velocities in this dense and predominantly muddy, bioclastic packstone to mudstone range from 3.81 to 6.42 km/s. Bulk density ranges from 2.35 to 2.69 g/cm³, porosity ranges from 0.45% to 25.78%, and water content from 0.17% to 12.30% (dry weight). Mean anisotropy of sonic velocity is 1.37% and fairly constant.

High sonic velocities between about 280 and 430 mbsf may be associated with the dense mudstone of lithologic Subunit IIC, but poor data coverage does not permit further subdivision into subunits.

Physical Property Unit 3 (430–1199 mbsf)

This unit correlates with a thick succession of clayey packstone and wackestone, with local algal lamination and dolomitic at the base, including an interval of coarse-sand sized oolitic grainstone (lithologic Units IV, V, and VI). This unit shows a characteristic, sinuous trend in sonic velocity with a gradual downward increase in range toward the base (see Figs. 53 and 54). The unit has been further subdivided into three subunits.

Physical Property Subunit 3a (430–535 mbsf)

Mass-index properties in this subunit show well-defined and gradual trends. Sonic velocity and bulk density decrease sharply downcore, whereas water content and porosity increase. On average, sonic velocity ranges from 2.55 to 3.83 km/s, bulk density ranges from 2.14 to 2.36 g/cm³, porosity from 20.51% to 33.51%, grain density varies from 2.71 to 2.72 g/cm³, and anisotropy from -16.484% to

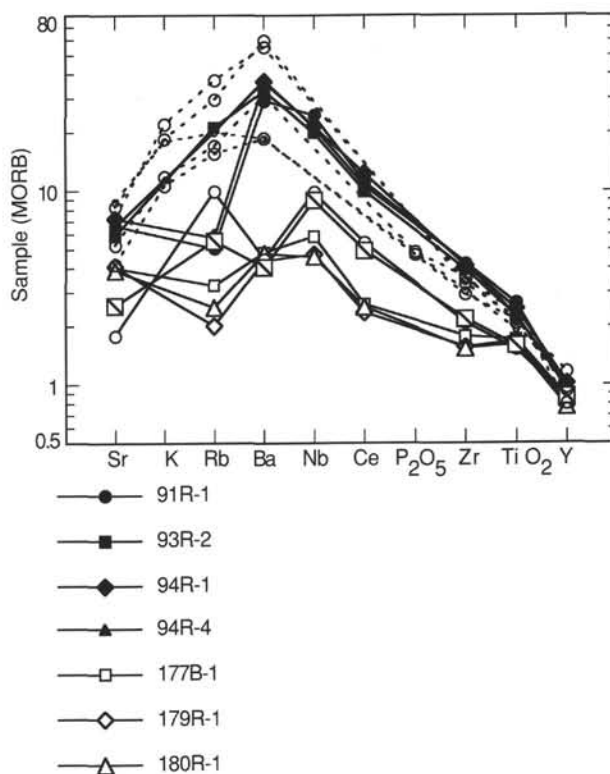


Figure 50. MORB-normalized incompatible element patterns for basalts from Hole 866A, compared with those for basalts from Hole 865A and dredged samples from Allison Guyot (Natland et al., 1992). MORB-normalizing values are from Pearce (1983).

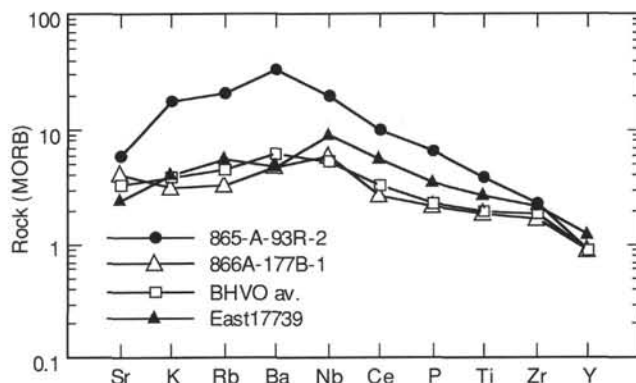


Figure 51. MORB-normalized incompatible element patterns for basalts from Holes 866A (Section 143-866A-177B-1) and 865A (Section 143-865A-93R-2), compared with tholeiites from Hawaii (BHVO-1) and Easter Island (East 17739; Baker et al., 1974, and unpubl. data).

7.333%. All physical properties have narrow and well-defined ranges. The upper boundary was placed at the abrupt and dramatic decrease in sonic velocity and density (430 mbsf) and corresponds to the change from the dense wackestone and packstone of lithologic Subunit IIIC to the clayey and organic-rich packstone and wackestone of Unit IV. The lower boundary of PP Subunit 3a shows the onset of a reversed (i.e., increasing sonic velocity and bulk density) downcore trend of physical properties, and is not reflected by a visible change in the lithologic succession.

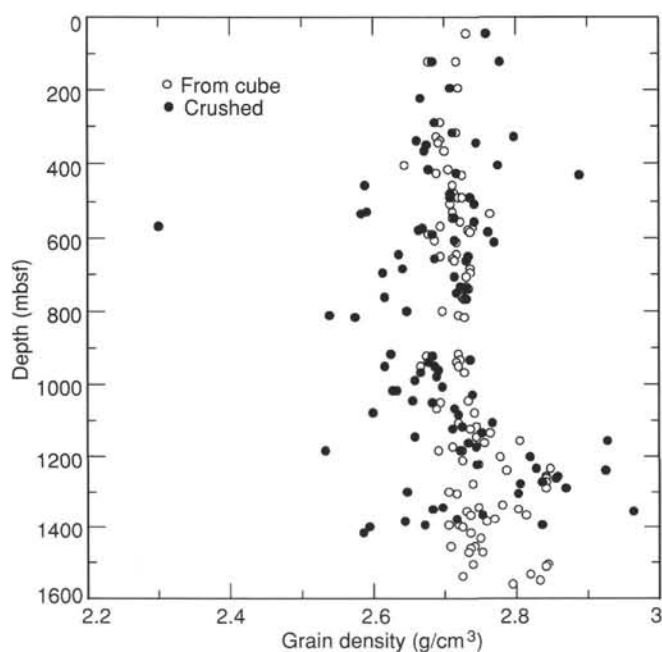


Figure 52. Plot of depth vs. grain density, calculated using two different methods: (1) by crushing subsamples and (2) by oven-drying entire cubes (see text for discussion).

Physical Property Subunit 3b (535–703 mbsf)

Physical properties in Subunit 3b show a gradual downcore increase in sonic velocity and bulk density, respectively, from about 2.0 to 3.5 km/s and from about 2.1 to 2.3 g/cm³. The distribution of the data is still confined to a relatively narrow band. On average, sonic velocity ranges from 1.95 to 3.46 km/s, bulk density ranges from 2.15 to 2.39 g/cm³, porosity from 18.1% to 33.7%, and grain density from 2.68 to 2.76 g/cm³. The upper and lower boundaries of this subunit have no visible correlation with the lithology. The upper boundary may correlate with the relative downcore increase in visible clay content. The lower boundary has been placed at approximately 703 mbsf. At this depth, sonic velocity and bulk density reach maximum values and are relatively constant, downcore, in PP Subunit 3c.

Physical Property Subunit 3c (703–1199 mbsf)

This nearly 500-m-thick interval has an average recovery of 5% to 25%. Physical properties remain relatively constant (i.e., show no general increase or decrease downcore) throughout the upper 400 m, but have more variation than in Subunits 3a and 3b. Sonic velocity in the upper part ranges from about 2 to 4 km/s, bulk density from 2.2 to 2.4 g/cm³, and porosity from about 15% to 20%. In the lower interval, about 1100 to 1200 mbsf, sonic velocity increases downcore up to about 3 to 5 km/s, bulk density up to about 2.2 to 2.5 g/cm³, and porosity decreases down to about 5% to 20%. No clear correlation exists in this subunit between physical properties and the lithologic units, which consist of (top to bottom) oolitic grainstone, clayey and organic-rich packstone and wackestone, and caprinid rustid debris beds. The downhole increases in sonic velocity and bulk density near the bottom of PP Subunit 3c may correlate with the downhole increase in the abundance of dolomite. In turn, this may be reflected in the slightly elevated values for grain density in the lower interval, up to 2.81 g/cm³. The lower boundary is sharp and abrupt and coincides with the first downhole occurrence of sucrosic, destructive dolomite.

Physical Property Unit 4 (1199–1620 mbsf)

This unit contains a series of subunits that are characterized by high variability in sonic velocity and index properties. These show rapid downhole changes in physical properties that are indicative of the presence of alternating lithologies with significantly different ranges in physical properties. Sediments are predominantly grainstone to rudstone containing ooids, oncoids, or peloids as the main component. Locally, the strata consist of wackestone to packstone. In general, this nearly 450-m-thick interval is characterized by the presence of coarse crystalline dolomite that replaced and altered the original depositional fabric.

Physical Property Subunit 4a (1199–1295 mbsf)

The top of PP Subunit 4a is well-defined and correlates with the change from lithologic Subunit VIC to Unit VII. Values for sonic velocity and bulk density are highly variable, but in general indicate an overall downhole increase and the presence of lithologies having different ranges in physical properties (see Fig. 58). Sonic velocity ranges from 2.61 to 6.8 km/s, bulk density ranges from 2.15 to 2.74 g/cm³, porosity from 2.03% to 34.32%, and sonic velocity-anisotropy from -28.393% to 5.725%, with a mean of -1.161%. Grain density ranges from 2.72 to 2.85 g/cm³. The higher values of sonic velocity and bulk density were measured in dense dolomitic fabrics. The lower boundary of this interval is sharp and abrupt and shows a substantial decrease in sonic velocity and bulk density values, which correlates to the change from lithologic Subunits VIIB to VIIC.

Physical Property Subunit 4b (1295–1399 mbsf)

Mass physical properties in Subunit 4b display an identical trend to those in the previous PP Subunit 4a. Sonic velocity and bulk density values show a rapid increase downhole after an initial sharp decrease with respect to the overlying Subunit 4a. Overall, sonic velocity ranges from 2.49 to 6.56 km/s, bulk density varies from 2.27 to 2.76 g/cm³, porosity ranges from 3.08% to 26.58%, and grain density ranges from 2.71 to 2.81 g/cm³. Mean sonic velocity-anisotropy is 1.583%. The lower boundary of this interval is sharp and abrupt and shows a decrease in sonic velocity and bulk density values. The corresponding change in lithology is between lithologic Subunits VIID and Unit VIII.

Physical Property Subunit 4c (1399–1503.7 mbsf)

Physical properties in this subunit are relatively stable downhole and have significantly lower values than those in overlying and underlying units. Sonic velocity ranges from 2.93 to 4.33 km/s, bulk density ranges from 2.16 to 2.43 g/cm³, porosity varies from 17.05% to 33.69%, and grain density ranges from 2.71 to 2.75 g/cm³. Anisotropy in sonic velocity has a mean value of -0.160%. Although the upper boundary coincides with the change from lithologic Subunit VIID to Unit VIII, the lower boundary does not correspond to a lithologic contact, but nevertheless forms a sharp and well-defined break in physical properties.

Physical Property Subunit 4d (1503.7–1641 mbsf)

Mass physical properties in Subunit 4d are highly variable, but show an overall steep downhole decrease in values for sonic velocity and bulk density. The upper boundary, sharp and abrupt in physical properties, is not defined as a change in lithology. The lower boundary is not sharp, owing to low recovery, but may be correlated to the first downhole occurrence of basalt. Sonic velocity decreases downhole with values from 6.83 to 2.41 km/s, bulk density decreases from 2.78 to 2.35 g/cm³, and porosity increases from 3.17% to 25.15%. Mean

Table 10. Index physical property data for Site 866 (combined Holes 866A and 866B).

Core, section, interval (cm)	Depth (mbsf)	Water content (%)	Bulk density (g/cm ³)	Grain density (g/cm ³)	Porosity (%)	Core, section, interval (cm)	Depth (mbsf)	Water content (%)	Bulk density (g/cm ³)	Grain density (g/cm ³)	Porosity (%)
143-866A-						129R-1, 132-134	1214.22	9.17	2.38	2.72	19.99
1R-1, 13-15	0.14	49.60	1.57	2.68	56.70	130R-1, 4-6	1222.65	19.02	2.15	2.75	34.32
1R-2, 23-25	1.74	122.10	1.62	2.71	76.60	131R-1, 118-121	1233.40	5.11	2.61	2.85	12.70
7R-CC, 30-32	48.11	7.45	2.44	2.73	16.90	132R-1, 83-85	1242.74	2.18	2.68	2.79	5.71
15R-CC, 11-13	125.12	5.90	2.48	2.72	13.86	133R-3, 46-48	1255.07	2.25	2.73	2.84	6.00
22R-CC, 17-18	193.96	6.50	2.46	2.72	15.02	134R-2, 62-65	1263.34	2.67	2.71	2.84	7.05
31R-1, 120-122	281.81	0.47	2.68	2.70	1.24	135R-1, 108-111	1272.00	5.29	2.60	2.84	13.08
32R-CC, 14-16	290.05	3.21	2.56	2.69	7.97	136R-1, 0-4	1280.22	11.82	2.31	2.74	24.47
35R-1, 79-81	319.70	4.49	2.53	2.72	10.88	137R-1, 26-30	1290.08	3.07	2.69	2.84	8.03
36R-1, 38-40	328.89	1.28	2.63	2.69	3.32	138R-1, 94-97	1300.46	11.39	2.30	2.71	23.57
37R-2, 14-16	338.15	3.03	2.57	2.69	7.55	139R-1, 27-30	1309.49	10.99	2.32	2.72	23.00
38R-1, 64-66	343.35	2.06	2.60	2.69	5.24	142R-1, 116-119	1339.37	11.01	2.36	2.78	23.43
41R-1, 26-28	367.27	5.92	2.47	2.70	13.79	143R-1, 1-3	1347.92	11.24	2.33	2.75	23.59
45R-CC, 29-31	405.90	0.30	2.63	2.65	0.79	143R-1, 81-83	1348.72	12.04	2.35	2.80	25.23
46R-2, 19-21	415.50	0.25	2.70	2.71	0.66	144R-1, 83-85	1358.34	5.56	2.50	2.73	13.18
47R-1, 56-58	425.27	0.17	2.68	2.69	0.45	145R-1, 12-14	1366.93	13.24	2.27	2.74	26.58
48R-1, 40-42	434.81	10.01	2.36	2.72	21.42	145R-1, 129-131	1368.10	1.13	2.76	2.81	3.08
50R-1, 20-22	453.90	12.51	2.28	2.72	25.39	146R-1, 123-125	1377.64	3.33	2.62	2.77	8.44
51R-1, 18-20	463.59	9.52	2.36	2.71	20.51	147R-1, 8-10	1386.19	2.16	2.66	2.76	5.63
53R-1, 67-69	483.38	10.23	2.34	2.71	21.73	148R-1, 51-53	1396.22	1.61	2.63	2.71	4.18
54R-1, 74-76	493.05	12.43	2.29	2.72	25.30	148R-2, 50-51	1397.70	2.39	2.61	2.72	6.10
56R-CC, 12-14	511.73	15.07	2.21	2.71	29.00	148R-4, 91-94	1401.13	7.54	2.43	2.73	17.05
58R-1, 51-53	531.51	18.59	2.14	2.71	33.51	150R-1, 115-117	1416.26	10.05	2.36	2.74	21.56
59R-1, 16-18	540.24	15.29	2.24	2.76	29.71	152R-1, 25-27	1434.76	18.47	2.16	2.75	33.69
60R-1, 33-34	550.33	17.72	2.16	2.71	32.46	154R-1, 58-60	1454.39	15.13	2.23	2.74	29.33
61R-1, 88-89	560.78	12.05	2.30	2.72	24.70	154R-2, 38-41	1455.70	13.24	2.26	2.71	26.38
62R-1, 101-106	570.61	15.01	2.21	2.70	28.81	155R-1, 100-102	1464.50	10.63	2.35	2.74	22.54
63R-1, 25-28	579.57	18.57	2.15	2.74	33.71	156R-1, 134-136	1474.55	9.57	2.39	2.75	20.85
63R-2, 63-66	581.45	12.20	2.30	2.73	25.02	156R-2, 81-83	1475.52	9.29	2.38	2.73	20.25
64R-1, 73-76	589.75	16.71	2.19	2.73	31.37	159R-2, 99-102	1503.41	9.78	2.37	2.74	21.13
65R-1, 130-132	590.91	14.71	2.20	2.68	28.26	159R-3, 6-8	1503.97	2.47	2.72	2.84	6.57
66R-1, 97-99	609.28	10.73	2.31	2.69	22.38	160R-1, 70-73	1512.42	2.63	2.71	2.84	6.95
67R-1, 15-17	618.16	10.63	2.33	2.72	22.42	162R-1, 102-104	1532.03	1.16	2.76	2.82	3.17
70R-1, 73-75	647.64	9.92	2.35	2.72	21.22	163R-1, 41-45	1540.73	1.68	2.65	2.72	4.38
71R-1, 58-60	657.05	8.20	2.39	2.69	18.10	164R-3, 2-5	1552.93	2.43	2.72	2.83	6.45
71R-2, 42-45	658.22	9.01	2.38	2.71	19.63	165R-2, 27-29	1561.38	2.23	2.69	2.79	5.86
72R-1, 73-75	666.94	12.34	2.28	2.71	25.09	166R-1, 79-82	1570.11	7.62	2.45	2.75	17.33
74R-1, 71-73	686.22	12.64	2.29	2.74	25.70	167R-1, 90-93	1581.32	3.65	2.58	2.74	9.11
75R-3, 57-59	698.68	13.57	2.27	2.74	27.07	167R-3, 80-83	1584.22	1.19	2.78	2.84	3.27
76R-3, 56-58	708.27	7.90	2.42	2.73	17.74	168R-2, 94-96	1592.55	2.63	2.67	2.79	6.83
79R-1, 122-127	735.04	10.44	2.35	2.73	22.18	168R-2, 86-88	1592.47	3.54	2.63	2.80	9.01
80R-1, 83-85	744.34	14.58	2.24	2.73	28.49	169R-1, 128-129	1601.08	6.49	2.50	2.76	15.21
81R-2, 78-80	754.41	13.09	2.27	2.72	26.29	169R-2, 88-90	1602.19	7.75	2.43	2.73	17.47
82R-2, 69-72	764.89	10.28	2.35	2.73	21.88	170R-1, 112-115	1610.54	8.83	2.39	2.73	19.40
83R-1, 50-53	773.02	14.17	2.25	2.73	27.88	171R-3, 67-69	1622.79	11.60	2.35	2.79	24.44
86R-1, 64-66	802.15	10.93	2.31	2.70	22.76	171R-4, 127-129	1624.88	11.48	2.44	2.93	25.15
87R-1, 100-102	812.21	9.58	2.36	2.72	20.66	177B-1, 7-8	1659.08	0.09	2.82	2.82	0.26
88R-1, 121-123	822.12	11.64	2.31	2.73	24.10	179R-1, 64-66	1660.05	5.65	2.52	2.76	13.50
89R-1, 118-120	831.79	12.32	2.34	2.81	25.77	179R-2, 104-106	1661.55	6.92	2.52	2.82	16.34
89R-2, 16-18	832.27	12.81	2.35	2.85	26.77	180R-2, 108-111	1669.99	1.53	2.85	2.94	4.29
91R-1, 46-48	849.97	10.74	2.38	2.79	23.10	180R-5, 12-15	1673.53	26.28	2.04	2.81	42.48
98R-1, 38-39	917.38	14.63	2.23	2.72	28.47	181R-1, 146-148	1677.27	14.18	2.37	2.94	29.45
99R-1, 74-76	924.65	13.26	2.24	2.68	26.19	182R-1, 96-98	1683.77	1.41	2.90	2.98	4.04
100R-1, 28-30	933.69	8.02	2.41	2.72	17.92	184R-1, 41-43	1692.85	2.94	2.72	2.87	7.78
101R-1, 30-33	943.42	7.86	2.42	2.72	17.59	184R-2, 129-131	1695.10	11.24	2.46	2.94	24.86
102R-1, 90-93	953.62	14.58	2.23	2.72	28.39	185R-3, 48-50	1700.79	2.15	2.81	2.92	5.90
102R-2, 34-35	954.54	10.28	2.31	2.67	21.52	186R-2, 26-28	1708.77	12.94	2.42	2.97	27.77
104R-1, 19-20	971.89	8.40	2.41	2.73	18.63	188R-1, 35-38	1726.67	10.85	2.48	2.95	24.27
105R-1, 47-49	981.78	17.18	2.19	2.75	32.08	188R-3, 14-17	1729.39	8.51	2.51	2.87	19.64
106R-1, 21-23	991.12	13.75	2.27	2.74	27.38	189R-1, 9-11	1735.00	2.08	2.94	3.06	5.98
108R-1, 12-14	1010.33	11.09	2.33	2.73	23.22	189R-3, 130-132	1739.14	7.42	2.59	2.94	17.90
109R-1, 78-80	1020.69	4.49	2.53	2.72	10.87	143-866B-					
109R-2, 43-45	1021.84	11.80	2.30	2.71	24.23	1M-1, 75-77	0.76	63.20	1.68	2.70	63.40
110R-2, 42-44	1031.53	6.31	2.48	2.73	14.69	1M-3, 75-77	5.26	74.60	1.61	2.67	67.10
112R-1, 35-37	1049.26	12.25	2.30	2.73	25.09	1M-CC, 18-20	5.51	64.80	1.68	2.67	64.30
112R-1, 90-93	1049.82	13.21	2.25	2.69	26.25	2M-1, 38-40	6.39	76.30	1.60	2.68	67.60
114R-1, 98-100	1069.19	10.27	2.32	2.69	21.63	2M-3, 75-77	9.71	64.00	1.70	2.70	64.90
115R-1, 34-36	1078.25	8.97	2.40	2.74	19.73	3M-1, 88-90	14.99	68.30	1.64	2.67	64.90
116R-1, 67-69	1088.18	12.16	2.29	2.72	24.85	3M-3, 75-77	17.86	65.40	1.66	2.68	63.90
118R-1, 71-74	1107.52	10.59	2.34	2.72	22.37	3M-5, 75-77	20.86	66.60	1.65	2.67	64.40
119R-1, 43-45	1116.94	12.68	2.29	2.74	25.82	3M-CC, 5-7	22.59	50.50	1.77	2.66	57.90
120R-1, 30-32	1126.41	7.84	2.43	2.74	17.66	4M-1, 33-35	23.84	10.67	2.39	2.80	23.02
121R-1, 8-10	1135.79	4.74	2.56	2.77	11.58	5M-1, 35-38	33.17	6.77	2.53	2.82	16.05
122R-1, 27-30	1145.69	11.08	2.34	2.74	23.31	6M-1, 86-89	43.08	12.31	2.35	2.82	25.78
123R-1, 16-19	1155.28	6.86	2.51	2.81	16.15	7M-1, 2-4	51.73	8.76	2.46	2.82	19.82
124R-1, 12-15	1164.94	7.33	2.46	2.75	16.80	8M-1, 68-69	61.77	5.62	2.54	2.78	13.52
125R-2, 54-56	1176.45	3.14	2.58	2.71	7.83	8M-2, 6-8	62.67	10.64	2.38	2.80	22.94
126R-1, 48-50	1184.49	1.92	2.61	2.69	4.92	9M-1, 3-5	70.54	5.72	2.55	2.80	13.82
126R-2, 47-49	1185.91	4.94	2.52	2.73	11.87						
128R-1, 48-50	1204.25	0.75	2.74	2.78	2.03						

Table 11. Sonic velocity, anisotropy, and bulk density at Site 866 (combined Holes 866A and 866B).

Core, section, interval (cm)	Depth (mbsf)	V_{pu} (cu) (km/s)	V_{pr} (cu) (km/s)	V_{pl} (cu) (km/s)	V_{pr} (mc) (km/s)	V_{pl} (mc) (km/s)	Anisotropy (cu) (%)	Anisotropy (mc) (%)	Bulk density (g/cm ³)
866A-									
7R-CC, 30-32	48.11	4.418							2.44
15R-CC, 11-13	125.12	5.255							2.48
22R-CC, 17-18	193.96	4.499							2.46
25R-CC, 31-33	223.02					4.760			
31R-1, 117-119	281.78					(1)			
31R-1, 120-122	281.81		6.222	5.687			8.985		2.68
32R-CC, 14-16	290.05		5.348	5.508			-2.951		2.56
35R-1, 79-81	319.70		5.061	4.958			2.062		2.53
36R-1, 38-40	328.89		5.844	5.618			3.927		2.63
37R-2, 14-16	338.15		5.791	6.242			-7.490		2.57
38R-1, 64-66	343.35		5.818	5.914			-1.628		2.60
39R-1, 44-46	348.15					5.711			
41R-1, 26-28	367.27		4.865	4.909			-0.912		2.47
45R-CC, 29-31	405.90		6.144	6.005			2.285		2.63
46R-2, 19-21	415.50		6.636	5.986			10.291		2.70
47R-1, 56-58	425.27		6.286	6.423			-2.165		2.68
48R-1, 40-42	434.81		3.645	3.676			-0.858		2.36
48R-1, 47-51	434.88					3.932			
50R-CC, 20-22	453.90		3.194	2.968			7.333		2.28
51R-1, 18-20	463.59		3.316	3.829			-14.362		2.36
53R-1, 67-69	483.38		3.046	3.328			-8.838		2.34
54R-1, 74-76	493.05		2.731	2.960			-8.042		2.29
56R-1, 12-14	511.73		2.358	2.781			-16.484		2.21
58R-1, 32-34	531.33					2.153			
58R-1, 51-53	531.51		2.396	2.546			-6.066		2.14
58R-1, 67-71	531.69					(1)			
59R-1, 16-18	540.24		2.507	2.230			11.681		2.24
60R-1, 33-34	550.33		2.263	2.302			-1.729		2.16
61R-1, 88-89	560.78		2.708	3.005			-10.380		2.30
62R-1, 101-106	570.61		2.450						2.21
62R-2, 5-7	571.16				2.357				
63R-1, 25-28	579.57		2.518	1.945			25.685		2.15
63R-2, 63-66	581.45		2.811	2.963			-5.240		2.30
64R-1, 73-76	589.75		2.270	2.442			-7.303		2.19
65R-1, 130-132	590.91		2.633	3.172			-18.581		2.20
66R-1, 97-99	609.28		2.969	3.129			-5.233		2.31
67R-1, 15-17	618.16		2.929	3.224			-9.599		2.33
70R-1, 73-75	647.64		3.287	3.342			-1.659		2.35
71R-1, 58-60	657.05		3.158	2.358			29.003		2.39
71R-2, 42-45	658.22		3.330	3.288			1.256		2.38
72R-1, 73-75	666.94		3.005	2.971			1.108		2.28
74R-1, 20-24	685.72					3.773			
74R-1, 25-27	685.76				3.217			-15.917	
74R-1, 71-73	686.22		2.993	3.328			-10.609		2.29
75R-3, 42-44	698.53				3.445				
75R-3, 52-55	698.64					4.005			
75R-3, 57-59	698.68		3.393	3.456			-1.865		2.27
76R-3, 34-36	708.05				4.581			10.722	
76R-3, 37-40	708.09					4.115			
76R-3, 56-58	708.27		3.689	3.715			-0.690		2.42
77R-2, 87-89	716.88				3.400				
77R-2, 89-93	716.91					3.836			
79R-1, 122-127	735.04		3.449	3.712			-7.345		2.35
79R-4, 2-4	738.12				2.939			-25.496	
79R-4, 8-10	738.18					3.798			
80R-1, 83-85	744.34		2.947	3.423			-14.951		2.24
81R-2, 78-80	754.41		3.151	3.363			-6.501		
82R-2, 62-64	764.81					3.786			
82R-2, 65-68	764.85				3.042			-21.778	
82R-2, 69-72	764.89		3.782	3.828			-1.203		2.35
83R-1, 50-53	773.02		3.946	3.686			6.813		2.25
85R-1, 49-51	792.30		3.997	3.924			1.828		
85R-2, 45-49	793.77				3.667			-1.395	
85R-2, 52-55	793.84					3.718			
86R-1, 64-66	802.15		3.345	3.314			0.932		2.31
87R-1, 100-102	812.21		2.908	2.845			2.201		2.36
88R-1, 121-123	822.12		3.726	3.315			11.678		2.31
89R-1, 118-120	831.79		3.125	3.122			-0.128		2.35
89R-2, 16-18	832.27		3.268	3.041			7.440		2.36
91R-1, 6-8	849.57				4.663			23.495	
91R-1, 46-48	849.97		3.380	3.447			-1.956		2.38
91R-1, 111-113	850.62					3.682			
93R-1, 21-24	868.93					(1)			
93R-1, 25-28	868.97				3.216				

Table 11 (continued).

Core, section, interval (cm)	Depth (mbsf)	V_{pu} (cu) (km/s)	V_{pr} (cu) (km/s)	V_{pi} (cu) (km/s)	V_{pr} (mc) (km/s)	V_{pi} (mc) (km/s)	Anisotropy (cu) (%)	Anisotropy (mc) (%)	Bulk density (g/cm ³)
866A-									
96R-1, 35-38	898.07					3.776			
98R-1, 38-39	917.38		2.568	2.404			6.587		2.23
98R-1, 57-58	917.57					2.921			
99R-1, 74-76	924.65		2.447	2.499			-2.110		2.24
100R-1, 28-30	933.69		3.502	3.333			4.942		2.41
101R-1, 30-33	943.42		2.994	3.035			-1.382		2.42
102R-1, 78-80	953.49				2.739				
102R-1, 90-93	953.62		2.554	3.070			-18.357		2.23
102R-2, 34-35	954.54		3.979	3.182			22.254		2.31
103R-1, 45-47	962.86					(1)			
103R-1, 50-52	962.91		2.806	2.814				-0.284	
104R-1, 19-20	971.89		3.644	3.068			17.167		2.41
105R-1, 47-49	981.78		2.554	2.323			9.501		2.19
106R-1, 21-23	991.12		2.954	2.754			7.006		2.27
108R-1, 12-14	1010.33		3.017	3.082			-2.134		2.33
109R-1, 78-80	1020.69		3.881	3.681			5.310		2.53
109R-2, 10-12	1021.51				2.828				
109R-2, 43-45	1021.84		3.221	2.762			15.364		2.30
110R-2, 42-44	1031.53		3.398	3.162			7.184		2.48
110R-1, 53-55	1030.14				2.958				
111R-1, 99-101	1040.31					4.323			
112R-1, 35-37	1049.26		2.823	2.610			7.850		2.30
112R-1, 90-93	1049.82		2.324	2.024			13.807		2.25
114R-1, 85-87	1069.02					3.410			
114R-1, 98-100	1069.19		3.576	2.685			28.486		2.32
115R-1, 34-36	1078.25	3.941							2.40
115R-1, 76-78	1078.67					3.849			
116R-1, 45-48	1087.97					2.890			
116R-1, 49-51	1088.00				2.662			-8.205	
116R-1, 67-69	1088.18		2.539	2.596			-2.183		2.29
118R-1, 71-74	1107.52		3.148	3.381			-7.160		2.34
118R-2, 138-143	1109.70					3.301			
119R-1, 43-45	1116.94		3.074	2.912			5.420		2.29
120R-1, 30-32	1126.41		4.575	3.996			13.513		2.43
121R-1, 8-10	1135.79		5.184	5.055			2.504		2.56
121R-1, 31-34	1136.03					4.808			
122R-1, 27-30	1145.69		3.536	3.895				-9.650	2.34
122R-1, 30-32	1145.71				3.310				
123R-1, 16-19	1155.28		4.897	4.897				-0.005	2.51
124R-1, 12-15	1164.94		3.261	3.130				4.079	2.46
124R-1, 30-33	1165.22					4.617			
125R-2, 54-56	1176.45		4.167	4.194				-0.631	2.58
125R-2, 56-60	1176.48				4.434				
126R-1, 54-56	1184.55					5.142			
126R-1, 48-50	1184.49		5.455	4.991			8.889		2.61
126R-2, 47-49	1185.91	4.473							2.52
128R-1, 48-50	1203.69		6.027	6.075			-0.800		2.74
128R-2, 0-5	1204.73					6.033			
128R-2, 6-9	1204.77				5.750			-4.805	
129R-2, 23-26	1213.15					3.376			
129R-1, 132-134	1214.22		3.626	3.564			1.714		2.38
130R-1, 4-6	1222.65		2.185						2.15
130R-2, 20-22	1224.31				6.081				
130R-2, 23-26	1224.35					6.439		-5.715	
131R-1, 118-121	1233.40		3.945	3.813			3.414		2.61
132R-1, 83-85	1242.74		4.236	5.638			-28.393		2.68
133R-2, 54-57	1253.66				4.545				
133R-3, 46-48	1255.07		5.012	4.825			3.808		2.73
134R-2, 62-65	1263.34		6.371	6.017			5.725		2.71
134R-2, 67-70	1263.39				5.878				
135R-1, 108-111	1272.00		4.855	4.829			0.544		2.60
135R-1, 113-116	1272.05					5.673			
136R-1, 0-4	1280.22		2.628	2.605			0.903		2.31
137R-1, 26-30	1290.08		5.663	5.515			2.638		2.69
137R-2, 79-81	1292.10				5.642				
138R-1, 94-97	1300.46		2.407	2.488			-3.310		2.30
139R-1, 27-30	1309.49		3.394	3.200			5.867		2.32
142R-1, 89-91	1339.10				3.546				
142R-1, 93-96	1339.15					(1)			
142R-1, 116-119	1339.37		2.895	2.915			-0.681		2.36
143R-1, 1-3	1347.92		3.083	3.310			-7.118		2.33
143R-1, 81-83	1348.72		4.073	3.283			21.488		2.35

Table 11 (continued).

Core, section, interval (cm)	Depth (mbsf)	V_{pu} (cu) (km/s)	V_{pr} (cu) (km/s)	V_{pi} (cu) (km/s)	V_{pr} (mc) (km/s)	V_{pi} (mc) (km/s)	Anisotropy (cu) (%)	Anisotropy (mc) (%)	Bulk density (g/cm ³)
866A-									
144R-1, 83-85	1358.34		4.690	4.689			0.029		2.50
144R-2, 51-53	1359.52				3.879			4.287	
144R-2, 54-59	1359.57					3.716			
145R-1, 12-14	1366.93		2.963	2.916			1.614		2.27
145R-1, 129-131	1368.10		6.716	6.560			2.357		2.76
145R-1, 131-134	1368.13				6.274				
146R-1, 79-81	1377.20						3.641		
146R-1, 123-125	1377.64		5.024	4.741			5.789		2.62
147R-1, 8-10	1386.19		5.455	5.688			-4.187		2.66
147R-2, 91-93	1388.52					5.185			
148R-1, 51-53	1396.22		6.075	6.217			-2.315		2.63
148R-1, 55-58	1396.27					5.868			
148R-2, 50-51	1397.70		5.279	5.308			-0.537		2.61
148R-4, 91-94	1401.13		3.983	4.333			-8.437		2.43
148R-4, 95-98	1401.17				4.026				
150R-1, 115-117	1416.26		3.567	3.791			-6.088		2.36
150R-4, 14-16	1419.75				3.246				
152R-1, 17-19	1434.38				3.272				
152R-1, 25-27	1434.76		3.358	3.183			5.324		2.16
154R-1, 58-60	1454.39		2.918	2.932			-0.493		2.23
154R-1, 63-66	1454.45				2.864			-2.741	
154R-1, 67-70	1454.49					2.944			
154R-2, 38-41	1455.70		2.962	3.051			-2.968		2.26
155R-1, 91-94	1464.43					3.583			
155R-1, 96-98	1464.46				3.571			-0.325	
155R-1, 100-102	1464.50		3.379	3.788			-11.405		2.35
156R-1, 134-136	1474.55		3.602	3.333			7.754		2.39
156R-2, 53-56	1475.25				3.336			-8.810	
156R-2, 57-61	1475.28					3.643			
156R-2, 81-83	1475.52		3.268	3.367			-2.982		2.38
159R-1, 99-101	1501.90				3.542				
159R-2, 99-102	1503.41		3.602	3.137			13.808		2.37
159R-3, 6-8	1503.97		4.582	5.206			-12.751		2.72
160R-1, 70-73	1512.42		6.320	5.942			6.174		2.71
162R-1, 102-104	1532.03		6.664	6.831			-2.480		2.76
162R-2, 2-5	1532.53					5.831			
163R-1, 41-45	1540.73		6.065	6.388			-5.185		2.65
164R-3, 2-5	1552.93		4.321	4.569			-5.579		2.72
165R-2, 27-29	1561.38		6.383	5.914			7.631		2.69
165R-2, 71-75	1561.83					5.787			
166R-1, 79-82	1570.11		3.200	3.024			5.643		2.45
166R-4, 85-89	1574.67					4.741			
167R-1, 90-93	1581.32		4.608	4.453			3.436		2.58
167R-3, 80-83	1584.22		5.518	5.328			3.512		2.78
167R-3, 101-103	1584.42				5.517				
168R-1, 128-130	1591.39					5.224			
168R-1, 132-134	1591.43				5.049			-3.410	
168R-2, 86-88	1592.47		5.682	5.242			8.055		2.63
168R-2, 94-96	1592.55		5.151	5.330			-3.409		2.67
168R-3, 72-74	1593.83					4.006			
169R-1, 128-129	1601.08		5.493	5.408			1.553		2.50
169R-2, 88-90	1602.19		4.197	3.893			7.522		2.43
170R-1, 109-112	1610.51					4.063			
170R-1, 112-115	1610.54		4.052	3.918			3.352		2.39
170R-1, 116-118	1610.58				4.017				
171R-3, 49-52	1622.61				2.651				
171R-3, 67-69	1622.79		3.276	2.957			10.225		2.35
171R-4, 127-129	1624.88		2.548	2.416			5.316		2.44
177B-1, 7-8	1659.08		5.640	5.980			5.852		2.82
179R-1, 64-66	1660.05		4.156	4.249			-2.130		2.52
179R-1, 71-75	1660.13					4.051			
179R-2, 104-106	1661.55		4.011	4.135			-3.069		2.52
179R-2, 108-112	1661.60					4.056			
179R-2, 116-119	1661.67				3.950			-2.648	
180R-2, 108-111	1669.99		6.164	6.386			-3.538		2.85
180R-4, 24-26	1672.15				5.857				
180R-5, 12-15	1673.53								2.04
181R-1, 146-148	1677.27		3.238	3.464			-6.744		2.37
182R-1, 93-95	1683.74					6.002			
182R-1, 96-98	1683.77		6.127	5.914			3.532		2.9
184R-1, 54-56	1692.85		4.830	4.884			-1.125		2.72
184R-2, 129-131	1695.10		3.166	3.060			3.409		2.46
185R-3, 48-50	1700.79		5.269	5.609			-6.259		2.15
185R-3, 51-54	1700.83					5.287			

Table 11 (continued).

Core, section, interval (cm)	Depth (mbsf)	V_{pu} (cu) (km/s)	V_{pt} (cu) (km/s)	V_{pl} (cu) (km/s)	V_{pu} (mc) (km/s)	V_{pt} (mc) (km/s)	Anisotropy (cu) (%)	Anisotropy (mc) (%)	Bulk density (g/cm ³)
866A-									
185R-3, 55-58	1700.87				4.891			-7.782	
186R-2, 26-28	1708.77		2.737	2.376			14.100		2.42
188R-1, 35-38	1726.67		3.455	3.625			-4.793		2.48
188R-3, 14-17	1729.39		3.529	3.483			1.303		2.51
189R-1, 9-11	1735.00		5.347	5.802			-8.158		2.94
189R-3, 130-132	1739.14		4.189	4.281			-2.170		2.59
189R-4, 33-36	1739.63					4.442			
189R-4, 37-39	1739.66				4.114			-7.667	
866B-									
4M-1, 33-35	23.84		4.451	4.211			4.968		2.39
5M-1, 35-38	33.17		4.952	5.157			-3.689		2.53
6M-1, 86-89	43.08		3.889	3.814			1.725		2.35
7M-1, 2-4	51.73		4.936	4.699			4.456		2.46
8M-1, 68-69	61.77		5.366	5.071			5.149		2.54
8M-1, 69-71	61.80					4.492			
8M-2, 6-8	62.67		4.183	3.873			6.164		2.38
8M-2, 9-11	62.70					4.149			
9M-1, 3-5	70.54		5.224	5.238			-0.243		2.55

Note: (cu) = cube; (mc) = minicore. Measurements have been labeled for direction and sample shapes: V_{pu} (cu) is from an unoriented cube; V_{pt} (cu) is transverse (horizontal) from a cube; V_{pl} (cu) is longitudinal (parallel core axis) from a cube; V_{pu} (mc) is transverse from a minicore; V_{pt} (mc) is longitudinal from a minicore; (l) indicates no data because of excessive sample length (will be analyzed in shore-based laboratory).

anisotropy in sonic velocity is 3.051%. Grain density varies between 2.72 and 2.93 g/cm³.

Physical Property Unit 5 (1620–1743.6 mbsf)

This unit consists of fresh and strongly altered layers of basalt, with highly variable physical properties, and does not show any specific trend. Sonic velocity ranges from 2.38 to 6.39 km/s, bulk density ranges from 2.04 to 2.94 g/cm³, porosity ranges from 0.26% to 42.48%, and grain density varies between 2.76 and 3.10 g/cm³. Mean value for anisotropy in sonic velocity is -0.699%. Overall, the range of values of physical properties, mainly sonic velocity and bulk density, are completely encompassed by those of the overlying carbonate platform sediments.

Discussion

Recovery in the carbonate-platform sediments and basalt in Hole 866A was relatively low, but yet sufficient to collect a database of physical properties that probably resembles that of the continuous lithologic sequence. Physical properties (see Fig. 54) show an overall tripartite subdivision: (1) at the top, a high-velocity/high-density interval with sparse recovery in the middle; (2) an interval with downhole increasing variability of physical properties; (3) at the bottom, an interval characterized by highly variable and changing physical properties. Correlation of variables, such as sonic velocity, bulk density, porosity and grain density, with the lithologic units and boundaries is good. Only in a few locations do uncertainties remain in the correlation of physical properties with the lithology (e.g., the lower boundary of PP Subunit 4a). The most likely factor controlling the pattern of sonic velocity and index properties in the lowermost part of Hole 866A is diagenesis. The downhole appearance of dolomite, and the intensity of dolomite replacement and fabric destruction at about 1100 mbsf, closely correlates with the onset of highly variable sonic-velocity and bulk-density values. The more consistent interval (535–1199 mbsf) has relatively more clay and organic material that may have prevented strong dolomitization and resulted in more narrow and subtle variability in sonic velocity and bulk density. Variations in the physical prop-

erties in the lower part of the carbonate buildup are of equal amplitude and frequency as those measured in the recovered basalt interval below. The carbonates possibly mask the seismic signature of the underlying basalt. As shown again in Holes 865A and 866A, shallow-water carbonate buildups, in contrast to deep-water carbonates, have highly variable, complex and unpredictable diagenetic histories. Diagenetic alteration of specific lithologic horizons generates impedance contrasts that either absorb or mask possible impedance changes over the contact of carbonates and underlying basement basalt. In addition, values of sonic velocity and bulk density for the basalt are extremely variable. Therefore, it is difficult to estimate sonic velocities and "depth to basement" from single-channel seismic records.

Figure 55 shows the distribution of anisotropy values for sonic velocity, calculated from transverse and longitudinal compressional wave velocities measured in cubes, with depth in Hole 866A. From 300 (no data for the shallower section because only unoriented samples were available) to 800 mbsf, anisotropy values show a gradual, more negative decrease that indicates a relative increase of the vertical sonic velocity over the horizontal velocity component. At about 800 mbsf, the anisotropy shifts back to more positive values and gradually decreases again down to approximately 1400 to 1500 mbsf. Here, anisotropy levels out to values near zero and, at the contact with the basalt, shows another shift to positive values. Finally, anisotropy decreases with depth in the basalt. The change at about 800 mbsf is significant and may well have implications for the depositional history of the carbonate buildup at Site 866. Note, however, that the change in anisotropy at about 800 mbsf is not reflected in sonic-velocity and index-property profiles (see Fig. 54, symbol "a" in open circle). Anisotropy may be indicative of post-depositional changes of the sediment fabric by compaction and cementation. One hypothesis explaining the shift at 800 mbsf may be a long period of nondeposition and/or erosion of the platform top. It is probably no coincidence that the shift in anisotropy correlates with the top of a shallow-water depositional unit and an elevated level of total organic carbon (TOC), which is most likely of terrigenous origin (see "Organic Geochemistry" section, this chapter).

Figure 56 shows plots of bulk density and porosity vs. sonic velocity measured in cubes. The overall relation between bulk density

Table 12. Summary of range and mean of physical properties for PP units, Site 866 (combined Holes 866A and 866B).

Unit (range)	V_{pt} (cu) (km/s)	V_{pt} (cu) (km/s)	V_{pt} (mc) (km/s)	V_{pt} (mc) (km/s)	Anisotropy (cu) (%)	Anisotropy (mc) (%)	Bulk density (g/cm ³)	Porosity (%)	Grain density (g/cm ³)	Water content (%)
1 (866A: 0–0.9 mbsf; 866B: 0–23.5 mbsf)										
min	^a nd	nd	nd	nd	nd	nd	1.57	56.7	2.66	49.60
max	nd	nd	nd	nd	nd	nd	1.77	76.6	2.71	122.10
mean	nd	nd	nd	nd	nd	nd	1.65	64.7	2.68	69.58
2 (866A and 866B: 0.9/23.5–430 mbsf)										
min	3.889	3.814	nd	4.149	-7.490	nd	2.35	0.45	2.65	0.17
max	6.636	6.424	nd	5.712	10.291	nd	2.69	25.78	2.83	12.30
mean	5.230	5.254	nd	4.778	1.372	nd	2.53	11.63	2.74	5.08
3a (866A: 430–535 mbsf)										
min	2.358	2.546	nd	2.153	-16.484	nd	2.14	20.51	2.71	9.52
max	3.645	3.829	nd	3.932	7.333	nd	2.36	33.51	2.72	18.59
mean	2.955	3.155	nd	3.042	-6.600	nd	2.28	25.23	2.71	12.62
3b (866A: 535–703 mbsf)										
min	2.263	1.945	2.357	3.773	-18.581	-15.917 ⁽¹⁾	2.15	18.10	2.68	8.20
max	3.393	3.456	3.445	4.005	29.003		2.39	33.71	2.76	18.57
mean	2.827	2.877	3.006	3.889	-0.321		2.27	25.98	2.72	13.08
3c (866A: 703–1199 mbsf)										
min	2.324	2.024	2.662	2.890	-18.357	25.496	2.19	4.92	2.67	1.92
max	5.455	5.055	4.663	5.142	28.486	23.495	2.61	32.08	2.81	17.18
mean	3.433	3.315	3.418	3.873	3.479	-3.776	2.36	21.05	2.72	10.06
4a (866A: 1199–1295 mbsf)										
min	2.185	2.605	4.545	3.376	-28.393	-5.715	2.15	2.03	2.72	0.75
max	6.371	6.075	6.081	6.439	5.725	-4.805	2.74	34.32	2.85	19.02
mean	4.454	4.764	5.564	5.380	-1.161	-5.260	2.56	13.34	2.80	6.13
4b (866A: 1295–1399 mbsf)										
min	2.407	2.488	3.546	3.641	-7.118	4.287 ⁽¹⁾	2.27	3.08	2.71	1.13
max	6.716	6.560	6.274	5.868	21.488		2.76	26.58	2.81	13.24
mean	4.338	4.276	4.835	4.603	1.583		2.48	15.50	2.75	7.17
4c (866A: 1399–1503.7 mbsf)										
min	2.918	2.932	2.864	2.944	-11.405	-8.810	2.16	17.05	2.71	7.54
max	3.983	4.333	4.026	3.643	13.808	-0.325	2.43	33.69	2.75	18.47
mean	3.404	3.435	3.408	3.390	-0.160	-3.959	2.32	23.64	2.74	11.52
4d (866A: 1503.7–1641 mbsf)										
min	2.548	2.416	2.651	4.006	-5.579	-3.410 ⁽¹⁾	2.35	3.17	2.72	1.16
max	6.664	6.831	5.517	5.831	10.225		2.78	25.15	2.93	11.60
mean	4.899	4.774	4.309	4.942	3.051		2.58	11.60	2.79	4.99
5 (866A: 1641–1743.6 mbsf)										
min	2.737	2.376	3.950	4.051	-8.158	-7.782	2.04	0.26	2.76	0.09
max	6.164	6.386	5.857	6.002	14.100	-2.648	2.94	42.48	3.10	26.28
mean	4.418	4.518	4.703	4.768	-0.699	-6.032	2.58	17.57	2.92	8.30

^a nd = no data.Velocity symbols as in Table 11; ⁽¹⁾ = limited data.

and porosity with sonic velocity is well-defined, and data points are well distributed and cluster along the generalized velocity-density relationship for sediments given by Gardner et al. (1974). For constructing synthetic seismograms, acoustic impedance is often calculated by using Gardner's law, which relates density and velocity with the empirical equation: density = $0.23 \times \text{velocity}^{(0.25)}$. Gardner's law is accurate for siliciclastics, but it is known that the velocity-density relationship in carbonates is more complicated. The carbonate sediments at Site 866 clearly have a general trend comparable to Gardner's law. The variation along this trend, however, is substantial. Comparison with a similar plot for the sediment at Site 865 shows that the data sets overlap, but unfortunately the comparison has been obscured by the sparse data from the latter site. Figure 57 shows similar cross plots with the addition that samples have been discriminated for lithology. The data set has been subdivided into four groups, regardless of depth in hole or lithologic unit: (1) pure limestones; (2) limestones with amounts of clay and organic matter; (3) dolomitic limestones; (4) basalt. Pure limestone (Fig. 57A) samples are well-distributed and show

a linear relationship between sonic velocity and bulk density. Sonic velocity ranges from 3 to 6.4 km/s, and bulk density ranges from 2.2 to 2.7 g/cm³. Limestone with clay and organic matter shows a similar relationship, but has relatively lower values for sonic velocity and bulk density. Sonic velocity ranges from 2 to 4 km/s, and bulk density varies between 2.1 and 2.5 g/cm³ (Fig. 57B). Values for sonic velocity and bulk density for dolomitic limestone show a cluster of data points near the high end of the pure limestone plot (see Fig. 57C). Sonic velocity ranges from 4.5 to 6.5 km/s, and bulk density from 2.6 to 2.8 g/cm³. No distinction has been made for values of relative percentage and for character (replacive or destructive, crystal size, etc.) of the dolomite. Basalt samples show a wide range of values that separate into two groups. Unaltered basalt has sonic velocities that range from 5 to 6 km/s and bulk densities from 2.7 to 3 g/cm³. Altered ("weathered") basalt has sonic velocities between 2.5 and 4.5 km/s and bulk densities that range from 2.3 to 2.6 g/cm³. No study was made onboard the ship to unravel the specific effects of diagenesis (among them dolomitization) and presence of clay and/or organic

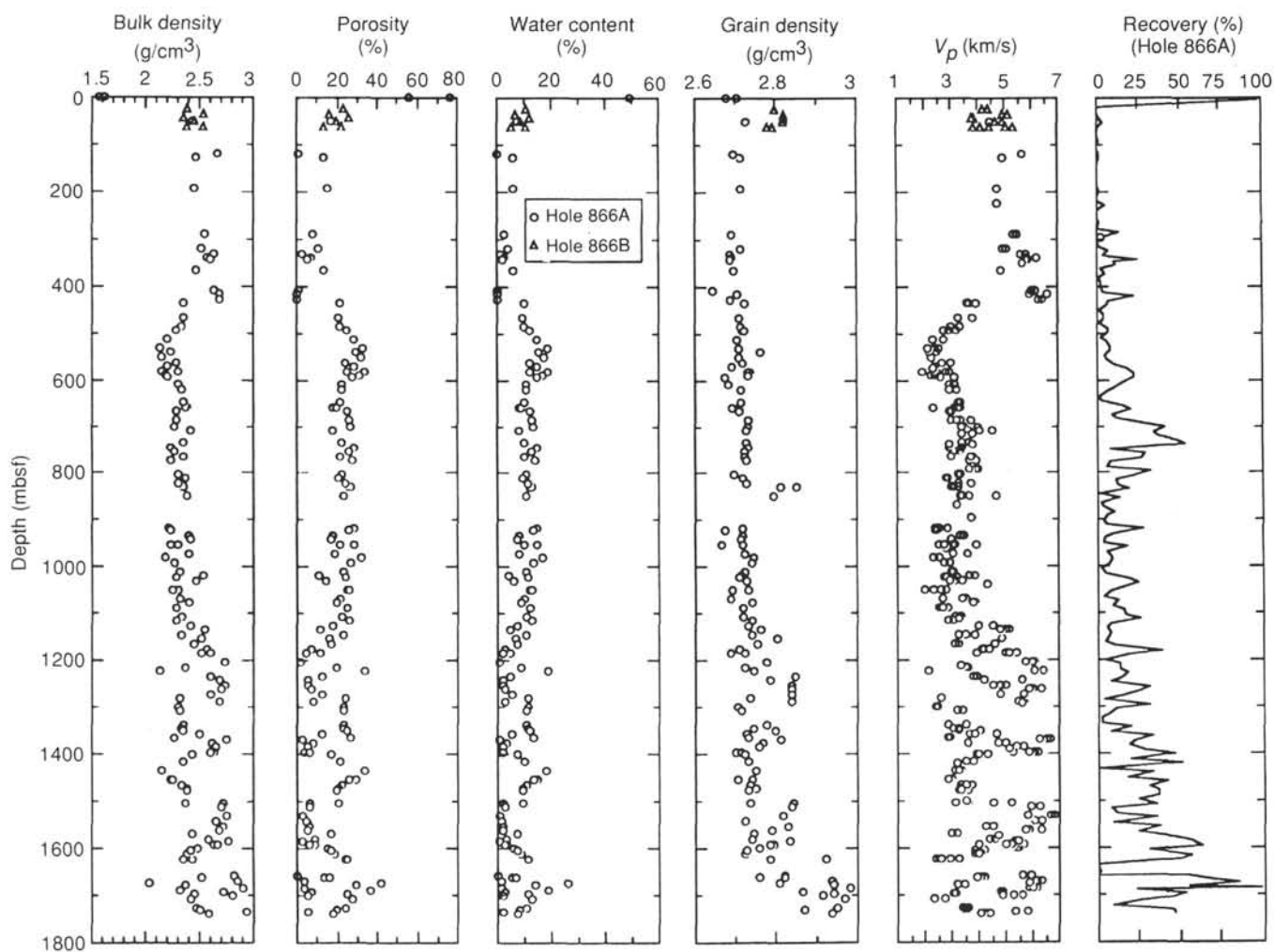


Figure 53. Index properties, sonic velocity and anisotropy, and recovery for Site 866 (combined Holes 866A and 866B).

material on the sonic velocity of the samples. It is evident though, that the presence of dolomite increases and the presence of clay and/or organic material lowers the final compressional-wave velocity. Sonic velocity characteristics of basalt are typically influenced by degree of weathering. Altered basalt has lower sonic velocities than those of unaltered basalt. Vesicular basalt, or basalt with abundant gas bubbles, has sonic velocities and bulk densities near the low end of the values for unaltered basalt.

A correlation between Sites 865 and 866 is tentative owing to the sparse data at Site 865, but suggests that both sonic velocity profiles (from discrete measurements) show an overall wine-glass contour. At Hole 865A, however, the bulge in the upper part of the glass shape was not representative of the total velocity profile from the sonic log.

Two major changes in bulk density and sonic velocity at Site 866 occur at 430 mbsf (boundary between PP Unit 2 and Subunit 3a) and between 1199 and 1295 mbsf (boundary between PP Subunits 3c to 4b), suggesting a correlation with the two most prominent reflectors on the single-channel seismic survey record (see "Seismic Stratigraphy" section, this chapter), at about 1.92 and 2.5 s twtt, respectively.

DOWNHOLE MEASUREMENTS

Introduction

Wireline measurements were conducted at this site to measure the in-situ properties of the lagoonal sediments and igneous basement of Resolution Guyot. Downhole measurements complement observa-

tions from the cores to correlate chemical, structural, physical, and magnetic properties of these sediments and rocks with depositional, tectonic, and diagenetic processes.

Reliability of Logs

The logging data from Hole 866A cover the interval from the bottom of the drill string (78.0 mbsf) to 1679.4 mbsf or less (see "Operations" section, this chapter, Table 1). The bottom of the hole was not viewed by any logging tools because of cave-ins at or below about 1680 mbsf. Because of mechanical problems, no valid data were recorded with the GST tool.

Hole size is the most important control on accuracy of logs from Hole 866A. Two caliper logs were obtained on two separate runs: the lithodensity-tool caliper, and the four-arm caliper of the formation microscanner (FMS). The two calipers generally give similar results, except that the FMS caliper has a maximum opening of 16 in. (40.64 cm), and the lithodensity caliper measures to a maximum of 18 in. (45.7 cm). Large hole diameter (>17.2 in or >43.7 cm) to a depth of 265 mbsf accounts for the high-porosity/low-density readings above this depth. Because of the large hole size, the FMS was not run above 253.0 mbsf. Most other logs do not require pad contact and, therefore, are relatively insensitive to the changes in borehole size.

Considerable evidence of either cycle skipping or noise can be seen in the sonic velocity logging data. In particular, the sonic log from the dolomitic and basaltic sections of the hole is subject to noise

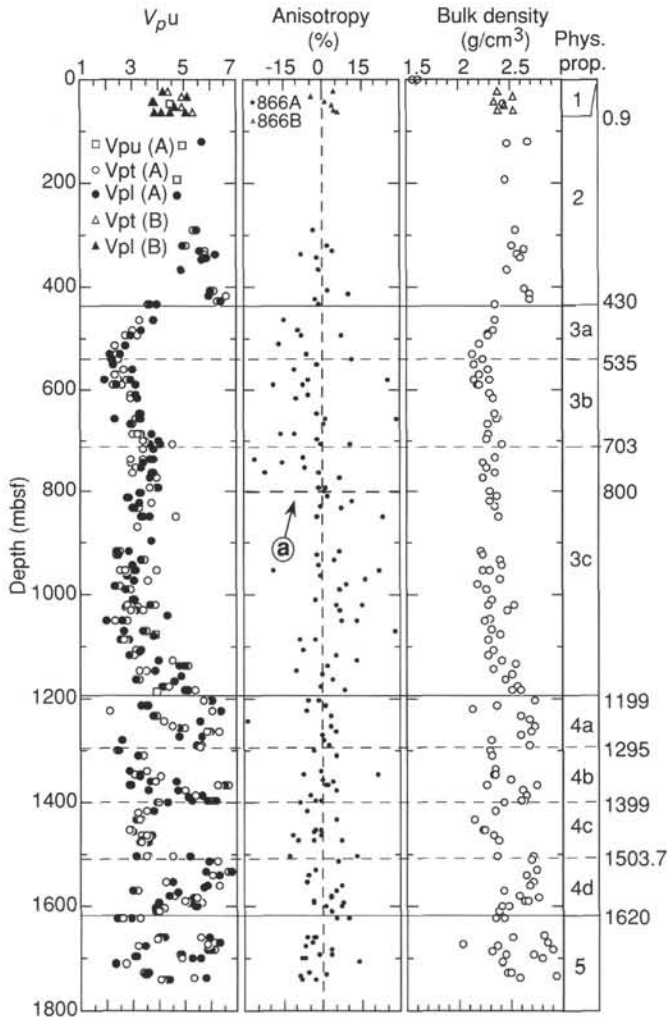


Figure 54. Physical property units for Site 866 (combined Holes 866A and 866B), based on sonic velocity, anisotropy and bulk density. V_{pu} is from an unoriented sample; V_{pt} is transverse (horizontal); V_{pl} is longitudinal (parallel core-axis); capital letters in legend indicate Hole 866A (A) and Hole 866B (B); "a" in open circle indicates position of reversal in anisotropy of velocity (see text for discussion).

(as "high-velocity spikes"). It may or may not be possible to remove these artifacts with post-cruise processing.

By correlating the gamma-ray logs between runs, each log was shifted in depth to correct for differences in the stretch of the logging cable. All logs were then corrected to the base of the drill pipe by subtracting the depth from rig floor to the seafloor (1372.6 m). These depths should be accurate to within ± 2 m.

Depths for the temperature tool were determined using the pressure recorded in the instrument, and a depth-vs.-pressure table was derived from time-depth stations taken during logging.

Temperature

The Lamont temperature tool was run at the bottom of all three Schlumberger tool strings (geophysical, FMS, and geochemical) to determine equilibrium temperatures in the hole. The temperature tool, because it is a self-recording tool, measured temperatures in both downward and upward directions. Data were recorded at a speed of 1400 m/hr from 100 m above the seafloor to 1671.4 mbsf on the geophysical tool string, and from 100 m above the seafloor to 1633.0 mbsf

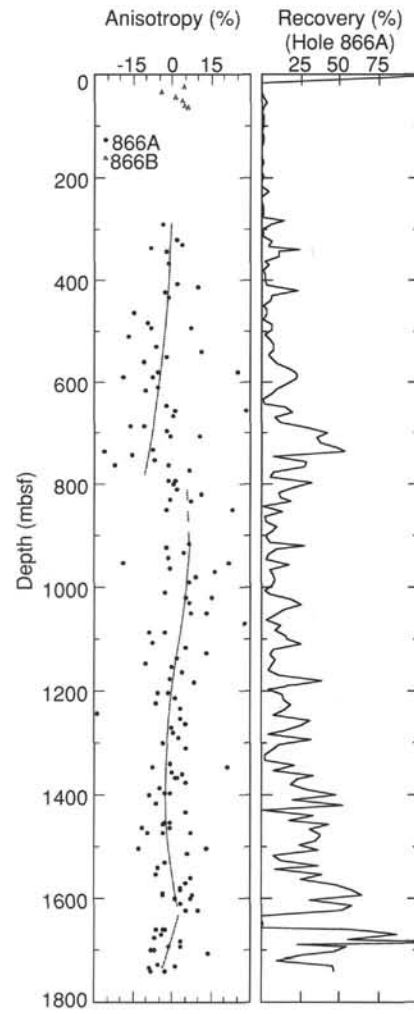


Figure 55. Plot of anisotropy vs. depth for Site 866 (combined Holes 866A and 866B). Shaded line represents average (interpreted) trend of anisotropy. Recovery is plotted to show low-recovery zones (see text for discussion).

on the FMS tool string. During the geochemical tool-string run, because logging speed was only 200 m/hr, the temperature tool recorded data from 100 m above the seafloor to 1624.2 mbsf, and back to 570 mbsf before running out of memory.

The borehole temperatures measured by the Lamont temperature tool are reduced by circulation during coring, by hole conditioning immediately prior to logging, and by pumping during logging to facilitate lowering of the lightweight tools (i.e., Japanese magnetometer and borehole televiewer). Therefore, the temperature measurements provide only a minimum estimate of the equilibrium temperature profile. Figure 59 displays the temperature log obtained from the first run (geophysical tool string) while logging uphole. The repeat section at approximately 675 mbsf is the result of a 15-m lowering of the logging cable during the uphole logging run.

The temperature profile is approximately linear throughout the borehole. The small changes in gradient most likely were caused by changes in cable speed. The temperature data from the other two lowerings must be processed and compared with those from the first run to determine if the gradient is indeed linear over the length of the borehole. A maximum temperature of 13.6°C was measured at 1671.5 mbsf. The hole temperatures recorded in Hole 866A at Resolution Guyot are consistent with those observed in the lower section of Hole 865A at Allison Guyot.

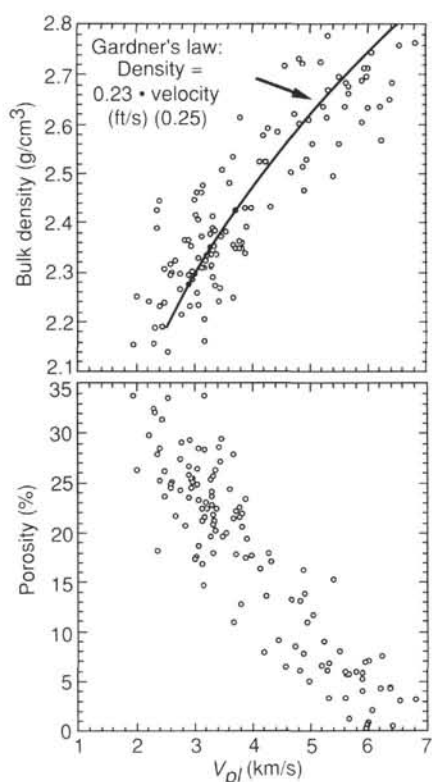


Figure 56. Plots of sonic velocity (from cubes) vs. bulk density and porosity, Hole 866A. Heavy line indicates correlation between velocity and density in carbonates, according to Gardner et al. (1974; see text for discussion).

Downhole Three-component Magnetometer Log

The magnetometer measured three components of the geomagnetic field within Hole 866A from 1595 to 1636 mbsf. Because the magnetometer measures the signal every 3 s, the sampling interval while the tool was run at 500 m/hr was about 0.4 m. The horizontal and vertical components of the magnetic field inside the hole were calculated from the observed three components of the magnetic field. The orientation of the tool with respect to the present geomagnetic field was also determined from the magnetic field, measured by two orthogonal horizontal axes of the magnetometer. These variations are shown in Figure 60.

At about 1622 mbsf, the vertical component of the geomagnetic field decreases abruptly. The horizontal component of the geomagnetic field also decreases at the same sub-bottom depth. These decreases coincide with the shallowest basaltic layer within the hole and are caused by the strong magnetization of the basaltic layer.

The decrease in the vertical magnetic field below 1622 mbsf indicates that the magnetization of the basaltic layer has a positive inclination. Between 1622 and 1630 mbsf, the horizontal component of the magnetic field also decreases. However, a sharp jump in the horizontal component occurs at about 1630 mbsf and the horizontal magnetic field increases below 1630 mbsf. This indicates that the declination of magnetization of the basaltic layer between 1622 and 1630 mbsf has a reverse direction and returns to the normal direction below 1630 mbsf. Thus, the basaltic layer below 1622 mbsf can be divided into two layers by the declination of the magnetization. Normal declination below 1630 mbsf may have been caused by the secondary magnetization of highly altered basalt and/or volcanic breccias.

Below 1622 mbsf, short wavelength variations (<3 m) were observed in both the vertical and horizontal components of the geomagnetic field. This indicates that the basaltic layer consists of many thin magnetic layers (<3 m).

Log-based Units

Sixteen log units (Figs. 61A and 61B) were identified on the basis of variability and baseline shifts in the geophysical and spectral gamma-ray logs. These units have been defined primarily on the basis of the gamma-ray, uranium, thorium, resistivity, and sonic logs.

Lithologic Units I and II, and the upper part of Subunit IIIA (see "Lithostratigraphy" section, this chapter) were logged through the pipe with the spectral gamma-ray tool. The pipe attenuation, about a factor of three, resulted in near-zero response on the gamma log and thus could not be used to determine the limits of these intervals on the logs.

Logging Unit 1 (Base of Pipe, 78.0–187.5 mbsf)

Within this interval, gamma values are low and range between 5 and 20 API units. Resistivity values are also low, and average about 3 ohm-m. This interval, which corresponds to lithologic Subunit IIIA, was described as a wackestone from the limited core recovered. Both the low gamma-ray and resistivity readings suggest that the entire unit is fairly homogenous, with little clay content.

Logging Unit 2 (187.5–265.0 mbsf)

This unit is differentiated from logging Unit 1 on the basis of greater variability in the resistivity logs (Fig. 61A). The individual peaks have values as high as 16 ohm-m, and appear to correspond to higher velocities as well. This unit corresponds to lithologic Subunit IIIB, a porous wackestone with thin calcrete crusts. The calcrete crusts may correspond to the low-porosity, high-resistivity intervals on the log profiles. On the whole, density and porosity values within this unit are unreliable because of the large (>17.2 in.; >43 cm) hole size.

Logging Unit 3 (265.0–430.5 mbsf)

Logging Unit 3 corresponds to lithologic Subunit IIIC, which is dominated by white mudstone and wackestone. Four calcrete layers were identified from the core data.

Within logging Unit 3, the resistivity log displays variability (Figs. 61A and 62A), with individual peaks reaching up to 130 ohm-m. As in logging Unit 2, the high-resistivity peaks appear to correspond to calcrete layers. In this unit, however, the calcrete intervals appear to be thicker (>5 m) than in the unit above. At least six distinct calcrete-rich intervals were identified in the resistivity logs. Because core recovery averaged 5.9% within this unit, the thickness of the calcrete layers inferred from the logs cannot be confirmed by the core data.

Gamma-ray values continue to be low (5–12 API units), but increase to approximately 20 API units toward the bottom of the interval. Below 265 mbsf, the hole diameter decreases to less than 17 in. (<43 cm); thus, the sonic, density, and porosity logs are more reliable within this unit (Fig. 63A). Density values range from 2.4 to 2.7 g/cm³, with porosities averaging about 15%. The sonic log indicates that velocities range between 4.5 and 5.3 km/s, with some velocities as high as 6.0 km/s within the calcrete layers. Higher density (2.6 g/cm³) and lower porosity (7%) over these intervals also characterize the calcrete intervals.

Logging Unit 4 (430.5–670.5 mbsf)

Unit 4 corresponds to lithologic Unit IV, a cyclic packstone-wackestone having local clay/organic-rich intervals. The presence of clay/organic-rich material within this unit is indicated in the logs by a gradual increase in gamma-rays and uranium. Gamma-ray values in individual peaks reach 34 API units and go as high as 77 API units at the base of logging Unit 4. This anomalously high peak in gamma rays and increase in uranium (Fig. 62A) at the base of logging Unit 4 may represent a major stratigraphic break (Rider, 1986).

Resistivity values within this unit are fairly low, varying only between 2.5 and 11 ohm-m. The shallow-focused resistivity log,

which has the highest vertical resolution of the three resistivity logs, appears to be cyclic within this unit, and averages about three cycles every 5 m (Fig. 64).

The density values decrease from 2.7 g/cm³ in the unit above to an average of 2.2 to 2.3 g/cm³ at the top of logging Unit 4 (Fig. 63A). Velocity within this interval averages about 3.25 km/s. Porosity at the top of the unit, where the hole diameter is less than 17 in. (43 cm), increases to 27%, compared with porosities of 5% at the base of logging Unit 3 (Fig. 63A). These distinct changes in the geophysical logs result from a change in lithology (i.e., from the calcrete-rich layers in logging Unit 3 to the packstone-wackestone interval below).

Logging Unit 5 (670.5–799.0 mbsf)

This unit corresponds to lithologic Unit V, an oolitic grainstone. The log values reflect the homogeneous nature of this interval. The gamma-ray intensity varies between 6 and 23 API units. Resistivity increases in intensity from the unit above, varying between 6 and 20 ohm-m in broad peaks that average wavelengths of about 20 m. The hole diameter is stable within this interval, and averages 13.5 in. (34.3 cm). The porosity and density values therefore are reliable within this unit. Density varies between 2.3 and 2.4 g/cm³, while porosity averages about 20% between 687 and 720 mbsf, and then increases to 24% below 720 mbsf. Velocity values decrease from 4 km/s at the top of the unit to 3.5 km/s at the bottom. The porosity and velocity changes at the bottom of the unit may reflect the vuggy porosity noted in the cores of lithologic Unit V.

Logging Unit 6 (799.0–858.6 mbsf)

This unit is distinct from logging Unit 5 because of the higher intensity and cyclical nature of the gamma-ray log. Gamma-ray values range from a low of 15 to more than 105 API units. This log unit correlates with lithologic Subunit VIA, a cyclic packstone-wackestone with algal laminites and numerous clay/organic-rich intervals.

Resistivity, velocity, and porosity values are not much different from those in logging Unit 5; however, rhythmic variation appears in the logs within this unit that averages wavelengths of about 1.5 m.

Logging Unit 7 (858.6–909.0 mbsf)

Logging Unit 7 corresponds to lithologic Subunit VIB. The logs indicate that the caprinid rudist debris bed within this interval is fairly uniform, with little change in velocity, density, and porosity. Velocity averages around 3.25 km/s, while density and porosity values average 2.3 g/cm³ and 27%, respectively.

Gamma-ray intensity within Unit 7 is low (6–10 API units) at the top of the interval and gradually increases (15–29 API units) toward the bottom (Fig. 62B), indicating a slight increase in clay content at the base of the unit. The increase in clay content noted in the gamma-ray log below 900 mbsf is confirmed by the presence of muddy sediment in Cores 143-866A-96R and -97R.

Logging Unit 8 (909.0–1178.0 mbsf)

This unit corresponds to lithologic Subunit VIC, a cyclic packstone wackestone having intervals of algal laminites and clay/organic-rich material. This lithologic subunit was identified from 917.0 to 1203.0 mbsf.

Logging Unit 8 (Fig. 61B) was identified on the basis of much higher gamma-ray intensity (peaks ranging from 25–75 API units) and higher frequency variations in resistivity, velocity, density, and porosity than those observed in logging Unit 7.

The interval is distinctive in that, between 985 and 1140 mbsf, it is composed of numerous repetitive packets about 20 m thick. Each packet is characterized in the gamma-ray log by a sharp increase in intensity, followed by a gradual decrease upward or coarsening-

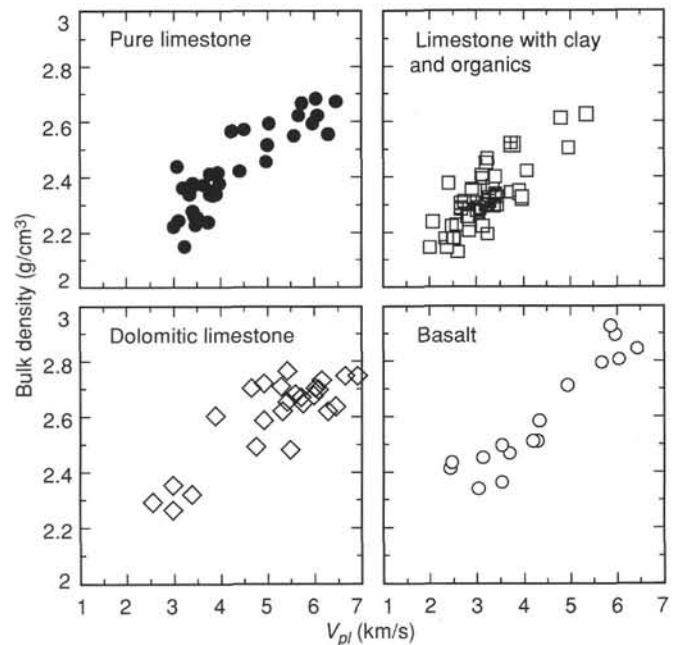


Figure 57. Cross plot of sonic velocity (from cubes) vs. bulk density, Hole 866A. Measurements of bulk density have been discriminated for lithologic fabric (see text for discussion).

upward effect. This rhythmic repetition also can be observed in the resistivity and porosity logs.

Superimposed on these large-scale rhythmic repetitions are small scale bundles of wavelengths 1- to 1.5-m long that also exhibit a coarsening-upward effect. These small-scale sequences also were observed in the cores and have been described as mudstone-wackestone with algal mats, bird's-eye vugs, and oncoids grading upward to peloidal wackestone-packstone. The larger-scale rhythmic events seen on the logs were neither described nor noted in the core descriptions.

Logging Unit 9 (1178–1249.5 mbsf)

Logging Unit 9 corresponds to lithologic Subunit VIIA, a dolomitized oolitic/peloidal grainstone that, like the unit above, contains algal laminites and clay/organic-rich intervals. The decreased gamma-ray intensity (peaks ranging from 25–37 API units) and lower uranium values in this interval suggest a decreased presence of clay and organic material. The baseline shift in the resistivity log (Fig. 63B) to higher values also implies an increase in carbonate material. Porosity values in this unit average about 24%, with densities between 2.4 to 2.5 g/cm³. The velocity log, although somewhat noisy, shows that velocity increases across the unit boundary from 4.25 km/s in Unit 8 to more than 5.0 km/s at the top of Unit 9. The top of logging Unit 9 has been correlated with the largest frequency contrast in the impedance log from Hole 866A. This shows up as a high-amplitude reflector on the seismic profile that was shot close to Site 866 (see "Seismic Stratigraphy" section, this chapter).

Logging Unit 10 (1249.5–1303.0 mbsf)

This unit corresponds to lithologic Subunit VIIB, a dolomitized peloidal grainstone. The low gamma-ray values (25 API units) reflect the absence of clay content in this interval.

Two very distinct resistivity peaks, which occur between 1262.0 and 1277.5 mbsf and 1294.0 and 1303.0 mbsf, dominate the interval. These high-resistivity (150 ohm-m) zones are also marked by low

porosity (10%–12%) and high density (2.6 g/cm³), as would be expected in a dolomite sequence (Serra, 1986).

Logging Unit 11 (1303.0–1359.4 mbsf)

Logging Unit 11 corresponds to lithologic Subunit VIIC, a peloidal grainstone. Resistivity and density readings are low, averaging 14 ohm-m and 2.4 g/cm³, respectively. Gamma-ray intensity is variable within this interval and ranges between 8 and 23 API units at the top, increasing toward the bottom to a maximum of 43 API units. This increase appears to correspond to the appearance of algal laminites noted at the base of lithologic Subunit VIIC. Unlike logging Units 10 above and 12 below, the low resistivity values indicate this interval is largely undolomitized.

Logging Unit 12 (1359.4–1403.5 mbsf)

This unit corresponds to the brown dolomitized peloidal grainstone and oncoidal wackestone of lithologic Subunit VIID. The presence of mudstone and interstratified algal laminites, observed in the cores, is confirmed by the high-intensity gamma-ray peaks that vary between 25 and 75 API units at approximately 5- to 6-m intervals. This succession, which is frequently repeated within this unit, is illustrated well in the FMS image from 1398.8 to 1402.2 mbsf (Fig. 65).

Dolomitization within this interval is inferred from the high (>100 ohm-m), 2- to 4-m-wavelength resistivity peaks observed throughout the unit (Fig. 62B). Porosity and density values (7% and 2.65 g/cm³, respectively; Fig. 63B) within the dolomitized zone agree with the values encountered in logging Unit 10. On the basis of increased gamma rays and uranium within the inferred dolomite intervals, we infer that the dolomites contain clay or organic matter, particularly at the base of this unit.

Logging Unit 13 (1403.5–1602.0 mbsf)

Logging Unit 13 corresponds to lithologic Subunit VIIIA, a dolomitized oolitic/oncoidal grainstone. Dolomitization is evident in the resistivity log from 1403.5 to 1465 mbsf, but is most prevalent in the interval from 1512 to 1602 mbsf (Fig. 62). Resistivity values in this interval are very high (>200 ohm-m) and rarely fall below 60 ohm-m, indicating a high degree of dolomitization. Gamma-ray intensity is low at the top of the unit, but increases progressively toward the bottom to an average of 30 API units (Fig. 62B). In the cores, algal laminites increase toward the bottom of Subunit VIIIA, as do occurrences of lignite and pyrite. The increased uranium values below 1540.0 mbsf confirm their presence in the formation.

Logging Unit 14 (1602.0–1623.4 mbsf)

Logging Unit 14 corresponds to lithologic Subunit VIIIB, a pyritic oolitic grainstone with altered grains of basalt that form the nuclei of some of the ooids. The variable gamma-ray values most likely reflect the presence of the basalt and pyrite grains in this interval. Resistivity values decrease to 16 to 60 ohm-m, indicating little or no dolomitization within this unit. Porosity values are low, averaging approximately 10%, with density values varying between 2.4 and 2.6 g/cm³.

Logging Unit 15 (1623.4–1630.0 mbsf)

The top of this unit represents the contact between the oolitic grainstone above and the underlying basalt. The logs indicate that this contact is sharp and distinct, but given that the maximum vertical resolution of most of the logs is about 45 cm, this may not reflect the true nature of the contact. The FMS images, which have a vertical resolution of 1 cm, show that the boundary is distinct (Fig. 66), but that the overlying sediment is at an angle to the basalt below. The FMS images, in fact, seem to confirm the core description that the overlying oolitic grainstone trends downward into the igneous rock in a small pocket or vein.

The interval between 1623.4 and 1630.0 mbsf appears to consist of basalt, as indicated by the high resistivities (>1,000 ohm-m), fairly low gamma-ray intensity (18–35 API units), and interbedded sediments (resistivity, ~2–3 ohm-m; gamma-ray intensity, ~10 API units).

Logging Unit 16 (1630.0–1642 mbsf)

This unit corresponds to moderately phryic olivine basalt. The high resistivities (>1,000 ohm-m; Fig. 62), low gamma-rays (18–35 API units), high velocities (5.5–6.25 km/s), and low porosity (~2%) suggest that this represents a relatively unaltered basalt.

Below 1642 mbsf, the 2- to 30-ohm-m resistivity readings suggest (1) either more clays, (2) a soil horizon, or (3) altered basalt is present. While the material in the recovered core suggests a soil horizon and altered basalt in this interval, no logs other than the resistivity logs were recorded within this interval; thus, logs cannot be used to aid in the interpretation.

Cyclicality Within Logs

Large sections of the log profile are characterized by rhythmic repetitions that range from 1 m to tens of meters in scale. The most noteworthy of these rhythmic pulses is in logging Units 4 (430.5–670.5 mbsf) and 8 (909.0–1178.0 mbsf). The top unit corresponds to lithologic Unit IV, where cyclic repetition of lithologies occurs between the organic-rich laminated wackestone-packstones (deposited in intertidal swamps or marshes) and the less organic-rich grainstones and white wackestones (deposited in a more marine lagoonal environment) (see “Lithostratigraphy” section, this chapter). These major lithologies were recognized within recurring meter-scale packets. The log data, particularly those of the shallow-focused resistivity and gamma-ray, suggest the same pattern of repetition. These small-scale sequences appear to coarsen-upward, based on a change in gamma-ray intensity from about 30 to 40 API units at the base, to a low of about 15 API units at the top of the sequence. Although the gamma-ray log is an indicator of clay content, a decrease in clay content is closely correlated to an increase in grain size, and thus shapes in the gamma log can be interpreted as grain-size trends, and by sedimentological association, as cycles (Rider, 1986).

In logging Unit 8 (lithologic Subunit VIC), the 1- to 1.5-m scale cycles are less well-developed in the resistivity and gamma-ray logs, in part owing to diagenetic overprinting by dolomite.

The small-scale repetitions observed in the gamma-ray and resistivity logs of both logging Units 4 and 8 have been superimposed on larger-scale sequences averaging 20 m thick. These sequences, like the smaller-scale versions, appear to coarsen upward, implying longer-term cyclic variations of the depositional environment.

Summary

The temperature log recorded in Hole 866A indicates a thermal gradient similar to that recorded in the lower part of Hole 865A at Allison Guyot. However, the change in gradient observed half-way down the borehole in Hole 865A was not observed in the temperature profile of this hole.

The logs provided critical and complimentary data for identifying the lithologies and lithologic boundaries in a borehole that had poor-to-moderate core recovery.

The gamma-ray and geophysical logs confirm the small-scale cycles observed in lithologic Units VI and IV. The log profiles have also identified large-scale rhythmic variations in lithology that were not identified in the cores, either because of poor recovery or because these variations occur over several cores.

The FMS images proved to be useful for identifying the facies changes, particularly in the poorly recovered intervals, and the thickness and succession of unrecovered lithologies.

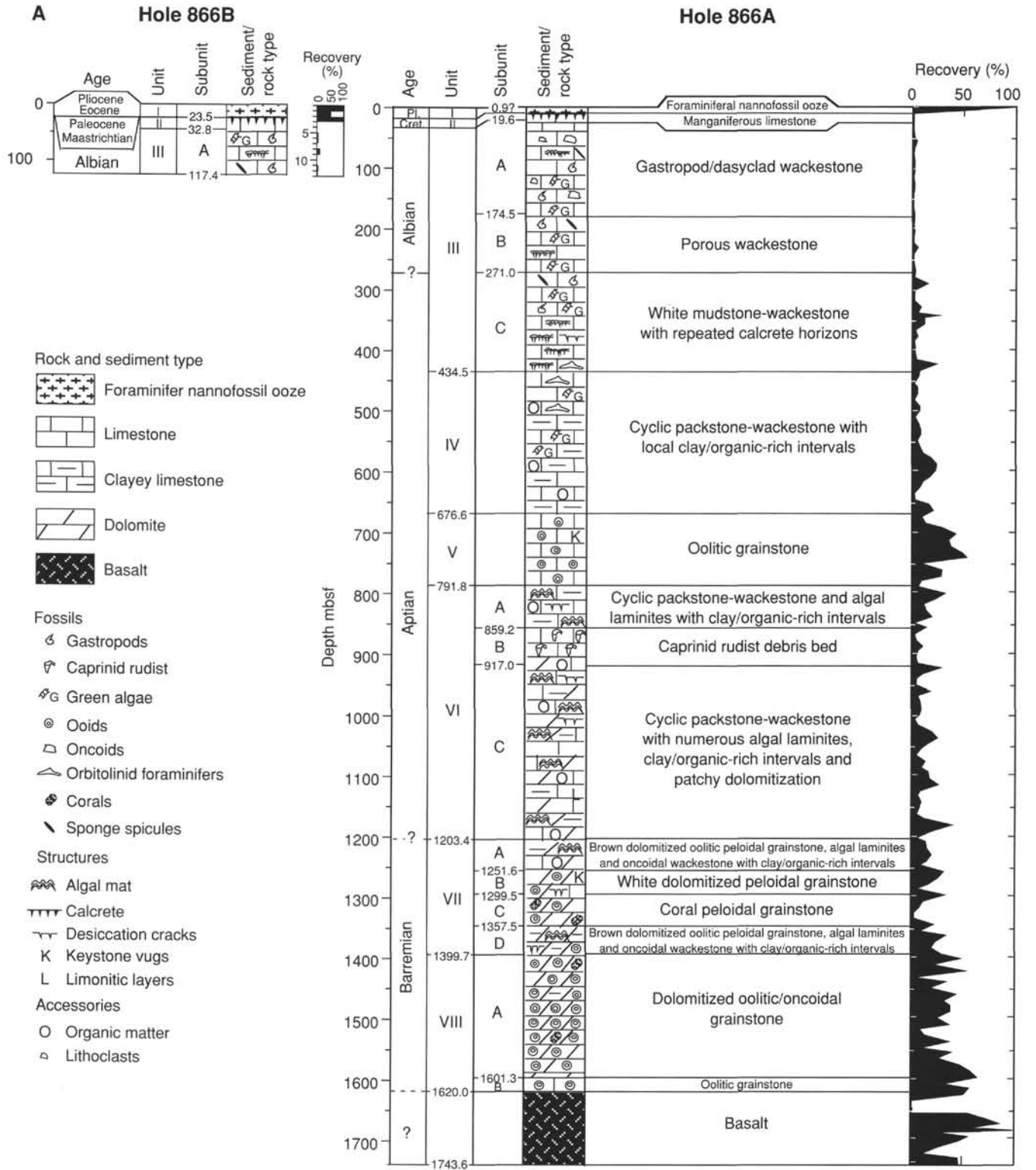


Figure 58. Summary of age, lithology, core recovery, physical properties, and downhole logs at Site 866. Measurements of velocity in discrete samples are labeled for direction: V_{pl} is unoriented; V_{pt} (A) is transverse (horizontal) in Hole 866A; V_{pl} (A) is longitudinal (parallel to core axis) in Hole 866A; V_{pt} (B) is transverse (B) and longitudinal in Hole 866B.

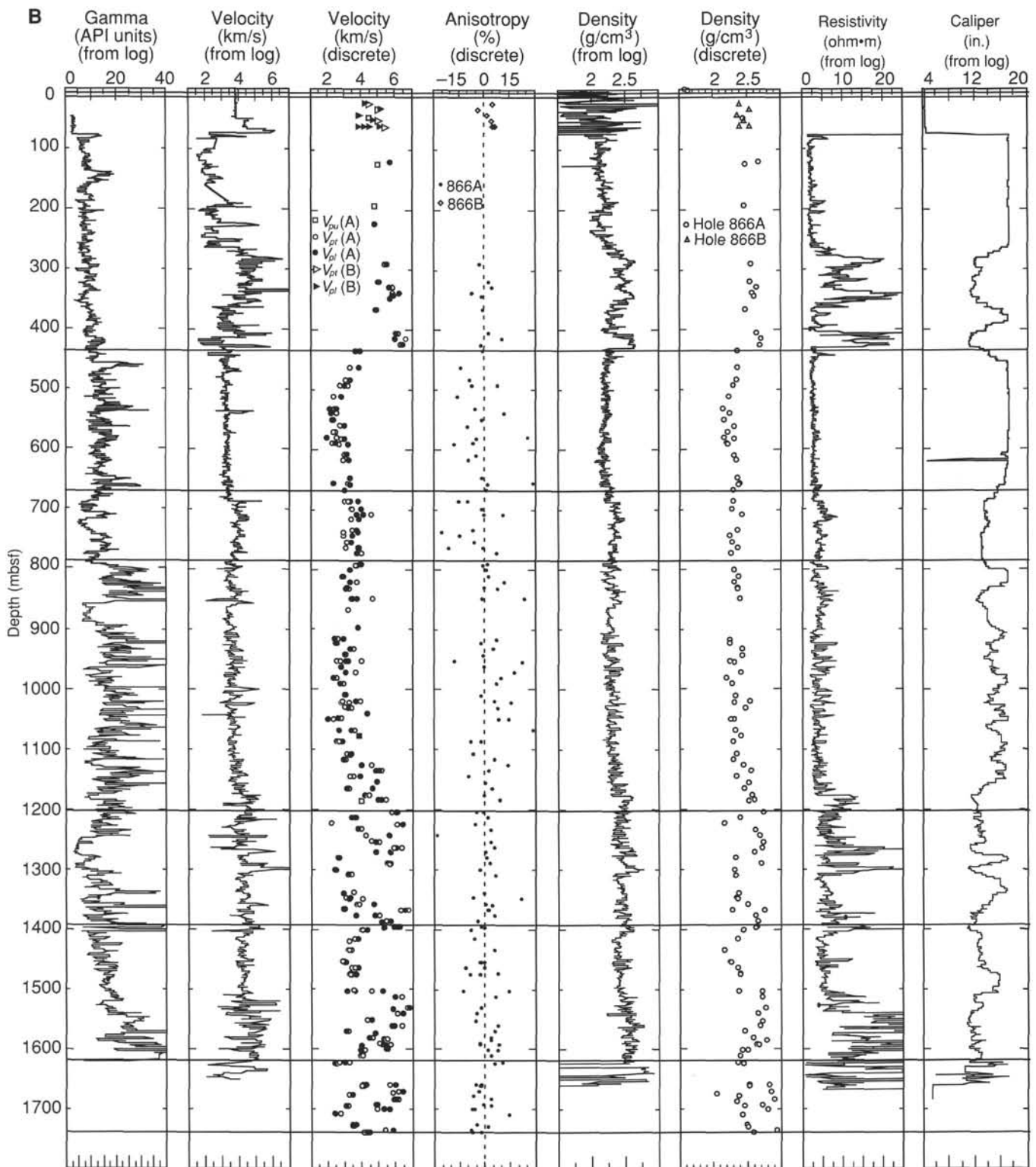


Figure 58 (continued).

SEISMIC STRATIGRAPHY

Correlation among the several classes of data relevant to the construction of a reliable seismic stratigraphy is not a straight-forward procedure, but involves a certain amount of trial and error. The immediate aim is to estimate the depth intervals in the drill hole where

changes in physical properties give rise to reflectors seen in seismic profiles taken over the drill site. The most applicable data comprise

1. Digitally recorded seismic records (Figs. 7 and 9), some of which can be processed to correct for the sound-source signature, and for multiples, side echoes, sloping reflectors, etc.;

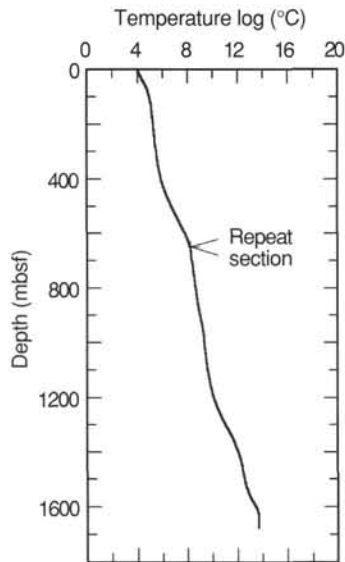


Figure 59. Temperature profile for Hole 866A from the geophysical tool string run. The repeat section at approximately 675 mbsf results from a 15-m lowering of the logging cable while recording the logging run uphole.

2. The lithologic succession derived from study of the recovered core material (Fig. 10);

3. Measurements of physical properties of small samples of the core materials, especially of sound velocity and bulk density (Fig. 58);

4. Coring-rate data, which, over intervals where nearly the same drilling technique was used (weight-on-bit, rate of bit rotation, pump pressure, and water-pumping rate), gives a rough measure of the "hardness" of the strata (Fig. 4); and

5. The downhole logs (Fig. 58), each of which is useful for providing information of the nature of the rocks penetrated by the drill hole, but the most pertinent of which are the sonic-velocity and density logs. From these two logs, two additional curves have been calculated, a depth-vs.-reflection-time curve (Fig. 67) and a depth-vs.-reflection-coefficient curve (Fig. 68).

Seismic Profiles Applicable to Site 866

A part of a processed seismic profile near Site 866, taken using an 80-in.³ water gun from the *Thomas Washington* during the site survey of Resolution Guyot, is shown in Figure 7. This profile followed a due-north course about 1.2 nmi west of Site 866, and therefore, these reflectors are not necessarily in exactly the same relative positions as they are beneath the site. A portion of this profile closest to Site 866 is shown in Figure 69, with the most prominent reflectors labeled with their two-way traveltimes. The positions of the most prominent reflectors in this profile, at the projected position of Site 866, are also given in Table 13. The deeper reflectors appear less continuous and more diffuse than reflectors in the upper part of the profile.

A profile passing virtually over the site, on a course of 174°, was made from the *JOIDES Resolution*, using a 200-in.³ water gun, during the approach to the site (Fig. 9). The relatively low frequency and long pulse length of this system yielded a record having relatively low resolution. This record dramatically illustrates the intermittent nature of some of the reflectors, which change markedly in amplitude as they are traced laterally. These lateral changes may result from primary lithologic differences or the effects of later diagenesis in the platform carbonates. The deeper reflectors, below about 2.8 s of twtt, are weak and discontinuous. The reflection times of the main reflectors seen in this profile are presented in Table 13.

Finally, a 3.5-kHz profile was taken aboard the *JOIDES Resolution* along the same track as the 200-in.³ water-gun profile, which is

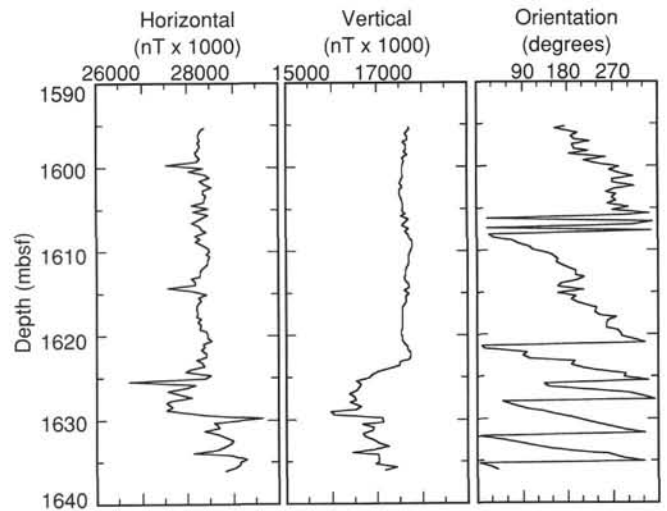


Figure 60. Variations of horizontal and vertical components of the geomagnetic field, and orientation of the tool with respect to the present geomagnetic field within Hole 866A from 1595 to 1636 mbsf.

shown in Figure 6. This record clearly depicts the contact between the pelagic sediments and the underlying Lower Cretaceous shallow-water carbonates and a few local and discontinuous reflectors within the pelagic section. The main reflectors in this profile are listed in Table 13.

Correlation Between Lithologic Changes and Seismic Reflectors at Site 866

The lithologic sequence penetrated in Hole 866A is shown as Figure 10. Several important contacts are likely candidates for reflectors, but many contacts do not juxtapose strata with markedly different sonic velocities and densities, and these do not find expression as seismic reflectors. On the other hand, some reflectors do not have an obvious correlation with a lithologic break. In sequence, from the top to bottom, the reflectors beneath Site 866 and the corresponding lithologic contacts are as follows:

1. The reflector at 0.031 s twtt, is strongly expressed in the 3.5-kHz record (Fig. 6). It corresponds to the irregular erosion surface at the top of the reef limestone beneath the pelagic cap, at 23.5 mbsf in Hole 866B. The interval velocity through the pelagic cap was calculated as 1.735 km/s.

2. A reflector at 0.10 s twtt in the seismic profile (Fig. 7) has no obvious expression in the rocks recovered, but keep in mind that the recovery rate was only a few percent in this part of the column. Downhole logs yielded suspect readings in the part of the hole just below the bottom of the BHA, where the reflector is most likely located, at about 100 m.

3. The strong reflector expected at the top of the hard Aptian mudstone/wackestone succession at about 271 mbsf is not easy to locate in the seismic profile. The top of the Aptian limestone is marked by a change in coring rate (Fig. 4) and by substantial increases in sonic velocity, density, and resistivity as measured by the logging tools (Fig. 58). The calculated reflection coefficient at this level is the highest in the entire logged column (Fig. 67), save for the peak at about 190 mbsf, which is probably an artifact caused by a gap in the velocity log. The calculated reflection time to this contact (Fig. 68) is only about 0.225 s twtt, whereas the most prominent reflector on the seismic profile in this vicinity is at 0.21 s twtt (Fig. 69).

4. The top of lithologic Unit II, at 434.5 mbsf, corresponds with a change in the character of the sonic-velocity log, from higher and more fluctuating values above, to lower and more uniform values

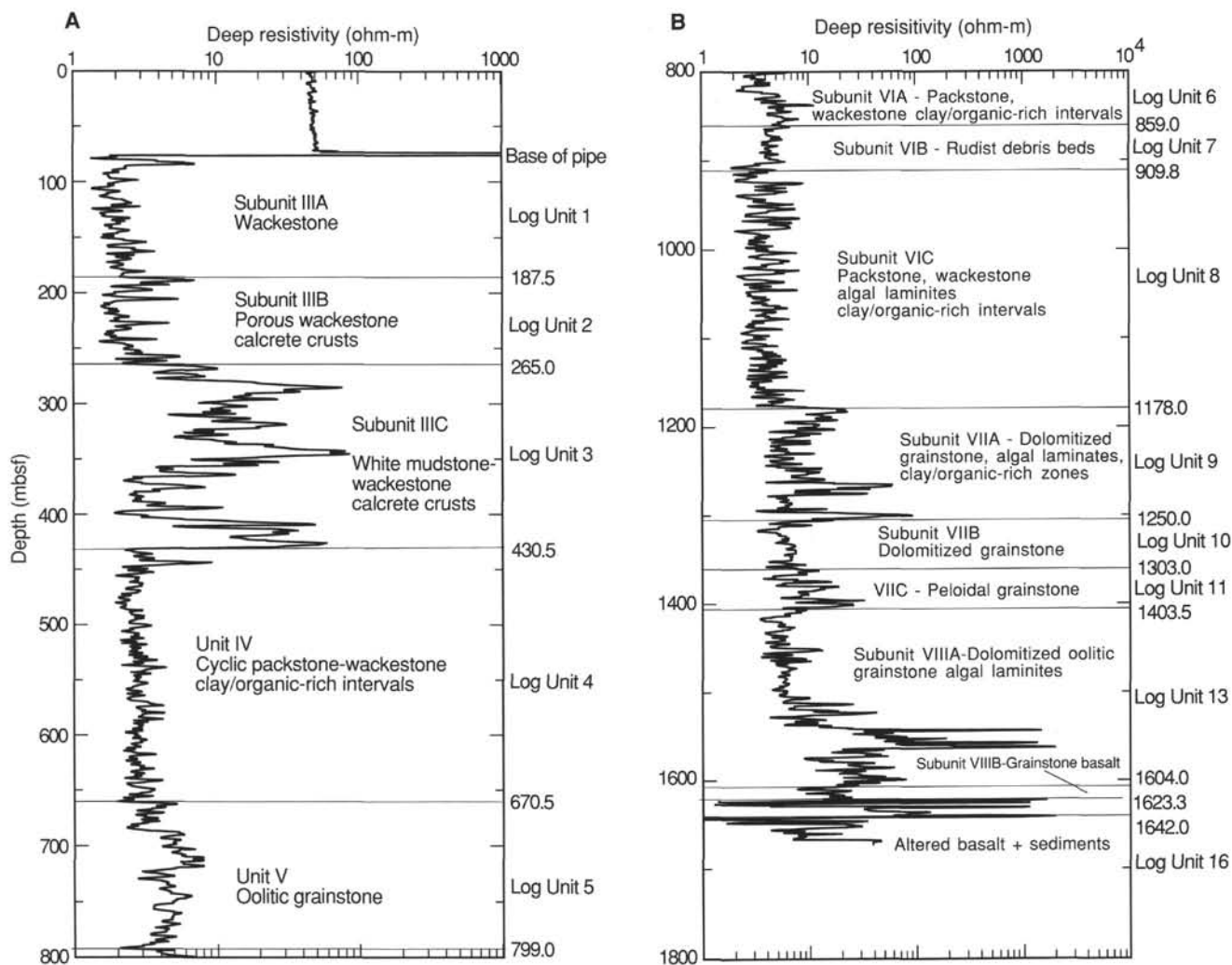


Figure 61. Deep resistivity log used to illustrate log units and the corresponding lithologic units from 78 to 800 mbsf (A) and 800 to 1666 (B) mbsf in Hole 866A.

below. Density decreases abruptly below the contact, as does the resistivity. Both density and velocity changes are also shown in the physical-property data.

5. The very prominent reflector at 0.26 s twtt in the seismic profile (Fig. 69) probably correlates with the major lithologic change at 434.5 mbsf, but the calculated position of this reflector, using the curve in Figure 67, is about 0.25 s twtt. Either the velocities (as read from the log) are too slow, or the reflector has changed position by 0.01 s twtt, between Hole 866A and the seismic profile. This latter possibility is probably the more likely, given the good correspondence between calculated times and depths deeper in Hole 866A.

6. The reflector at 0.47 s twtt has no obvious correlation to the lithologic column. Its calculated depth is 725 m, in the middle of the oolite grainstones of lithologic Unit V.

7. The reflector at 0.55 s twtt may correlate with the top of the rudist limestone at 859.2 mbsf. Its calculated depth is 870 m.

8. The reflector at 0.72 s twtt correlates well with the top of lithologic Unit VII, at 1203.4 mbsf, below which, dolomite is the dominant rock type. Virtually all the logs and measurements indicates a significant break close to this depth. The reflection-coefficient curve (Fig. 68) shows closely spaced, strong negative and positive peaks near the depth of the lithologic break.

9. The deepest reflector clearly discernible in the seismic profile is at 0.94 s twtt, and has a calculated depth of 1625 m. This reflector

is most plausibly correlative to the top of the volcanic basement, which was at a depth of 1620.0 mbsf in Hole 866A.

REFERENCES*

- Baker, P.E., Buckley, F., and Holland, J.G., 1974. Petrology and geochemistry of Easter Island. *Contrib. Mineral. Petrol.*, 44:85-100.
- Bathurst, R.G.C., 1975. *Carbonate Sediments and Their Diagenesis* (2nd ed.): Amsterdam (Elsevier).
- Chase, T.E., Menard, H.W., and Mammerickx, J., 1971. *Topography of the North Pacific: La Jolla* (Univ. of Calif.).
- Dean, W.E., Claypool, G.E., and Thiede, J., 1981. Origin of organic-carbon-rich Mid-Cretaceous limestones, Mid-Pacific Mountains and southern Hess Rise. In Thiede, J., Vallier, T.L., et al., *Init. Repts. DSDP*, 62: Washington (U.S. Govt. Printing Office), 877-890.
- Deconinck, F.J., and Strasser, A., 1987. Sedimentology, clay mineralogy and depositional environment of Purbeckian green marls (Swiss and French Jura). *Eclogae Geol. Helv.*, 80:753-772.
- Gardner, G.H.F., Gardner, L.W., and Gregory, A.R., 1974. Formation velocity and density—the diagnostic basics for stratigraphic traps. *Geophysics*, 39:770-780.

* Abbreviations for names of organizations and publication titles in ODP reference lists follow the style given in *Chemical Abstracts Service Source Index* (published by American Chemical Society).

- Gordon, R., 1990. Test for bias in paleomagnetically determined paleolatitudes from Pacific Plate Deep Sea Drilling Project sediments. *J. Geophys. Res.*, 95:8397–8404.
- Haggerty, J.A., and Premoli Silva, I., 1986. Ooids and shallow-water debris in Aptian-Albian sediments from the East Mariana Basin, Deep Sea Drilling Project Site 585: implications for the environment of formation of ooids. In Moberly, R., Schlanger, S.O., et al., *Init. Repts DSDP*, 89: Washington (U.S. Govt. Printing Office), 399–412.
- Inden, F.R., and Moore, H.C., 1983. Beach. In Scholle, P.A., Bebout, D.G., Moore, H.C. (Eds.), *Carbonate Depositional Environments*. AAPG Mem., 33:211–265.
- James, P.N., 1977. Shallowing-upward sequences in carbonates. *Geosci. Can.*, 4:126–136.
- Kent, D.V., and Gradstein, F.M., 1985. A Cretaceous and Jurassic geochronology. *Geol. Soc. Am. Bull.*, 96:1419–1427.
- Maillard, J., 1965. Le passage Barrémien-Aptien et ses rapports avec l'Urgonien dans le couloir rhodanien. (Colloque sur le Crétacé inférieur, Lyon, 1963). *Mem. BRGM*, 34:146–156.
- Mammerickx, J., and Smith, S.M., 1985. *Bathymetry of the North Central Pacific*. Geol. Soc. Am., Map and Chart Ser., MC-52.
- Martini, E., 1971. Standard Tertiary and Quaternary calcareous nannoplankton zonation. In Farinacci, A. (Ed.), *Proc. 2nd Planktonic Conf. (Roma)*, 2:739–785.
- McFadden, P.L., and Reid, A.B., 1982. Analysis of paleomagnetic inclination data. *Geophys. J. R. Astron. Soc.*, 69:307–319.
- Nakanishi, M., Tamaki, K., and Kobayashi, K., 1989. Mesozoic magnetic anomaly lineations and seafloor spreading history of the Northwestern Pacific. *J. Geophys. Res.*, 94:15437–15462.
- , 1992. Magnetic anomaly lineations from Late Jurassic to Early Cretaceous in the west-central Pacific Ocean. *Geophys. J. Int.*, 109:701–719.
- Natland, J.H., Dieu, J.J., and Wright, E., in press. Petrology of volcanic rocks dredged from Cretaceous guyots of the central and western Pacific. In Pringle, M.S., Sager, W.W., Sliter, W.V., and Stein, S. (Eds.), *The Mesozoic Pacific*. Am. Geophys. Union, Geophys. Monogr.
- Nemoto, K., and Kroenke, L.W., 1985. Sio Guyot: a complex volcanic edifice in the western Mid-Pacific Mountains. *Geo. Mar. Lett.*, 5:83–89.
- Pacquier, V., 1903. Les rudistes urgoniens. *Soc. Geol. Fr. Mem. Paleontol.*, 29.
- Palmer, R., 1928. The rudistids of southern Mexico. *Occas. Pap. Calif. Acad. Sci.*, 14:1–137.
- Pearce, J.A., 1983. The role of sub-continental lithosphere in magma genesis at active continental margins. In Hawkesworth, C.J., and Norry, M.J. (Eds.), *Continental Basalts and Mantle Xenoliths*: Nantwich (Shiva Publ.), 230–250.
- Rider, M.H., 1986. *The Geologic Interpretation of Well Logs*: London (Blackie/Halsted Press).
- Roth, P.H., 1978. Cretaceous nannoplankton biostratigraphy and oceanography of the northwestern Atlantic Ocean. In Benson, W.E., Sheridan, R.E., et al., *Init. Repts. DSDP*, 44: Washington (U.S. Govt. Printing Office), 731–760.
- Sandberg, P.A., 1983. An oscillating trend in Phanerozoic non-skeletal carbonate mineralogy. *Nature*, 305:19–22.
- Serra, O., 1986. *Fundamentals of Well Log Interpretation (Vol. 2): The Interpretation of Logging Data*: Amsterdam (Elsevier).
- Shinn, E.A., 1983. Tidal flat environment. In Scholle, P.A., Bebout, D.G., and Moore, C. H. (Eds.), *Carbonate Depositional Environments*. AAPG Mem., 33:171–210.
- Sissingh, W., 1977. Biostratigraphy of Cretaceous calcareous nannoplankton. *Geol. Mijnbouw*, 56:37–65.
- Skelton, P., 1982. Aptian and Barremian rudist bivalves of the New World: some old world similarities. *Cretaceous Res.*, 3:145–153.
- Strasser, A., 1984. Black-pebble occurrence and genesis in Holocene carbonate sediments (Florida Keys, Bahamas, and Tunisia). *J. Sediment. Petrol.*, 54:1097–1109.
- , 1991. Lagoonal-peritidal sequences in carbonate environments: autocyclic and allocyclic processes. In Einsele, G., Ricken, W., and Seilacher, A. (Eds.), *Cycles and Events in Stratigraphy*: Berlin (Springer-Verlag).
- Tarduno, J.A., 1990. Absolute inclination values from deep sea sediments: a reexamination of the Cretaceous Pacific record. *Geophys. Res. Lett.*, 17:101–104.
- Tarduno, J., Sliter, W.V., Bralower, T.J., McWilliams, M., Premoli Silva, I., and Ogg, J.G., 1989. M-sequence reversals recorded in DSDP sediment cores from the western Mid-Pacific Mountains and Magellan Rise. *Geol. Soc. Am. Bull.*, 101:1306–1316.
- Tedesco, P.L., and Wanless, H., 1991. Generation of sedimentary fabrics and facies by repetitive excavation and storm infilling of burrow networks, Holocene of South Florida and Caicos Platform, B.W.I. *Palaios*, 6:326–343.
- Thiede, J., Vallier, T.L., et al., 1981. *Init. Repts DSDP*, 62: Washington (U.S. Govt. Printing Office).
- van Waasbergen, R.J., 1992. Western Pacific guyots: summit geomorphology, sedimentology, and structure of drowned Cretaceous carbonate platforms. [Ph.D. dissert.]. Univ. Calif., San Diego.
- van Waasbergen, R.J., and Winterer, E.L., in press. Summit geomorphology of Western Pacific guyots. In Pringle, M.S., Sager, W.W., Sliter, W.V., and Stein, S. (Eds.), *The Mesozoic Pacific*. Am. Geophys. Union, Geophys. Monogr. Ser.

Ms 143IR-107

NOTE: For all sites drilled, core-description forms (“barrel sheets”) and core photographs have been reproduced on coated paper and can be found in Section 3, beginning on page 381. Forms containing smear-slide data can be found in Section 4, beginning on page 691. Thin-section data are given in Section 5, beginning on page 709. Conventional and geochemical-log, FMS, and dipmeter data can be found in CD-ROM form (back pocket).

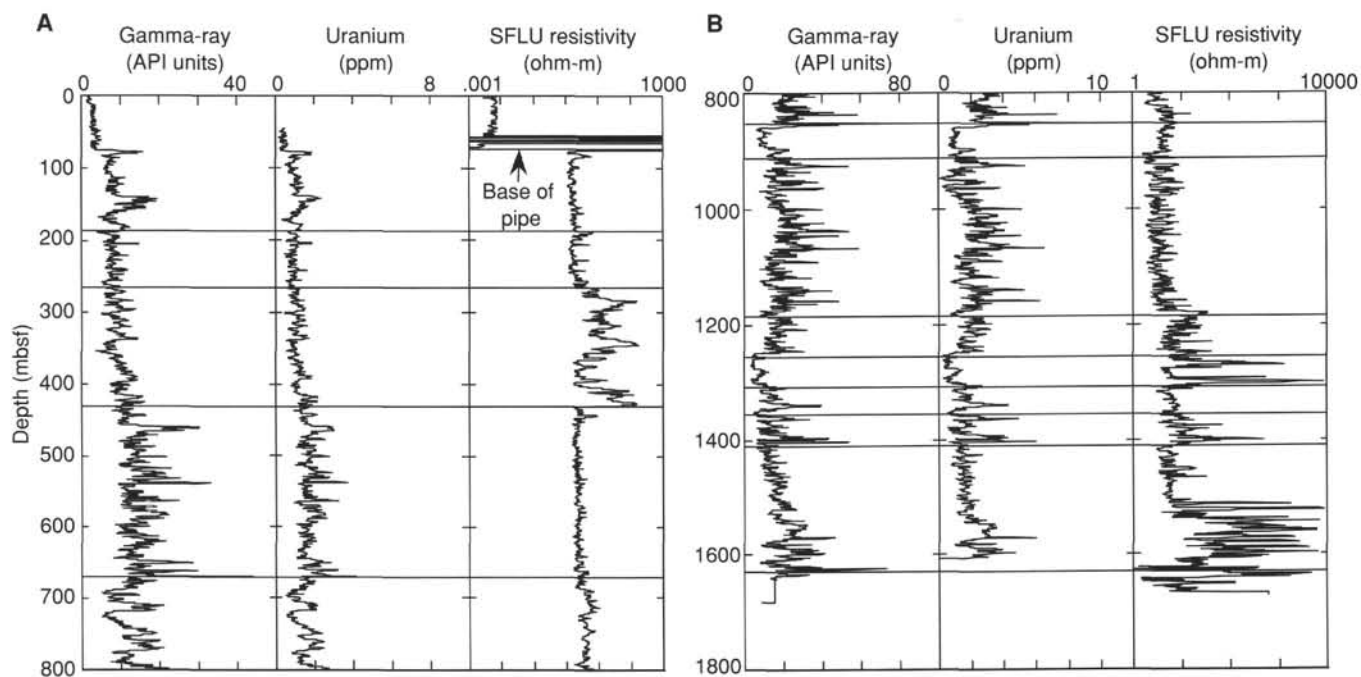


Figure 62. Gamma-ray, uranium, and shallow-focused resistivity logs (SFLU). Horizontal lines denote the boundaries (A, 0–800 mbsf; B, 800–1666 mbsf) of the log units discussed in the text.

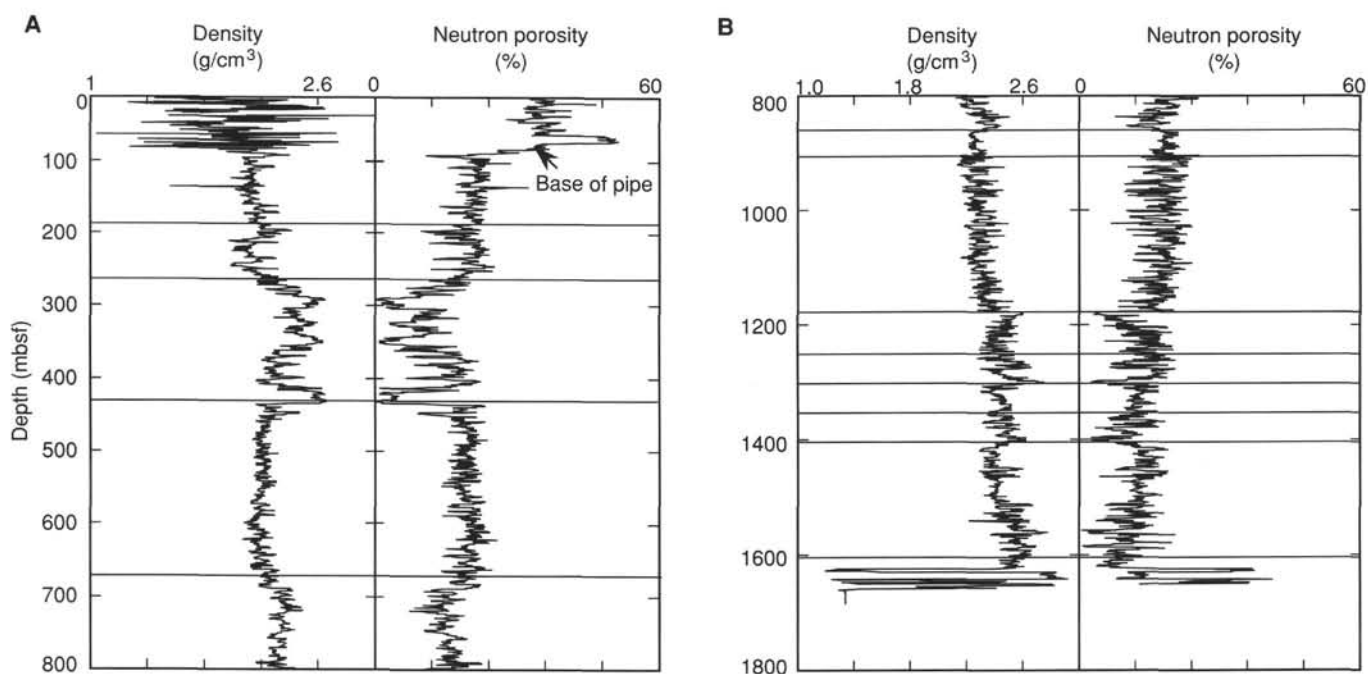


Figure 63. Density and neutron porosity logs, Hole 866A; horizontal lines denote the boundaries (A, 0–800 mbsf; B, 800–1666 mbsf) of the log units discussed in the text.

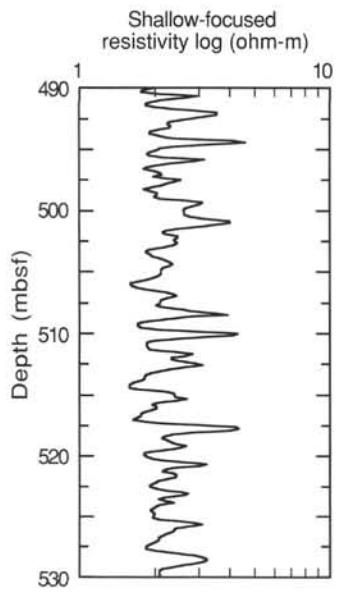


Figure 64. Shallow-focused resistivity profile from log Unit 4, illustrating the cyclicity of the log data.

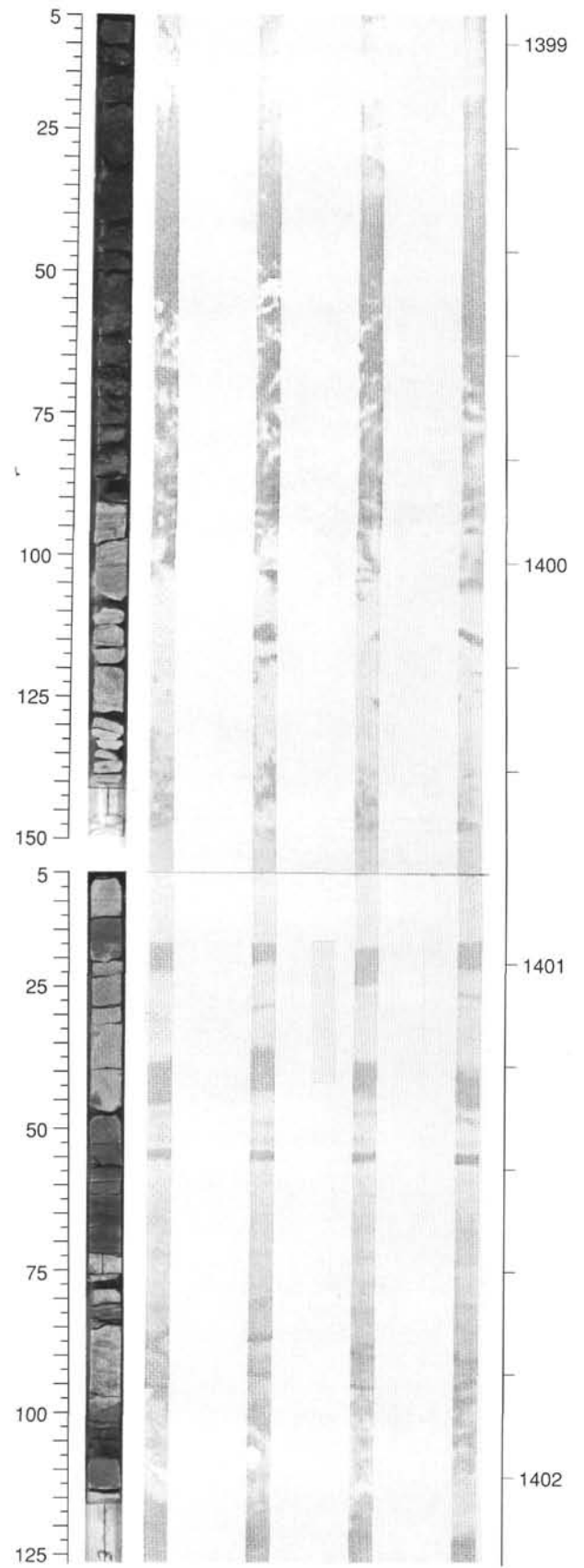


Figure 65. FMS image from 1399 to 1402 mbsf (log depth), compared with a photograph of the corresponding interval of core.

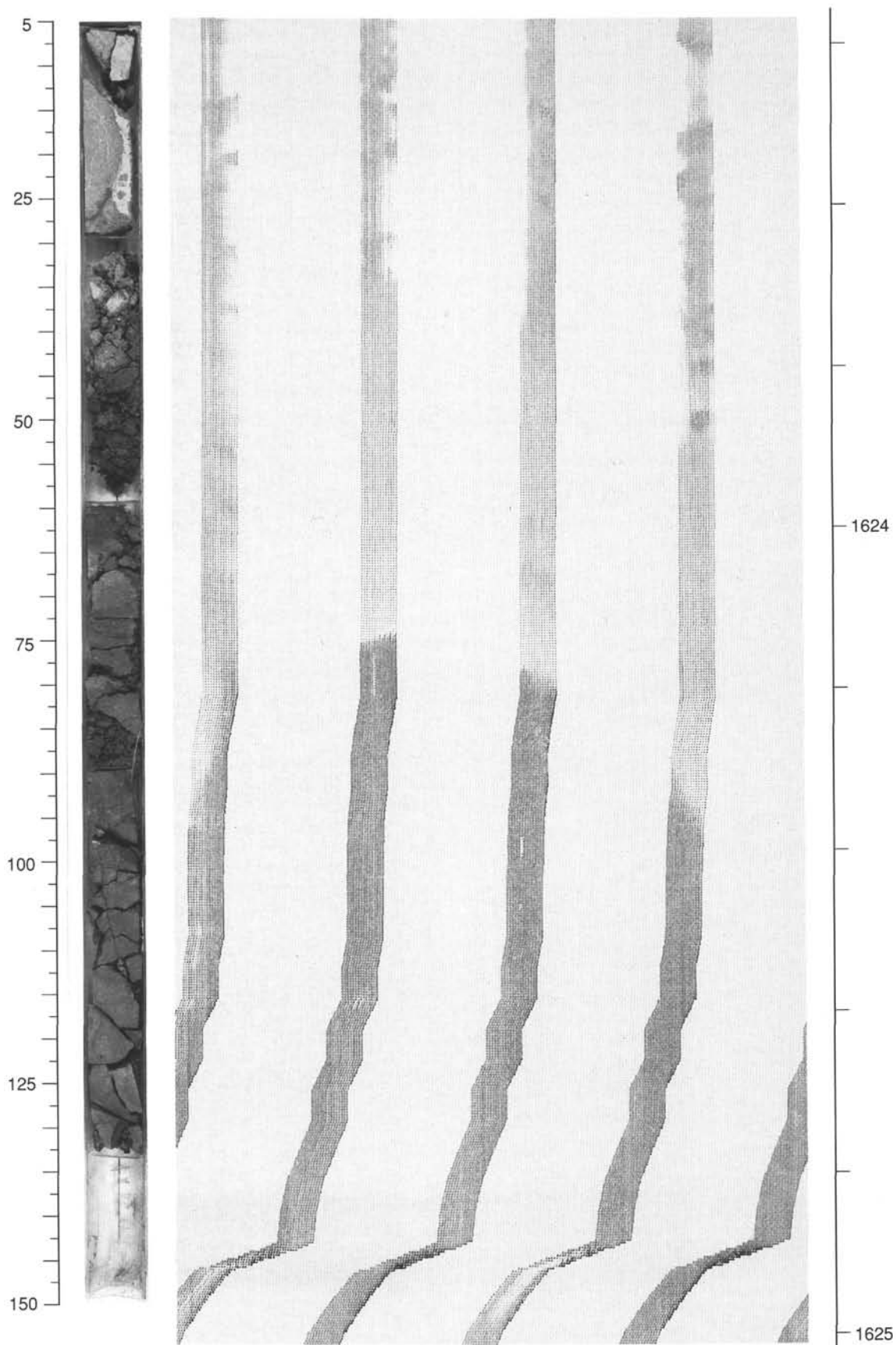


Figure 66. FMS image of the sediment/basalt contact at 1624.2 mbsf (log depth).

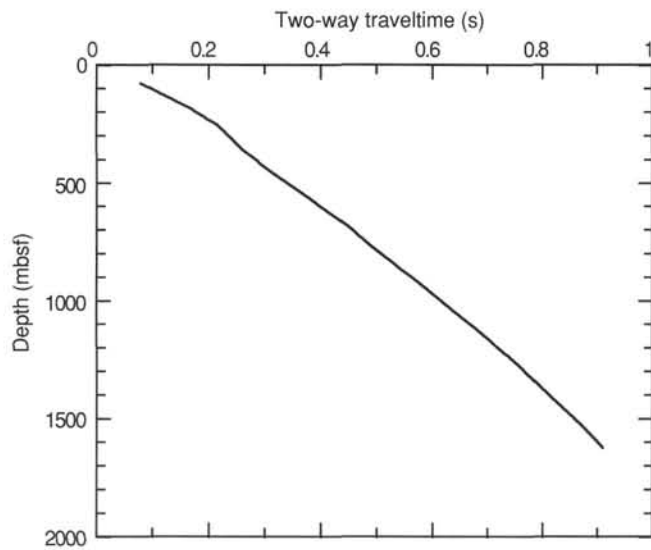


Figure 67. Plot of seismic traveltime vs. depth in Hole 866A. The curve was derived using average sonic velocities over successive 0.5-m intervals, taken from the sonic log of the hole. A starting value was estimated for the top of the curve, because the uppermost part of the hole was shielded by the BHA and, therefore, no sonic log could be obtained there.

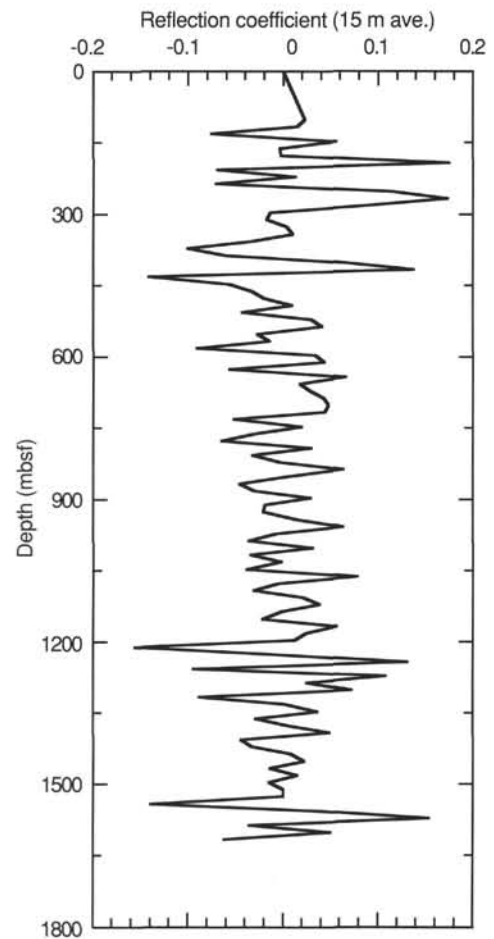


Figure 68. Plot of calculated reflection coefficient vs. depth in Hole 866A. The curve was calculated by first using the 0.5-m averages of sonic velocity and density from the downhole logs to compute average acoustic impedances for each 15-m segment of the hole. Then, the corresponding reflection coefficients for 15-m intervals were computed. The 15-m value was used because it is roughly one-half the wave length of the seismic waves (50–100 Hz, at 3 km/s) and thus should be roughly tuned to the seismic profile.

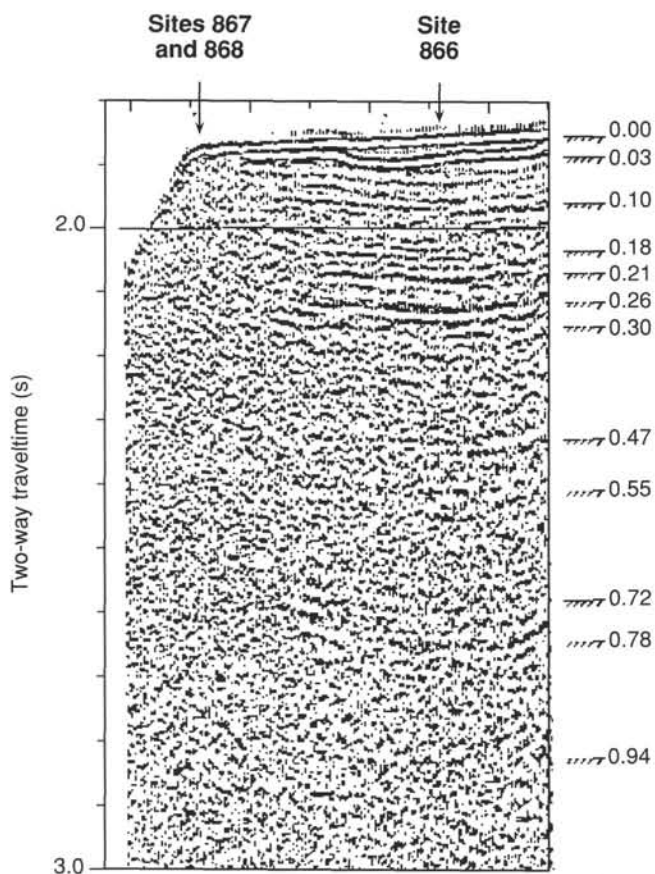


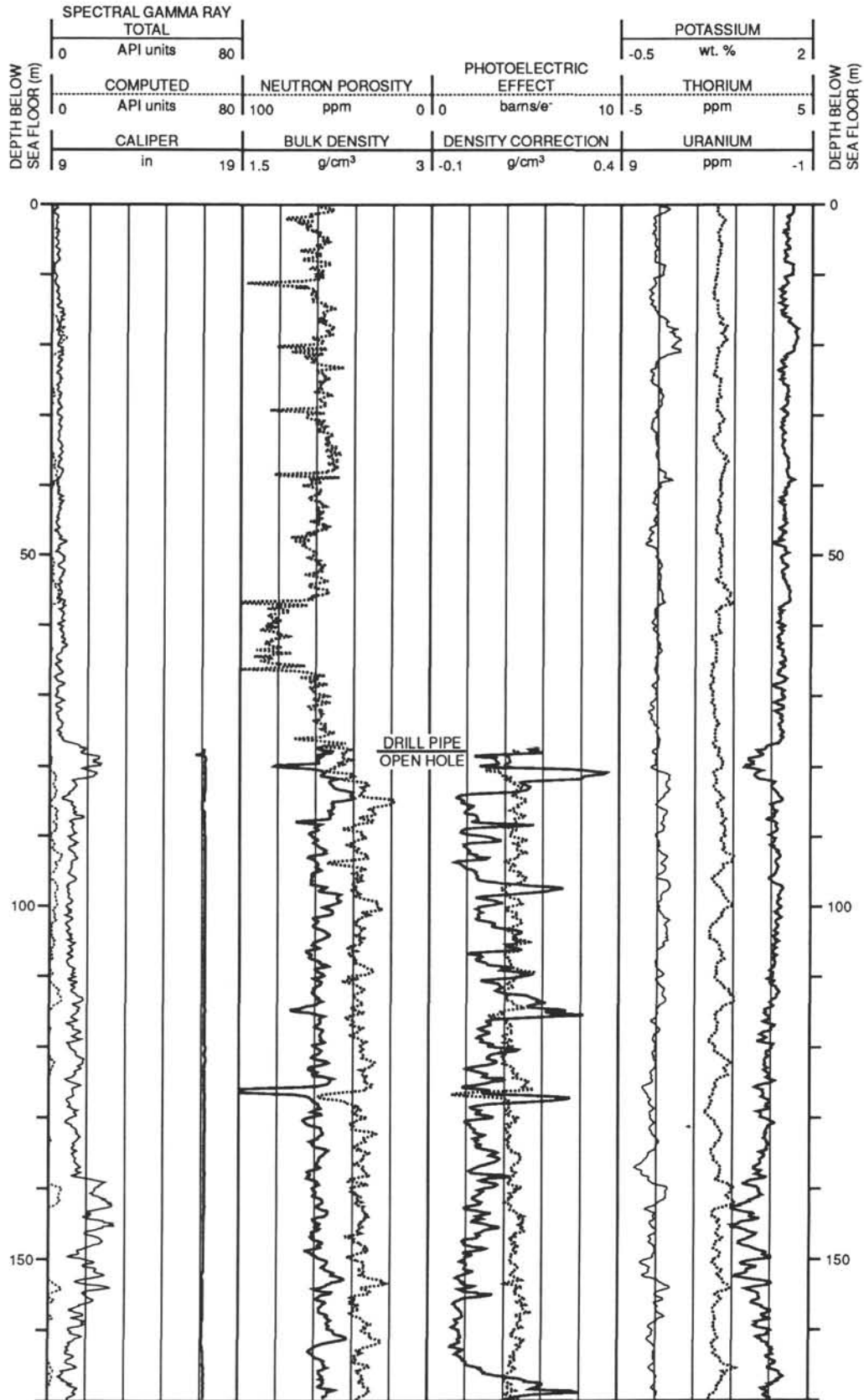
Table 13. Seismic reflector depths at Site 866.

Reflector twtt (s)	Calculated depth (mbsf)	Reflection coefficient >1, <-1 (m)	Physical-properties break depth (m)	Lithologic unit tops (mbsf)
0.00	0			0
0.03				27
0.10	100			
0.18				
0.21	245			
0.26	350	270(+)		271
		410(+)		
		435(-)	(-)430	434.5
				676.5
0.47	725			791.8
0.55	870			
0.72	1200	1210(-)	(+)1199	1203.4
			1240(+)	1251.6
			1275(-)	
0.78	1310			1399.5
			1545(-)	
0.94	1625		1575	1619.9
				(+)1641

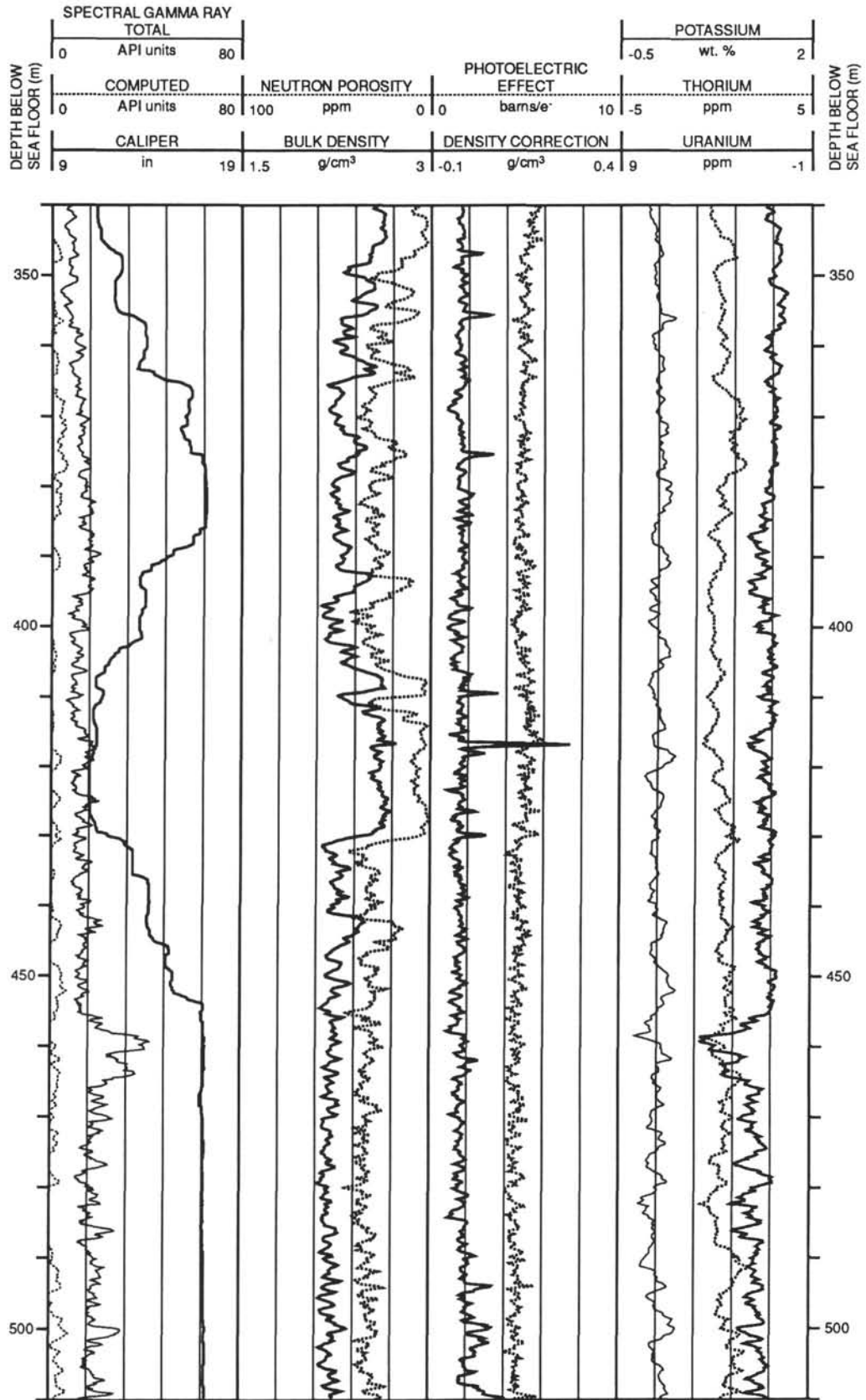
Note: Column 1 = reflectors in seismic profile near Site 866 (Fig. 69). Column 2 = calculated depth to reflectors (see Fig. 67). Column 3 = depths where reflection coefficient is greater than +0.1 or less than -0.1 (see Fig. 68). Column 4 = depths of marked changes in density and/or sonic velocity measured in core samples from Hole 866A (see Fig. 58). Column 5 = depths to major lithologic changes (see Fig. 58).

Figure 69. Portion of the seismic profile made from the *Thomas Washington* over Resolution Guyot (see Fig. 7), showing principal reflectors beneath Site 866. The actual position of Site 866 is about 1.2 km east-northeast of the profile, but along the same broad troughlike structure. Slight differences may exist between the positions of the reflectors between the site and the profile line.

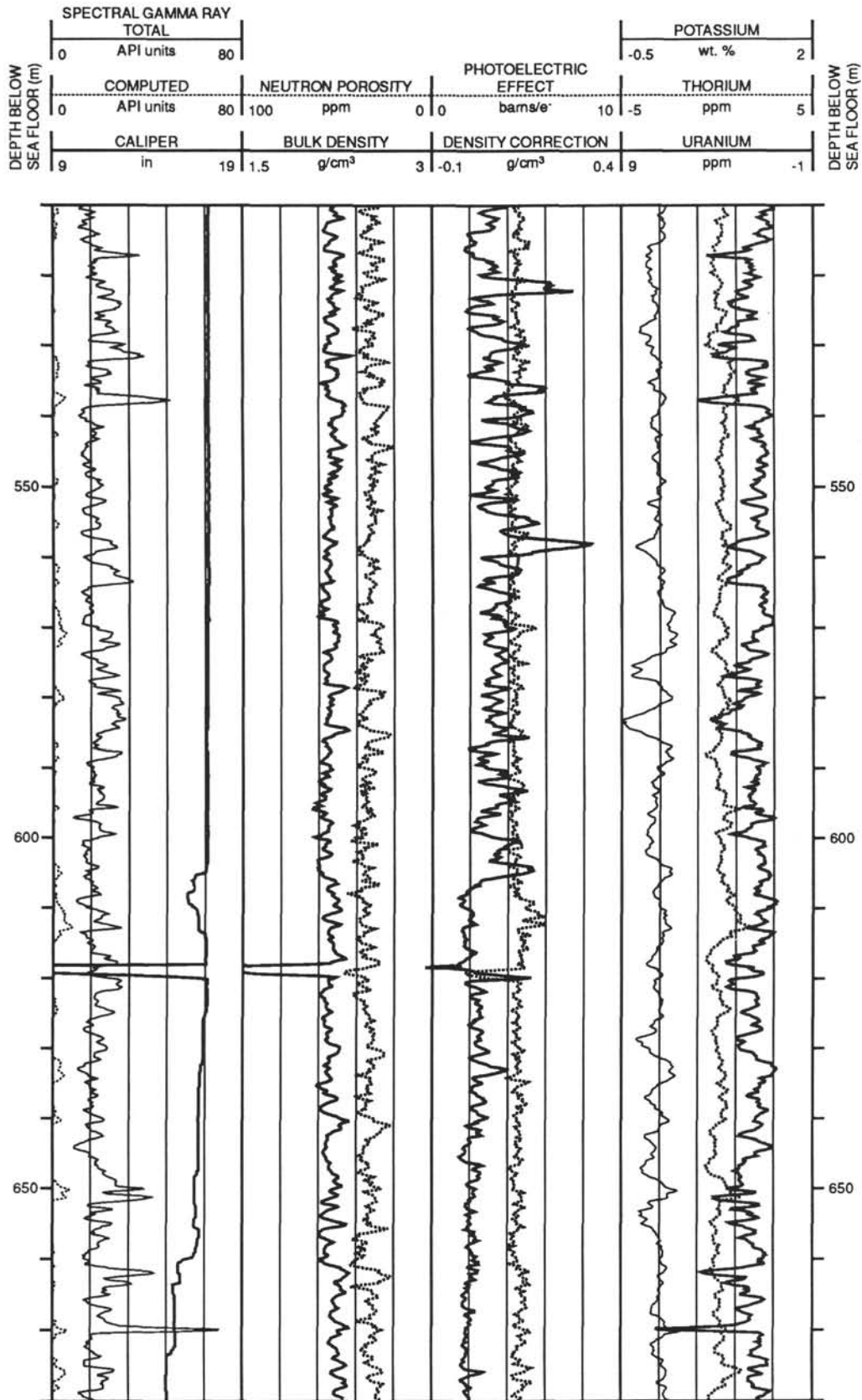
Hole 866A: Density-Porosity-Natural Gamma Ray Log Summary



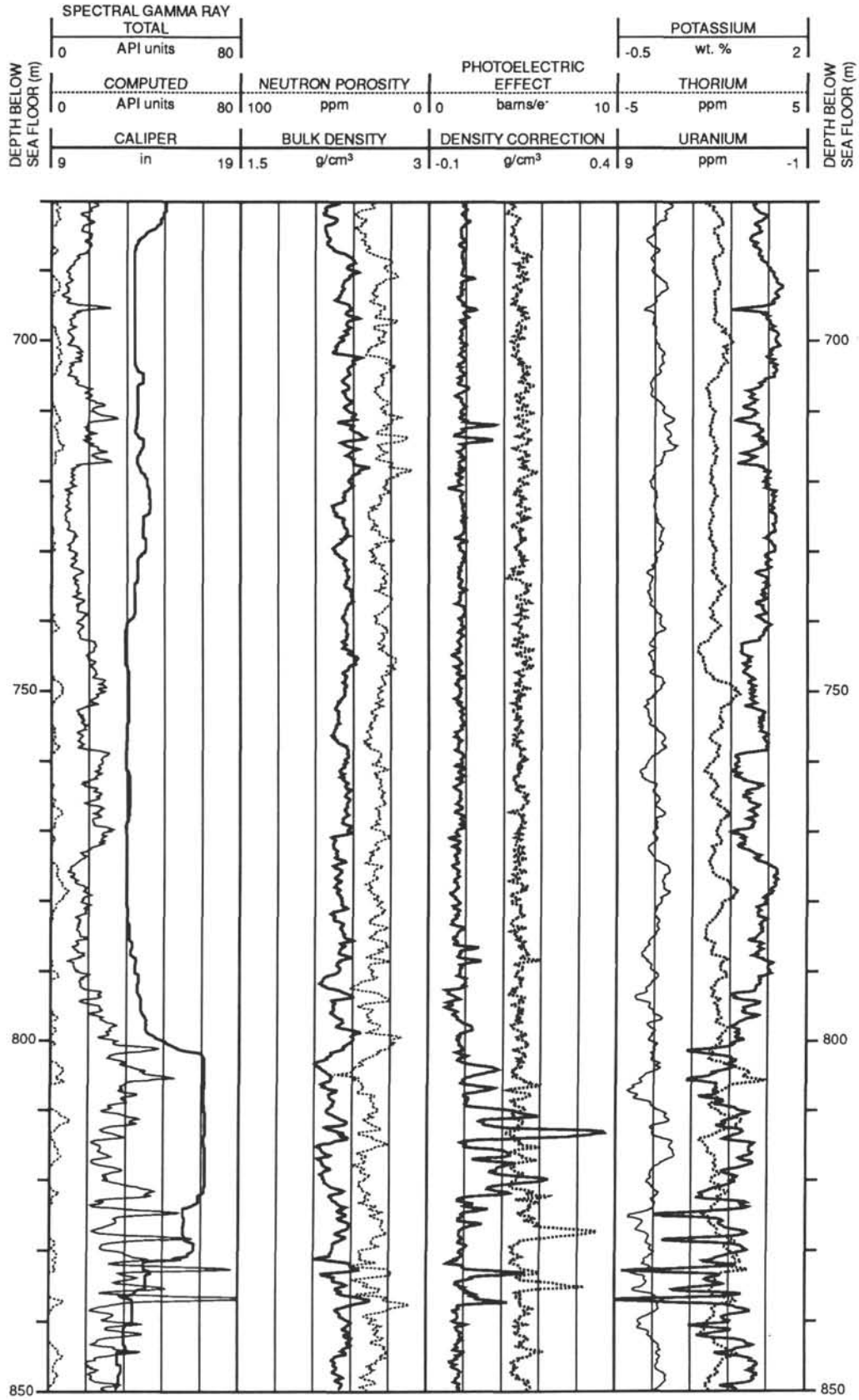
Hole 866A: Density-Porosity-Natural Gamma Ray Log Summary (continued)



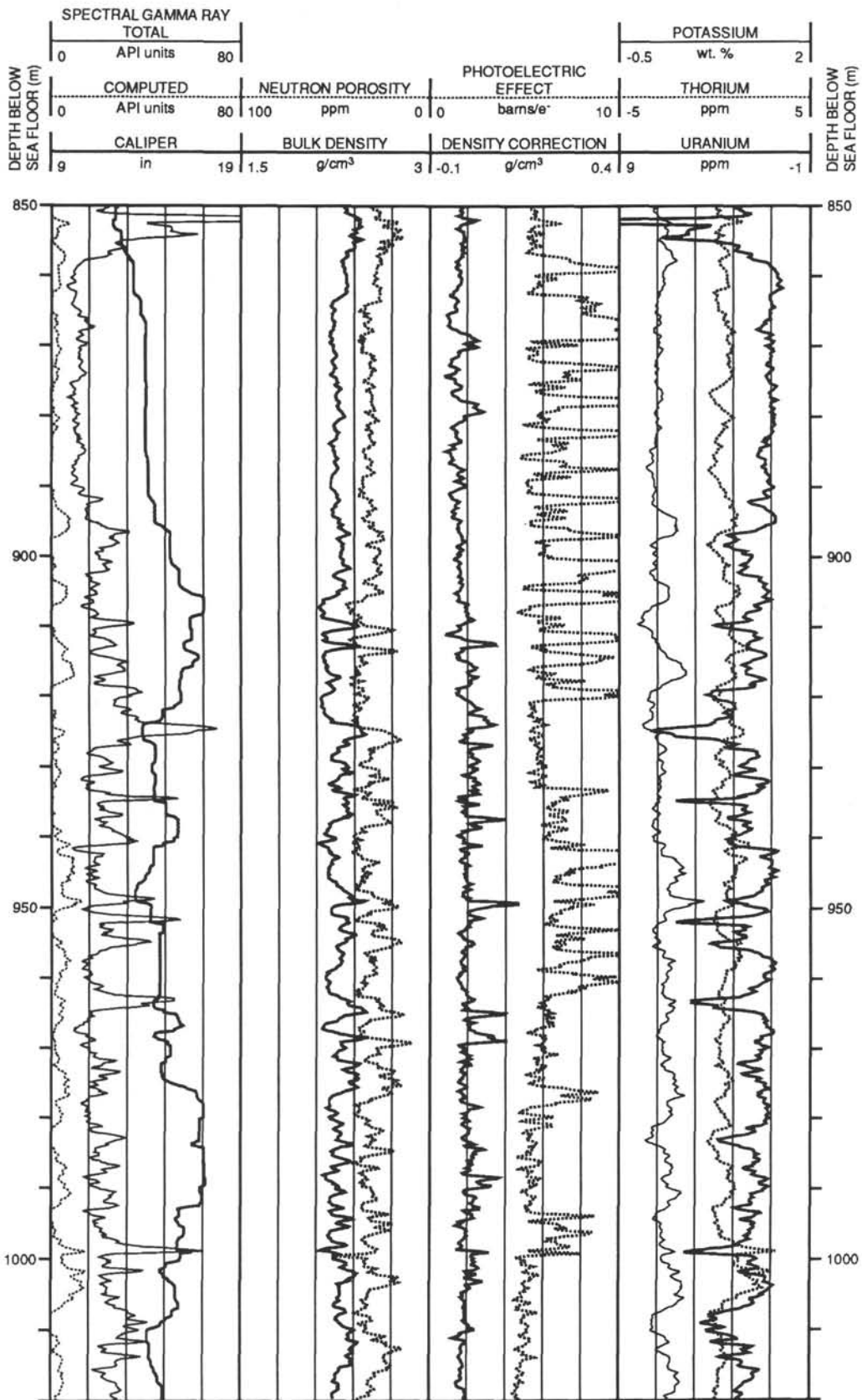
Hole 866A: Density-Porosity-Natural Gamma Ray Log Summary (continued)



Hole 866A: Density-Porosity-Natural Gamma Ray Log Summary (continued)

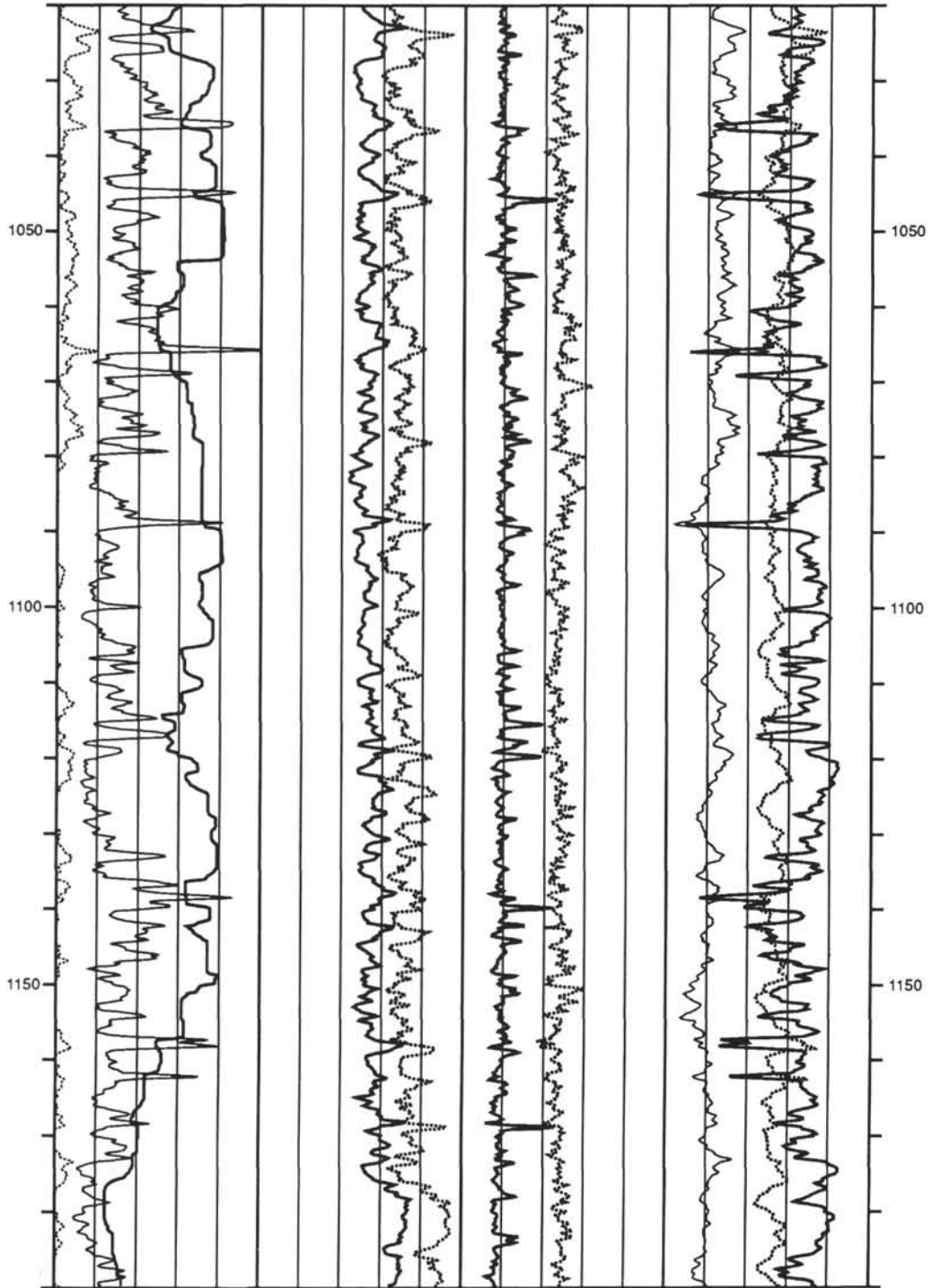


Hole 866A: Density-Porosity-Natural Gamma Ray Log Summary (continued)

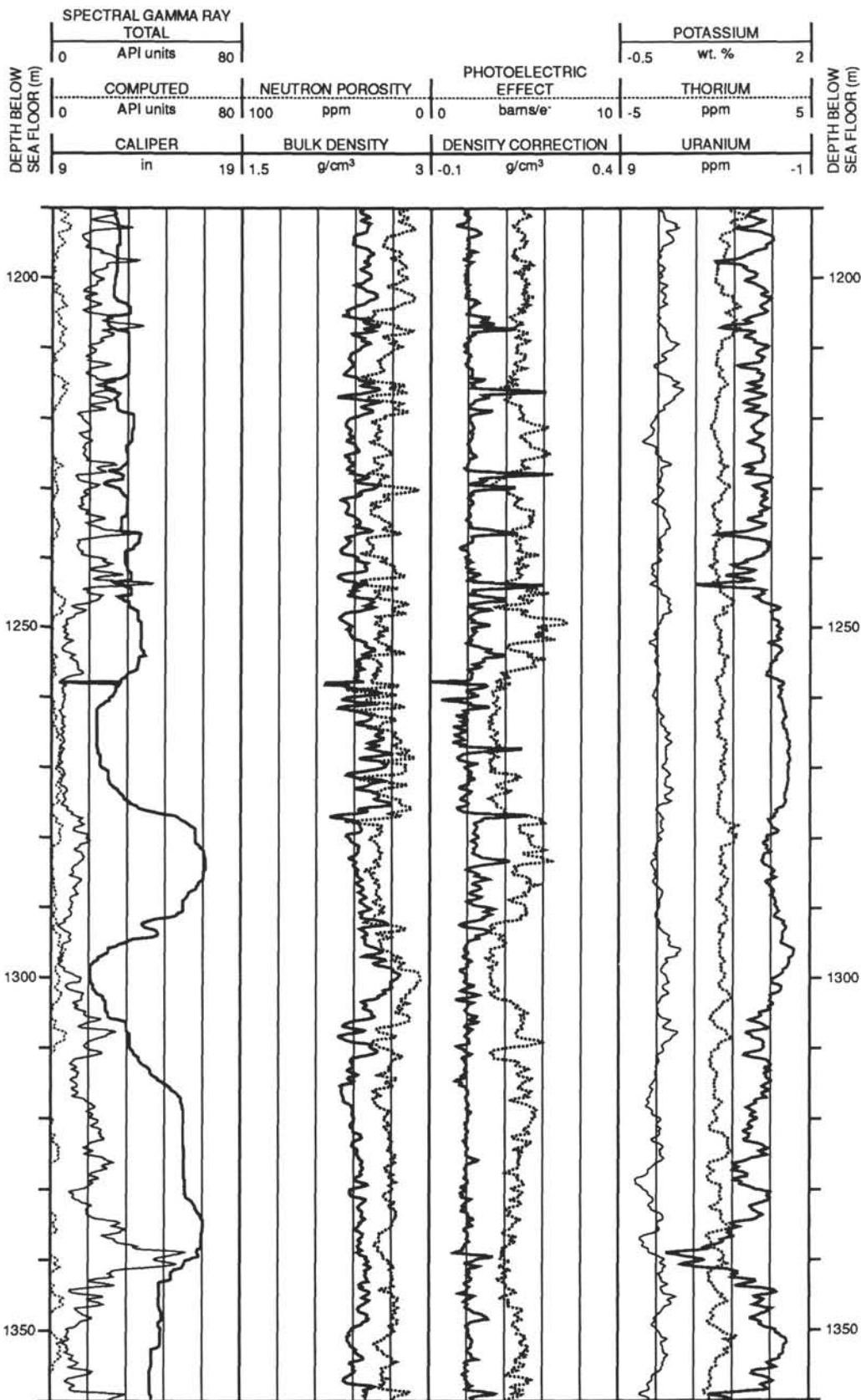


Hole 866A: Density-Porosity-Natural Gamma Ray Log Summary (continued)

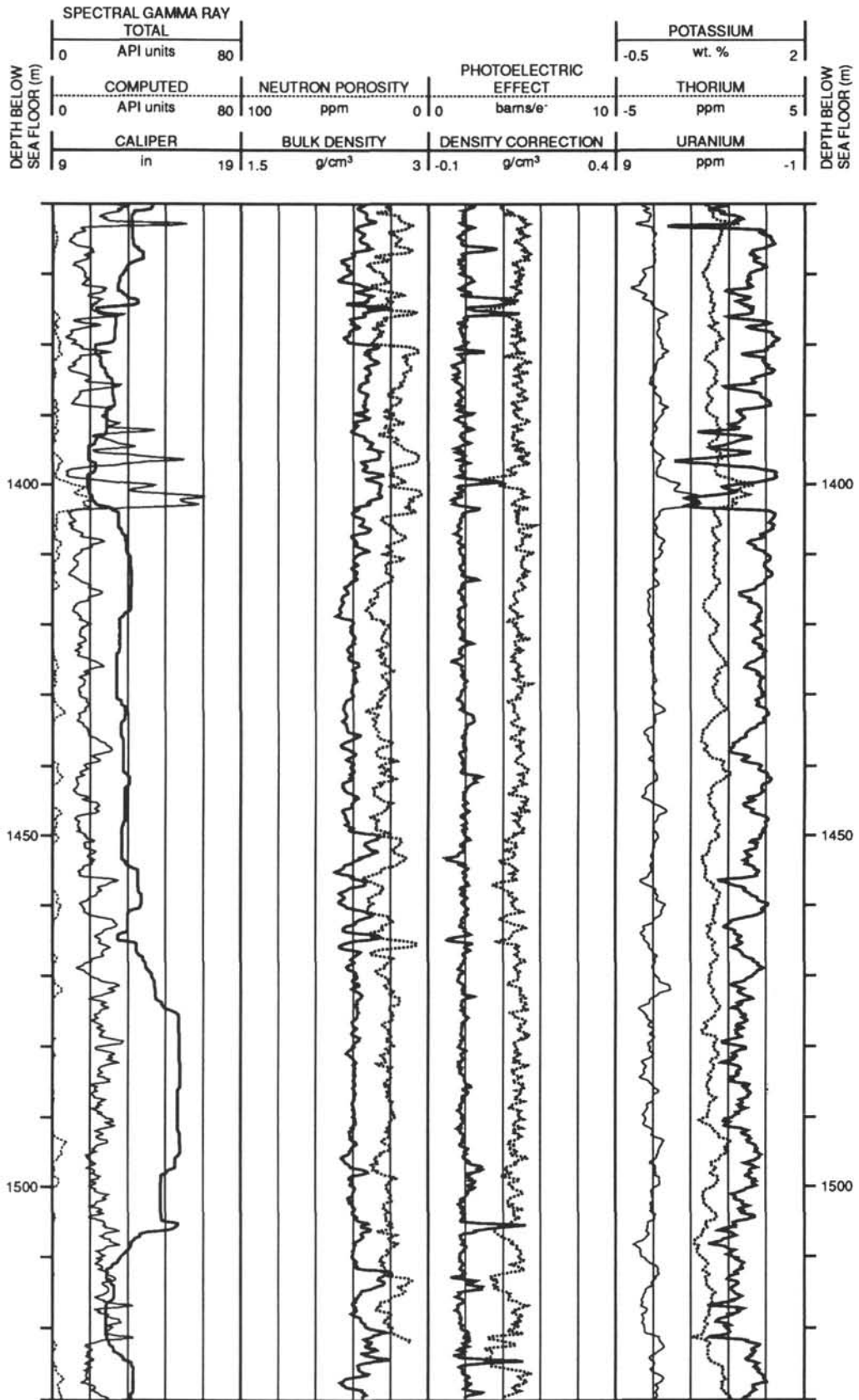
DEPTH BELOW SEA FLOOR (m)	SPECTRAL GAMMA RAY				PHOTOELECTRIC EFFECT				POTASSIUM		DEPTH BELOW SEA FLOOR (m)
	TOTAL		NEUTRON POROSITY	EFFECT	THORIUM						
	API units	API units			ppm	ppm					
0	0	80	100	0	0	10	-5	5	2		
	COMPUTED		BULK DENSITY	DENSITY CORRECTION	URANIUM						
	API units	API units			g/cm ³	g/cm ³	ppm				
9	19	19	1.5	3	-0.1	0.4	9	-1			



Hole 866A: Density-Porosity-Natural Gamma Ray Log Summary (continued)

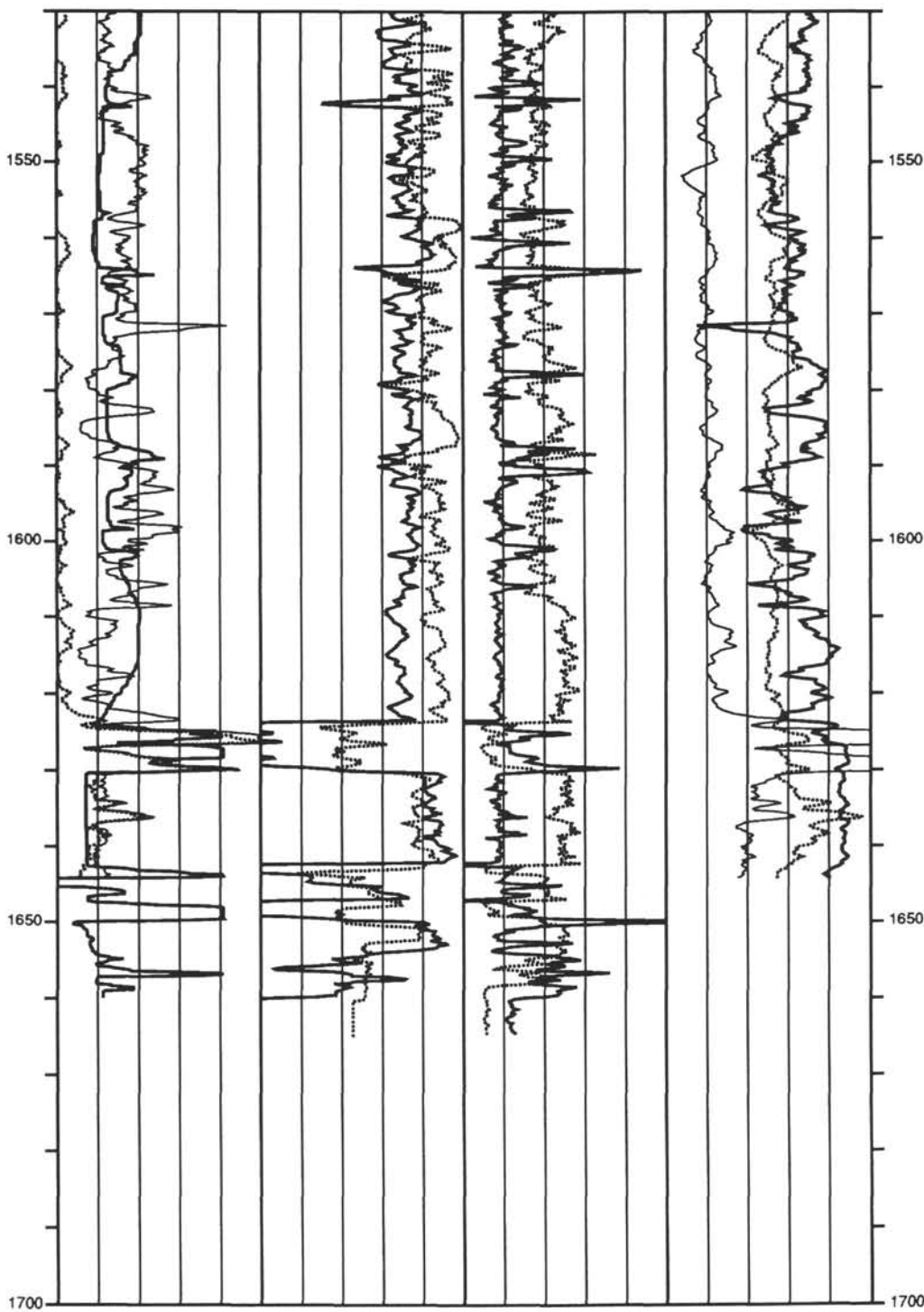


Hole 866A: Density-Porosity-Natural Gamma Ray Log Summary (continued)

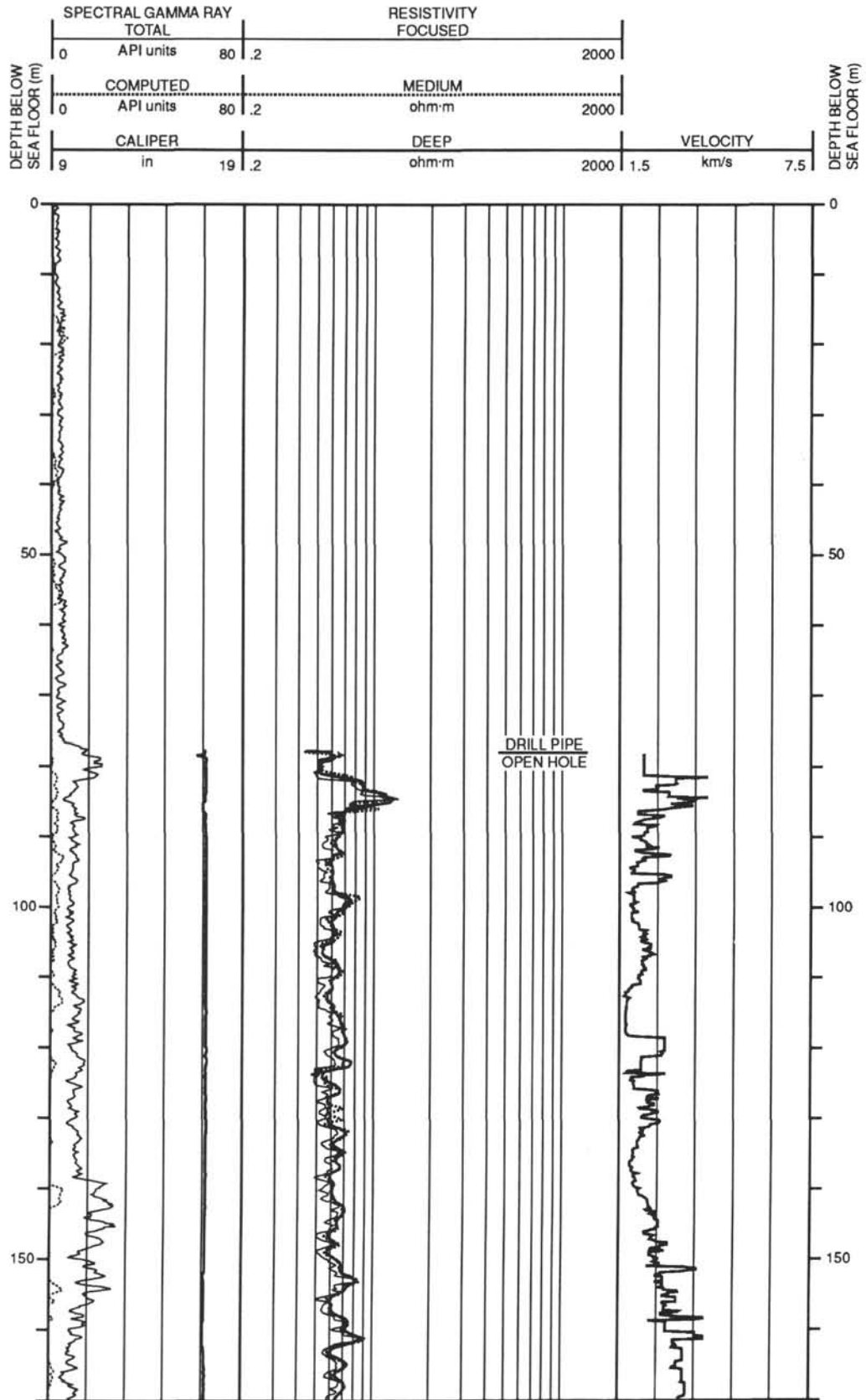


Hole 866A: Density-Porosity-Natural Gamma Ray Log Summary (continued)

SPECTRAL GAMMA RAY				POTASSIUM	
TOTAL				wt. %	
0	API units	80		-0.5	2
COMPUTED		NEUTRON POROSITY		PHOTOELECTRIC EFFECT	
API units		ppm		barns/e	
0	80	100	0	0	10
CALIPER		BULK DENSITY		DENSITY CORRECTION	
in		g/cm ³		g/cm ³	
9	19	1.5	3	-0.1	0.4
				URANIUM	
				ppm	
				9	-1

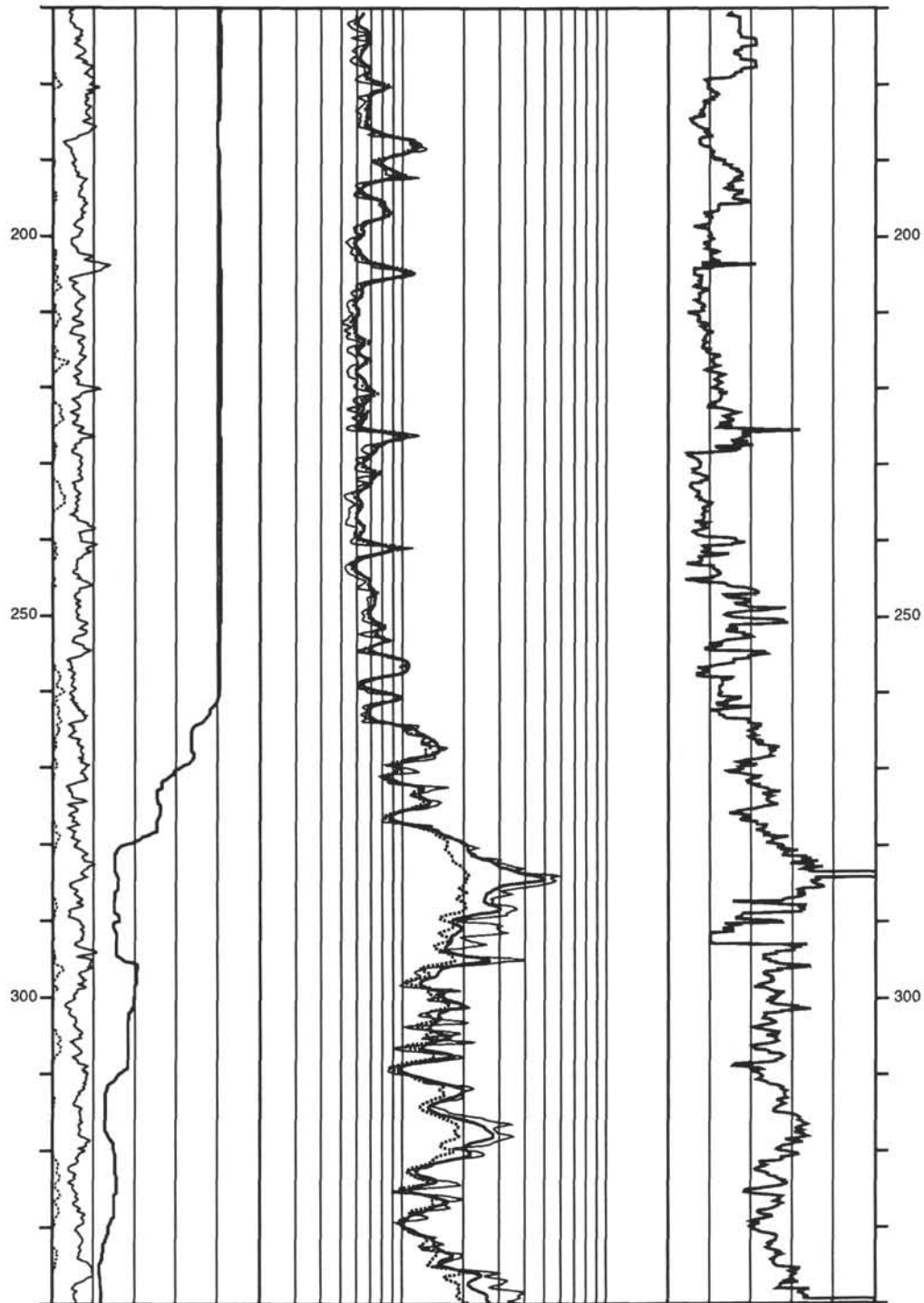


Hole 866A: Resistivity-Sonic-Natural Gamma Ray Log Summary

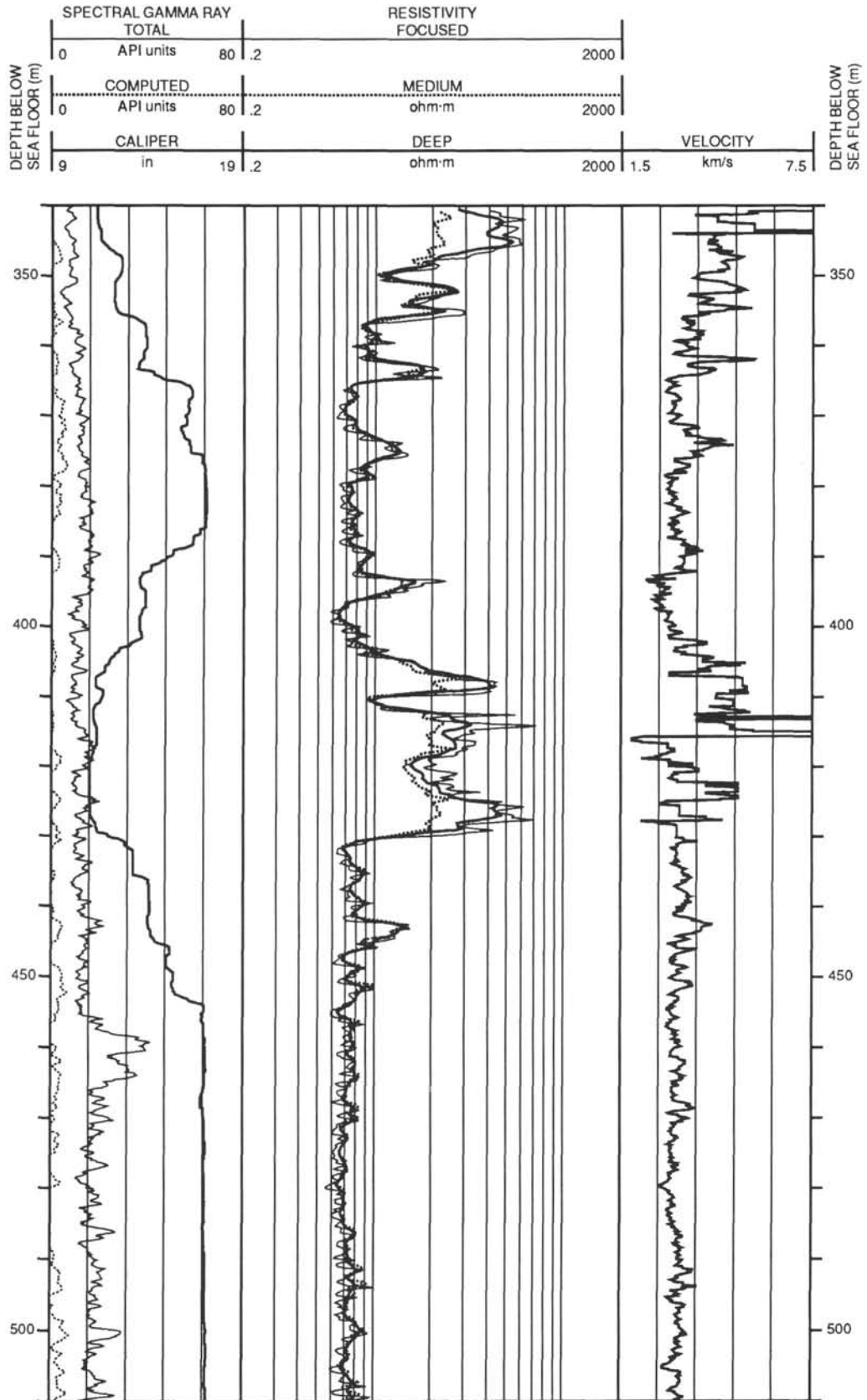


Hole 866A: Resistivity-Sonic-Natural Gamma Ray Log Summary (continued)

SPECTRAL GAMMA RAY				RESISTIVITY			
TOTAL				FOCUSED			
0	API units	80	.2	2000			
COMPUTED				MEDIUM			
0	API units	80	.2	ohm·m			
CALIPER				DEEP		VELOCITY	
9	in	19	.2	ohm·m	2000	1.5	km/s
						7.5	

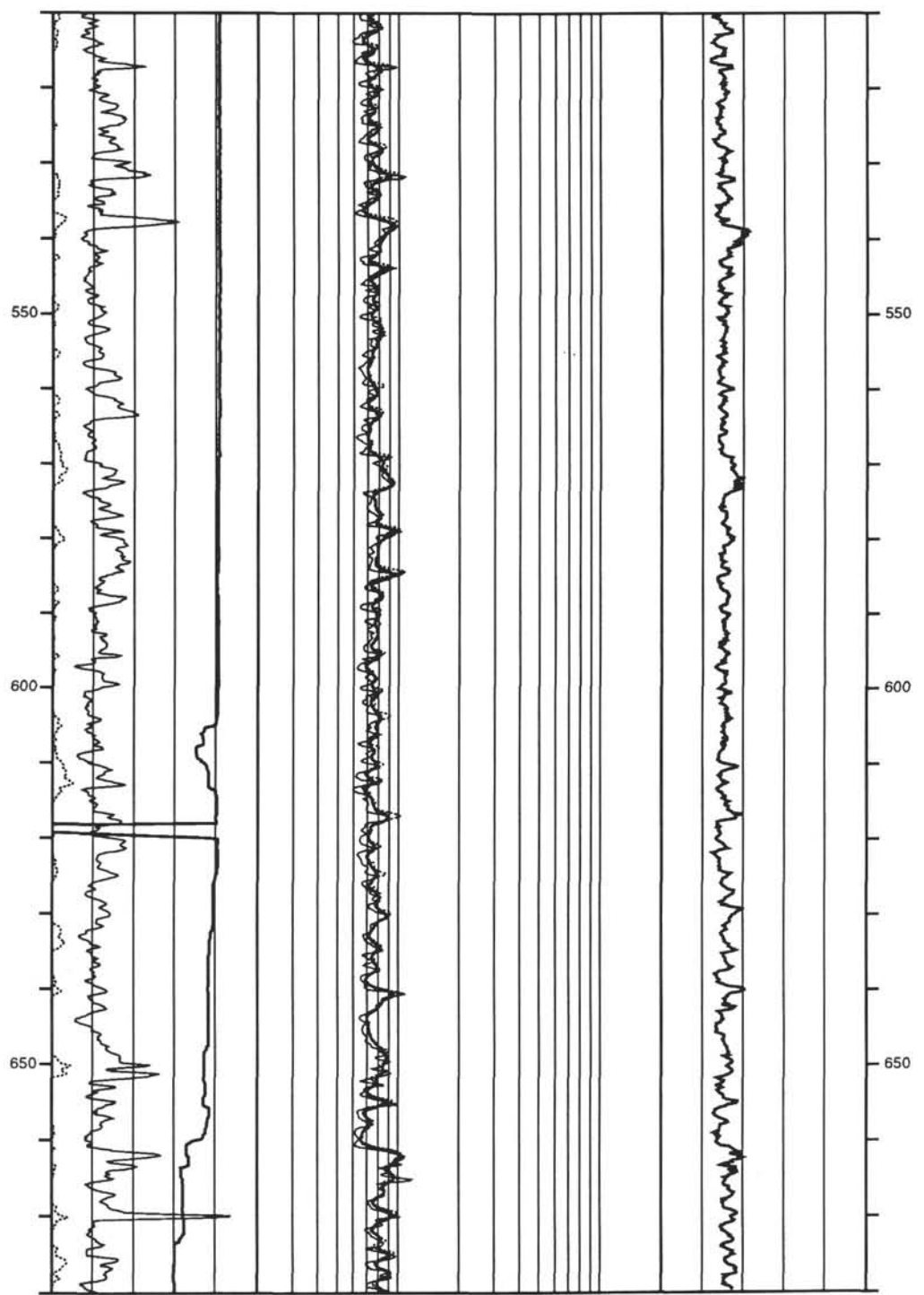


Hole 866A: Resistivity-Sonic-Natural Gamma Ray Log Summary (continued)

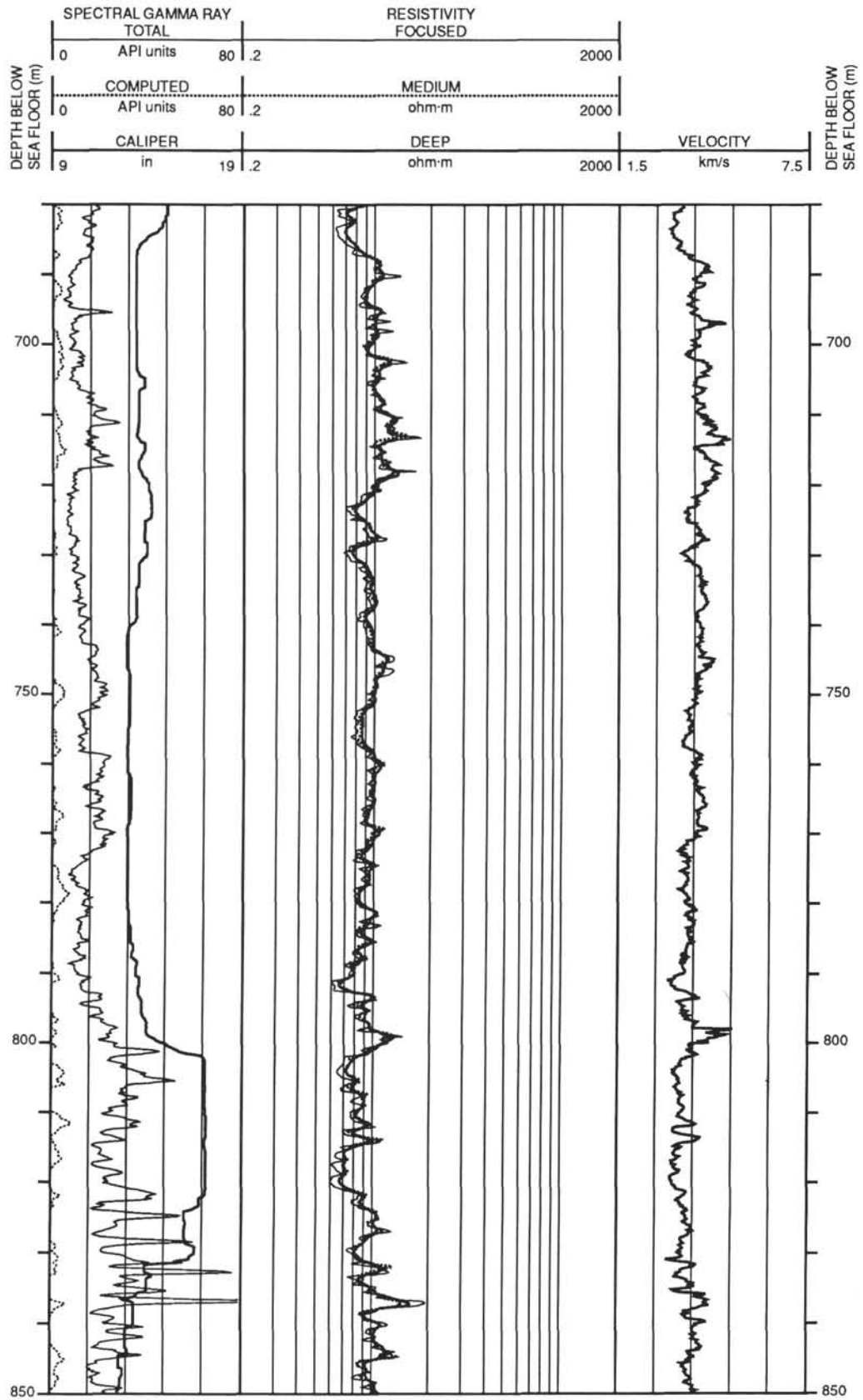


Hole 866A: Resistivity-Sonic-Natural Gamma Ray Log Summary (continued)

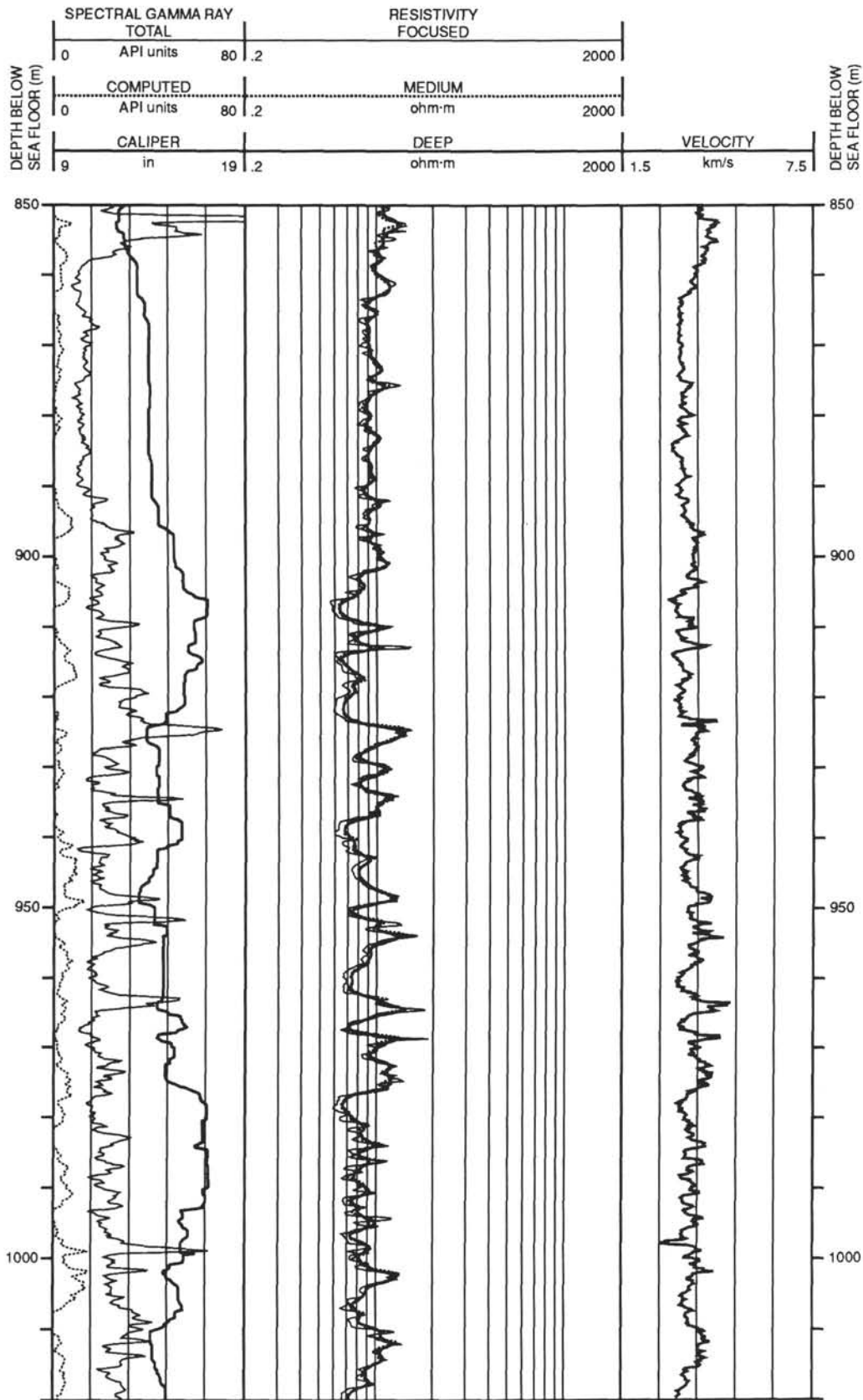
DEPTH BELOW SEA FLOOR (m)	SPECTRAL GAMMA RAY			RESISTIVITY			DEPTH BELOW SEA FLOOR (m)
	TOTAL			FOCUSED			
	0	API units	80 .2	2000			
0	COMPUTED			MEDIUM			2000
	API units			ohm-m			
9	CALIPER			DEEP			VELOCITY
	in			ohm-m			



Hole 866A: Resistivity-Sonic-Natural Gamma Ray Log Summary (continued)

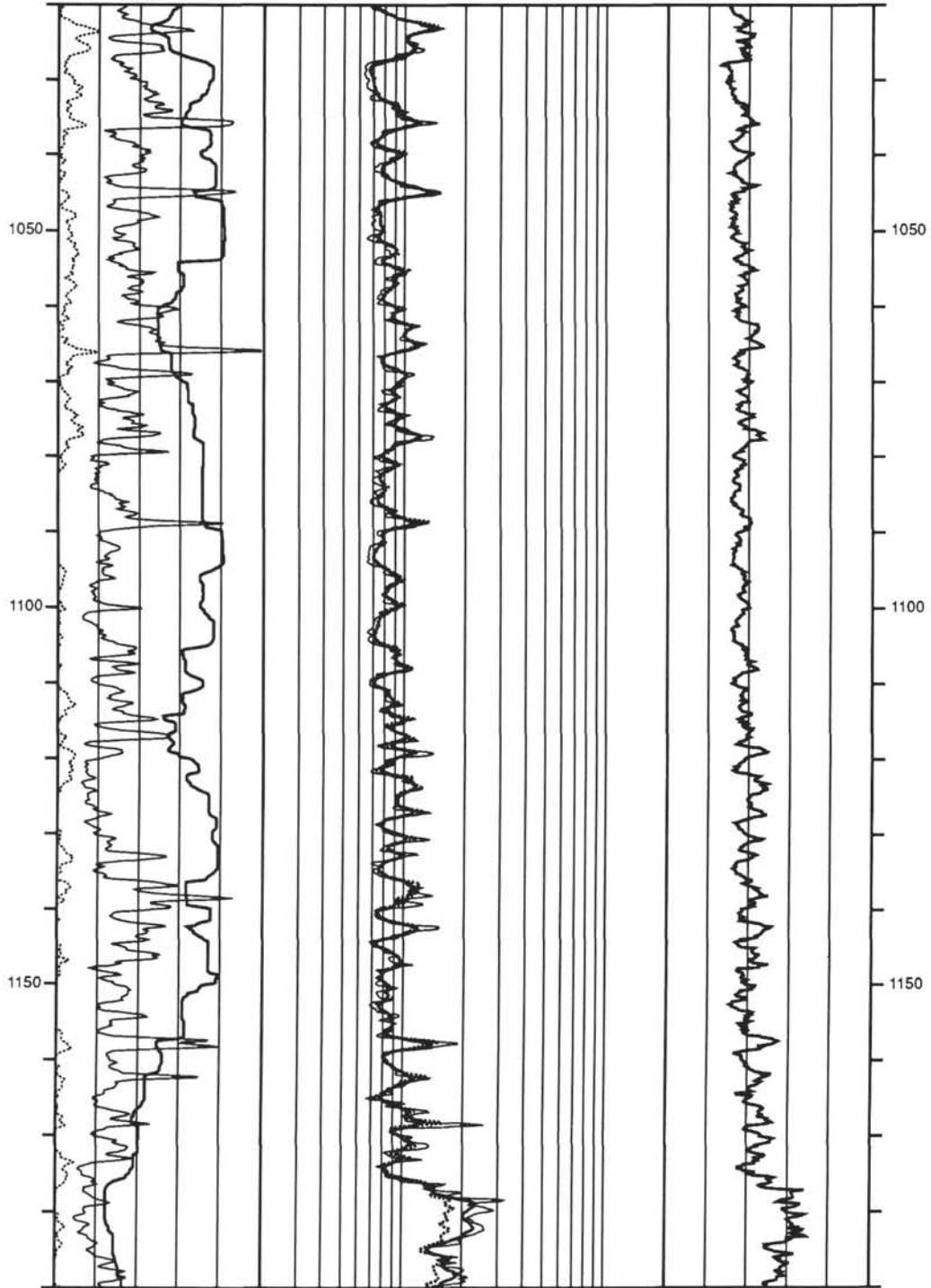


Hole 866A: Resistivity-Sonic-Natural Gamma Ray Log Summary (continued)



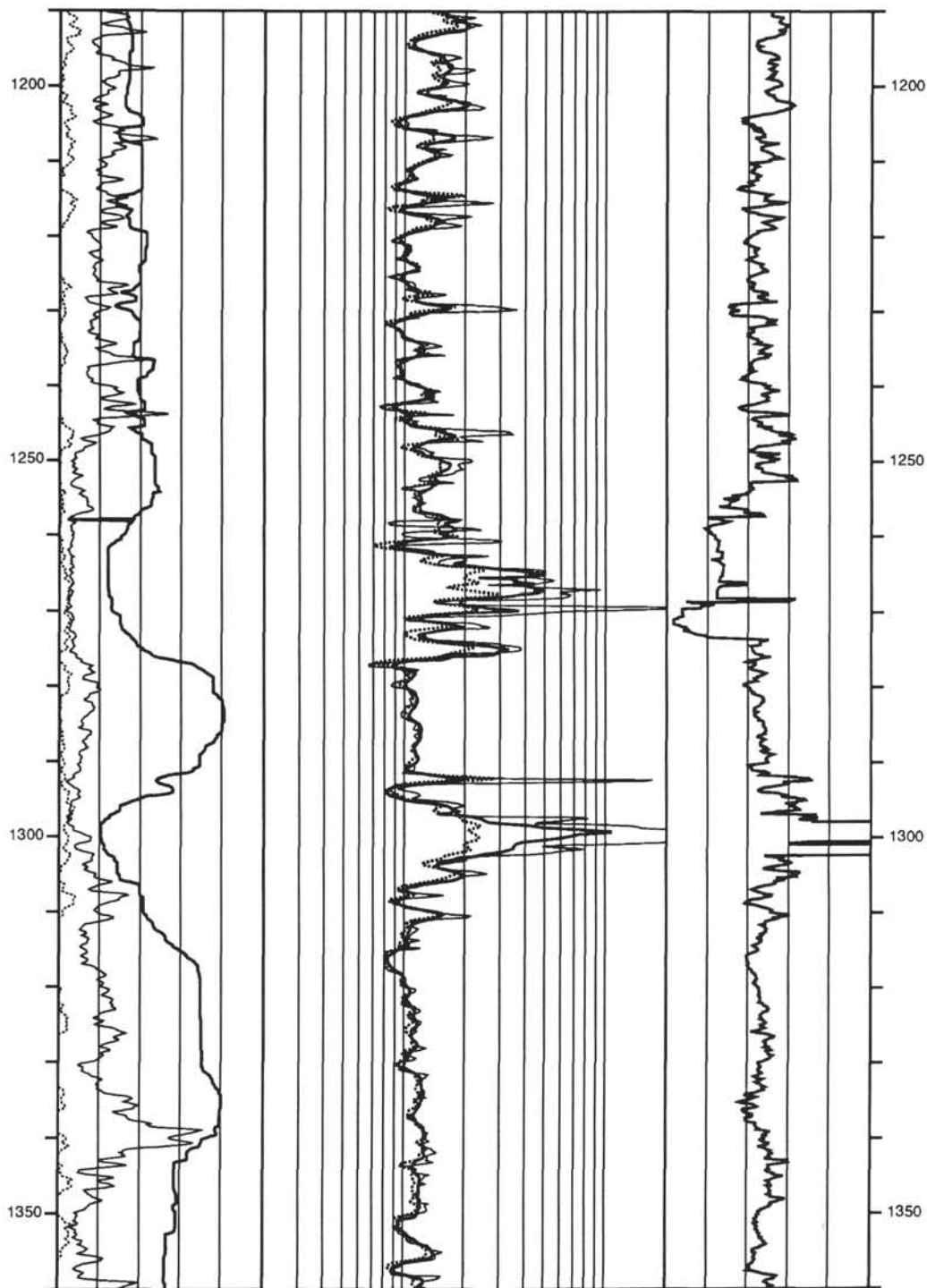
Hole 866A: Resistivity-Sonic-Natural Gamma Ray Log Summary (continued)

DEPTH BELOW SEA FLOOR (m)	SPECTRAL GAMMA RAY		RESISTIVITY		VELOCITY	DEPTH BELOW SEA FLOOR (m)
	TOTAL		FOCUSED			
0	API units	80 .2	2000			
0	COMPUTED		MEDIUM			
0	API units	80 .2	ohm-m	2000		
9	CALIPER		DEEP		1.5	
	in	19 .2	ohm-m	2000	km/s	7.5



Hole 866A: Resistivity-Sonic-Natural Gamma Ray Log Summary (continued)

SPECTRAL GAMMA RAY				RESISTIVITY				VELOCITY					
TOTAL				FOCUSED									
0	API units	80	.2	2000									
COMPUTED				MEDIUM									
0	API units	80	.2	ohm·m	2000								
CALIPER				DEEP				VELOCITY					
9	in	19	.2	ohm·m	2000	1.5	km/s	7.5					



Hole 866A: Resistivity-Sonic-Natural Gamma Ray Log Summary (continued)

DEPTH BELOW SEA FLOOR (m)	SPECTRAL GAMMA RAY			RESISTIVITY			DEPTH BELOW SEA FLOOR (m)
	TOTAL			FOCUSED			
	API units	80	1.2	2000			
0							
	COMPUTED			MEDIUM			
0	API units	80	1.2	ohm-m			2000
	CALIPER			DEEP			
9	in	19	1.2	ohm-m	2000	1.5	VELOCITY km/s 7.5

